THE UNIVERSITY *of* EDINBURGH

Magneto-Structural Studies of Paramagnetic Metal Cages

Hector Fraser

A Thesis Submitted for the degree of Doctor of Philosophy

School of Chemistry

Faculty of Science and Engineering

The University of Edinburgh

August 2018

For Grandma

Abstract

A central concern within the field of molecular magnetism has been the elucidation of magneto-structural correlations. This thesis describes a variety of systems and endeavours to study the relationship between structure and magnetic properties in these systems. The first body of work (chapters 2 and 3) studies Cr^{III} dimers, with the metal centres displaying a dialkoxo bridging moiety and latterly an additional carboxylate bridge to direct the synthesis of ferromagnetic analogues. The second section of work (chapters 4-6) moves forward to the study of larger, heterometallic 3d-3d compounds, through the synthesis of a large family of Anderson type $M^{III}_2M^{II}_5$ wheels and a subsequent family of $(V^{IV}O)_2M^{II}_5$ wheels.

Chapter 2 describes a series of di-alkoxo bridged Cr(III) dimers, synthesised using the pyridine alcohol ligands 2-pyridinemethanol (hmpH) and 2-pyridineethanol (hepH) as well as 2-picolinic acid (picH). The structures fall into four general categories and are of formula: $[Cr_2(OMe)_2(pic)_4]$, $[Cr_2(hmp)_2(pic)_2X_2]$ (where X = Cl, Br), $[Cr_2(L)_2Cl_4(A)_2]$ (where L = hmp, A = H_2O; L = hmp, A = pyridine; L = hmp, A = 4-picoline; L = hep, A = H_2O), and $[Cr(hmp)(hmpH)Cl_2$. Magnetic studies show relatively weak antiferromagnetic exchange interactions between the Cr(III) centres and DFT calculations are used to develop magneto-structural correlations, showing that the magnitude and sign of the *J* value is strongly dependent upon the orientation of the dihedral angle formed between the bridging Cr_2O_2 plane and the O–R vector of the bridging group, and the Cr–O–Cr–O dihedral angle.

Chapter 3 builds on the work from the previous chapter with discussion of a large family of chromium(III) dimers, synthesised using a combination of carboxylate and diethanolamine type ligands. The compounds have the general formula $[Cr_2(R^1\text{-deaH})_2(O_2CR^2)Cl_2]Cl$ where R^1 = Me and R^2 = H, Me, CMe_3, Ph, 3,5-$(Cl)_2$Ph, $(Me)_5$Ph, R^1 = Et and R^2 = H, Ph. The compound $[Cr_2(Me\text{-deaH})_2Cl_4]$ was also synthesised in order to study the effect of removing/adding the carboxylate bridge to the observed magnetic behaviour. Magnetic studies reveal ferromagnetic exchange interactions between the Cr(III) centres in the carboxylate bridged family with coupling constants in the range $+0.37 < J < +8.02$ cm^{-1}. Removal of the carboxylate to produce the dialkoxide-bridged compound results in antiferromagnetic exchange between the Cr(III) ions. DFT calculations to further develop the magneto-structural correlations reveal the ferromagnetic exchange is the result of an orbital counter-complementarity effect occurring upon introduction of the bridging carboxylate.

Chapter 4 reports a family of heterometallic Anderson-type 'wheels' of general formula $[M^{III}_2M^{II}_5(hmp)_{12}](ClO_4)_4$ (where M^{III} = Cr or Al and M^{II} = Ni or Zn giving $[Cr_2Ni_5]$, $[Cr_2Zn_5]$, $[Al_2Ni_5]$ and $[Al_2Zn_5]$; hmpH = 2-pyridinemethanol) synthesised solvothermally. The metallic skeleton describes a centred hexagon with the M^{III} sites disordered around the outer wheel. The structural disorder is characterised *via* single crystal X-ray crystallography, 1-3D ^{1}H and ^{13}C solution-state NMR spectroscopy of the diamagnetic analogue, and solid-state ^{27}Al MAS NMR spectroscopy of the Al containing analogues. Alongside ESI mass spectrometry, these techniques show that structure is retained in solution, and that the disorder is present in both the solution and solid-state. Solid-state dc susceptibility and magnetisation measurements on $[Cr_2Zn_5]$ and $[Al_2Ni_5]$ reveal the Cr-Cr and Ni-Ni exchange interactions to be $J_{Cr\text{-}Cr}$ = -1 cm^{-1} and $J_{Ni\text{-}Ni,r}$ = -5 cm^{-1}, $J_{Ni\text{-}Ni,c}$ = 10 cm^{-1}. Fixing these values allows us to extract $J_{Cr\text{-}Ni,r}$ = -1.2 cm^{-1}, $J_{Cr\text{-}Ni,c}$ = 2.6 cm^{-1}, the exchange between adjacent Ni and Cr ions on the ring is antiferromagnetic and between Cr ions on the ring and the central Ni ion is ferromagnetic.

Chapter 5 focusses on planar molecules, espanding the family of heterometallic Anderson-type 'wheels' discussed in chapter 4 to include M^{III} = Cr, Al and M^{II} = Co, Fe, Mn, Cu, affording five new species of formulae $[Cr_2Co_5(hmp)_{12}](ClO_4)_4$, $[Cr_2Fe_5(hmp)_{12}](ClO_4)_4$, $[Cr_2Mn_5(hmp)_{12}](ClO_4)_4$, $[Cr_2Cu_5(hmp)_{12}](ClO_4)_2(NO_3)_2$ and $[Al_2Co_5(hmp)_{12}](ClO_4)_4$. As per previous family members, the two M^{III} sites are disordered around the outer wheel, with the exception of $[Cr_2Cu_5]$ where the the Cu^{II} sites are localised. A structurally related, but enlarged planar disc possessing a $[M^{III}_6M^{II}]$ hexagon capped on each edge by a Cu^{II} ion is also reported, which is formed only when M^{III} = Al and M^{II} = Cu. In $[Al^{III}_6Cu^{II}_7(OH)_{12}(hmp)_{12}](ClO_4)_6(NO_3)_2$ the Anderson moiety contains a central, (symmetry-imposed) octahedral Cu^{II} ion surrounded by a wheel of Al^{III} ions. Solid-state dc susceptibility and magnetisation measurements reveal the presence of competing exchange interactions in the Anderson wheels family, and weak antiferromagnetic exchange between the Cu^{II} ions in $[Al_6Cu_7]$.

Chapter 6 describes two heterometallic wheels of formula $[(V^{IV}O)_2M^{II}_5(hmp)_{10}Cl_2](ClO_4)_2{\cdot}2MeOH$ (where M^{II} = Ni or Co) displaying the same Anderson-type structure as seen in chapters 4 and 5, however the use of the vanadyl moiety has the effect of removing the disorder, with the two vanadyl ions sitting on opposing sides of the ring. The magnetic properties of both show competing antiferro- and ferromagnetic interactions.

Lay Summary

The body of work described in this thesis sits within the field of molecular magnetism, an area centred around the study of magnetic properties in individual molecules, specifically metal complexes. The first part of this thesis aims to investigate the structural and magnetic properties of molecules containing the 3d-transition metal chromium. By developing a detailed understanding of both, it then aims to describe the relationships which link structure and magnetism within the compounds and thus elucidate what are known as magneto-structural correlations in order to facilitate future design of compounds of this type. The second part involves the study of larger molecules containing chromium alongside other transition metals (known as heterometallic molecules) and investigating and quantifying the interesting magnetic properties that arise from these combinations.

Acknowledgements

First and foremost I have to thank my supervisor, Prof. Euan Brechin, for his endless interest and enthusiasm and for always being around for a chat. He has given me the chance to travel all over the world as well as sample some of Edinburgh's finest restaurants (and shown me many of Copenhagen's best bars). I can honestly say I have thoroughly enjoyed my project, which I have found interesting, challenging and rewarding. The freedom he gave me to do my own thing and make the project my own has really made it for me.

Secondly I would like to thank Dr Murray Low and Ms Elaine Sutherland for allowing me to get so involved with undergraduate teaching and in particular Murray for sticking his neck out and putting me in front of students to lecture (and almost keeping his cool despite constant comments about his height), I have hugely enjoyed the teaching I have done and have learnt a great deal.

I would also like to thank the rest of the Brechin group, Robbie deserves a special mention for being the best person I could have started and finished the experience with, but also Julia, Marco, Helen, Anders, Priyanka and Ross for the endless sports chat and for being gracious in defeat when I ran away with the football predictor – "the leagues mad this year, it's all just luck".

I would like to thank my family and friends for always trying to take an interest even if they don't understand. Props to my mum for embarking on her chemistry lessons with me and often getting it nearly right when she explains it to others. A special mention to my gran, pushing 90 and still absolutely killing it, it has been so nice to follow in her footsteps and study chemistry here where she studied it nearly 70 years ago, she has consistently known the most in the family about what I am doing.

Last but not least I have to thank Chloe, always interested and always pushing me, never just congratulating but always saying "that's okay but how are you going to get more?". She has kept me motivated and driven me on while also going on some amazing trips with me to make all the hard work worthwhile. She has had to listen to endless chat about my work and has always supported me.

Declaration

I hereby declare that except where specific reference is made to other sources, the work contained in this thesis is the original work of the author. It has been composed by the candidate and has not been submitted, in whole or in part, for any other degree, diploma, or other qualification.

Hector Fraser

Table of Contents

Format of the Thesis

Each chapter of this thesis, with the exception of chapter 1, is made up of contributions to peer-reviewed papers, which have already been published or submitted for publication. To fulfil the requirements of The University of Edinburgh regarding the preparation and submission of a thesis for the degree of PhD, they have been reformatted accordingly.

Chapter 1: Introduction

A history of magneto-structural correlations in molecular magnetism.

Chapter 2: Magneto-structural correlations in a family of di-alkoxo bridged chromium dimers

Structural and magnetic studies of a family of antiferromagnetic Cr^{III} dimers with pyridine alcohol type ligands leading to magneto-structural correlations.

Chapter 3: A simple methodology for constructing ferromagnetically coupled Cr(III) compounds

Structural and magnetic studies of a family of ferromagnetic Cr^{III} dimers with diethanolamine ligands leading to magneto-structural correlations.

Chapter 4: Order in disorder: solution and solid-state studies of $[M^{III}_2 M^{II}_5]$ wheels (M^{III} = Cr, Al; M^{II} = Ni, Zn)

Structural and magnetic studies of a family of heterometallic Anderson-type wheels displaying positional disorder of the M^{III} ion leading to magnetic fitting of the title compound.

Chapter 5: Cages on a plane: a structural matrix for molecular 'sheets'

Investigation of planar compounds based on the $[M_3O_4]^{n+}$ partial cubane, including structural and magnetic studies of additional members of the family of heterometallic Anderson-type wheels and extension of this family to a larger planar compound.

Chapter 6: Vanadyl-based heterometallic wheels

Structural and magnetic studies of a family of heterometallic vanadyl based Anderson-type wheels in which the positional disorder is removed by the vanadyl unit.

Chapter 8: Conclusions and future perspectives

External collaborator contributions

Chapter 2:

DFT studies carried out by Dr Gunasekaran Velmurugan and Prof. Gopalan Rajaraman

Crystallographic measurements carried out by Dr Gary Nichol

Chapter 3:

DFT studies carried out by Dr Sourav Dey and Prof. Gopalan Rajaraman

Crystallographic measurements carried out by Dr Gary Nichol

Chapter 4:

Solution state NMR studies carried out and analysed with the assistance of Dr Dušan Uhrín

Solid state NMR carried out by Prof. Ulla Gro Nielsen

Fitting of magnetic data carried out by Prof. Jürgen Schnack

Crystallographic measurements carried out by Dr Gary Nichol

Chapter 5:

Crystallographic measurements carried out by Dr Gary Nichol

Chapter 6:

Magnetic measurements and fitting carried out by Dr Stergios Piligkos

Crystallographic measurements carried out by Dr Gary Nichol

Publications

In Preparation

"Alleviating the frustration in a new family of polyoxometalates: from [Fe_{34}] to [Fe30]"
Hector W. L. Fraser, Alice Dearle, Edward Lee, Gary S. Nichol, Marco Evangelisti, Jürgen Schnack, Leroy Cronin and Euan K. Brechin, *Angew. Chem. Int. Ed.*, 2018, To Be Submitted.

"A ferromagnetically coupled, bell-shaped [Ni_4Gd_5] cluster with an S = 43/2 ground-state"
Foteini E. Kakaroni, Demetrios I. Tzimopoulos, Hector W. L. Fraser, Milosz Siczek, Tadeusz Lis, Marco Evangelisti, Euan K. Brechin and Constantinos J. Milios, Chem. Comm., 2018, To Be Submitted.

"Towards polyoxometalates with Fe(III): a spin frustrated [Fe_{34}] molecular metal oxide"
Alice Dearle, Hector W. L. Fraser, Sergio Sanz, Edward Lee, Gary S. Nichol, Marco Evangelisti, Jürgen Schnack, Leroy Cronin and Euan K. Brechin, *Angew. Chem. Int. Ed.*, 2018, To Be Submitted.

"Cages on a plane: a structural matrix for molecular 'sheets'"
Hector W. L. Fraser,[a] Gary S. Nichol,[a] Amgalanbaatar Baldansuren,[b] Eric J. L. McInnes[b] and Euan K. Brechin, *Dalton Trans.*, 2018, Submitted.

"Vanadyl-based heterometallic wheels"
Hector W. L. Fraser, Gary S. Nichol, Stergios Piligkos, and Euan K. Brechin, *Chem. Comm.*, 2018, To Be Submitted.

"Oxidation State Distributions Provide Insight into Parameters Directing the Assembly of Metal-Organic Nanocapsules"
Asanka S. Rathnayake, Hector W. L. Fraser, Euan K. Brechin, Scott J. Dalgarno, Jacob E. Baumeister, Pokpong Rungthanaphatsophon, Justin R. Walensky, Charles L. Barnes, and Jerry L. Atwood, *J. Am. Chem. Soc.*, 2018. DOI: 10.1021/jacs.8b07775

"Unveiling Hidden Coordination Sites in an Fe^{II}/Fe^{III}-seamed Pyrogallol[4]arene Nanocapsule" Asanka S. Rathnayake, Hector W. L. Fraser, Euan K. Brechin, Scott J. Dalgarno, Jakob E. Baumeister, Joshua White, Pokpong Rungthanaphatsophon, Justin R. Walensky, Charles L. Barnes, and Jerry L. Atwood, *J. Am. Chem. Soc.*, 2018, Submitted.

2018

"A simple methodology for constructing ferromagnetically coupled Cr(III) compounds"
Hector W. L. Fraser, Lucy Smythe, Sourav Dey, Gary S. Nichol, Stergios Piligkos, Gopalan Rajaraman and Euan K. Brechin, *Dalton Trans.*, 2018, **47**, 8100-8109. DOI: 10.1039/c8dt01963k

"In situ redox reactions facilitate the assembly of a mixed-valence metal-organic nanocapsule" Asanka S. Rathnayake, Hector W.L. Fraser, Euan K. Brechin, Scott J. Dalgarno, Jakob E. Baumeister, Joshua White, Pokpong Rungthanaphatsophon, Justin R. Walensky, Charles L. Barnes, Simon J. Teat and Jerry L. Atwood, *Nat. Commun.*, 2018, **9**, 2119. DOI: 10.1038/s41467-018-04541-w

"Order in disorder: solution and solid-state studies of $[M^{III}_2\ M^{II}_5]$ wheels (M^{III} = Cr, Al; M^{II} = Ni, Zn)"
Hector W. L. Fraser, Gary S. Nichol, Dušan Uhrín, Ulla Gro Nielsen, Marco Evangelisti, Jürgen Schnack and Euan K. Brechin, *Dalton Trans.*, 2018, **47**, 11834-11842. DOI: 10.1039/C8DT00685G

2017

"Magneto-structural correlations in a family of di-alkoxo bridged chromium dimers"
Hector W. L. Fraser, Gary S. Nichol, Gunasekaran Velmurugan, Gopalan Rajaraman and Euan K. Brechin, *Dalton Trans.*, 2017, **46**, 7159-7168. DOI: 10.1039/c7dt01197k

Conferences Attended

2018

International Conference on Coordination Chemistry (ICCC), Sendai, Japan

Poster Presentation — 30th July - 4th August 2018

2017

Universities of Scotland Inorganic Conference (USIC), University of St Andrews, UK

Oral Communication — 11th-12th August 2016

EuCheMS Inorganic Chemistry Conference (EICC), Copenhagen, Denmark

Poster Presentation — 2nd-5th July 2017

Joseph Black Chemistry Conference, The University of Edinburgh, UK

Poster Presentation — 1st June 2017

2016

International Conference on Molecule-Based Magnets (ICMM), Sendai, Japan

Poster Presentation — 4th-8th September 2016

EaStChem Conference for Early-career Researchers (ECECR), The University of Edinburgh, UK

25th August 2016

Universities of Scotland Inorganic Conference (USIC), University of Strathclyde, UK

Poster Presentation — 11th-12th August 2016

Scottish Dalton Meeting, The University of Edinburgh, UK

3rd June 2016

Joseph Black Chemistry Conference, The University of Edinburgh, UK

26th May 2016

Abbreviations

FM	Ferromagnetic
AFM	Antiferromagnetic
QTM	Quantum tunnelling of the magnetisation
QIP	Quantum information processing
SMM	Single-molecule magnet
SCM	Single-chain magnet
SIM	Single-ion magnet
M-S	Magneto-structural
GHP	Glerup Hodge Pedersen
AOM	Angular overlap model
TM	Transition metal
MCE	Magneto-caloric effect
POM	Polyoxometalate
ASU	Asymmetric unit

CHAPTER 1: INTRODUCTION

A HISTORY OF MAGNETO–STRUCTURAL CORRELATIONS IN MOLECULAR MAGNETISM

1.1 The birth of the field

The study of molecular magnetism is relatively modern in the context of the wider studies of the sciences, however in the past few decades it has matured and expanded into a dynamic interdisciplinary field. This field is of course born from the wider field of magnetism, a comparatively ancient field with the first written accounts of magnetic behaviour appearing over 2500 years ago in ancient Greece with the term often attributed to the region Magnesia, and additional evidence of early application for compasses in China. Despite these early observations, understanding and explaining this phenomena took many great scientific minds with some truly famous names; Coulomb's work on polarising molecules with magnetisation, Oersted's seminal experiment in 1820 showing that an electric current influences a compass needle's orientation, Ampere suggesting internal currents giving rise to magnetism, and Faraday conceiving the concept of a magnetic field and the terms diamagnetism and paramagnetism. Important in building on this work was the mathematical work of Maxwell to help describe electromagnetism, and Curie's investigation of temperature dependence (Curie law) and introduction of the term ferromagnet. The sheer number of these household names tells of the importance of this field. The final major piece of the jigsaw in providing the tools for explaining magnetic phenomena was the quantum mechanical revolution.

From this vast and important field the birth of molecular magnetism could be pinned down to the 1950s with the study of the dinuclear copper(II) acetate "paddlewheel", $[Cu_2(OAc)_4(H_2O)_2]$ (Figure 1), the first polynuclear metal complex to undergo magnetic studies.[1, 2] The investigation of the magnetic properties of this compound revealed strong, through bond antiferromagnetic coupling between the copper centres,[3] a new concept and one which ignited a hunt to explain the findings and discover other systems exhibiting such properties. The emergence of this field came amidst a surge of interest in molecular based functionality on the back of a wave of understanding from quantum mechanics and the beginning of a, still increasingly pertinent today, fashion for miniaturisation. Certainly today you can find a multitude of fields described as molecular, the benefits of understanding and manipulating (designing) matter at the most fundamental scale are obvious. With the arrival of the field came a need for both developing an understanding of new magnetic phenomena at a molecular level, and for the synthesis and design of new molecular substances displaying magnetic properties as well as experimental characterisation of these properties. This tight-

rope walk across the boundary of chemistry and physics required the synthetic expertise of chemists and theoretical unravelling of phenomena by physicists leading to close collaboration in a truly interdisciplinary area which persists today. While the first book on the area came in 1973, beginning to bring together some of the concepts of magnetic properties in metal complexes, this remained a specialised topic.[4] A NATO ASI held in 1983 in Italy could be highlighted as the point at which the field unified and emerged as a divergent field of research preceding the ASIs publication "Magneto-structural correlations in exchange coupled systems" in 1985 and the publication of Olivier Kahn's work "Molecular Magnetism" in 1993, broadening the knowledge of the area and beginning more widespread appeal.[5, 6] In the proceeding years this field has expanded greatly, with arguably the key discovery being the observation of single-molecule magnetism,[7, 8] a phenomena where a molecule retains its magnetisation upon removal of an applied magnetic field.[9, 10] This discovery, in the compound $[Mn_{12}O_{12}(OAc)_{16}(H_2O)_4]$,[7] galvanised the field and in the following years it branched out into other interesting areas such as single-chain magnets (SCMs),[11, 12] single-ion magnets (SIMs),[13-15] and a multitude of areas consisting of multifunctional magnetic materials.[16-19] Expansion of the field has heralded the discovery of new phenomena such as quantum tunnelling of magnetisation[20] and quantum information processing,[21] which may lead to an array of exciting new applications and technologies.

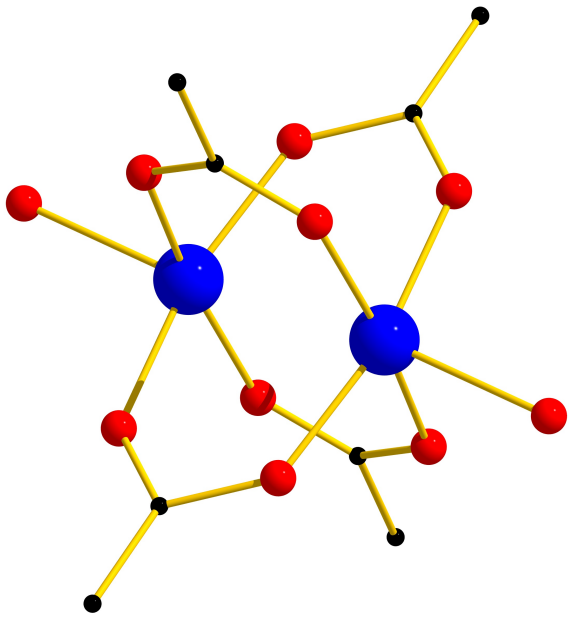

Figure 1. Structural representation of the Cu_2 paddlewheel. Colour code: Cu = blue, O = red, C = black. H-atoms omitted for clarity.

1.2 Magneto-structural correlations

The field of molecular magnetism began with the observation of through bond magnetic exchange in copper(II) "paddlewheels".[1, 2] The mechanism whereby two metal centres can magnetically communicate with one another via the bridging atoms that link the metal centres is termed superexchange. The nature and magnitude of this coupling is described by the exchange parameter, *J*, with an individual exchange being categorised as ferromagnetic (FM) (positive *J* by convention; $\hat{H} = -2J\hat{S}_i\hat{S}_j$) when the spins of the metal centres are aligned parallel, or antiferromagnetic (AFM) (negative *J* by convention) when the spins are aligned antiparallel. The sign and strength of this exchange is dictated by the identity, number and geometry of the bridging atoms with *J* values ranging from over one thousand wavenumbers to fractions of wavenumbers. In simple systems it is relatively straightforward to study the interactions as the pathway of exchange is clearly defined; however, in more complex systems where many exchange pathways are operating it becomes increasingly complicated (Figure 2).

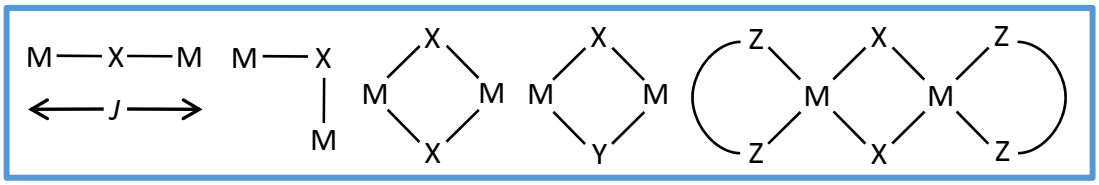

Figure 2. Illustration of different bridging between metal centres, where *J* is the exchange constant between the metals, X and Y are bridging atoms (e.g. O), and Z represents the bonding atom on a chelating ligand which can be innocent or non-innocent.

As the field expanded and more compounds were studied, it became possible to both quantify and rationalise the magnetic properties of a compound with respect to its structural parameters. Such magneto-structural (M-S) correlations became of fundamental importance in the deconvolution of magnetic behaviour, and in uncovering the mechanisms of magnetic exchange in order to direct future design toward the 'improvement' of magnetic behaviours.[5] Dimeric species present ideal systems for this type of study due to their simplicity, and thus formed the majority of the elementary research in this area. An understanding of these simple systems is crucial if one is to quantify larger, more complex systems whose structures may be composed of similar building blocks. From here onwards, all distances will be reported in angstroms (Å) and all angles in degrees (°).

Copper dimers

The first magneto-structural correlation to be developed was on planar dihydroxo bridged copper(II) dimers of the form $[Cu(L)OH]_2^{2+}$, by Hatfield and Hodgson.[22] They showed that the magnetic superexchange between copper centres was strongly dependent upon the Cu-O-Cu bridging angle and to a lesser extent on the Cu-O distance, parameters which have since been shown to have relevance in a plethora of bridged Transition Metal (TM) systems. Over this vast series of compounds they observed exchange constants in the range $86 > J > -255$ cm^{-1} for Cu-O-Cu angles of 95.6° to 104.1°. Their M-S correlations yielded two equations (1 and 2) derived from the lines of best fit for the dependence of J on each parameter individually (Figure 3). For the Cu-O-Cu bridging angle (here denoted as ϕ):

$$2J = (-74.53\phi + 7270)\ cm^{-1} \quad (1)$$

For the Cu-Cu distance (here denoted as $R_{Cu\text{-}Cu}$):

$$2J = (-4508R_{Cu\text{-}Cu} + 13018)\ cm^{-1} \quad (2)$$

The inter-copper separation ($R_{Cu\text{-}Cu}$ in Å) displays good correlations across a breadth of species as the vast majority of compounds display very nearly planar Cu_2O_2 bridging units, with the Cu-O distances varying very little. In systems where the bridging unit is non-planar however, the correlations break down. Their model showed a linear dependence between each parameter and the J value and concluded that the magnetic exchange changed sign at 97.5° with FM exchange below and AFM exchange above that value (Figure 3).[22, 23]

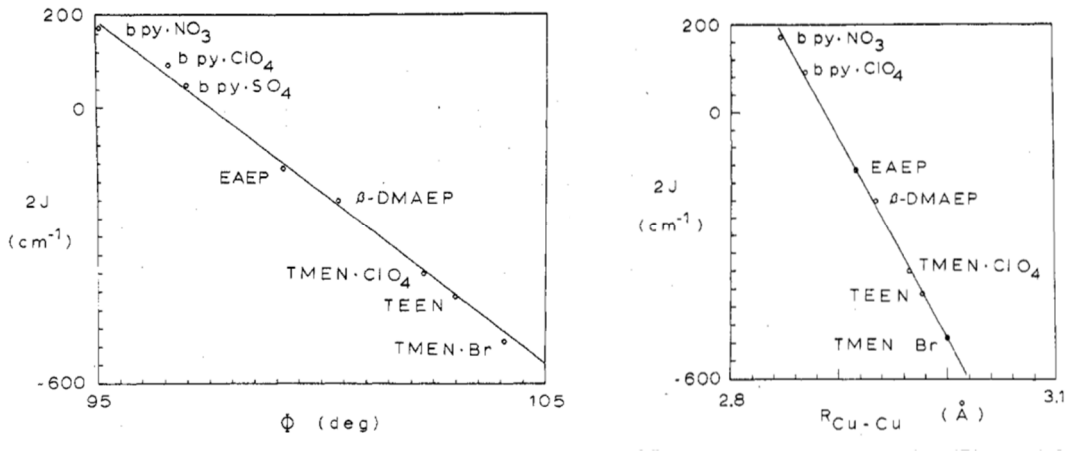

Figure 3. A graphical depiction of the linear dependence of $2J$ on the bridging angle (ϕ) (left) and the Cu-Cu distance ($R_{Cu\text{-}Cu}$) (right) in hydroxo-bridged copper(II) dimers. The straight lines are calculated from equations 1 (left) and 2 (right).[22]

Chromium dimers

A similar study on dihydoxo bridged chromium(III) dimers found that in addition to both the Cr-O distance (r) and the Cr-O-Cr bridging angle (ϕ) being influential, of greater importance was the variation of the dihedral angle between the O-H vector of the bridging group and the bridging Cr_2O_2 plane (θ), i.e. the hybridisation of the bridging oxygen atom (Figure 4).[24, 25]

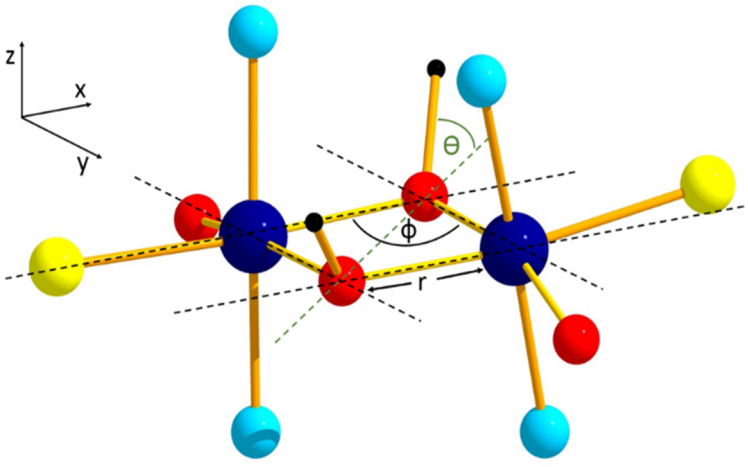

Figure 4. Diagrammatic representation of the key structural parameters influencing the sign and magnitude of magnetic exchange in $[Cr^{III}_2(OH)_2]$ dimers where r = Cr-O distance ϕ = Cr-O-Cr bridging angle and θ = dihedral angle between the O-H vector and the Cr_2O_2 plane.

This model treats the interactions between the Cr^{III} centres as being composed of a combination of AFM and FM contributions, thus $J = J_{AF} + J_F$. Based on this model, the vast majority of complexes show AFM exchange, with FM exchange only possible for a small window of ϕ and θ values. While the GHP model (Glerup-Hodgson-Pedersen), based on the principles of the angular overlap model (AOM),[26] predicts well systems which display AFM or weakly FM exchange, it does not predict the presence of moderate-strong FM exchange in any scenario. This is at odds with a FM coupled Cr^{III} dimer synthesised in 2014 ($(Ph_4P)_4)[(SCN)_4Cr(OH)_2Cr(NCS)_4]$), which the GHP model predicted to be AFM; this stimulated a new DFT study which was carried in order to improve the MS correlation.[27] This study suggested that the GHP model underestimates the FM contribution (or overestimates the AFM contribution) to the overall exchange. The new correlation (Figure 5) predicts FM exchange for ϕ angles between 97.5° and 102°, and for θ > 39°. While the Cr-O bond length is theoretically important, experimentally it varies very little (1.93-1.99 Å) in chromium

diols.[27] The experimentally accessible ϕ range lies between 99° and 104°, and while it does play a part, the value of θ has a more important effect on *J* within the experimentally accessible range. The new DFT model is significantly better for reproducing experimental data – in particular not overestimating AFM contributions.

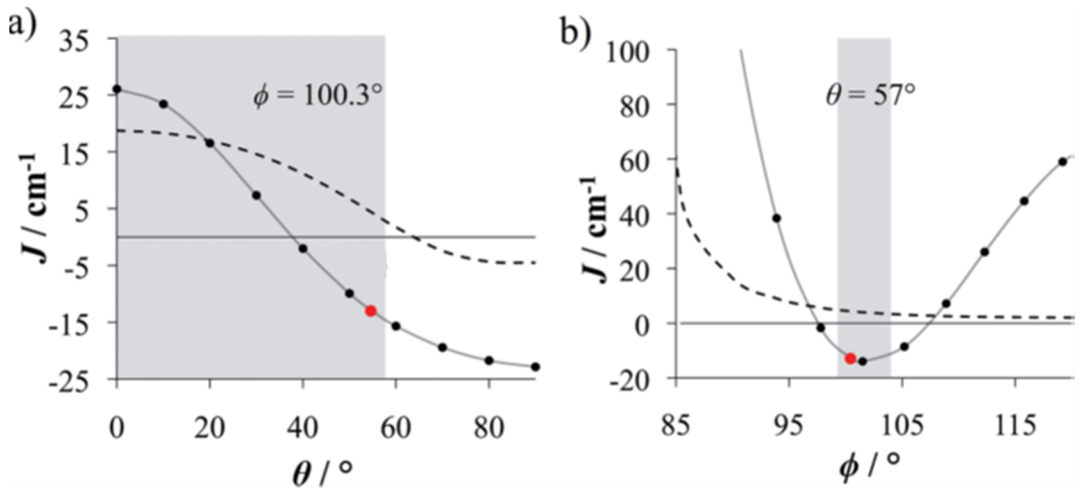

Figure 5. DFT computed M-S correlations for hydroxo bridged chromium(III) dimers depicting the dependence of *J* on (a) θ and b) ϕ, the GHP model for the same angle variations is shown as a dotted line and the grey shaded area shows the experimentally accessible ranges.[27]

Iron dimers

M-S correlations on oxo-bridged iron(III) dimers have also been much studied. A correlation was first developed by Gorun and Lippard in 1991 which attempted to cover doubly and triply (but not singly) bridged dinuclear iron(III) compounds, with O^{2-}, OR^-, OPh^-, OH^- or O_2X^- bridges.[28] Gorun and Lippard incorrectly suggested that the Fe-O-Fe bridging angle should be considered less important, and even hinted that it holds no correlation with *J*.[29, 30] In their study they attempted to correlate *J* (cm^{-1}) to a single structural parameter, *P* (Å), which corresponded to half of the length of the shortest Fe-O-Fe bridge in a complex.[28] This gave the relation:

$-J = A \exp(BP)$ where $A = 8.763 \times 10^{11}$ cm^{-1} and $B = -12.663$ $Å^{-1}$

In 1997 Weihe and Güdel refined the relationship for di-oxo bridged Fe(III) dimers, clarifying the key structural parameters involved.[31] They employed three parameters, r_1, r_2 and ϕ (Figure 6) and attempted to address the question of why *J* is apparently insensitive to the

bridging angle – a parameter on which the M-S correlations in other oxo-bridged dimers depend dramatically on. Their AOM study developed the best fit relation:

$J_{model} = 1.337 \times 10^8(3.536 + 2.488 \cos \phi + \cos^2 \phi) \times \exp(-7.909r)$

Here, *r* is the mean Fe-O bond length (Å). Figure 6 shows the graphical relationship proving that *J* and *r* are indeed correlated, but also shows *J* and ϕ to be correlated, albeit to a lesser degree. The smaller dependence of ϕ is attributed to competing exchange pathways which maximise and minimise at different values and thus partially compensate.[31] This model, along with another model developed in 2001 by Werner et al. have been combined in the program, wxJFinder, which can be used to calculate coupling constants in oxo bridged iron systems.[32, 33]

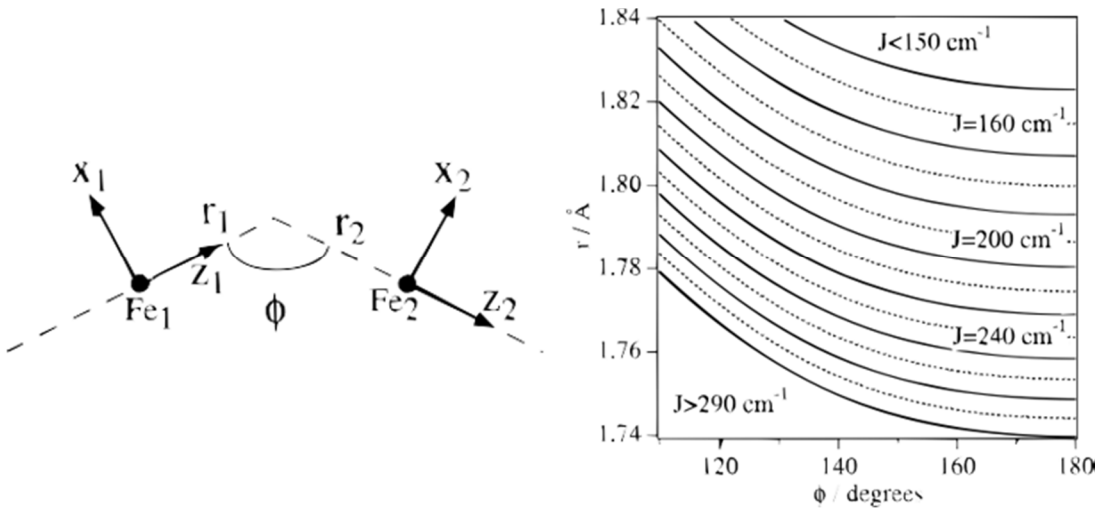

Figure 6. Left: Structural representation of the pertinent bridging parameters for oxo-bridged iron(III) dimers. Right: The M-S correlation developed for this system showing the dependence of *J* on *r* and ϕ.[31]

Manganese dimers

Manganese complexes arguably represent the largest family of TM dimers studied to date. M-S correlations for manganese(III) compounds of formula $[Mn^{III}_2O(R\text{-}sao)(tpa)_2](ClO_4)_2$ (where R-saoH_2 is a derivatised phenolic oxime and tpa is tris(2-pyridyl-methyl)amine), have been developed;[34] the combination of two bridging motifs – one μ-O^{2-} and one Mn-O-N-Mn bridge – makes this an interesting example of an asymmetrically bridged dimer (Figure 7 dimer type a). It was found that the dominant structural parameter in this case is the dihedral Mn-O-N-Mn torsion angle, a linear correlation between this angle and the magnitude of *J*

was found, with increasing torsion angle giving reduced AFM exchange. This is due to the $d_{yz}|\pi^*|d_{yz}$ interaction decreasing (the notation A|B|C denotes the interaction between the metal orbitals A and C via the bridging ligand orbital B), affording dominant FM coupling at higher angles, in this case occurring above 18°.[34] A similar study was carried out on a structurally related family of manganese(III) dimers using dpa as a co-ligand (dpa = di-(2-picolyl)-amine). Here, the metal centres are connected via two Mn-O-N-Mn bridges giving compounds of general formula $[Mn^{III}_2(R\text{-}sao)_2(dpa)_2](ClO_4)_2$ (Figure 7 dimer type c).[35] Two cases were discussed with the orientation of the Jahn-Teller (J-T) axes crucial, in one case the J-T axes lie in the bridging plane leading to FM exchange (Figure 7 type b) and in the other they arrange perpendicular to it as in the previously discussed family (Figure 7 type c). When the J-T axes are in the plane, an "accidental" orthogonality is created between the Mn-N-O plane of one ion and the J-T axis of the other and the exchange depends strongly on the torsion angle of the oxime moiety. In the second case, the change in the J-T axes positions leads to weak AFM exchange with Mn-O-N-Mn torsion angles of **less** than 20° giving FM exchange (Figure 7).[35]

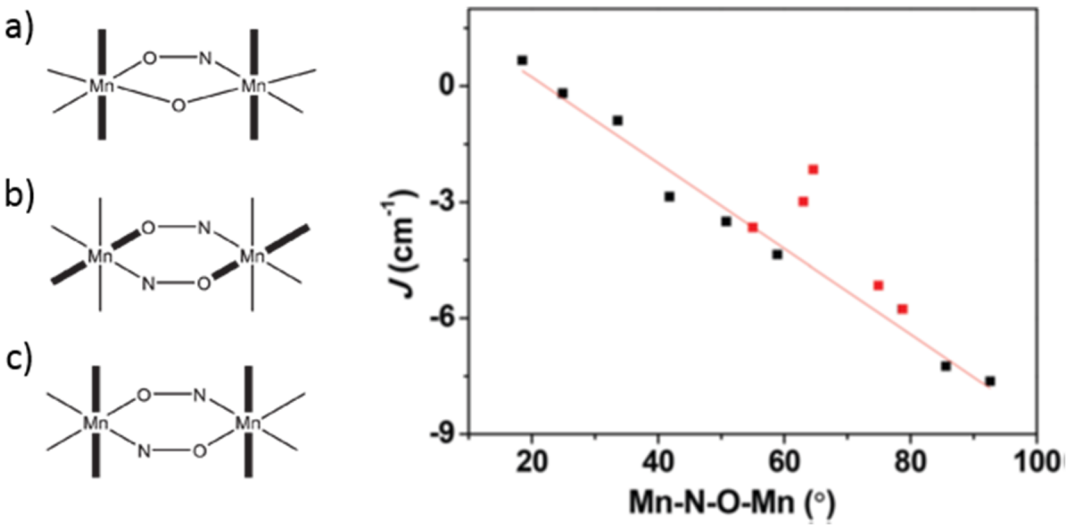

Figure 7. Left: Structural representation of Mn^{III} dimers type a, b and c highlighting the bridging moieties and the positions of the J-T axes (bold). Right: M-S correlation for the dependence of J on Mn-O-N-Mn torsion angle in dimers of type c showing computationally determined points (black) and experimental points (red).[35]

Iron butterflies

More complex M-S correlations have been carried out on larger clusters including tetranuclear iron(III) butterfly complexes[36, 37] where the structure is based on the $[Fe_4O_2]^{8+}$ framework with two types of Fe^{III} ions, two inner ions in the "body" (Fe_b) and two outer ions as the "wings" (Fe_w). In these compounds three exchange pathways are considered: the interaction between the two Fe_b ions (J_{bb}), the interaction between the Fe_b and Fe_w ions (J_{bw}), and the (much weaker) interaction between the two Fe_w ions (J_{ww}) (Figure 8). The strongest of these is an AFM interaction between the body and the wing, J_{bw}, via a μ_3-O bridge, while J_{ww} shows weak AFM exchange and J_{bb} can be FM or AFM depending on the particular structural parameters. Analysis shows a relatively strong dependence of J_{bw} and J_{bb} on the Fe-O distances and Fe-O-Fe angle in the central Fe_2O_2 body. A well-defined linear correlation between the interaction of the "wing" to the "body" of the butterfly and the square of the overlap of the magnetic orbitals is observed.[37] These MS correlations are of further interest as this tetranuclear unit appears frequently in larger iron complexes such as Fe_6,[38] Fe_8,[39] Fe_{10},[40] and Fe_{19}.[41]

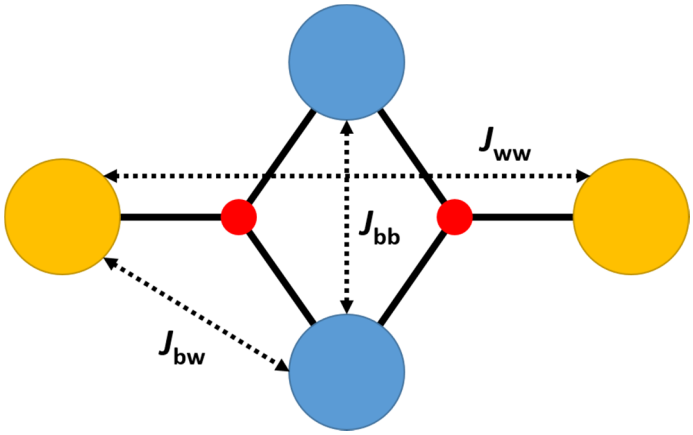

Figure 8. Structural representation of the $[M_4O_2]$ butterfly core, where the blue spheres are the "body" metal ions, the orange spheres are the "wing" metal ions and the red spheres are bridging oxygen ions. The diagram illustrates the three superexchange interactions: J_{bb}, J_{bw} and J_{ww}.

Manganese butterflies

Magneto-structural studies of mixed-valence manganese butterflies which display SMM behaviour, have also been developed.[42] Twelve unique compounds all containing the

tetranuclear [$Mn^{II}_2Mn^{III}_2$] metallic core were used for the study, with examples where the Mn^{III} ions are in the "body" positions named Class 1, and those where the Mn^{III} ions occupy the "wing" positions named as Class 2. Magnetic exchange pathways were named as in the previous example with J_{bw}, J_{bb} and J_{ww} the three superexchange parameters (Figure 8). It was found that J_{bw} is usually FM, J_{bb} is generally FM for Class 1 and AFM for Class 2 (and is also usually the strongest interaction for Class 1), and that J_{ww} is usually weak AFM. The study also concluded that electron-withdrawing or donating substituents on the bridging carboxylates or peripheral ligands can alter both the nature of the magnetic exchange and the anisotropy, suggesting a possible route for tuning magnetic anisotropy. It was shown that J_{bb} is strongly dependent on the Mn_b-O-Mn_b angle and J_{bw} strongly dependent on the Mn_b-O-Mn_b-O dihedral angle for both classes of compound, indicating these as key parameters to target when attempting to manipulate the magnetic exchange in these compounds.[42]

Hexanuclear manganese cages

Brechin et al elucidated a correlation for a Mn^{III}_6 family of compounds, extensively studied in the mid to late 2000s. The first of the family was the SMM [$Mn^{III}_6O_2$(Et-sao)$_6$(O_2CPh(Me)$_2$)$_2$(EtOH)$_6$] (Et-saoH$_2$ = 2-hydroxyphenylpropanone oxime), the first compound to break the record anisotropy barrier of the Mn_{12} family.[43] The authors extended the family to twenty four compounds all based on the same hexametallic core, [$Mn^{III}_6O_2$(R-sao)$_6$]$^{2+}$, composed of two linked [Mn^{III}_3O(R-sao)$_3$]$^+$ triangles, where R represents the alkyl/aryl substituent on the oximic carbon atom of the phenolic oxime (Figure 9). These compounds showed a variety of spin ground states ranging from S = 4 to S = 12, with each Mn_2 pair linked through a Mn-O-N-Mn bond (as well as the μ_3-O at the centre of each triangle); the key structural parameter was determined to be the Mn-O-N-Mn torsion angle (α). In all cases the interaction between the [Mn_3] triangles is FM in nature, however within each triangle the ground state could be $2 \leq S \leq 6$. It was concluded that the magnetic exchange within the molecule could be controlled by deliberate structural distortion of the core through judicial choice of R which changed the Mn-O-N-Mn torsion angle. The use of planar non-derivatised oximes leads to relatively flat or unpuckered compounds with small α angles displaying dominant AFM intra-triangle exchange with S = 4 ground states. In contrast, by employing bulkier R groups increasingly puckered structures with larger α angles could be made, where dominant FM intra-triangle exchange is observed, stabilising S = 12

ground states.[44, 45] Based on this a MS correlation was developed with a linear dependence between the Mn-O-N-Mn torsion angles and *J*, with the switch from AFM to FM occurring at angles above ~31° (Figure 9).[45, 46, 47] As well as being the first family of SMMs for which M-S correlations were developed this work is also impressive due to the relatively high nuclearity of the species and the number of individual *J* values present (with each Mn_2 pair and its associated torsion angle having to be treated independently), as well as the heteroleptic nature of the compound. The same MS parameters were then also applied to a family of Mn^{III}_3 compounds which represent "half" of the Mn^{III}_6 unit and also displayed SMM behaviour.[48] The correlation was found to hold for the Mn^{III}_3 systems (and in more than fifty different Mn_6/Mn_3 cages) but with the added advantage that they offered more opportunities for structural distortion than their parent compounds due to both faces of the triangle being available for reaction. Distortion could be achieved through derivatisation of the oxime as before, but also through use of a tripodal capping ligand such as ClO_4^- or ReO_4^-. This allowed greater torsion angles and therefore more isolated ground states, and the use of bulky ligands allowed the molecular units to be separated from each other in the solid state, removing intermolecular interactions.[49]

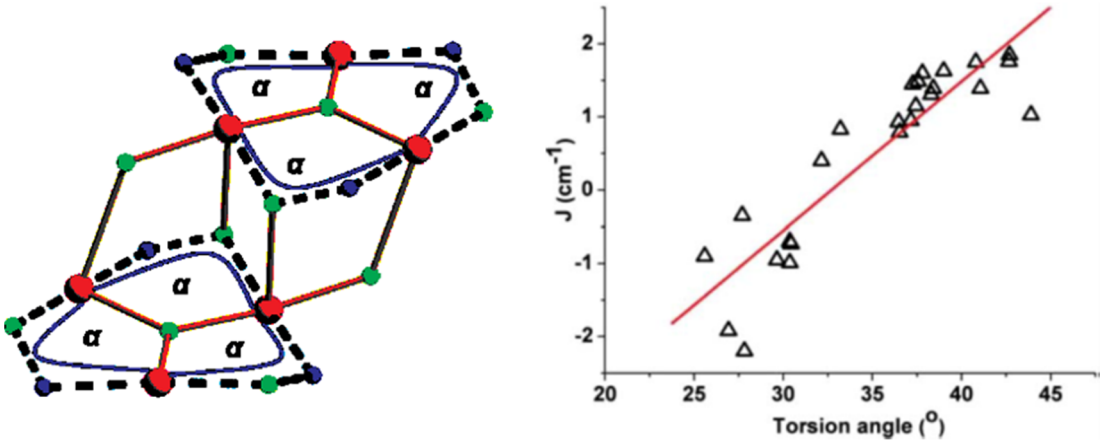

Figure 9. Left: Structural representation of the Mn^{III}_6 core with the Mn-O-N-Mn torsion angle illustrated (α). Right: A graphical depiction of the magneto-structural correlation for this family (red line) with the experimentally determined values for the compounds in the family (triangles).[44, 45]

Cyanometalates

When studying the rules governing the nature of magnetic exchange, the work on cyanometalates has been crucial. The Prussian blue family of compounds have provided a large homologous series of compounds in which to systematically study both the nature of superexchange through the cyano bridges and the mechanisms of exchange between different metal centres.[50] The first of the Prussian blue type compounds, $Fe_4[Fe(CN)_6]_3$, is often argued to be the oldest coordination compound.[51] Despite being used as a coloured pigment since 1704 and first reported in 1724, the structure was only resolved in 1977, it described a (defective) cubic structure with Fe^{3+} ions bridged to the $[Fe(CN)_6]^{4-}$ moieties by the cyano bridges,[52] with ferromagnetic ordering below 5.5 K.[53] This basic structure has formed the foundations for a large body of work, with the metal cations (M') substituted for a wide range of transition metal ions, and the cyanometallate anions (M) also easily replaced. Although the M-CN-M' link is almost never linear, in the majority of cases the C-N-M' angle > 160°, meaning that the magnetic coupling follows the rules of orbital overlap and orthogonality. Thus the superexchange interactions through the cyano bridge are governed by the concept that wavefunctions which are allowed to mix by symmetry (can overlap directly) will promote AFM exchange, and wavefunctions whose overlap is orthogonal and mixing is symmetry forbidden will interact ferromagnetically. The deliberate manipulation of orthogonal magnetic orbitals is a concept which had already been exploited, for example in Kahn's work on Cu^{II}-$V^{IV}O$ dimers, where the metals were chosen to deliberately promote FM exchange.[54] The result of this is that in the case of transition metal d-orbitals in octahedral coordination environments, t_{2g}-t_{2g} (π-π) interactions are AFM in nature, and t_{2g}-e_g (π-σ^*) interactions produce FM contributions (Figure 10).

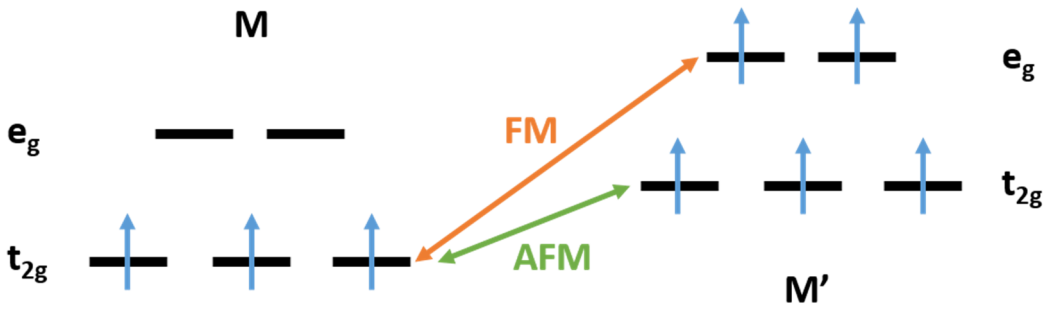

Figure 10. Scheme showing the interaction between unpaired electrons in their respective orbitals on two metals in an example Prussian blue system. Where M is the cyanometalate and M' is the metal cation.

Thus the magnetic exchange between two metals in this framework can be predicted based on their unpaired electron occupancies. It is also worth noting that the cyanometalate metal ion (M), bonded to the carbon of the ligand can always be assumed to be low-spin, due to the strong field nature of the ligand, while the M' ion linked to the nitrogen will likely be high-spin. The simpler cases such as Ni^{II} ($t_{2g}^6e_g^2$) combined with Cr^{III} (t_{2g}^3), in $Ni_3[Cr(CN)_6]_2{\cdot}9H_2O$,[55] lead to obvious conclusions – the nickel has only unpaired electrons in the e_g orbitals and the chromium only in the t_{2g}, therefore FM exchange dominates, as shown by experimental observations which show FM ordering below 60 K.[55] In the case of V^{II} (t_{2g}^3) and Cr^{III} (t_{2g}^3), in $KV[Cr(CN)_6]_2{\cdot}2H_2O$,[56] both metals only contain unpaired electrons in their t_{2g} orbitals and therefore AFM exchange dominates and magnetic ordering is seen experimentally up to temperatures as high as 376 K.[56] More complicated examples occur when there are unpaired electrons in both the t_{2g} and e_g orbitals, such as the combination of V^{II} (t_{2g}^3) with high-spin Mn^{II} ($t_{2g}^3e_g^2$) in $Cs_2Mn[V(CN)_6]$,[57] or Cr^{III} (t_{2g}^3) with high-spin Cr^{II} ($t_{2g}^3e_g^1$), in $Cr_3[Cr(CN)_6]_2{\cdot}10H_2O$ (Figure 10).[58] In these cases there exist both FM and AFM contributions. Although this makes predictions less clear, the latter normally wins as the t_{2g}-t_{2g} overlap is symmetry allowed and therefore stronger – usually leading to overall AFM behaviour. The experimental results in these cases can also be rationalised based on the relative number of exchange pathways for the AFM contribution and FM contributions.[59] In both cases experimental results show overall ferrimagnetic interactions (with ordering temperatures of 125 K and 240 K, respectively) where a non-zero spin ground state arises due to AFM exchange between metal ions with different spin ground states.[57, 58] In addition to discussion of the dependence of the magnetic exchange on the identity of the metal ion, one can also consider the effect of the bridging angles on the exchange. This becomes important when the number of exchange pathways is similar for the AFM and FM contributions (and so they are similar in magnitude).[59] Such a study was carried out on Cr^{III}-CN-Ni^{II} systems to determine the dependence of the magnitude of the ferromagnetic exchange on the C-N-Ni^{II} angle (Figure 11). As above, when the linkage is linear (or close to) the orthogonality of the orbitals containing the unpaired electrons gives FM exchange, however as the bridging motif is bent (C-N-Ni^{II} angle decreased), the overlap between the magnetic orbitals becomes non-zero and an AFM contribution arises.[60] A study on a dinuclear cyano bridged model fragment showed that this contribution becomes increasingly strong with decreasing angle, weakening the FM exchange until the sign of the exchange changes at 148° (Figure 11).[60]

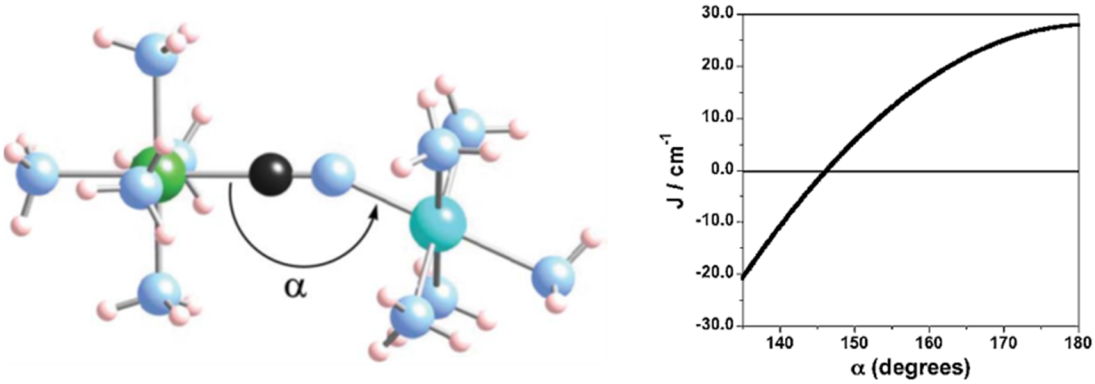

Figure 11. Left: Structural representation of the theoretical model Cr^{III}-CN-Ni^{II} system, illustrating the C-N-Ni^{II} angle (α). Right: resulting computationally determined M-S correlation for the system showing angular dependence of *J* on α.[60]

4d/5d systems

Magneto-structural correlations have also been extended to homometallic 4d and 5d systems as well as heterometallic 3d/5d systems. A particularly elegant study of a family of Re^{IV} dimers was carried out where the Re^{IV} ions were bridged to one another by pyrazine, pyrimidine or triazine, giving a family of compounds of general formula $(NBu_4)_2[(ReX_5)_2(\mu\text{-}L)]$ (L = pyz, pym or triz and X = Cl or Br).[61] The result was two pyrazine dimers with an even number of bridging atoms showing AFM exchange and two dimers with an odd number of bridging atoms showing FM exchange (Figure 12).

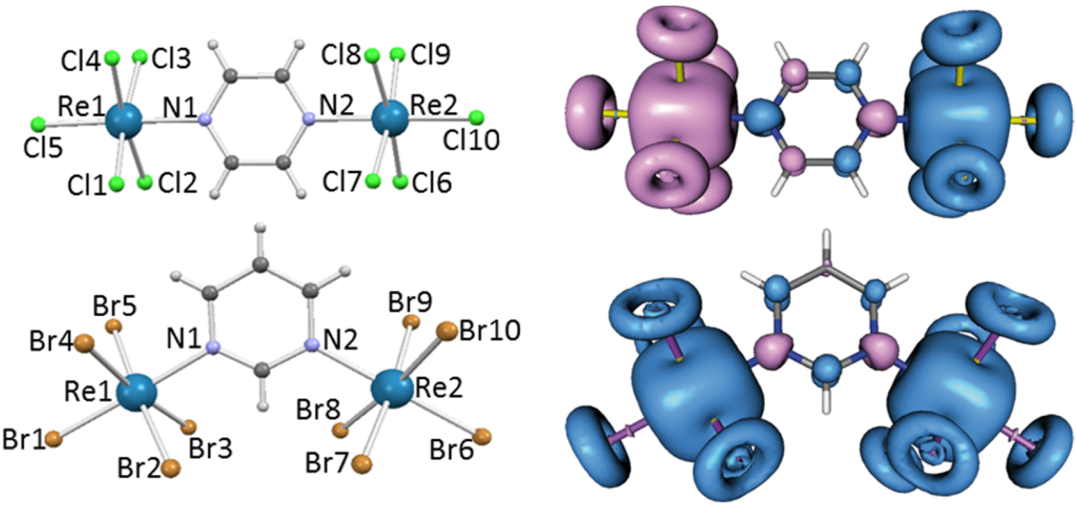

Figure 12. Left: Structural representations of two of the rhenium(IV) dimers from this study, one with an even number of bridging atoms – a pyrazine bridge (top) and one with an odd

number of bridging atoms – a pyrimidine bridge (bottom). Right: The spin density plots of the two dimers shown on the left, illustrating the spin polarization, where the pyrazine bridge gives AFM exchange (top) and a pyrimidine bridge gives FM exchange (bottom).[61]

This was shown to be due to the McConnell mechanism,[62] whereby spin polarization (up, down, up, down) leads to an even number of intervening atoms in the exchange pathway (with pyrazine) giving AFM interactions, and an odd number (as with pyrimidine and triazine) giving FM interactions (Figure 12).[61] This is a well-known phenomenon, and one which has been utilised in the past to switch between FM and AFM exchange in a variety of complexes.[63]

Magneto-structural studies have also been carried out on heterometallic Re^{IV}/Cu^{II} chains. Six analogous one-dimensional chloro-bridged complexes of formula $([Cu(L)_4][ReCl_6])_n$, composed of hexachlororhenate metalloligands joined by octahedral Cu^{II} centres were synthesised, with L being a series of imidazole derivatives or DMF (Figure 13).[64]

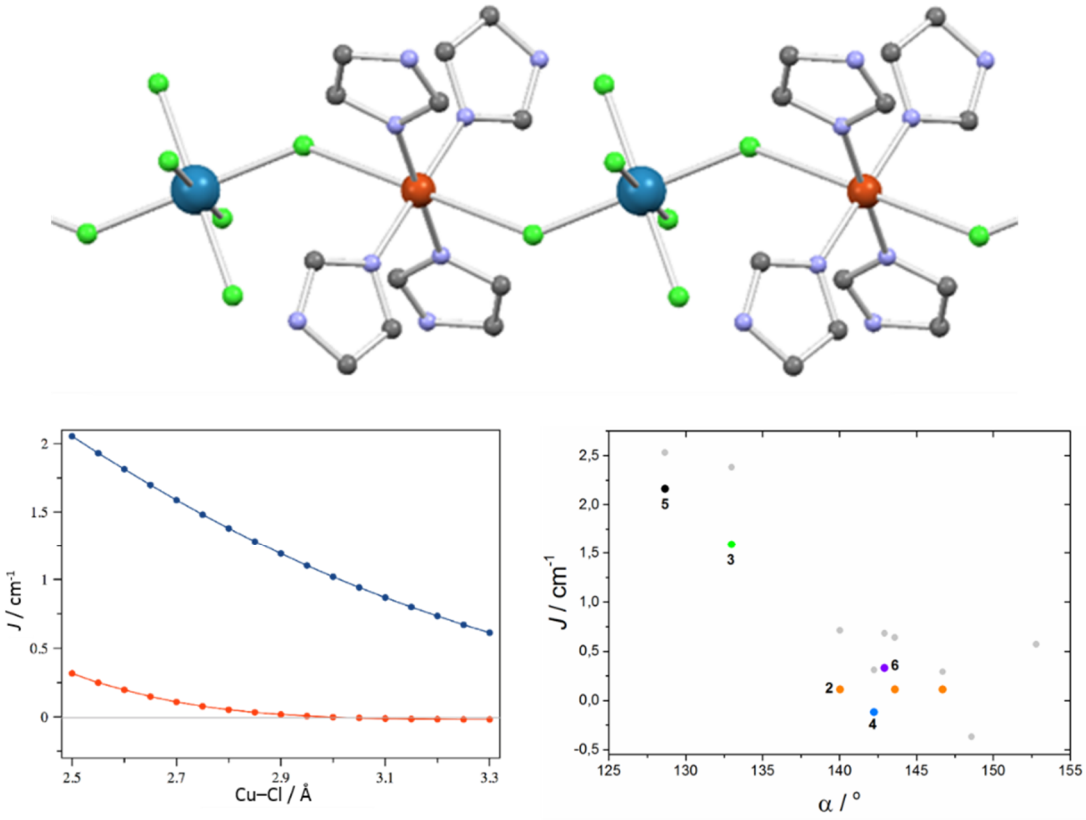

Figure 13. Top: Structural representation of a section of the $([Cu(L)_4][ReCl_6])_n$ chain. Colour code: Re, cyan; Cu, brown; Cl, green; O, red; N, blue; C, grey. Bottom left: Graph of the MS correlation for the dependence of *J* on Cu-Cl distance. Bottom right: Graph of the dependence of *J* on Re-Cl-Cu angle (α).[64]

By varying the size and thus the sterics of L, significant changes in the crystal packing of the chains were achieved, the result being variations in both the Cu-Cl bond lengths and the Re-Cl-Cu bridging angles (α) and thus variations in the magnetic behaviour. These chains displayed primarily ferromagnetic exchange, with the M-S correlation revealing that shorter bond lengths and smaller bridging angles lead to an increase in the magnitude of *J* (Figure 13).[64]

Copper-Gadolinium

Finally we turn to complexes containing 3d metals coordinated to lanthanide ions, and in particular the curious case of ferromagnetic Cu^{II}-Gd^{III} interactions. The first magnetically characterised Cu^{II}-Gd^{III} compound was synthesised in 1985,[65] and the ferromagnetic interactions these compounds displayed were met with surprise.[66] Since then a large number of examples have been synthesised also showing FM exchange, consolidating this observation, with only a handful of examples of AFM exchange being reported.[67-69] This FM interaction seems to occur almost irrespective of the ligand type. Gatteschi et al argued that the origin of the behaviour is spin polarisation, namely interaction between the 6s orbital of gadolinium and the 3d orbital (d_{x2-y2}) of the copper.[70, 71] Kahn surmised however that a single electron jump between the 3d orbital of Cu^{II} and the vacant 5d orbitals of Gd^{III} ion produce a configuration interaction activity of states.[6, 66] A more recent, comprehensive computational study analysed both of these hypotheses and concluded that the stabilised $S = 4$ ground state is intrinsic to the Cu^{II}-Gd^{III} pair (FM exchange) and that the two previously proposed explanations are not necessarily contradictory but interconvertible by appropriate transformations of the magnetic orbitals.[72] The conclusion being that the involved orbitals are not genuine atomic orbitals but molecular orbitals and that the system effectively adopts an orbital orthogonal exchange pathway with the main interaction being between $b_2[Cu^{II}L]$ and $a_2[Gd^{III}]$ orbitals.[72]

The above summary highlights the details and difficulties associated with developing quantitative magneto-structural correlations in complexes containing paramagnetic metal centres. Even for simple dimeric species, a host of different structural parameters must be evaluated/included in models, with an exponential increase in difficulty occurring upon

increasing metal nuclearity. Despite this, it is rather surprising to see that there are very few M-S correlations developed for the numerous families of homo- and heterometallic 3-5d and 4f complexes that have been reported in the literature. The following chapters detail our contributions to this field.

1.3 References

1. B. C. Guha, *Proc. R. Soc. London, Ser. A*, 1951, **206**, 353-373.
2. J. N. Vanniekerk and F. R. L. Schoening, *Acta Crystallogr.*, 1953, **6**, 227-232.
3. B. Bleaney and K. D. Bowers, *Proc. R. Soc. London, Ser. A*, 1952, **214**, 451-465.
4. F. E. Mabbs and D. J. Machin, *Magnetism and Transition-Metal Complexes*, Chapman & Hall, London, 1973.
5. R. D. Willett, D. Gatteschi and O. Kahn, *Magneto-Structural Correlations in Exchange Coupled Systems*, D. Reidel, Dordrecht, 1985.
6. O. Kahn, *Molecular Magnetism*, Wiley, 1993.
7. A. Caneschi, D. Gatteschi, R. Sessoli, A. L. Barra, L. C. Brunel and M. Guillot, *J. Am. Chem. Soc.*, 1991, **113**, 5873-5874.
8. S. M. J. Aubin, M. W. Wemple, D. M. Adams, H. L. Tsai, G. Christou and D. N. Hendrickson, *J. Am. Chem. Soc.*, 1996, **118**, 7746-7754.
9. R. Sessoli, D. Gatteschi, A. Caneschi and M. A. Novak, *Nature*, 1993, **365**, 141-143.
10. N. E. Chakov, S. C. Lee, A. G. Harter, P. L. Kuhns, A. P. Reyes, S. O. Hill, N. S. Dalal, W. Wernsdorfer, K. A. Abboud and G. Christou, *J. Am. Chem. Soc.*, 2006, **128**, 6975-6989.
11. A. Caneschi, D. Gatteschi, N. Lalioti, C. Sangregorio, R. Sessoli, G. Venturi, A. Vindigni, A. Rettori, M. G. Pini and M. A. Novak, *Angew. Chem. Int. Ed.*, 2001, **40**, 1760-1763.
12. R. Clérac, H. Miyasaka, M. Yamashita and C. Coulon, *J. Am. Chem. Soc.*, 2002, **124**, 12837-12844.
13. J. M. Zadrozny, J. J. Liu, N. A. Piro, C. J. Chang, S. Hill and J. R. Long, *Chem. Commun.*, 2012, **48**, 3927-3929.
14. F. S. Guo, B. M. Day, Y. C. Chen, M. L. Tong, A. Mansikkamäki and R. A. Layfield, *Angew. Chem. Int. Ed.*, 2017, **56**, 11445-11449.
15. C. A. P. Goodwin, F. Ortu, D. Reta, N. F. Chilton and D. P. Mills, *Nature*, 2017, **548**, 439.
16. X. N. Cheng, W. X. Zhang, Y. Y. Lin, Y. Z. Zheng and X. M. Chen, *Adv. Mater.*, 2007, **19**, 1494-1498.
17. D. Aulakh, J. B. Pyser, X. Zhang, A. A. Yakovenko, K. R. Dunbar and M. Wriedt, *J. Am. Chem. Soc.*, 2015, **137**, 9254-9257.
18. S. I. Ohkoshi and H. Tokoro, *Acc. Chem. Res.*, 2012, **45**, 1749-1758.
19. E. Coronado, J. R. Galan-Mascaros, C. J. Gomez-Garcia and V. Laukhin, *Nature*, 2000, **408**, 447-449.
20. D. Gatteschi and R. Sessoli, *Angew. Chem. Int. Ed.*, 2003, **42**, 268-297.
21. R. E. P. Winpenny, *Angew. Chem. Int. Ed.*, 2008, **47**, 7992-7994.
22. V. H. Crawford, H. W. Richardson, J. R. Wasson, D. J. Hodgson and W. E. Hatfield, *Inorg. Chem.*, 1976, **15**, 2107-2110.
23. W. E. Hatfield, *Comments Inorg. Chem.*, 1981, **1**, 105-121.
24. J. Glerup, D. J. Hodgson and E. Pedersen, *Acta Chem. Scand. A.*, 1983, **37**, 161-164.
25. M. F. Charlot, O. Kahn and M. Drillon, *Chem. Phys.*, 1982, **70**, 177-187.
26. E. Larsen and G. N. La Mar, *J. Chem. Educ.*, 1974, **51**, 633.
27. T. J. Morsing, H. Weihe and J. Bendix, *Eur. J. Inorg. Chem.*, 2014, **2014**, 5990-5996.
28. S. M. Gorun and S. J. Lippard, *Inorg. Chem.*, 1991, **30**, 1625-1630.
29. F. E. Mabbs, V. N. McLachlan, D. McFadden and A. T. McPhail, *J. Chem. Soc., Dalton Trans.*, 1973, 2016-2021.

30. R. E. Norman, R. C. Holz, S. Menage, C. J. Oconnor, J. H. Zhang and L. Que, *Inorg. Chem.*, 1990, **29**, 4629-4637.
31. H. Weihe and H. U. Güdel, *J. Am. Chem. Soc.*, 1997, **119**, 6539-6543.
32. R. Werner, S. Ostrovsky, K. Griesar and W. Haase, *Inorg. Chim. Acta*, 2001, **326**, 78-88.
33. O. Botezat, J. van Leusen, V. C. Kravtsov, A. Ellern, P. Kogerler and S. G. Baca, *Dalton Trans.*, 2015, **44**, 20753-20762.
34. W. P. Barros, R. Inglis, G. S. Nichol, T. Rajeshkumar, G. Rajaraman, S. Piligkos, H. O. Stumpf and E. K. Brechin, *Dalton Trans.*, 2013, **42**, 16510-16517.
35. P. Comar, T. Rajeshkumar, G. S. Nichol, M. B. Pitak, S. J. Coles, G. Rajaraman and E. K. Brechin, *Dalton Trans.*, 2015, **44**, 19805-19811.
36. F. Neese, *J. Am. Chem. Soc.*, 2006, **128**, 10213-10222.
37. T. Cauchy, E. Ruiz and S. Alvarez, *J. Am. Chem. Soc.*, 2006, **128**, 15722-15727.
38. C. J. Harding, R. K. Henderson and A. K. Powell, *Angew. Chem.-Int. Edit. Engl.*, 1993, **32**, 570-572.
39. E. Ruiz, J. Cano and S. Alvarez, *Chem. Eur. J.*, 2005, **11**, 4767-4771.
40. C. Benelli, S. Parsons, G. A. Solan and R. E. P. Winpenny, *Angew. Chem.-Int. Edit. Engl.*, 1996, **35**, 1825-1828.
41. A. K. Powell, S. L. Heath, D. Gatteschi, L. Pardi, R. Sessoli, G. Spina, F. Delgiallo and F. Pieralli, *J. Am. Chem. Soc.*, 1995, **117**, 2491-2502.
42. K. R. Vignesh, S. K. Langley, C. J. Gartshore, B. Moubaraki, K. S. Murray and G. Rajaraman, *Inorg. Chem.*, 2017, **56**, 1932-1949.
43. C. J. Milios, A. Vinslava, W. Wernsdorfer, S. Moggach, S. Parsons, S. P. Perlepes, G. Christou and E. K. Brechin, *J. Am. Chem. Soc.*, 2007, **129**, 2754-2755.
44. C. J. Milios, R. Inglis, A. Vinslava, R. Bagai, W. Wernsdorfer, S. Parsons, S. P. Perlepes, G. Christou and E. K. Brechin, *J. Am. Chem. Soc.*, 2007, **129**, 12505-12511.
45. R. Inglis, L. F. Jones, C. J. Milios, S. Datta, A. Collins, S. Parsons, W. Wernsdorfer, S. Hill, S. P. Perlepes, S. Piligkos and E. K. Brechin, *Dalton Trans.*, 2009, 3403-3412.
46. S. Carretta, T. Guidi, P. Santini, G. Amoretti, O. Pieper, B. Lake, J. van Slageren, F. El Hallak, W. Wernsdorfer, H. Mutka, M. Russina, C. J. Milios and E. K. Brechin, *Phys. Rev. Lett.*, 2008, **100**, 4.
47. S. Bahr, C. J. Milios, L. F. Jones, E. K. Brechin, V. Mosser and W. Wernsdorfer, *Phys. Rev. B*, 2008, **78**.
48. R. Inglis, S. M. Taylor, L. F. Jones, G. S. Papaefstathiou, S. P. Perlepes, S. Datta, S. Hill, W. Wernsdorfer and E. K. Brechin, *Dalton Trans.*, 2009, 9157-9168.
49. R. Inglis, C. J. Milios, L. F. Jones, S. Piligkos and E. K. Brechin, *Chem. Commun.*, 2012, **48**, 181-190.
50. K. R. Dunbar and R. A. Heintz, *Prog. Inorg. Chem.*, 1997, **45**, 283-391.
51. J. Woodward, *Philos. Trans. R. Soc. London*, 1724, **33**, 15-17.
52. H. J. Buser, D. Schwarzenbach, W. Petter and A. Ludi, *Inorg. Chem.*, 1977, **16**, 2704-2710.
53. M. B. Robin, *Inorg. Chem.*, 1962, **1**, 337-342.
54. O. Kahn, J. Galy, Y. Journaux, J. Jaud and I. Morgensternbadarau, *J. Am. Chem. Soc.*, 1982, **104**, 2165-2176.
55. V. Gadet, T. Mallah, I. Castro, M. Verdaguer and P. Veillet, *J. Am. Chem. Soc.*, 1992, **114**, 9213-9214.
56. S. M. Holmes and G. S. Girolami, *J. Am. Chem. Soc.*, 1999, **121**, 5593-5594.
57. W. R. Entley and G. S. Girolami, *Science*, 1995, **268**, 397-400.
58. T. Mallah, S. Thiebaut, M. Verdaguer and P. Veillet, *Science*, 1993, **262**, 1554-1557.

59. J. N. Rebilly and T. Mallah, *Single-Molecule Magnets and Related Phenomena*, 2006, **122**, 103-131.
60. L. Toma, L. M. Toma, R. Lescouezec, D. Armentano, G. De Munno, M. Andruh, J. Cano, F. Lloret and M. Julve, *Dalton Trans.*, 2005, 1357-1364.
61. A. H. Pedersen, M. Julve, J. Martinez-Lillo, J. Cano and E. K. Brechin, *Dalton Trans.*, 2017, **46**, 11890-11897.
62. H. M. McConnell, *Proc. R. A. Welch Found. Chem. Res.*, 1967, **11**, 144.
63. J. A. McCleverty and M. D. Ward, *Acc. Chem. Res.*, 1998, **31**, 842-851.
64. A. H. Pedersen, M. Julve, J. Martinez-Lillo, J. Cano and E. K. Brechin, *Dalton Trans.*, 2017, **46**, 16025-16033.
65. A. Bencini, C. Benelli, A. Caneschi, R. L. Carlin, A. Dei and D. Gatteschi, *J. Am. Chem. Soc.*, 1985, **107**, 8128-8136.
66. O. Kahn, *Struct. Bond.*, 1987, **68**, 89-167.
67. C. Benelli and D. Gatteschi, *Chem. Rev.*, 2002, **102**, 2369-2387.
68. J. P. Costes, F. Dahan and A. Dupuis, *Inorg. Chem.*, 2000, **39**, 5994-6000.
69. J. P. Costes, F. Dahan, A. Dupuis and J. P. Laurent, *Inorg. Chem.*, 2000, **39**, 169-173.
70. C. Benelli, A. Caneschi, A. C. Fabretti, D. Gatteschi and L. Pardi, *Inorg. Chem.*, 1990, **29**, 4153-4155.
71. C. Benelli, A. Caneschi, D. Gatteschi, O. Guillou and L. Pardi, *Inorg. Chem.*, 1990, **29**, 1750-1755.
72. J. Paulovič, F. Cimpoesu, M. Ferbinteanu and K. Hirao, *J. Am. Chem. Soc.*, 2004, **126**, 3321-3331.

CHAPTER 2:

MAGNETO–STRUCTURAL CORRELATIONS IN A FAMILY OF DI–ALKOXO BRIDGED CHROMIUM DIMERS

2.1 Introduction

Since the late 1980s the study of paramagnetic metal complexes has become a prolific area of research, with much focus on polymetallic 3*d* clusters, initially dominated by the chemistry of Mn and Fe.[1-3] The coordination and structural chemistry of polynuclear Cr(III) cages by comparison is less well developed. This may be due to the lack of a metalloenzyme containing a polymetallic chromium compound,[4, 5] the relative kinetic inertness of the octahedral d^3 ion and the requirement for elevated temperatures for reaction, the inherent stability of low nuclearity species, and the dominance of antiferromagnetic exchange between isotropic *s* = 3/2 ions.[6] However, solution stability and slow ligand exchange can be manipulated to exert a degree of control over structure and post-synthetic reactivity that can be difficult for more labile 3*d* ions. This, and the realisation that Cr cages may have potential application in quantum information processing, has seen a revival in Cr(III) cluster chemistry, resulting in the synthesis of some beautiful new cages, possessing fascinating low temperature physics - perhaps best exemplified by the extensive family of homo- and heterometallic, even and odd numbered Cr(III) rings.[7, 8]

The vast majority of Cr(III) clusters employ bridging carboxylate ligands; indeed for compounds of nuclearity three or more they appear in approximately 85% of deposited structures in the Cambridge Structural Database. Historically, the first of these were the ubiquitous oxo-centred triangles of general formula $[Cr_3O(O_2CR)_6(H_2O)_3]X$ (X = anion, R = alkyl or aryl),[9-14] all of which display antiferromagnetic exchange interactions between the metal ions.[9-15] The stability of this structural unit saw it widely employed thereafter as a starting material for the synthesis of a range of novel complexes, such as $[Cr_4O_4]^{8+}$ butterflies,[16] an unusual tetrahedral $[Cr_4S]^{10+}$ cage which displays ferromagnetic interactions resulting in the stabilisation of an *S* = 6 ground state,[17] and an extensive family of Cr_6, Cr_8 and Cr_{10} wheels.[18-24] These rings are bridged by a combination of carboxylate ligands and F^- or OH^- ions, leading, in the main, to complexes with *S* = 0 ground states; the exception being the complex $[Cr_{10}(OMe)_{20}(O_2CMe)_{10}]$ which shows weak ferromagnetic exchange and an *S* = 15 ground state.[20] A number of other $[Cr_8]$ and $[Cr_{12}]$ clusters with different topologies have also been reported: these include a $[Cr_{12}O_9]^{18+}$ centred, pentacapped trigonal prism, a $[Cr_8O_4]^{16+}$ capped cubane, and a $[Cr_{12}O_8]^{20+}$ capped tricubane.[13, 18, 25, 26] Two additional octanuclear $\{Cr_8O_2\}^{20+}$ complexes with structures derived from fused octahedra are notable due to the lack of carboxylates, employing instead the tripodal alcohol ligands H_3thme and H_4peol.[27] The

largest homometallic Cr(III) complex reported to date, $[Cr_{14}(bta)_6O_6(OMe)_{18}Cl_6]$ (btaH = benzotriazole), whose metallic skeleton describes a hexacapped hexagonal bipyramid also contains no carboxylates.[28] These latter two species hint that structurally novel clusters may be obtained by employing different ligand sets than those traditionally used.

In contrast, dinuclear chromium complexes are plentiful and have been widely studied, with monohydroxo-, dihydroxo- (often referred to as "diols"), and oxo-bridged systems being particularly well documented.[29-41] Magneto-structural correlations for the "diols" revealed that the key structural parameters dominating the magnetic exchange interaction are the Cr-O-Cr bridging angle (ϕ), the Cr-O bond length (r), and the dihedral angle between the bridging Cr_2O_2 plane and the OH vector of the bridging group (θ) (Figure 1).[42] The magnetic exchange in the majority of these dimers is antiferromagnetic in nature, with ferromagnetic exchange being found only in a small window of θ and ϕ values.[43] For H-bonded dimers it has been shown that both the O···H···O distance (d) and the Cr-O···O-Cr torsion angle (a) influence magnetic exchange.[44, 45]

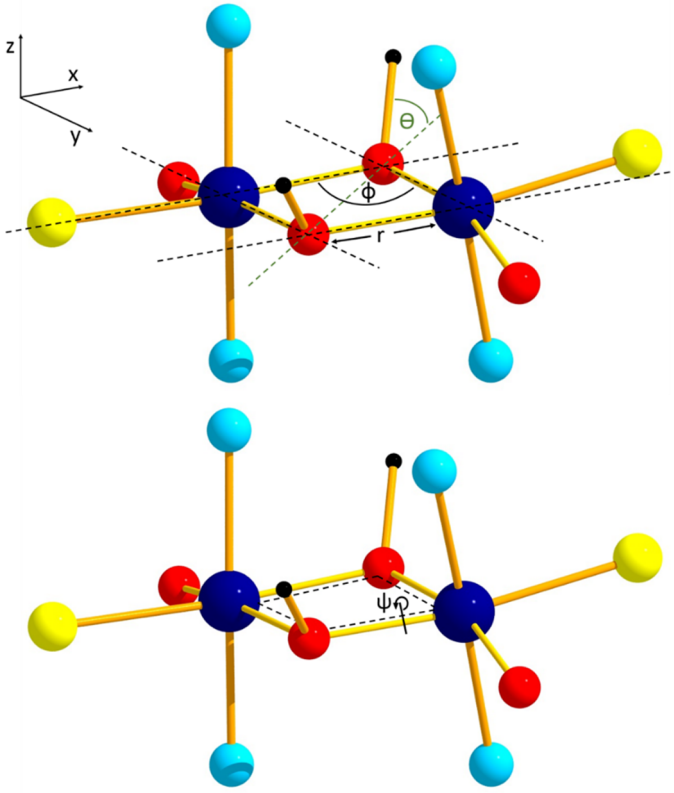

Figure 1. Diagrammatic representation of the key structural parameters influencing the sign and magnitude of magnetic exchange in $[Cr^{III}_2(OH)_2]$ dimers (top) and of another parameter,

ψ, the Cr-O-Cr-O dihedral angle, used in this study (bottom). Colour code: Cr = dark blue, O = red, C = black. The light blue and yellow spheres represent generic donor atoms.

In order to extend these studies from di-hydroxo to di-alkoxo bridged chromium dimers, and to investigate if the same magneto-structural correlation persists, we have made a family of $[Cr^{III}_2(OR)_2]$ complexes with the pyridine alcohol ligands 2-pyridinemethanol (hmpH), 2-pyridineethanol (hepH) and the oxidised version of hmpH, 2-picolinic acid (picH) (Figure 2). These compounds have been structurally characterised using single crystal X-ray crystallography and their magnetic behaviour investigated through a combination of magnetometry and theoretical analysis.

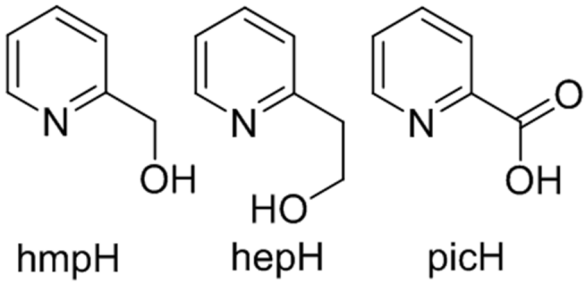

Figure 2. Molecular structures of the pro-ligands (left to right) hmpH, hepH and picH.

2.2 Experimental

Materials and physical measurements

All chemicals were procured from commercial suppliers and used as received (reagent grade). Elemental analyses for C, H, N and Cr on all compounds were performed by Medac Ltd.

Synthesis of $[Cr_2(MeO)_2(pic)_4]\cdot½MeOH\cdot½Et_2O$ (1)

Method 1: $Cr(NO_3)_3\cdot 9H_2O$ (0.800 g, 2 mmol) was dissolved with hmpH (0.190 ml, 2 mmol), NEt_3 (0.279 ml, 2 mmol) and NaO_2CPh (0.288 g, 2 mmol) in MeOH (25 ml). The reaction was left overnight with continuous stirring. 10 ml samples of the resulting dark blue solution were heated in Teflon-lined autoclaves at 140°C for 24 hours. Pink block-shaped crystals suitable for X-ray diffraction were formed over a period of 2 weeks, upon vapour diffusion with diethyl ether. Yield 7.1 mg (2.01% by hmpH weight). Anal. Calcd (%) for $C_{26}H_{22}Cr_2N_4O_{10}$: C 47.72, H 3.39, Cr 15.89, N 8.56; found: C 47.97 H 3.93, Cr 15.30, N 8.04.

Method 2: $Cr(NO_3)_3 \cdot 9H_2O$ (0.800 g, 2 mmol) was dissolved with picH (0.492 g, 4 mmol) in MeOH (20 ml). NEt_3 (0.558 ml, 4 mmol) was then added dropwise and the reaction was left overnight with continuous stirring. 10 ml samples of the resulting dark blue solution were heated in Teflon-lined autoclaves at 140°C for 24 hours. Slow cooling to room temperature yielded thin purple plate crystals which were suitable for X-ray diffraction. Yield 215.8 mg (30.50% by chromium weight). Anal. Calcd (%) for $C_{26}H_{22}Cr_2N_4O_{10}$: C 47.72, H 3.39, Cr 15.89, N 8.56; found: C 47.82 H 3.77, Cr 15.75, N 8.98.

Synthesis of $[Cr_2(hmp)_2(pic)_2Cl_2]$ (2)

Method 1: $CrCl_3 \cdot 6H_2O$ (0.533 g, 2 mmol) was dissolved with hmpH (0.380 ml, 4 mmol) in MeCN (25 ml) with continuous stirring. NaOMe (0.216 g, 4 mmol) was then added to the solution and the reaction was left to stir overnight at room temperature. The mixture was then heated for 1.5 hours at 60°C, affording a dark green solution. 10 ml samples of the resulting solution were heated in Teflon-lined autoclaves at 120°C for 12 hours. Slow cooling to room temperature yielded brown block-shaped crystals, which were suitable for X-ray diffraction. Yield 101.8 mg (16.02% by chromium weight). Anal. Calcd (%) for $C_{24}H_{20}Cl_2Cr_2N_4O_6$: C 45.37, H 3.17, Cr 16.37, N 8.82; found: C 45.03, H 3.29, Cr 15.83, N 8.52.

Method 2: $CrCl_3 \cdot 6H_2O$ (0.533 g, 2 mmol) was dissolved with hmpH (0.190 ml, 2 mmol) and picH (0.246 g, 2 mmol) in MeCN (20 ml) with continuous stirring. NaOMe (0.216 g, 4 mmol) was then added to the solution and the reaction was left to stir overnight at room temperature. 10 ml samples of the resulting dark green solution were heated in Teflon-lined autoclaves at 120°C for 12 hours. Slow cooling to room temperature yielded brown rod-shaped crystals, which were suitable for X-ray diffraction. Yield 532.6 mg (83.83% by chromium weight). Anal. Calcd (%) for $C_{24}H_{20}Cl_2Cr_2N_4O_6$: C 45.37, H 3.17, Cr 16.37, N 8.82; found: C 45.84, H 3.50, Cr 15.89, N 8.50.

Synthesis of $[Cr_2(hmp)_2(pic)_2Br_2]$ (3)

Method 1: $CrBr_3 \cdot 6H_2O$ (0.800 g, 2 mmol) was dissolved with hmpH (0.380 ml, 4 mmol) in MeCN (25 ml) with continuous stirring. NaOMe (0.216 g, 4 mmol) was then added to the solution and the reaction was left to stir overnight at room temperature. The mixture was then heated for 1.5 hours at 60°C, giving a dark green solution. 10 ml samples of this solution were heated in Teflon-lined autoclaves at 120°C for 12 hours. Slow cooling to room temperature yielded purple prism-shaped and purple rod-shaped crystals, which were

suitable for X-ray diffraction studies. Both crystal types were of the same structure. Yield 169.3 mg (23.38% by chromium weight). Anal. Calcd (%) for $C_{24}H_{20}Br_2Cr_2N_4O_6$: C 39.80, H 2.78, Cr 14.36, N 7.74; found: C 40.09, H 2.63, Cr 14.06, N 7.45.

Method 2: $CrBr_3 \cdot 6H_2O$ (0.800 g, 2 mmol) was dissolved with hmpH (0.190 ml, 2 mmol) and picH (0.246 g, 2 mmol) in MeCN (20 ml) with continuous stirring. NaOMe (0.216 g, 4 mmol) was then added to the solution and the reaction was left to stir overnight at room temperature. 10 ml samples of the resulting dark green solution were heated in Teflon-lined autoclaves at 120°C for 12 hours. Slow cooling to room temperature yielded purple rod-shaped crystals, which were suitable for X-ray diffraction studies. Yield 417.6 mg (57.66% by chromium weight). Anal. Calcd (%) for $C_{24}H_{20}Br_2Cr_2N_4O_6$: C 39.80, H 2.78, Cr 14.36, N 7.74; found: C 39.64, H 2.82, Cr 13.94, N 7.74.

Synthesis of $[Cr_2(hmp)_2Cl_4(H_2O)_2] \cdot 2Et_2O$ (4)

$CrCl_3 \cdot 6H_2O$ (0.533 g, 2 mmol) was dissolved with hmpH (0.190 ml, 2 mmol) in MeCN (25 ml) with continuous stirring. NaOMe (0.108 g, 2 mmol) was then added to the solution and the reaction was left to stir overnight at room temperature. The mixture was then heated for 1.5 hours at 60°C to produce a dark green solution. The solution was then filtered and diffused with diethyl ether. Green block-shaped crystals suitable for X-ray diffraction formed over a period of 1 week. Yield 98.2 mg (19.71% by chromium weight). Anal. Calcd (%) for $C_{12}H_{16}Cl_4Cr_2N_2O_4$: C 28.94, H 3.24, Cr 20.88, N 5.62; found: C 29.08, H 3.22, Cr 20.81, N 5.55.

Synthesis of $[Cr_2(hmp)_2Cl_4(pyr)_2] \cdot 2pyr$ (5)

Powdered $[Cr_2(hmp)_2Cl_4(H_2O)_2].2Et_2O$ (**4**) (14 mg, 0.028 mmol) was dissolved in pyridine (10 ml) with continuous stirring for 30 mins. The resulting green solution was filtered and a vapour diffusion was set up with diethyl ether. Dark green block-shaped crystals were formed after 2 days, which were suitable for X-ray diffraction studies. Yield 8.4 mg (38.53% by chromium weight). Anal. Calcd (%) for $C_{32}H_{32}Cl_4Cr_2N_6O_2$: C 49.37, H 4.14, Cr 13.36, N 10.80; found: C 48.97, H 3.81, Cr 13.39, N 10.49.

Synthesis of $[Cr_2(hmp)_2Cl_4(4\text{-picoline})_2]$ (6)

Powdered $[Cr_2(hmp)_2Cl_4(H_2O)_2].2Et_2O$ (**4**) (16.6 mg, 0.033 mmol) was dissolved in 4-picoline (10 ml) with continuous stirring for 30 mins. The resulting green solution was filtered and a vapour diffusion was set up with hexane. Blue block-shaped crystals were formed after 5

days, which were suitable for X-ray diffraction studies. Yield 5.3 mg (24.77% by chromium weight). Anal. Calcd (%) for $C_{24}H_{26}Cl_4Cr_2N_4O_2$: C 44.46, H 4.04, Cr 16.04, N 8.64; found: C 43.99, H 4.02, Cr 15.89, N 8.41.

Synthesis of $[Cr_2(hep)_2Cl_4(H_2O)_2]\cdot 2MeCN$ (7)

$CrCl_3\cdot 6H_2O$ (0.533 g, 2 mmol) was dissolved with hepH (0.383 ml, 3 mmol) in MeCN (25 ml) with continuous stirring. $NaBF_4$ (0.329 g, 3 mmol) was then added to the solution and the reaction mixture left to stir for 4 hours at room temperature. The resulting cloudy green/grey solution was filtered and diffused with hexane. Brown block-shaped crystals suitable for X-ray diffraction were formed over a period of 2 weeks. Yield 52.2 mg (9.92% by chromium weight). Anal. Calcd (%) for $C_{14}H_{20}Cl_4Cr_2N_2O_4$: C 31.96, H 3.83, Cr 19.77, N 5.32; found: C 32.04, H 3.73, Cr 20.09, N 5.77.

Synthesis of $[Cr(hmp)(hmpH)Cl_2]\cdot MeCN$ (8)

A solution of hmpH (0.285 ml, 3 mmol) and NEt_3 (0.420 ml, 3 mmol) dissolved in MeCN (25 ml) was continuously stirred for 10 minutes. $CrCl_3\cdot 6H_2O$ (0.533 g, 2 mmol) was then added and the reaction was left to stir for 2.5 hours at room temperature. The resulting cloudy brown solution was filtered and a vapour diffused with diethyl ether. Dark green block-shaped crystals suitable for X-ray diffraction were formed after 3 days. Yield 4.7 mg (0.92% by hmpH weight). Anal. Calcd (%) for $C_{12}H_{13}Cl_2CrN_2O_2$: C 42.37, H 3.85, Cr 15.29, N 8.24; found: C 42.03, H 4.10, Cr 15.04, N 8.35.

X-ray crystallography

Diffraction data for samples **1**-**8** were collected using a Rigaku Oxford Diffraction SuperNova diffractometer with MoK_α (**1**-**4**, **8**) and CuK_α (**5**, **6**, **7**) radiation, and are given in Tables 4 and 5 in the Supplementary Information. An Oxford Cryosystems Cryostream 700+ low temperature device was used to maintain a crystal temperature of 120 K. The structures were solved using ShelXT or ShelXS by direct (**1**-**3**, **5**, **6**, **8**) or Patterson methods (**4**, **7**) and refined with version 2014/6 of ShelXL interfaced with Olex2.[46, 47] All non-hydrogen atoms were refined using anisotropic displacement parameters. In structures **1** and **3**-**8** O/N-bound H atoms were initially identified from a difference Fourier map and refined with geometric restraints as appropriate. C-bound H atoms were placed in calculated positions geometrically and refined using the riding model. In structure **2** all H atoms were identified from a difference map and refined freely. CCDC: 1482832-1482837 and 1540438-1540439.

Magnetic data collection

Magnetic susceptibility measurements in the temperature range *T* = 2-300 K were performed on a Quantum Design MPMS XL SQUID magnetometer equipped with a 7 T dc magnet on finely ground samples of **1**-**8**. The observed paramagnetic susceptibilities were corrected for diamagnetic contributions using Pascal's constants (see SI p42).[48] The measurements were performed under magnetic fields of 0.1 T (**2**-**5**, **7**), 0.5 T (**6**, **8**) and 1 T (**1**).

Computational details

All calculations were carried out with the Gaussian09 program package using the UB3LYP functional with TZV basis sets.[49,50,51, 52] Although additional polarisation function could be important, it was found that TZV alone yielded good numerical accuracy, as seen in previous studies.[53] The broken-symmetry approach has been employed to describe the unrestricted solutions of the high spin (E-HS) and low spin (E-BS) states, and the corresponding *J* values were computed from the difference between E-HS and E-BS.[54] A quadratic convergence method was employed to determine the more stable wave functions in the SCF process. We have previously established a computational approach for reliably computing exchange coupling constants in dinuclear complexes using broken-symmetry DFT and this methodology has been employed here.[55-57]

2.3 Results and discussion

Syntheses

Both hmpH and hepH (Figure 2) have found widespread use in the coordination chemistry of an array of 3d metals, including Mn,[58, 59] Fe,[60] Ni,[61] Co,[62] Cu,[63] Ti,[64] Zn,[65] and V,[66] but as yet nothing has been reported with Cr(III). Our primary interest was therefore to examine simple reactions between pyridine alcohol ligands and Cr(III) salts in the absence of any other chelating or bridging ligands. In order to do this, reactions were carried out using a general reaction scheme whereby the metal salt, ligand and base were combined in either MeCN or MeOH. Given the kinetic inertness of the Cr(III) ion we began by examining solvothermal methods, initially at *T* = 140°C. However, under these conditions the hmpH ligand is oxidised to picolinic acid, affording compound **1**. We presume this is also the reason, or at least one contributory factor, for the very small yield of **1**, and repetition of the reaction with picolinic

acid in place of hmpH produces **1** in much higher yield. In addition the yields of complexes **2** and **3**, in which partial oxidation of the ligand occurs, are greatly increased by the equivalent reactions with picolinic acid. In order to try to prevent ligand oxidation we then reduced the temperature to *T* = 120°C, leading to partial oxidation and structures **2** and **3**. Upon further reduction of the temperature (*T* = 100 K and below) no ligand oxidation took place and complexes **4**-**8** were formed. This was also the case for reactions carried out on the bench at *T* < 60°C. It is interesting to note that both compounds **7** and **8** were synthesised under ambient conditions, and for compound **8** the order of addition also appears crucial, since no crystalline material was obtained in alternative reactions in which the same ingredients were added in different sequences to that described in the experimental section.

Structure Description

The molecular structures of the five different structure types (**1**, **2**, **5**, **7** & **8**) are presented in Figure 3, with the important metric parameters listed in Tables 1 and 2. The structures of compounds **3**, **4** and **6** are entirely analogous to that of compounds **2**, **7** and **5**, respectively. Complex **1** (Figure 3A) crystallises in the monoclinic space group $P2_1/n$ with the whole cluster in the asymmetric unit (ASU). The Cr centres are bridged by two μ_2-OMe groups (Cr1-O-Cr2 = 100.61°, 101.76°), with the distorted octahedral coordination sphere on each metal centre completed by two N-atoms and two O-atoms from two bidentate picolinate anions, which lie perpendicular to each other. In the extended structure the cluster and solvent of crystallisation form alternating zig-zag chains along the *a*-axis of the cell (Figure S1), with H-bonds between the solvent and the picolinate ligands forming layers. Between these sheets exist intermolecular π- π interactions between the pyridine rings of the picolinate ligands (C···C, ~3.6 Å).

The second structural type is seen in compounds **2** and **3** (Figure 3B shows compound **2**). Both complexes crystallise in the orthorhombic space group *Pnn*2 with half the molecule in the ASU. The metal centres are bridged by two μ_2-OR groups belonging to the hmp^- ligands, with Cr-O-Cr angles of 101.11° (**2**) and 100.91° (**3**). The distorted octahedral coordination sphere at each Cr(III) ion is completed by the N-atom from the bridging hmp^-, a chelating picolinate ligand and a chloride ion. The pic^- ions sit above, and the hmp^- ions below the $[Cr_2O_2]$ plane (as drawn in Figure 3B), resulting in the methylene C-atoms of the hmp^- ligands also being significantly below this plane. The aromatic rings of the same ligand type sit in a near parallel fashion with respect to each other at C···C distances of ~3.3 Å. In the crystal the

dimers pack in a head-to-tail fashion forming columnar arrays down the *c*-axis of the cell (Figure S2). There are numerous short contacts between the picolinate O-atoms/terminal chlorides on one molecule and aromatic H-atoms on neighbouring molecules throughout the extended structure.

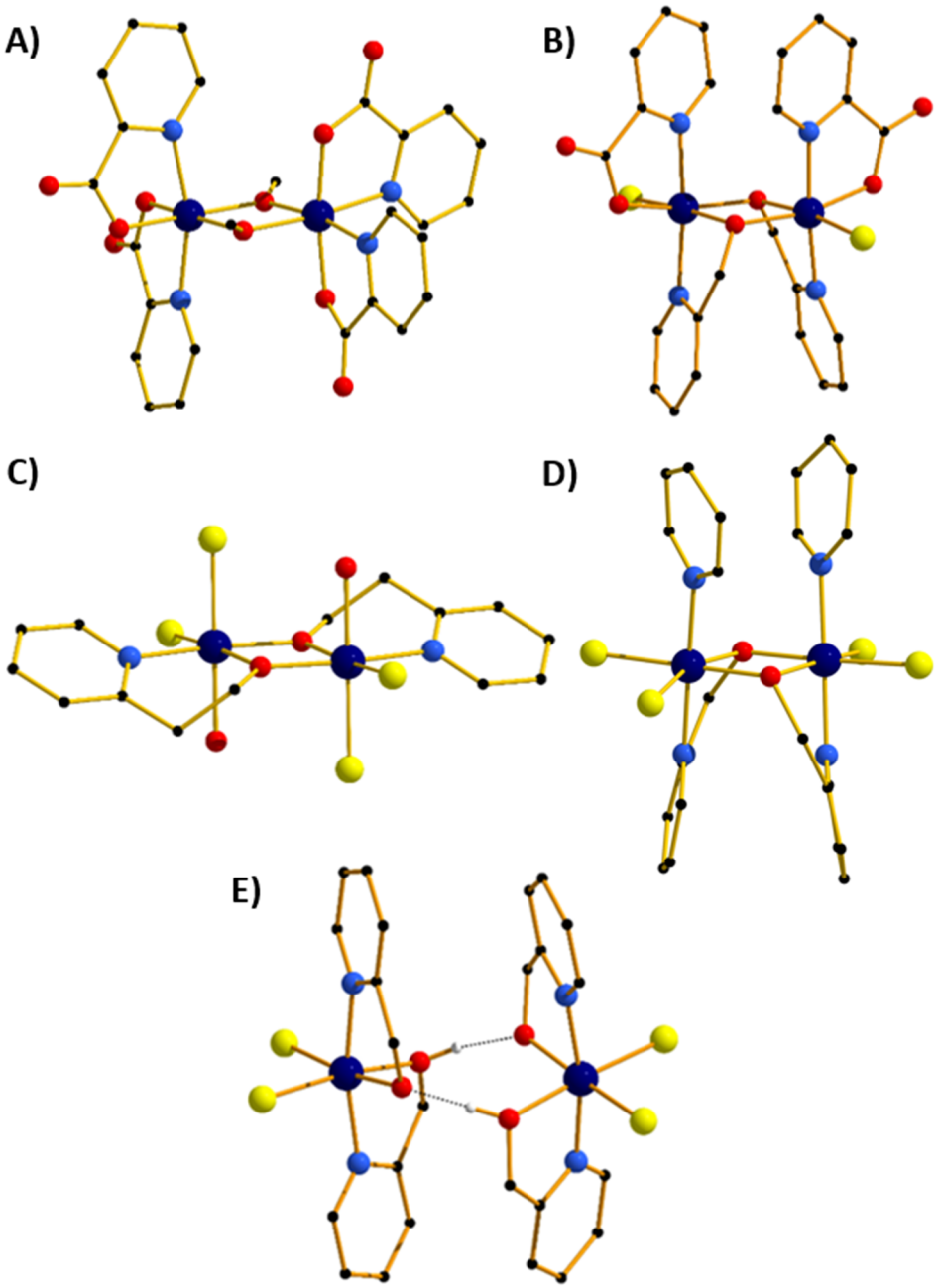

Figure 3. Molecular structures of compounds **1** (A), **2** (**3** isostructural) (B), **7** (**4** isostructural) (C), **5** (**6** isostructural) (D) and **8** (E). Colour code: Cr = dark blue, O = red, N = light blue, C = black, Cl = yellow. H-atoms and solvent molecules of crystallisation omitted for clarity. The dashed lines in (E) represent H-bonds.

Table 1. Pertinent structural parameters for the di-alkoxo bridged compounds **1**-**7**. r = Cr-O bond length, ϕ = Cr-O-Cr bridging angle, θ = dihedral angle between the bridging Cr_2O_2 plane and the OR vector of the bridging group, ψ = Cr-O-Cr-O dihedral angle.

Compound	Cr-Cr [Å]	r [Å]	ϕ [°]	θ [°]	ψ [°]
1	3.029	1.951-1.970	100.67,101.	21.13,3.45	0.91
2	3.058	1.979-1.982	101.11	45.27	2.43
3	3.050	1.975-1.980	100.91	45.71	3.21
4	3.029	1.943-1.969	101.50	23.78	0.00
	3.039	1.958-1.964	101.61	17.70	0.00
5	3.035	1.967-1.977	100.63	55.44	1.55
	3.059	1.974-2.000	100.65	48.84	4.90
6	3.091	1.987-1.992	101.99	46.06	1.89
	3.099	1.980-2.005	102.10	46.25	0.44
7	3.057	1.943-1.963	102.99	7.00	0.00

Table 2. Important structural parameters for the H-bridged dimer **8**. r = Cr-O bond length, d = O···H···O distance, a = Cr-O···O-Cr torsion angle.

Compound	Cr-Cr [Å]	r [Å]	d [Å]	a [°]
8	5.093	1.965	2.399	58.18

Compounds **4** and **7** (Figure 3C shows compound **7**) crystallise in the triclinic space group *P*-1. Crystals of **4** contain two crystallographically distinct dimers, **7** just one. In each case the Cr(III) ions are bridged by two μ_2-alkoxide O-atoms belonging to the pyridine alcohol ligands (hmp^-, **4**; hep^-, **7**) with Cr-O-Cr angles of 101.61°/101.50 (**4**) and 102.99° (**7**). The remaining coordination sites of the octahedral Cr(III) ion contain a water molecule, two *cis* chloride ions and the N-atom from the pyridine alcohol. In contrast to complexes **1** and **2** (and **8**), the pyridine alcohol ligands lie approximately in the same plane as the $[Cr_2O_2]$ moiety; the extra methylene group in the hep^- ligand in **7** causing the aromatic rings to be tilted out of the plane somewhat. In **4** the terminal water molecules are H-bonded to diethyl ether molecules of crystallisation (O···O, 2.697 Å, 2,766 Å) which sit above/below the aromatic rings (Figure S3), creating layers of solvent molecules between layers of dimers. Within these layers the closest intermolecular interactions involve π- π (C···C, ~3.5 Å) and Cl···C(Ar) (~3.7 Å) interactions. In **7** the terminally bonded water molecules are H-bonded to MeCN molecules of crystallisation in a manner akin to that of **4**, again creating a layered structure with π-π

(C···C, ~3.6 Å) and Cl···C(Ar) (~3.5 Å) interactions between neighbouring molecules (Figure S6).

Substitution of the water molecules in **4** with pyridine to give complex **5**, or 4-methylpyridine to give **6**, leads to dramatic structural changes. The result is that the hmp^- ligands twist out of the plane to face each other, and the pyridines sit above the plane parallel to each other. Complex **5** crystallises in the tetragonal space group $I4_1$, **6** in the monoclinic space group $P2/c$ and both have two clusters in the ASU. The Cr ions are bridged by two μ_2-OR groups belonging to the hmp^- ligands, with Cr-O-Cr angles of 100-102°. The remaining coordination sites of the distorted octahedral Cr(III) ion contain a pyridine molecule, two *cis* chloride ions and the N-atom from the pyridine alcohol. The pyridine molecules sit above, and the hmp^- ions below the $[Cr_2O_2]$ plane (as drawn in Figure 3D), resulting in the methylene C-atoms of the hmp^- ligands also being significantly below this plane. The aromatic rings of the same ligand type sit in a near parallel fashion with respect to each other at C···C distances of ~3.2-3.4 Å. In the crystal of **5**, the dimers pack in columnar arrays down the *c*-axis of the cell, each rotated 90° in the c-axis with respect to the next. This arrangement leaves channels down the *c*-axis which are occupied by pyridine molecules of crystallisation (Figure S4). In **6** there is no solvent of crystallisation present. Columns of identically oriented molecules are seen down the *b*-axis with rows of columns in *c* which rotate the molecule 45° between two repeating rows (Figure S5).

Compound **8** crystallises in the tetragonal space group $P4_2/nbc$, and describes an H-bonded dimer of $[Cr(hmp)(hmpH)Cl_2]$ moieties (Figure 3E). Each monomer contains two bidentate hmp^- ligands situated such that their N-atoms are *trans* to one another, and two *cis* Cl^- ions. The monomers sit face-to-face with their nearest neighbours, linked by two H-bonds between the O-atoms of the hmpH/hmp^- ligands (O···H···O, 2.399 Å) with one proton being shared between the two O-atoms. The two monomers are slightly twisted with respect to one another (Cl-Cr···Cr-Cl, ~10.6°), with the aromatic rings above and below the "$[Cr_2O_2]$" plane aligned in a parallel fashion (C···C, >3.5 Å]. In the extended structure (Figure 4) the dimers pack in a columnar fashion down the *c*-axis of the cell, with one dimer rotated 90° with respect to its neighbour, creating an aesthetically pleasing square tile type of architecture, with tubular pores accounting for approximately 9% of the unit cell volume. The closest intermolecular interactions occur between neighbouring aromatic rings (π-π, ~3.4 Å).

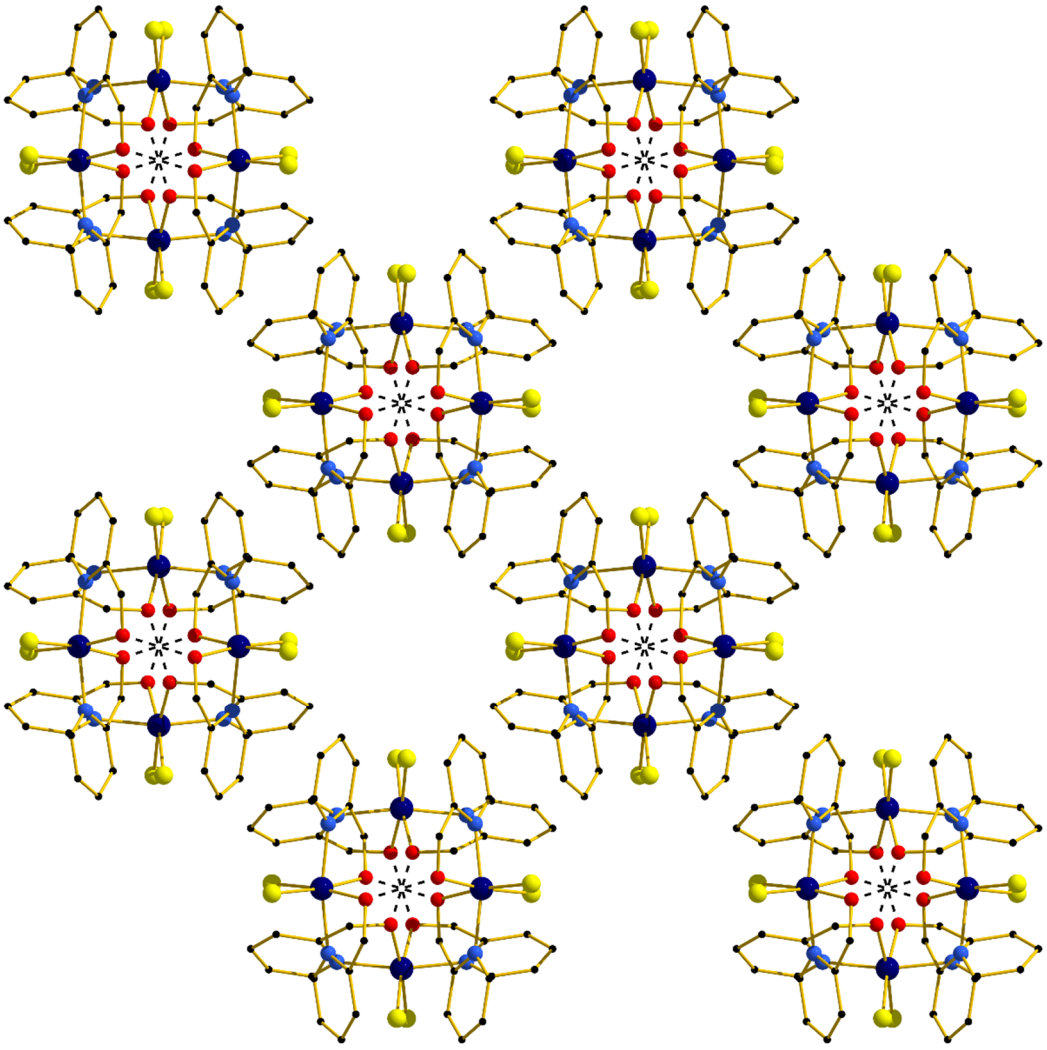

Figure 4. The extended structure in compound **8** viewed down the *c*-axis, highlighting the square tile like architecture. H-bonds are shown as dashed lines.

SQUID Magnetometry

DC magnetic susceptibility measurements were carried out on powdered polycrystalline samples of compounds **1**-**8** in applied magnetic fields of 0.1 T (**2**-**5**, **7**), 0.5 T (**6**, **8**) and 1 T (**1**) over the temperature range T = 2-300 K. The experimental results are plotted in Figure 5 as the $\chi_M T$ product versus T, where χ_M is the molar magnetic susceptibility.

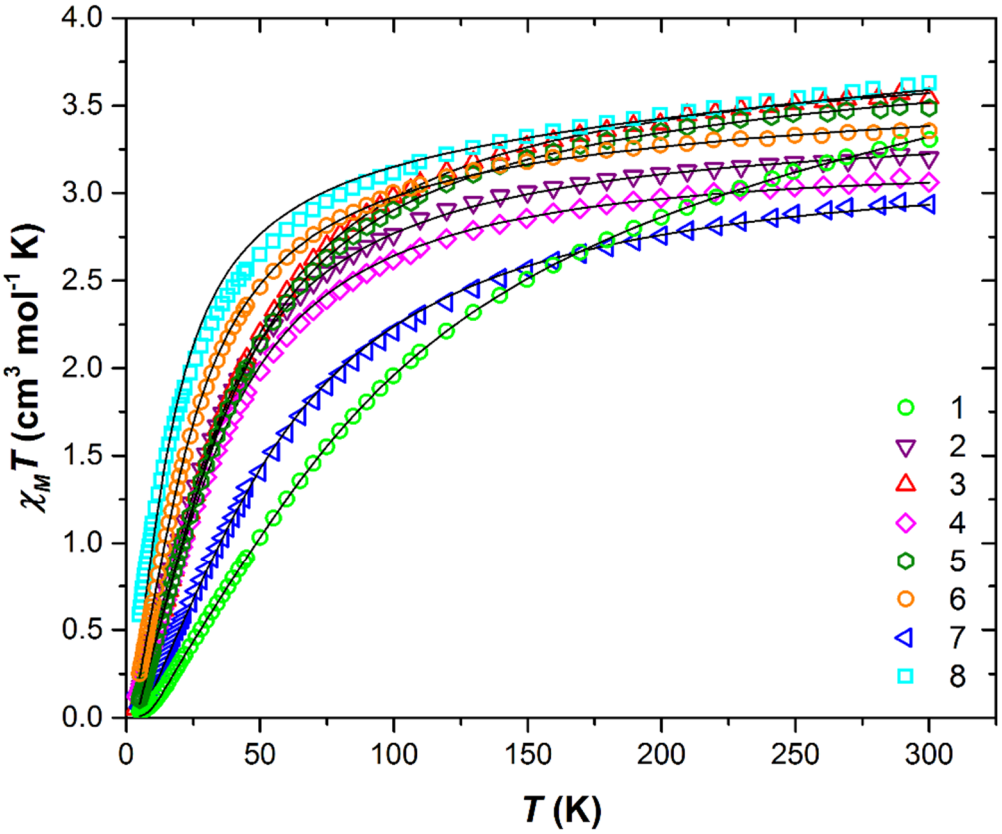

Figure 5. Plot of the $\chi_M T$ product versus T for compounds **1**-**8**. The solid black lines are a fit of the experimental data to spin-Hamiltonian (1). See text for full details.

At 300 K the $\chi_M T$ values of approximately 3.31 (**1**), 3.20 (**2**), 3.54 (**3**), 3.06 (**4**), 3.49 (**5**), 3.36 (**6**) 2.94 (**7**) and 3.63 (**8**) cm^3 K mol^{-1} are somewhat lower than that expected for two s = 3/2 non-interacting ions with g = 2.00 (3.75 cm^3 K mol^{-1}). For all eight compounds the value of $\chi_M T$ decreases gradually with decreasing temperature to reach T = 2 K values of 0.04 (**1**), 0.14 (**2**), 0.10 (**3**), 0.16 (**4**), 0.10 (**5**), 0.06 (**6**) 0.06 (**7**) and 0.59 (**8**) cm^3 K mol^{-1}. This indicates the presence of relatively weak antiferromagnetic interactions between the Cr(III) ions and the stabilisation of diamagnetic ground states in all eight cases (Figure S7-14).

$$\hat{H} = \mu_B B \sum_i g_i \hat{S}_i - 2J \sum_{ij} \hat{S}_i \hat{S}_j \qquad (1)$$

In order to fit the data, the isotropic spin Hamiltonian (1) was employed, where the indices i and j refer to the two Cr(III) ions, μ_B is the Bohr magneton, B is the applied magnetic field, g is the g-factor of the Cr(III) ions (2.00), $\hat{S}$ is a spin operator and J is the isotropic exchange interaction parameter. This model afforded the best-fit parameters J = -14.13 (**1**), -5.37 (**2**), -

6.23 (**3**), -5.77 (**4**), -6.16 (**5**), -3.97 (**6**), -9.35 (**7**) and -2.71 (**8**) cm^{-1}. Table 3 lists these values together with those derived from DFT calculations for comparison (*vide infra*).

Theoretical Studies

Theoretical studies have been carried out on complexes **1-8** in order to evaluate the magnitude and sign of the exchange parameters, and to investigate the relationship between various structural parameters. The DFT computed *J* values (J_{calc}) in cm^{-1} for complexes **1-8** are -12.64, 3.63, -4.63, -6.56, -5.50, -5.85 (averaged from the two molecules in the ASU: -10.17 and -1.53), -3.28 (averaged from the two molecules in the ASU: -2.52 and -4.03), -9.32, -0.67, respectively (Table 3). All the complexes were found to exhibit antiferromagnetic exchange interactions, with the computed *J* values reproducing both the sign and magnitude extracted from experiment.

Table 3. Comparison of the experimentally determined J_{exp} values of compounds **1**-**8** with the theoretical J_{calc} and $J_{calc\ average}$ values derived from DFT calculations.

Compound	J_{exp} [cm^{-1}]	$J_{calc\ average}$ [cm^{-1}]	J_{calc} [cm^{-1}]
1	-14.13		-12.64
2	-5.37		-3.63
3	-6.23		-4.63
4	-5.77		-6.56
5	-6.16	-5.85	-10.17
			-1.53
6	-3.97	-3.28	-2.52
			-4.03
7	-9.35		-9.32
8	-2.71		-0.67

To understand the nature of the magnetic exchange, we have analysed the overlap integrals. The notation A|B|C will be used to denote the interaction between the metal orbitals A and C via the bridging ligand orbital B. The dominant overlap integrals in all cases are found to be the π ($d_{xz}|p_z|d_{yz}$) pairs, as shown in Figures 6-7 (Tables S5-S16). This interaction is facilitated by the π (p_z) orbitals of the oxygen atoms. When the θ value is zero (Figure 1), the O(p_z)-C(p_z) sigma bonding of the bridging -OR group is perpendicular to the π interaction described above. However, when the θ value increases, this leads to mixing of the orbitals leading to the reduction of the π interaction and hence the overlap integrals. Since this overlap integral

is monotonically dependent upon J_{AF}, there is therefore a reduction in the magnitude of *J*. In the extreme case, where θ = 90°, the sigma O-C interactions are described by O(p_z)-C(p_z) orbitals leading to the lone pairs on the O-atoms being projected along the {Cr_2O_2} plane. This drastically diminishes the π($d_{xz}|p_z|d_{yz}$) overlap and leads to weak ferromagnetic exchange at large θ values (Figure 6b).

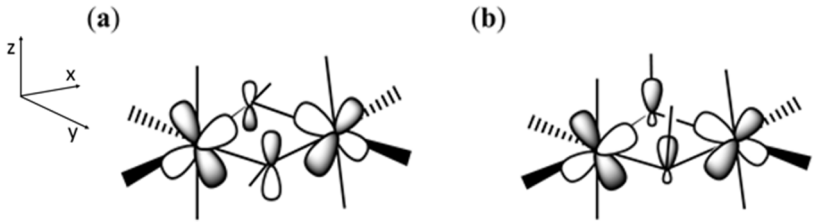

Figure 6. Schematic representation of the π($d_{xz}|p_z|d_{yz}$) overlap in complex **1** when the θ is small (a) and large (b).

The Cr-O-Cr-O dihedral (ψ) angle also varies between structures, albeit only slightly. The dominant $d_{xz}|p_z|d_{yz}$ overlap is expected to decrease as we move away from a planar Cr-O-Cr-O geometry (ψ = 0.0), and thus large angles would be expected to yield weaker antiferromagnetic coupling. This qualitative picture is indeed reflected in calculations where for ψ = 0.9°, the dominant overlap integrals are found to be π ($d_{xz}|p_z|d_{yz}$) pairs and this facilitates the strong antiferromagnetic interaction observed. However, at ψ = 17.4°, the π ($d_{xz}|p_z|d_{yz}$) overlap integral decreases significantly and leads to weak antiferromagnetic interaction. At an angle of ψ = 27.6° the exchange becomes weakly ferromagnetic.

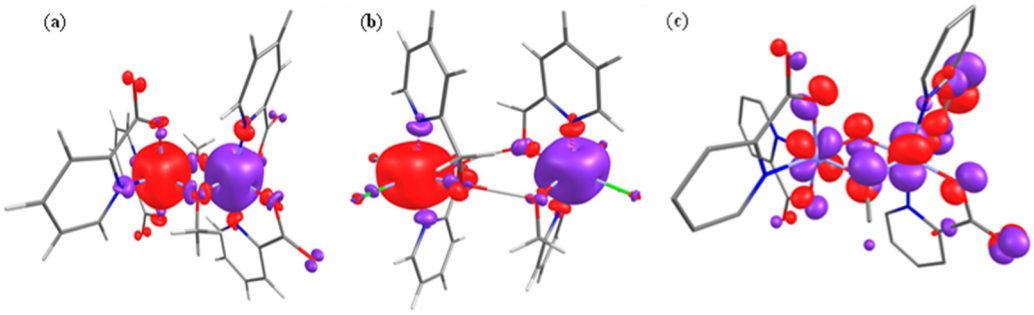

Figure 7. Computed spin density BS1 (broken symmetry) plots for complexes **1** (a) and **8** (b). (c) The π($d_{xz}|p_x|d_{yz}$) overlap observed in complex 1.

Spin density plots computed for complexes **1** and **8** are shown in Figure 7 (see ESI Figure S15 and S16 for complexes **2**-**7**). A cubic shaped spin density is observed on the Cr(III) ions,

deriving from the t_{2g}^3 configuration, with dominant spin polarization, leading to larger than the expected spin density values at the Cr(III) centres. For complex **8**, the magnetic exchange is mediated only by two H-bonding interactions and here the dominant overlap is computed to *via* $d_{xz}|d_{yz}$; as expected the magnitude of the overlap integral is small reflecting the weak AF exchange computed.

To understand the variation in the magnitude of the *J* values, and in particular to probe if larger θ values could yield ferromagnetic exchange, magneto-structural correlations have been developed for complex **1** (Figure 8). Our correlation affords a linear regression in *J* with increasing θ, yielding weak ferromagnetic coupling at very large θ values and strong antiferromagnetic coupling at smaller θ values. The computed overlap integrals for these points reflect the reduction in the π-type overlap as θ increases. The experimental *J* values show a similar trend. The computed *J* values are correlated to the overlap integrals and found to match nicely with the spin densities on the bridging oxygen atoms, with larger negative spin densities yielding stronger AF exchange (Figure 8).

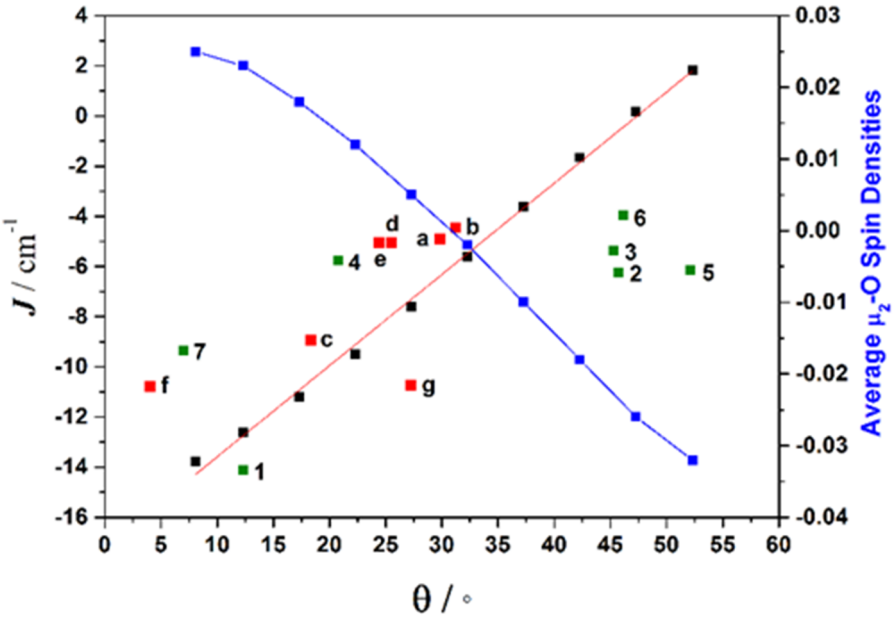

Figure 8. Magneto-structural correlations developed by varying θ in complex **1** (black squares represent computationally determined values from the variation of compound **1**), along with the experimental *J* values from compounds **1**-**7** (green squares), experimental J values for compounds **a**-**g** from the literature (red squares) (see Table S17 for details on literature compounds),[67-72] and the average bridging oxygen spin densities (blue squares). This is calculated for a ψ dihedral angle, ψ = 0°, the reader's attention is directed to Figure 1 on page 23 for a visual representation of the appropriate angles.

The correlation developed by DFT predicts a switch from AF→F exchange coupling at θ > 47.3°. However, this does not match experiment (Tables 2-3), and it is clear from Figure 8 that several complexes show experimentally determined *J* values that deviate from this linear fit. This suggests that the ψ parameter is also likely to play a key role in determining *J*. A closer look at the structures of the dimers reveals that when θ becomes larger it is accompanied by a variation in the ψ dihedral angles, *i.e.* θ and ψ are correlated. To ascertain the combined effect of both parameters, we have developed a magneto-structural correlation by varying both θ and ψ simultaneously, with the results shown in the three dimensional plot of Figure 9 and the contour plot of Figure 10.

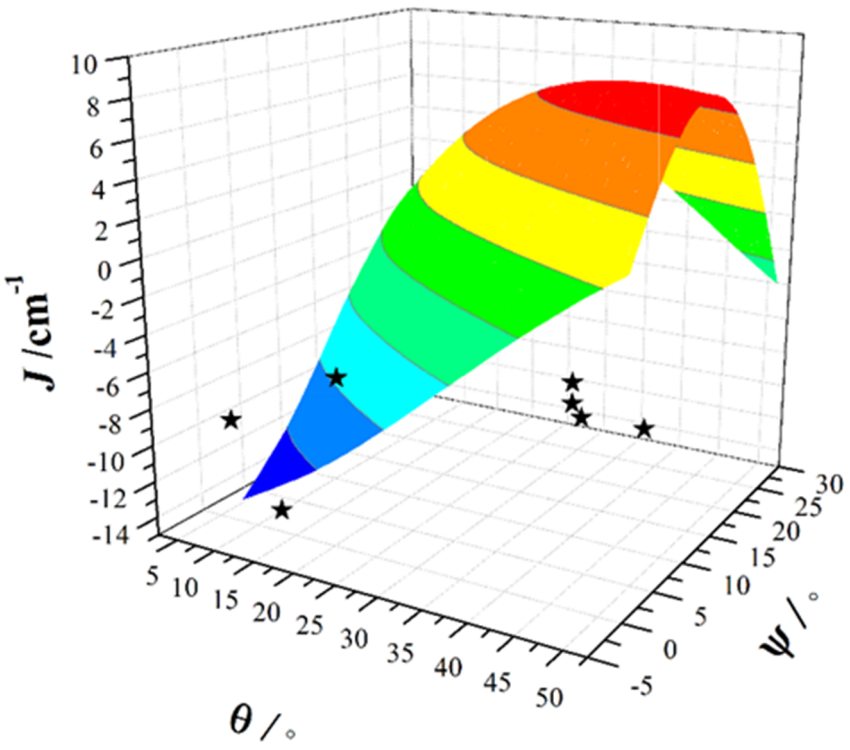

Figure 9. Magneto-structural correlations developed by varying θ and ψ simultaneously in complex **1**. The black stars are experimental *J* values for complexes **1**-**7**.

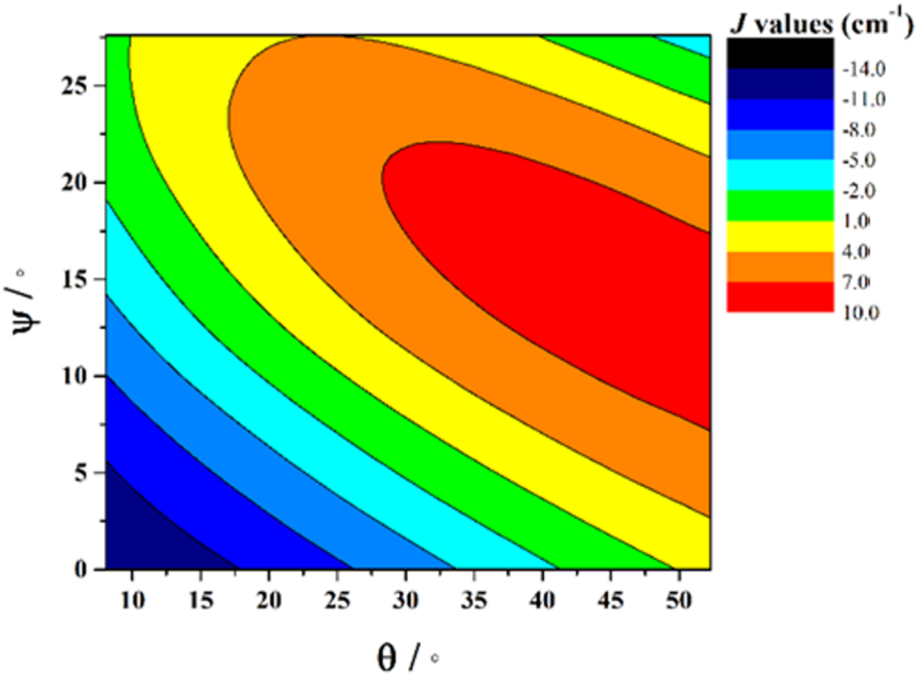

Figure 10. 2D contour plot showing the magneto-structural correlations developed by varying θ and ψ simultaneously in complex **1**.

The developed correlation suggests a strong dependence of J on both parameters, with the possibility of obtaining ferromagnetic exchange even with relatively small θ values, if, and only if, the corresponding ψ values are relatively large. The experimentally observed ψ dihedral angles are however all small, in the range 0 - 4.9°, whilst the correlation developed for ψ predicts a switch from AF→F at angles larger than 17.4°. The correlation reveals that when ψ = 0°, varying the θ even beyond 45° does not yield ferromagnetic exchange. However for ψ = 25°, θ values above 10° yield ferromagnetic coupling. While the above correlations clearly establish the importance of both θ and ψ in controlling the magnitude of *J*, we note that calculations were limited to complex **1** where the presence of the bridging methoxide group allowed for simple alterations of both parameters independently. For complexes **2**-**7**, where the methoxide is replaced by the alkoxide arm of the hmp^-/hep^- ligands this is not the case, with the bridging moieties offering additional Cr(1)-N-C-C-O-Cr(2) exchange pathways, which would likely result in minor variations in the computed magnitude of the *J* values. In addition variation of parameters in compounds **2**-**7** would be complicated by the knock on effect these variations would have on other structural aspects, making it impossible to isolate and study individual changes by this method.

2.4 Conclusions

The initial use of pyridine alcohol ligands in Cr(III) coordination chemistry, in the absence of any additional co-ligands, has led to the formation of a family of di-alkoxo-bridged $[Cr_2(OR)_2]$ dimers. DC magnetic susceptibility measurements reveal weak antiferromagnetic interactions in all cases. DFT calculations reproduce the sign and approximate magnitude of the exchange coupling constants. Our computationally developed magneto-structural correlation reveals the importance of both the angle between the Cr_2O_2 plane and the O-R vector of the bridging group (θ) and the Cr-O-Cr-O dihedral angles (ψ) in modulating the sign and strength of *J*.

2.5 Supplementary Information

Table S1. Crystallographic information for compounds **1**-**4**.

Compound	**1**	**2**	**3**	**4**
Formula	$C_{28.5}H_{29}Cr_2N_4O_{11}$	$C_{24}H_{20}Cl_2Cr_2N_4O_6$	$C_{24}H_{20}Br_2Cr_2N_4O_6$	$C_{20}H_{36}Cl_4Cr_2N_2O_6$
$D_{calc.}$/ g cm^{-3}	1.419	1.693	1.879	1.520
μ/mm^{-1}	0.717	1.136	4.019	1.183
FW/g mol^{-1}	707.56	635.34	724.26	646.31
Colour	pink	brown	light purple	green
Shape	block	block	prism	block
Size/mm^3	0.25x0.12x0.09	0.33x0.18x0.18	0.24x0.10x0.09	0.19x0.16x0.11
T/K	120.00	120.00	120.0	120.0
Crystal System	monoclinic	orthorhombic	orthorhombic	triclinic
Flack/Hooft Parameters	-	-0.003(5)/-0.018(4)	0.010(7)/0.028(7)	-
Space Group	$P2_1/n$	$Pnn2$	$Pnn2$	P-1
a/Å	12.2931(8)	7.81306(10)	7.8068(2)	9.7732(4)
b/Å	21.3092(16)	12.17220(15)	12.2423(4)	10.4693(3)
c/Å	13.2192(8)	13.10384(16)	13.3916(4)	14.0067(7)
α/°	90	90	90	92.473(4)
β/°	106.939(7)	90	90	99.099(4)
γ/°	90	90	90	91.960(3)
V/Å^3	3312.6(4)	1246.20(3)	1279.88(7)	1412.58(10)
Z (Z')	4 (1)	2 (0.5)	2 (0.5)	2 (1)
Wavelength/Å	0.71073	0.71073	0.71073	0.71073
Radiation type	MoK_α	MoK_α	MoK_α	MoK_α
Θ_{min}/° - Θ_{max}/°	3.222 - 24.996	3.035 - 32.892	3.042 - 29.769	3.288 - 28.854
Measured Refl.	47599	45650	11349	22598
Independent Refl.	5824	4514	3209	6514
Reflections Used	4892	4406	3011	5624
R_{int}	0.0970	0.0356	0.0369	0.0452
Parameters	454	212	172	324
Restraints	31	1	1	6
Largest Peak	0.768	0.308	0.423	0.829
Deepest Hole	-0.585	-0.300	-0.500	-0.632
GooF	1.151	1.051	1.066	1.266
wR_2 (all data) (wR_2)	0.2129 (0.2054)	0.0528 (0.0522)	0.0570 (0.0549)	0.1652 (0.1608)
R_1 (all data) (R_1)	0.0979 (0.0830)	0.0225 (0.0215)	0.0344 (0.0304)	0.0862 (0.0728)
CCDC Number	1482832	1482833	1482834	1482835

Pascals constants for diamagnetic corrections of relevant atoms and counter ions (χ_D/1x10^{-6}cm^{3}mol^{-1}):

H	-2.9	C	-6.0
N (ring)	-4.6	N (open chain)	-5.6
O (alcohol)	-4.6	O (carbonyl)	-1.7
Cl	-20.1	Br	-30.6
O^{2-}	-12.0	Cl^-	-23.4
Br^-	-34.6	NO_3^-	-18.9
ClO_4^-	-32.0		

Table S2. Crystallographic information for compounds **5**-**8**.

Compound	**5**	**6**	**7**	**8**
Formula	$C_{32}H_{32}Cl_4Cr_2N_6O_2$	$C_{24}H_{26}Cl_4Cr_2N_4O_2$	$C_{18}H_{26}Cl_4Cr_2N_4O_4$	$C_{14}H_{16}Cl_2CrN_3O_2$
$D_{calc.}$/ g cm^{-3}	1.531	1.625	1.628	1.713
μ/mm^{-1}	8.539	10.720	11.459	1.145
FW/g mol^{-1}	778.43	648.29	608.23	381.20
Colour	dark green	blue	brown	green
Shape	block	block	block	block
Size/mm^3	0.24x0.14x0.05	0.20×0.09×0.03	0.09x0.06x0.04	0.22x0.05x0.04
T/K	120.0	120.0	120.0	120.0
Crystal System	tetragonal	monoclinic	triclinic	tetragonal
Flack/Hooft Parameters	(n/a)/0.255(8)	-	-	-
Space Group	$I4_1$	P2/c	*P*-1	$P4_2/nbc$
a/Å	16.2418(2)	14.29325(19)	8.2906(3)	15.4761(3)
b/Å	16.2418(2)	14.06348(14)	8.5467(3)	15.4761(3)
c/Å	25.6069(6)	14.8511(2)	10.1679(4)	12.3453(3)
α/°	90	90	112.400(4)	90
β/°	90	117.3958(17)	101.243(3)	90
γ/°	90	90	102.099(3)	90
V/Å^3	6755.0(2)	2650.46(7)	620.49(4)	2956.82(13)
Z (*Z'*)	8 (1)	4 (1)	1 (0.5)	8 (0.5)
Wavelength/Å	1.54178	1.54178	1.54178	0.71073
Radiation type	CuK_α	CuK_α	CuK_α	MoK_α
Θ_{min}/° - Θ_{max}/°	4.938 - 76.392	3.142 – 76.778	4.938 - 76.392	3.107 - 26.369
Measured Refl.	28737	43244	10079	134457
Independent Refl.	6396	5513	2577	1520
Reflections Used	5590	5054	2421	1516
R_{int}	0.0730	0.0554	0.0566	0.0725
Parameters	432	327	153	90
Restraints	247	0	3	3
Largest Peak	0.830	0.524	0.788	0.452
Deepest Hole	-0.608	-0.677	-0.520	-0.358
GooF	1.044	1.038	1.062	1.330
wR_2 (all data) (wR_2)	0.2107 (0.1952)	0.1227 (0.1198)	0.1287 (0.1262)	0.1087 (0.1086)
R_1 (all data) (R_1)	0.0858 (0.0739)	0.0455 (0.0428)	0.0488 (0.0466)	0.0491 (0.0489)
CCDC Number	1540438	1540439	1482836	1482837

For Figures S1-S16 and Tables S2-S17 please refer to the “Chapter 2 SI” file on the memory stick supplied with the thesis.

2.5 References

1. S. M. Gorun, G. C. Papaefthymiou, R. B. Frankel and S. J. Lippard, *J. Am. Chem. Soc.*, 1987, **109**, 3337-3348.
2. R. Bagai and G. Christou, *Chem. Soc. Rev.*, 2009, **38**, 1011-1026.
3. A. Caneschi, D. Gatteschi, R. Sessoli and P. Rey, *Acc. Chem. Res.*, 1989, **22**, 392-398.
4. S. Srinivasan and R. Seshan, in *Chromium VI Reagents: Synthetic Applications*, Springer Berlin Heidelberg, Berlin, Heidelberg, 2011, DOI: 10.1007/978-3-642-20817-1_6, pp. 63-66.
5. I. Mulyani, A. Levina and P. A. Lay, *Angew. Chem. Int. Ed.*, 2004, **43**, 4504-4507.
6. R. D. Cannon and R. P. White, *Prog. Inorg. Chem.*, 1988, **36**, 195-298.
7. E. J. McInnes, G. A. Timco, G. F. Whitehead and R. E. Winpenny, *Angew. Chem. Int. Ed.*, 2015, **54**, 14244-14269.
8. E. J. L. McInnes, S. Piligkos, G. A. Timco and R. E. P. Winpenny, *Coord. Chem. Rev.*, 2005, **249**, 2577-2590.
9. B. N. Figgis and G. B. Robertson, *Nature*, 1965, **205**, 694-695.
10. R. F. Weinland, *Ber. Dtsch. Chem. Ges.*, 1908, **41**, 3236-3245.
11. A. Werner, *Ber. Dtsch. Chem. Ges.*, 1908, **41**, 3447-3465.
12. T. Fujihara, J. Aonahata, S. Kumakura, A. Nagasawa, K. Murakami and T. Ito, *Inorg. Chem.*, 1998, **37**, 3779-3784.
13. S. Parsons, A. A. Smith and R. E. P. Winpenny, *Chem. Commun.*, 2000, 579-580.
14. A. Ghirri, J. van Tol, I. Vitorica-Yrezabal, G. A. Timco and R. E. Winpenny, *Dalton Trans.*, 2015, **44**, 14027-14033.
15. P. Kögerler, B. Tsukerblat and A. Müller, *Dalton Trans.*, 2010, **39**, 21-36.
16. T. Ellis, M. Glass, A. Harton, K. Folting, J. C. Huffman and J. B. Vincent, *Inorg. Chem.*, 1994, **33**, 5522-5527.
17. A. Bino, D. C. Johnston, D. P. Goshorn, T. R. Halbert and E. I. Stiefel, *Science*, 1988, **241**, 1479-1481.
18. I. M. Atkinson, C. Benelli, M. Murrie, S. Parsons and R. E. P. Winpenny, *Chem. Commun.*, 1999, 285-286.
19. M. Eshel, A. Bino, I. Felner, D. C. Johnston, M. Luban and L. L. Miller, *Inorg. Chem.*, 2000, **39**, 1376-1380.
20. E. J. L. McInnes, C. Anson, A. K. Powell, A. J. Thomson, S. Poussereau and R. Sessoli, *Chem. Commun.*, 2001, 89-90.
21. M. Eshel and A. Bino, *Inorg. Chim. Acta*, 2002, **329**, 45-50.
22. J. van Slageren, R. Sessoli, D. Gatteschi, A. A. Smith, M. Helliwell, R. E. P. Winpenny, A. Cornia, A.-L. Barra, A. G. M. Jansen, E. Rentschler and G. A. Timco, *Chem. Eur. J.*, 2002, **8**, 277-285.
23. P. Christian, G. Rajaraman, A. Harrison, J. J. W. McDouall, J. T. Raftery and R. E. P. Winpenny, *Dalton Trans.*, 2004, 1511-1512.
24. D. M. Low, G. Rajaraman, M. Helliwell, G. Timco, J. van Slageren, R. Sessoli, S. T. Ochsenbein, R. Bircher, C. Dobe, O. Waldmann, H. U. Güdel, M. A. Adams, E. Ruiz, S. Alvarez and E. J. L. McInnes, *Chem. Eur. J.*, 2006, **12**, 1385-1396.
25. A. S. Batsanov, G. A. Timko, Y. T. Struchkov, N. V. Gerbeleu and K. M. Indrichan, *Koord. Khim.*, 1991, **17**, 662-669.
26. F. E. Mabbs, E. J. L. McInnes, M. Murrie, S. Parsons, G. M. Smith, C. C. Wilson and R. E. P. Winpenny, *Chem. Commun.*, 1999, 643-644.
27. C. E. Talbot-Eeckelaers, G. Rajaraman, J. Cano, G. Aromí, E. Ruiz and E. K. Brechin, *Eur. J. Inorg. Chem.*, 2006, 3382-3392.

28. R. Shaw, R. H. Laye, L. F. Jones, D. M. Low, C. Talbot-Eeckelaers, Q. Wei, C. J. Milios, S. Teat, M. Helliwell, J. Raftery, M. Evangelisti, M. Affronte, D. Collison, E. K. Brechin and E. J. L. McInnes, *Inorg. Chem.*, 2007, **46**, 4968-4978.
29. A. Døssing, *Coord. Chem. Rev.*, 2014, **280**, 38-53.
30. N. H. Andersen, A. Dossing and A. Molgaard, *Inorg. Chem.*, 2003, **42**, 6050-6055.
31. J. Glerup and H. Weihe, *Inorg. Chem.*, 1997, **36**, 2816-2819.
32. B. G. Gafford, R. A. Holwerda, H. J. Schugar and J. A. Potenza, *Inorg. Chem.*, 1988, **27**, 1126-1128.
33. T. F. Tekut, C. J. O'Connor and R. A. Holwerda, *Inorg. Chem.*, 1993, **32**, 324-328.
34. T. J. Morsing, J. Bendix, H. Weihe and A. Dossing, *Inorg. Chem.*, 2014, **53**, 2996-3003.
35. R. A. Holwerda, T. F. Tekut, B. G. Gafford, J. H. Zhang and C. J. O'Connor, *J. Chem. Soc., Dalton Trans.*, 1991, 1051-1055.
36. D. J. Hodgson, M. H. Zietlow, E. Pedersen and H. Toftlund, *Inorg. Chim. Acta*, 1988, **149**, 111-117.
37. D. M. Stearns and W. H. Armstrong, *Inorg. Chem.*, 1992, **31**, 5178-5184.
38. T. Fujihara, A. Fuyuhiro and S. Kaizaki, *J. Chem. Soc., Dalton Trans.*, 1995, 1813-1821.
39. A. Drljaca, D. C. R. Hockless, B. Moubaraki, K. S. Murray and L. Spiccia, *Inorg. Chem.*, 1997, **36**, 1988-1989.
40. G. Novitchi, J. P. Costes, V. Ciornea, S. Shova, I. Filippova, Y. A. Simonov and A. Gulea, *Eur. J. Inorg. Chem.*, 2005, **5**, 929-937.
41. J. Glerup, P. A. Goodson, D. J. Hodgson, M. A. Masood and K. Michelsen, *Inorg. Chim. Acta*, 2005, **358**, 295-302.
42. J. Glerup, D. J. Hodgson and E. Pedersen, *Acta Chem. Scand. A.*, 1983, **37**, 161-164.
43. T. J. Morsing, H. Weihe and J. Bendix, *Eur. J. Inorg. Chem.*, 2014, **2014**, 5990-5996.
44. M. Ardon, A. Bino, K. Michelsen and E. Pedersen, *J. Am. Chem. Soc.*, 1987, **109**, 5855-5856.
45. P. A. Goodson, J. Glerup, D. J. Hodgson, K. Michelsen and U. Rychlewska, *Inorg. Chem.*, 1994, **33**, 359-366.
46. G. M. Sheldrick, *Acta Crystallogr. Sect. C: Cryst. Struct. Commun.*, 2015, **71**, 3-8.
47. O. V. Dolomanov, L. J. Bourhis, R. J. Gildea, J. A. K. Howard and H. Puschmann, *J. Appl. Crystallogr.*, 2009, **42**, 339-341.
48. G. A. Bain and J. F. Berry, *J. Chem. Educ.*, 2008, **85**, 532.
49. M. J. Frisch, G. W. Trucks, H. B. Schlegel, G. E. Scuseria, M. A. Robb, J. R. Cheeseman, G. Scalmani, V. Barone, B. Mennucci, G. A. Petersson, H. Nakatsuji, M. Caricato, X. Li, H. P. Hratchian, A. F. Izmaylov, J. Bloino, G. Zheng, J. L. Sonnenberg, M. Hada, M. Ehara, K. Toyota, R. Fukuda, J. Hasegawa, M. Ishida, T. Nakajima, Y. Honda, O. Kitao, H. Nakai, T. Vreven, J. A. Montgomery Jr., J. E. Peralta, F. Ogliaro, M. Bearpark, J. J. Heyd, E. Brothers, K. N. Kudin, V. N. Staroverov, R. Kobayashi, J. Normand, K. Raghavachari, A. Rendell, J. C. Burant, S. S. Iyengar, J. Tomasi, M. Cossi, N. Rega, J. M. Millam, M. Klene, J. E. Knox, J. B. Cross, V. Bakken, C. Adamo, J. Jaramillo, R. Gomperts, R. E. Stratmann, O. Yazyev, A. J. Austin, R. Cammi, C. Pomelli, J. W. Ochterski, R. L. Martin, K. Morokuma, V. G. Zakrzewski, G. A. Voth, P. Salvador, J. J. Dannenberg, S. Dapprich, A. D. Daniels, O. Farkas, J. B. Foresman, J. V. Ortiz and J. Cioslowski and D. J. Fox, *GAUSSIAN 09 (Revision A.02), Gaussian, Inc., Wallingford, CT*, 2009.
50. A. D. Becke, *J. Chem. Phys.*, 1993, **98**, 5648-5652.
51. A. Schafer, H. Horn and R. Ahlrichs, *J. Chem. Phys.*, 1992, **97**, 2571-2577.
52. A. Schafer, C. Huber and R. Ahlrichs, *J. Chem. Phys.*, 1994, **100**, 5829-5835.

53. M. Atanasov, P. Comba, S. Hausberg and B. Martin, *Coord. Chem. Rev.*, 2009, **253**, 2306-2314.
54. L. Noodleman, *J. Chem. Phys.*, 1981, **74**, 5737-5743.
55. W. P. Barros, R. Inglis, G. S. Nichol, T. Rajeshkumar, G. Rajaraman, S. Piligkos, H. O. Stumpf and E. K. Brechin, *Dalton Trans.*, 2013, **42**, 16510-16517.
56. N. Berg, T. Rajeshkumar, S. M. Taylor, E. K. Brechin, G. Rajaraman and L. F. Jones, *Chem. Eur. J.*, 2012, **18**, 5906-5918.
57. P. Comar, T. Rajeshkumar, G. S. Nichol, M. B. Pitak, S. J. Coles, G. Rajaraman and E. K. Brechin, *Dalton Trans.*, 2015, **44**, 19805-19811.
58. M. A. Bolcar, S. M. J. Aubin, K. Folting, D. N. Hendrickson and G. Christou, *Chem. Commun.*, 1997, 1485-1486.
59. E. K. Brechin, E. C. Sañudo, W. Wernsdorfer, C. Boskovic, J. Yoo, D. N. Hendrickson, A. Yamaguchi, H. Ishimoto, T. E. Concolino, A. L. Rheingold and G. Christou, *Inorg. Chem.*, 2005, **44**, 502-511.
60. E. K. Brechin, M. J. Knapp, J. C. Huffman, D. N. Hendrickson and G. Christou, *Inorg. Chim. Acta*, 2000, **297**, 389-399.
61. E. C. Yang, W. Wernsdorfer, S. Hill, R. S. Edwards, M. Nakano, S. Maccagnano, L. N. Zakharov, A. L. Rheingold, G. Christou and D. N. Hendrickson, *Polyhedron*, 2003, **22**, 1727-1733.
62. E. C. Yang, D. N. Hendrickson, W. Wernsdorfer, M. Nakano, L. N. Zakharov, R. D. Sommer, A. L. Rheingold, M. Ledezma-Gairaud and G. Christou, *J. Appl. Phys.*, 2002, **91**, 7382-7384.
63. J. Moncol, K. Jomova, L. Zelenicky, T. Lis and M. Valko, *Acta Crystallogr. Sect. C: Cryst. Struct. Commun.*, 2011, **67**, M318-M320.
64. T. J. Boyle, L. A. M. Ottley, M. A. Rodriguez, R. M. Sewell, T. M. Alam and S. K. McIntyre, *Inorg. Chem.*, 2008, **47**, 10708-10717.
65. B. Müller, A. Schneider, M. Tesmer and H. Vahrenkamp, *Inorg. Chem.*, 1999, **38**, 1900-1907.
66. R. J. Fites, A. T. Yeager, T. L. Sarvela, W. A. Howard, G. Zhu and K. L. Pang, *Inorg. Chim. Acta*, 2006, **359**, 248-256.
67. H. R. Fischer, J. Glerup, D. J. Hodgson and E. Pedersen, *Inorg. Chem.*, 1982, **21**, 3063-3066.
68. H. R. Fischer, D. J. Hodgson and E. Pedersen, *Inorg. Chem.*, 1984, **23**, 4755-4758.
69. E. D. Estes, R. P. Scaringe, W. E. Hatfield and D. J. Hodgson, *Inorg. Chem.*, 1977, **16**, 1605-1610.
70. E. D. Estes, R. P. Scaringe, W. E. Hatfield and D. J. Hodgson, *Inorg. Chem.*, 1976, **15**, 1179-1182.
71. B. Liu, J. Chai, S. S. Feng and B. S. Yang, *Spectrochim. Acta Mol. Biomol. Spectrosc.*, 2015, **140**, 437-443.
72. N. Clement, C. Toussaint, G. Rogez, C. Loose, J. Kortus, L. Brelot, S. Choua, S. Dagorne, P. Turek and R. Welter, *Dalton Trans.*, 2010, **39**, 4579-4585.

CHAPTER 3:

A SIMPLE METHODOLOGY FOR CONSTRUCTING FERROMAGNETICALLY COUPLED Cr(III) COMPOUNDS

3.1 Introduction

Magneto-structural studies of Cr(III) dimers have been reported extensively since the 1970s, with the vast majority revealing antiferromagnetic exchange between the two metal centres.[1-3] Indeed, although more than 40 years have passed since the publication of the first ferromagnetically coupled complex in 1976, namely $Na_4[Cr(mal)_2OH]_2$,[4, 5] there have been only three further examples: the di-hydroxo bridged compound $[(H_2O)_4Cr(OH)]_2[(CH_3)_3C_6H_2SO_3]_4$ reported in 1987,[6] the di-fluoro bridged $[Cr(BTS)F]_2$ published in 1996,[7] and the most recent example a di-hydroxo bridged species of formula $(Ph_4P)_4[Cr(NCS)_4OH]_2$ published in 2014.[8] Larger Cr(III) clusters displaying ferromagnetic exchange are even more rare, with only two examples known.[9, 10] The first is an unusual sulfide-centred tetrahedron externally bridged with acetates, $[Cr_4S(O_2CCH_3)_8(H_2O)_4](BF_4)_2$,[9] and the second a family of aesthetically pleasing decametallic wheels of general formula $[Cr_{10}(OR)_{20}(O_2CR')_{10}]$ (R = Me or Et, R' = Me, Et, CMe_3).[10] In the latter case the bridging unit between pairs of neighbouring Cr(III) ions consists of two alkoxides and one carboxylate. Perhaps of most interest is the observation that the methoxide bridged versions were found to be ferromagnetically coupled to give S = 15 spin ground states, while the ethoxide bridged analogues were antiferromagnetically coupled to afford diamagnetic S = 0 spin ground states. This rather dramatic difference, albeit with a just a small difference in the overall magnitude of $|J|$, was attributed to a change in electron density at the bridging oxygen atom, with the more inductive ethoxide group leading to stronger antiferromagnetic exchange.[11] Unfortunately the development of detailed/quantitative magneto-structural correlations for the wheels was hampered by the low symmetry of the molecules, disorder in the ligand framework, and the presence of significant intermolecular exchange interactions at low temperature.[11]

Note that both tetrametallic and decametallic species are heteroleptic, containing two different bridging ligands, including one carboxylate. This perhaps suggests that exploitation of the orbital counter-complementarity effect may be a promising route toward the development of polymetallic Cr(III) species displaying ferromagnetic exchange interactions.[12] To this end we recently began a project to examine the magnetic exchange, and uncover the magneto-structural relationship, between the metal ions in $[Cr^{III}(OR)_2Cr^{III}]$ and $[Cr^{III}(OR)_2(O_2CR)Cr^{III}]$ dimers. Our initial study of the di-

alkoxo bridged family of dimers showed that the exchange is dependent upon the Cr-O-Cr bridging angle, the orientation of the dihedral angle formed between the bridging Cr_2O_2 plane and the O-R vector of the bridging group, and the Cr-O-Cr-O dihedral angle.[13] The geometric restrictions placed upon dimers of this type essentially means that all such species will be antiferromagnetically coupled, except when a particular, and rather peculiar combination of such values are satisfied, in agreement with the study of Bendix *et al*.[8]

Here we extend our study to the $[Cr^{III}(OR)_2(O_2CR)Cr^{III}]$ family of dimers **1**-**8** whose structures are similar to the alkoxide bridged species in reference 13, but with the addition of a single carboxylate bridge. We also include the carboxylate free analogue **9** for direct comparison. The alkoxides employed are diethanolamine ligands ($deaH_2$), which have been successfully used as flexible bridging supports in the synthesis of a number of interesting 3d,[14, 15] 3d-3d,[16] 4f,[17] and 3d-4f compounds.[18] Its range of bridging modes, including a very unusual non-chelating end-on bridging mode,[19] have allowed for a plethora of different structural types,[20] as recently reviewed by Perlepes and Tasiopoulos.[21] In Cr(III) chemistry they have been shown to be successful in the formation of heterometallic cages, with families of Cr_23d_2 butterflies,[22] Cr_2Ln_2 butterflies,[23] and an octanuclear Cr_4Dy_4 reported.[24] Surprisingly however, no homometallic Cr(III) complexes are registered on the CCDC.

3.2 Experimental

Materials and physical measurements

All chemicals were procured from commercial suppliers and used as received (reagent grade). Elemental analyses for C, H, N and Cr were performed by Medac Ltd.

Synthesis of $[Cr_2(Me\text{-}deaH)_2(O_2CH)Cl_2]Cl$ (1)

$CrCl_3{\cdot}6H_2O$ (0.533 g, 2 mmol) was dissolved with NaOMe (0.054 g, 1 mmol) in MeCN (15 ml) with continuous stirring. Me-$deaH_2$ (0.23 ml, 2 mmol) was dissolved in MeCN (10 ml) with continuous stirring and added to the first solution. The resulting light blue solution was left to stir overnight at room temperature. A 10 ml sample of this solution was heated in a Teflon-lined autoclave at 100°C for 12 hours. Slow cooling to room

temperature yielded blue rod-shaped crystals, which were suitable for X-ray diffraction. Yield 1.8 mg (0.4% by chromium weight). Anal. Calcd (%) for $C_{11}H_{25}Cl_3Cr_2N_2O_6$: C 26.87, H 5.13, Cr 21.15, N 5.70; found: C 26.53, H 5.07, Cr 21.21, N 5.68.

Synthesis of $[Cr_2(Me\text{-}deaH)_2(O_2CMe)Cl_2]Cl$ (2)

$CrCl_3 \cdot 6H_2O$ (0.533 g, 2 mmol) was dissolved with NaO_2CMe (0.082 g, 1 mmol) in MeCN (25 ml) with continuous stirring. Me-deaH_2 (0.23 ml, 2 mmol) was added and the resulting blue solution was left to stir overnight at room temperature. A 10 ml sample of this solution was heated in a Teflon-lined autoclave at 100°C for 12 hours. Slow cooling to room temperature yielded purple block-shaped crystals, which were suitable for X-ray diffraction. Yield 119.8 mg (23.7% by chromium weight). Anal. Calcd (%) for $C_{12}H_{27}Cl_3Cr_2N_2O_6$: C 28.50, H 5.38, Cr 20.56, N 5.54; found: C 29.00, H 4.97, Cr 22.21, N 5.46.

Synthesis of $[Cr_2(Me\text{-}deaH)_2(O_2CCMe_3)Cl_2]Cl$ (3)

$CrCl_3 \cdot 6H_2O$ (0.533 g, 2 mmol) was dissolved with NaO_2CCMe_3 (0.124 g, 1 mmol) in MeCN (25 ml) with continuous stirring. Me-deaH_2 (0.23 ml, 2 mmol) was added and the resulting blue solution was left to stir overnight at room temperature. A 10 ml sample of this solution was heated in a Teflon-lined autoclave at 100°C for 12 hours. Slow cooling to room temperature yielded purple plate-shaped crystals, which were suitable for X-ray diffraction. Yield 178.6 mg (32.6% by chromium weight). Anal. Calcd (%) for $C_{15}H_{33}Cl_3Cr_2N_2O_6$: C 32.89, H 6.07, Cr 18.98, N 5.11; found: C 32.83, H 5.83, Cr 18.99, N 5.11.

Synthesis of $[Cr_2(Me\text{-}deaH)_2(O_2CPh)Cl_2]Cl$ (4)

$CrCl_3 \cdot 6H_2O$ (0.533 g, 2 mmol) was dissolved with NaO_2CPh (0.144 g, 1 mmol) in MeCN (25 ml) with continuous stirring. CH_3-deaH_2 (0.23 ml, 2 mmol) was added and the resulting blue solution was left to stir overnight at room temperature. A 10 ml sample of this solution was heated in a Teflon-lined autoclave at 100°C for 12 hours. Slow cooling to room temperature yielded dark purple block-shaped crystals, which were suitable for X-ray diffraction. Yield 193.8 mg (34.1% by chromium weight). Anal. Calcd

(%) for $C_{17}H_{29}Cl_3Cr_2N_2O_6$: C 35.96, H 5.15, Cr 18.32, N 4.93; found: C 35.85, H 4.82, Cr 18.18, N 4.81.

Synthesis of $[Cr_2(Me\text{-}deaH)_2(O_2C(Cl)_2Ph)Cl_2]Cl$ (5)

$CrCl_3 \cdot 6H_2O$ (0.533 g, 2 mmol) was dissolved with $NaO_2C\text{-}3,5\text{-}Cl_2Ph$ (0.213 g, 1 mmol) in MeCN (25 ml) with continuous stirring for 3 hours. Me-$deaH_2$ (0.23 ml, 2 mmol) was added and the resulting green solution was left to stir overnight at room temperature. A 10 ml sample of the green solution was heated in a Teflon-lined autoclave at 100°C for 12 hours. The solution was then filtered. Layering with 2-propanol yielded dark purple plate-shaped crystals, which were suitable for X-ray diffraction. Yield 50.4 mg (7.9% by chromium weight). Anal. Calcd (%) for $C_{17}H_{27}Cl_5Cr_2N_2O_6$: C 32.07, H 4.27, Cr 16.33, N 4.40; found: C 31.26, H 4.41, Cr 15.82, N 4.54.

Synthesis of $[Cr_2(Me\text{-}deaH)_2(O_2C(Me)_5Ph)Cl_2]Cl$ (6)

$CrCl_3 \cdot 6H_2O$ (0.533 g, 2 mmol) was dissolved with $NaO_2(Me)_5Ph$ (0.214 g, 1 mmol) in MeCN (25 ml) with continuous stirring. Me-$deaH_2$ (0.23 ml, 2 mmol) was added and the resulting blue solution was left to stir overnight at room temperature. A 10 ml sample of this solution was heated in a Teflon-lined autoclave at 100°C for 12 hours. The blue solution was then filtered, layering with 2-propanol yielded purple coloured plate-shaped crystals, which were suitable for X-ray diffraction. Yield 67.6 mg (10.6% by chromium weight). Anal. Calcd (%) for $C_{22}H_{39}Cl_3Cr_2N_2O_6$: C 41.42, H 6.16, Cr 16.30, N 4.39; found: C 40.42, H 6.15, Cr 16.06, N 4.55.

Synthesis of $[Cr_2(Et\text{-}deaH)_2(O_2CH)Cl_2]Cl$ (7)

$CrCl_3 \cdot 6H_2O$ (0.533 g, 2 mmol) was dissolved with NaOMe (0.054 g, 1 mmol) in MeCN (15 ml) with continuous stirring. Et-$deaH_2$ (0.26 ml, 2 mmol) was also dissolved in MeCN (10 ml) with continuous stirring and added to the first solution. The resulting green solution was left to stir overnight at room temperature. A 10 ml sample of this solution was heated in a Teflon-lined autoclave at 100°C for 12 hours. Vapour diffusion of the filtered blue solution with ethyl acetate yielded dark green block-shaped crystals, which were suitable for X-ray diffraction. Yield 5.5 mg (1.1% by chromium

weight). Anal. Calcd (%) for $C_{13}H_{29}Cl_3Cr_2N_2O_6$: C 30.04, H 5.62, Cr 20.01, N 5.39; found: C 29.87, H 5.50, Cr 20.65, N 5.22.

Synthesis of $[Cr_2(Et\text{-}deaH)_2(O_2CPh)Cl_2]Cl\cdot½Et_2O$ (8)

$CrCl_3\cdot6H_2O$ (0.533 g, 2 mmol) was dissolved with NaO_2CPh (0.144 g, 1 mmol) in MeCN (25 ml) with continuous stirring. Et-deaH_2 (0.26 ml, 2 mmol) was added to the green solution and the resulting blue solution was left to stir overnight at room temperature. A 10 ml sample of this solution was heated in a Teflon-lined autoclave at 100°C for 12 hours. Vapour diffusion of the filtered solution with diethyl ether yielded dark purple rod-shaped crystals, which were suitable for X-ray diffraction. Yield 1.2 mg (0.2% by chromium weight). Anal. Calcd (%) for $C_{19}H_{33}Cl_3Cr_2N_2O_6$: C 38.30, H 5.58, Cr 17.45, N 4.70; found: C 37.82, H 5.52, Cr 18.01, N 4.51.

Synthesis of $[Cr_2(Me\text{-}deaH)_2Cl_4]$ (9)

$CrCl_3\cdot6H_2O$ (0.533 g, 2 mmol) was dissolved in MeCN (25 ml) with continuous stirring. Me-deaH_2 (0.23 ml, 2 mmol) was added and the resulting blue solution was left to stir overnight at room temperature. A 10 ml sample of this solution was heated in a Teflon-lined autoclave at 100°C for 12 hours. Slow cooling to room temperature yielded dark green rod-shaped crystals, which were suitable for X-ray diffraction. Yield 41.0 mg (8.5% by chromium weight). Anal. Calcd (%) for $C_{10}H_{24}Cl_4Cr_2N_2O_4$: C 24.91, H 5.02, Cr 21.57, N 5.81; found: C 23.94, H 4.65, Cr 22.20, N 5.46.

X-ray crystallography

Diffraction data for samples **1**-**9** were collected using a Rigaku Oxford Diffraction SuperNova diffractometer with MoK_α (**1**-**4**, **6**-**9**) and CuK_α (**5**) radiation, and are given in Tables 4,5 and 6 in the supplementary information. An Oxford Cryosystems Cryostream 700+ low temperature device was used to maintain a crystal temperature of 120 K. The structures were solved using ShelXT or ShelXS by direct (**2**-**7**, **9**) or intrinsic phasing solution methods (**1**, **8**) and refined with version 2016/6 of ShelXL interfaced with Olex2.[25, 26] All non-hydrogen atoms were refined using anisotropic displacement parameters. C-bound H atoms were placed in calculated positions geometrically and refined using the riding model. In structures **1**, **2**, **4**, **6** and **9**, O-

bound H atoms were identified from a difference Fourier map and refined freely. In **3**, **5**, **7** and **8**, O-bound H atoms were identified from a difference Fourier map and refined as riding, with geometric restraints. CCDC: 1579642-1579645 & 1579647-1579651.

SQUID Magnetometry

Magnetic susceptibility and magnetisation measurements in the temperature range *T* = 2-300 K were performed on a Quantum Design MPMS XL SQUID magnetometer equipped with a 7 T dc magnet on finely ground samples of **1**-**9**. The observed paramagnetic susceptibilities were corrected for diamagnetic contributions using Pascal's constants.[27] Susceptibility measurements were performed under magnetic fields of 0.1 T, 0.5 T and 1.0 T. Variable-temperature-variable-field dc magnetisation experiments were carried out in the 2-7 K and 0.5-7.0 T temperature and magnetic field ranges, respectively.

Computational details

All theoretical calculations were performed using the hybrid B3LYP functional with Ahlrichs triple-ξ basis set as implemented in Gaussian 09.[28-31] This methodology has yielded good numerical estimates of the *J* values in a variety of systems, including several Cr(III) clusters.[13, 32-39] *J* values were computed from the energy difference between the HS state and BS state. The energy of the HS state was calculated using the single determinant approach, with the energy of the BS state calculated using the broken symmetry approach developed by Noodleman.[40] A quadratic convergence method was employed to obtain the most stable wave function. For orbital analysis using the HTH model,[41] β orbitals of the HS state were employed as these orbitals have been shown to better represent the interaction between the metal ions.[42, 43]

3.3 Results and discussion

Structure description

The structures of compounds **1**-**9** are given in Figure 1 (representative **2** and **9**) and Figures S1-9, with the most pertinent structural parameters listed in Table 1.

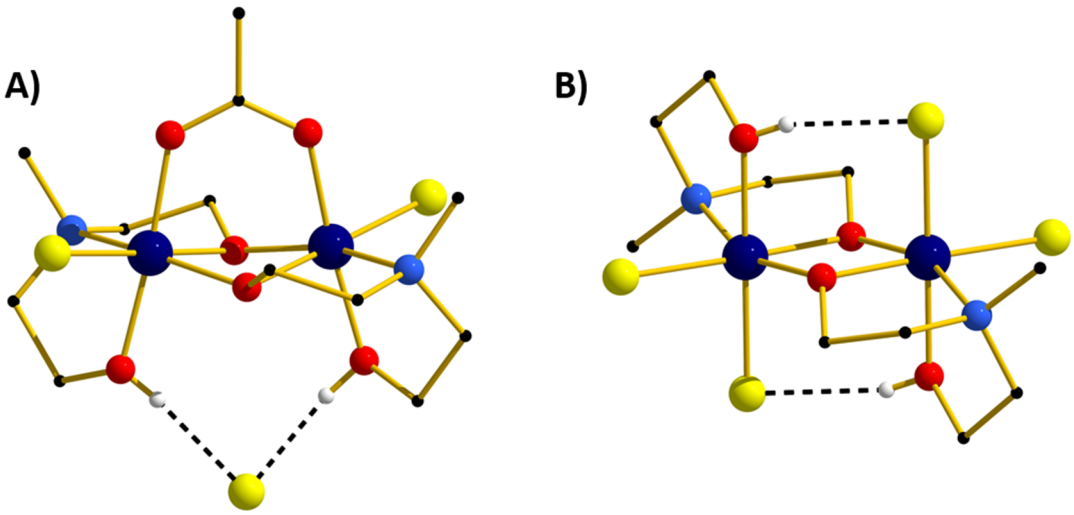

Figure 1. The molecular structures of complexes **2** (A) and **9** (B). Colour code: Cr = dark blue, O = red, N = light blue, C = black, Cl = yellow, H = white. H-atoms are omitted for clarity, except for those on the protonated arm of the Me-deaH$^-$ ligands. H-bonds are drawn as dashed black lines.

There are two different structure types. The first structure type is that seen in compounds **1**-**8**; the second that exhibited by compound **9** (Figure 1). Complexes **1**-**8** consist of two Cr(III) ions bridged by two μ-OR groups belonging to the singly deprotonated Me-deaH ligands, and one μ-O_2CR carboxylate bridge. The three remaining coordination sites on the octahedral Cr(III) ions are occupied by the N atom and protonated O atom from a Me-deaH ligand, and a terminally bonded chloride ion. The carboxylate sits above the [Cr_2] moiety (as drawn in Figure 1) causing the two μ_2-OR bridges to be pushed downwards, distorting the planarity of the [Cr_2O_2] unit (Table 1). The OH groups from the R-deaH ligands sit below the [Cr_2O_2] 'plane' and are H-bonded to the charge balancing chloride anion (OH···Cl, ~2.1 Å), which sits midway between the two Cr(III) ions. There are numerous inter-dimer interactions in the extended structures of **1**-**8**, with the closest contacts typically being between the terminal Cl ions and methyl H-atoms of R-deaH ligands on neighbouring molecules (~2.7-2.9 Å). The most relevant interactions are summarized in Table 2 and Figures S10-S11.

Table 1. Pertinent structural parameters for compounds **1**-**9**. r = Cr-$O_{alkoxide}$ bond length, ϕ = Cr-O-Cr bridging angle, θ = dihedral angle between the bridging Cr_2O_2 plane and the OR vector of the bridging group, ψ = Cr-O-Cr-O dihedral angle.

Compound	Cr-Cr [Å]	r [Å]	ϕ [°]	θ [°]	ψ [°]
1	2.967	1.957-1.971	98.41,97.87	38.76,40.79	18.41
2	2.968	1.957-1.972	98.55,97.91	37.85,40.85	18.74
3	2.957	1.946-1.962	98.39,98.34	21.80,41.35	18.72
4	2.959	1.956-1.965	98.20,97.71	39.46,39.98	18.57
5	2.965	1.954-1.965	98.39,98.32	40.98,39.53	18.11
	2.958	1.944-1.964	98.38,98.24	40.35,30.07	17.85
6	2.955	1.942-1.956	98.60,98.37	39.63,18.21	18.33
7	2.964	1.953-1.960	98.57,98.44	33.86,40.65	17.44
8	2.971	1.954-1.966	98.89,98.39	36.12,40.04	19.66
9	3.023	1.961-1.964	100.73	33.77	0.00

Table 2. Pertinent crystal structure information and closest intermolecular interactions for compounds **1**-**9**. $d_{H(Me)-Cl}$ = closest Cl···H(Me) interaction distance, $d_{\pi-\pi}$ = closest π(C)···π(C) interaction distance.

Compound	Crystal system	Space Group	$d_{H(Me)-Cl}$ [Å]	$d_{\pi-\pi}$ [Å]
1	Monoclinic	$P2_1/c$	2.777	-
2	Monoclinic	$P2_1$	2.860	-
3	Orthorhombic	*Pbca*	2.875	-
4	Monoclinic	$P2_1/c$	2.703	3.524
5	Triclinic	*P*-1	2.641	3.495
6	Orthorhombic	*Pbca*	2.771	4.487
7	Monoclinic	$P2_1/c$	2.593	-
8	Monoclinic	$P2_1/c$	2.893	3.359
9	Monoclinic	$P2_1/n$	2.806	-

The second structure type is seen in compound **9** (Figure 1B, Table 1), and describes a simple di-alkoxo bridged [$Cr^{III}(\mu\text{-}OR)_2Cr^{III}$] dimer. Complex **9** crystallises in the monoclinic space group $P2_1/n$, with the asymmetric unit containing half the molecule. The two deaH ligands are again singly deprotonated with the N atom and protonated O atom terminally bonded to a Cr(III) ion. The remaining coordination sites on the metal are occupied by two terminally bonded Cl ions, which H-bond to the protonated arm of the Me-deaH ligands (O-H···Cl, ~2.3 Å) . The result is a fully planar [$Cr_2(OR)_2$] bridging unit, in contrast to that seen in **1**-**8**. In the extended structure the closest inter-dimer interactions are between the terminally bonded Cl ions and the Me groups of the Me-deaH ligands, at a (C-H···Cl) distance of ~2.9 Å (Table 2, Figure S10).

Magnetic measurements

DC magnetic susceptibility measurements were carried out on powdered polycrystalline samples of compounds **1**-**9** in applied magnetic fields of 0.1 T, 0.5 T and 1.0 T, over the temperature range T = 2-300 K. Figures 2a and 2b show the experimental results as the $\chi_M T$ product versus T, where χ_M is the molar magnetic susceptibility.

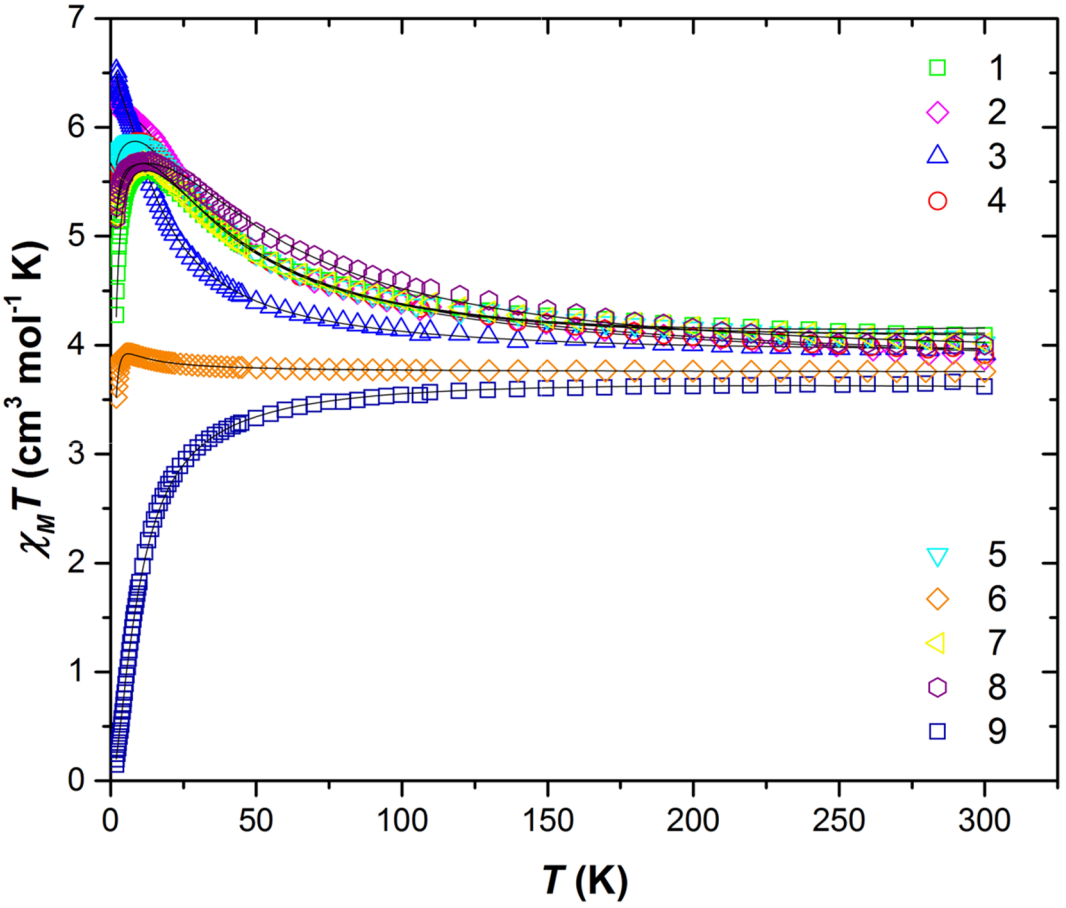

Figure 2a. Plot of the $\chi_M T$ product versus T for complexes **1**-**9** in an applied field of 0.1 T (**1**-**7**, **9**) and 0.5 T (**8**). The solid black lines are a fit of the experimental data. See text for details.

At T = 300 K the $\chi_M T$ values were found to be 4.08 (**1**), 3.87 (**2**), 3.92 (**3**), 3.92 (**4**), 4.02 (**5**), 3.73 (**6**), 4.02 (**7**), 4.00 (**8**) and 3.62 (**9**) cm^3 K mol^{-1}. The values for compounds **1** - **8** are slightly higher than that expected for two non-interacting s = 3/2 ions with g = 2.00 (3.75 cm^3 K mol^{-}

[1]), while that for compound **9** is somewhat lower. For compound **9** the value of $\chi_M T$ decreases gradually with decreasing temperature to reach a T = 2 K value of 0.15 cm^3 K mol^{-1}. This is indicative of relatively weak antiferromagnetic (AFM) exchange interactions between the Cr(III) ions, and the stabilisation of a diamagnetic ground state. In contrast, the experimental data for compounds **1** - **8** show a gradual increase in the value of $\chi_M T$ with decreasing temperature to reach T = 2 K values of 4.28 (peak at 5.61) (**1**), 6.35 (**2**), 6.52 (**3**), 5.18 (peak at 5.87) (**4**), 5.65 (peak at 5.88) (**5**), 3.52 (peak at 3.92) (**6**), 5.17 (peak at 5.69) (**7**) and 5.16 (peak at 5.69) (**8**) cm^3 K mol^{-1}, indicative of weak ferromagnetic (FM) exchange interactions, leading to S = 3 ground states.

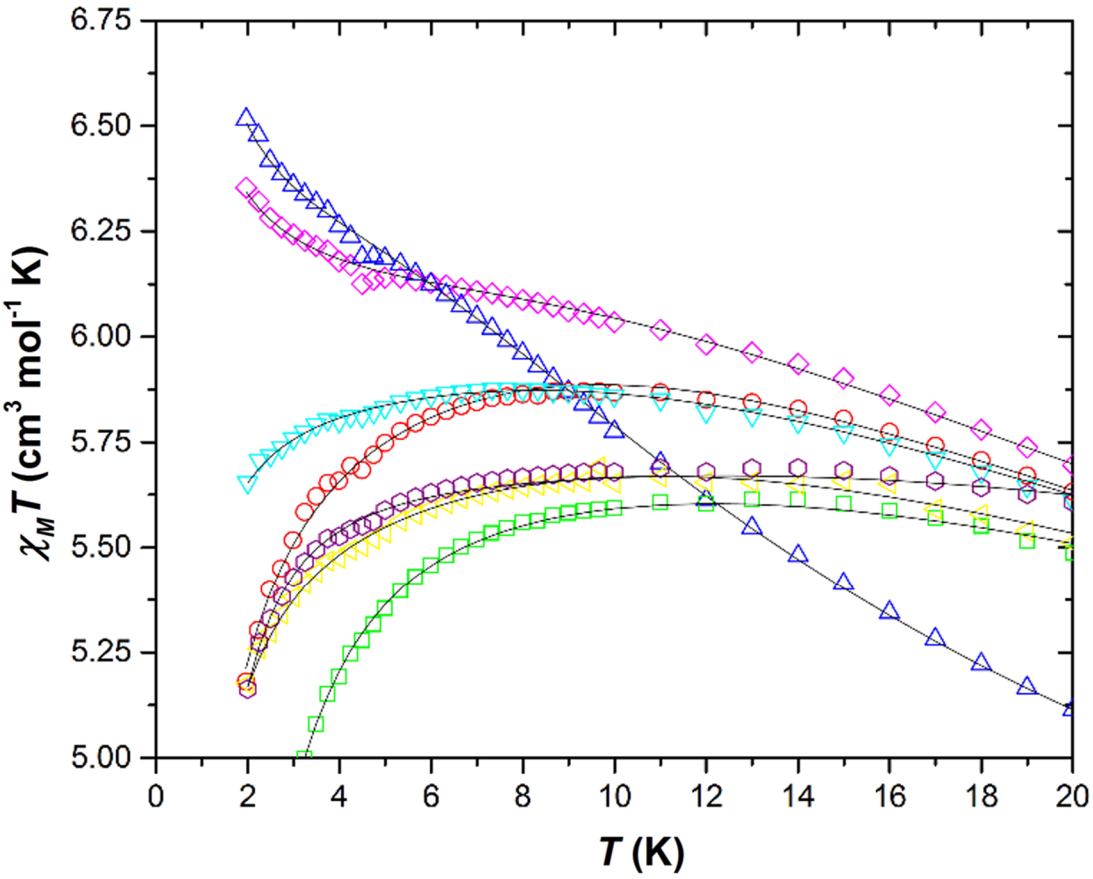

Figure 2b. Plot of the $\chi_M T$ product versus T for complexes **1**-**9** in an applied field of 0.1 T (**1**-**7**, **9**) and 0.5 T (**8**) at low temperature highlighting inter dimer interactions. The solid black lines are a fit of the experimental data. See text for details.

Variable-temperature variable-field (VTVB) magnetisation measurements, performed in the H = 0.5-7 T and T = 2-7 K field and temperature ranges, confirm this assessment (Figures S12-19). The $\chi_M T$ vs. T and M vs. H data were fitted simultaneously using isotropic spin-Hamiltonian (1), where the indices i and j refer to each of the Cr(III) ions, μ_B is the Bohr magneton, H is the applied magnetic field, g is the g-factor of the Cr(III) ions (fixed at g = 2.00), $\hat{S}$ is a spin operator and J is the isotropic exchange interaction. Using this model, best-fit parameters were J = +6.04 (**1**), +4.66 (**2**), +2.48 (**3**), +4.86 (**4**), +4.82 (**5**), +0.37 (**6**), +5.41 (**7**), +8.02 (**8**) and -1.65 (**9**) cm^{-1}. These values are listed in Table 3, and compared with values calculated using DFT (*vide infra*).

$$\hat{H} = \mu_B B \sum_i g_i \hat{S}_i - 2J \sum_{ij} \hat{S}_i \hat{S}_j \qquad (1)$$

As can be seen in the Figure 2b, there is some deviation in the very low temperature (T < 10 K) susceptibility data for compounds **1**-**8**. If one assumes that D_{Cr} is negligible, then these differences can be attributed to the inter-dimer interactions highlighted above. In the case of compounds **2** and **3** the low temperature $\chi_M T$ value reaches a maximum at ~11 K and then increases to higher values. In the case of compounds **1** and **4**-**8**, the opposite occurs and a low temperature decrease is observed. This would appear to indicate the presence of FM and AFM intermolecular interactions, respectively – a fit of the data in this region within a mean field approximation affording zJ = -2.742×10^{-3} (**1**), $+5.21\times10^{-3}$ (**2**), $+7.43\times10^{-3}$ (**3**), -1.06×10^{-2} (**4**), -9.88×10^{-2} (**5**), -5.24×10^{-2} (**6**), -2.44×10^{-1} (**7**) and -2.15×10^{-2} (**8**) K. In **2** and **3** the closest intermolecular contacts are mediated *via* Cl···H(Me) interactions. In **4**, **5**, **6** and **8** these same interactions are present, but occur in combination with numerous π···π interactions, the latter most commonly associated with AFM dipolar exchange. The intermolecular nature of the exchange in this temperature regime is confirmed *via* the field-dependence of the $\chi_M T$ inflection for all three compounds (Figure S20-27).

Table 3. Comparison of the experimentally determined J_{exp} values of compounds **1**-**9** with the theoretical J_{calc} values derived from DFT calculations. For **5**, where there are two slightly different dimers in the unit cell, the average value is reported.

Compound	J_{exp} [cm^{-1}]	J_{calc} [cm^{-1}]
1	+6.04	+6.3
2	+4.66	+6.0
3	+2.48	+3.5
4	+4.86	+5.9
5	+4.82	+6.2
6	+0.37	+1.8
7	+5.41	+5.8
8	+8.02	+6.9
9	-1.65	-0.4

Theoretical studies

To uncover the origin of the ferromagnetic exchange coupling in this class of dimers, DFT calculations have been carried out on complexes **1**-**9** with the resulting computed *J* values shown in Table 3. Calculations reproduce both the sign and relative magnitude of these values well in all cases. Calculations reveal the strongest FM coupling occurs in complexes **1** and **8**, and AFM coupling in **9**, consistent with the experimental *J* values. In order to analyse the trend in the observed exchange, one has to analyse all the structural parameters that could control the sign and magnitude of the exchange, namely the Cr-O bond lengths (r = alkoxide; τ = carboxylate), Cr-O-Cr bond angles (ϕ), Cr-O-Cr-O dihedral angles (ψ), and the out-of-plane shift between the bridging Cr_2O_2 plane and the OR vector of the bridging group (θ) (Figure 3, Table 1).

For compounds **1**-**8**, the variations in r, τ, ϕ and ψ are fairly small, with more variation apparent in θ. Use of the "GHP" model (which considers only r, ϕ and θ) previously employed to extract the magneto-structural correlation for the $[Cr(OH)]_2$ core,[1] leads to poor reproduction of both the sign and magnitude of *J*, due to the presence of the additional carboxylate bridge (Table S3). Indeed, the "GHP" model also failed to reproduce the data for a previously reported family of $[Cr(OR)]_2$ dimers where the hydroxide bridges were replaced with alkoxide bridges.[13]

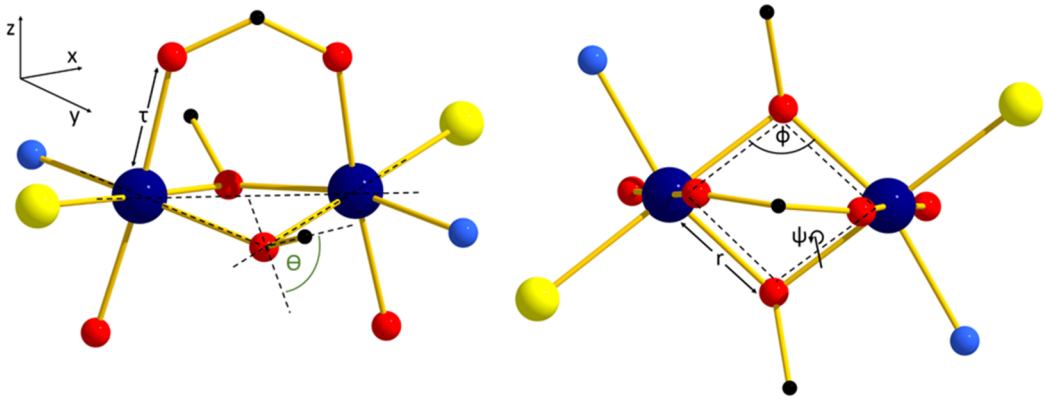

Figure 3. Diagrammatic representation of the structural parameters influencing the sign and magnitude of magnetic exchange in Cr^{III} dimers. The Cr-O_{carb} distances fall in the range $1.967 < \tau < 1.989$ Å.

The net exchange *J* has two contributions, J_{AFM} and J_{FM}, denoting the antiferromagnetic and ferromagnetic parts, respectively. Qualitative models based on Hey-Thibeault-Hoffmann (HTH) and Kahn methodologies are widely used to analyse the origin of magnetic exchange in dinuclear complexes.[44-48] While the HTH model analyses the differences in energies of symmetric and antisymmetric combinations of the SOMOs, the Kahn model takes into account the overlap between the SOMOs to arrive at a qualitative understanding. Herein, both models are employed in order to probe the origin of the unusual ferromagnetic coupling in **1**-**8**.

Initially a qualitative MO diagram for complex **1** was developed to analyse the energy gap between the symmetric (s) and antisymmetric (as) combinations (Figure 4). Due to the π-donor Cl ions, the degeneracy of the t_{2g} set of orbitals at the individual Cr(III) centres is lifted, with the d_{xz} and d_{yz} orbitals destabilised compared to the d_{xy} orbital. According to the HTH model, the square of the orbital energies between the symmetric and antisymmetic combinations of d_{xy}, d_{xz} and d_{yz} orbitals is directly proportional to the J_{AFM} component of the exchange. The $[(d_{xy})_s\text{-}(d_{xy})_{as}]$ gap is found to be the largest in all complexes studied (green arrows in Figure 4), followed by $[(d_{yz})_s\text{-}(d_{yz})_{as}]$ and $[(d_{xz})_s\text{-}(d_{xz})_{as}]$ in all complexes except **2**, **3** and **6**. For complex **9**, the $[(d_{yz})_s\text{-}(d_{yz})_{as}]$ and $[(d_{xz})_s\text{-}(d_{xz})_{as}]$ gaps are nearly the same, suggesting degeneracy. The addition of the bridging carboxylate means that the carboxylate MOs mix with the metal $(d_{yz})_s$ orbital leading to an increase in its energy and a decrease in the $[(d_{yz})_s\text{-}$

$(d_{yz})_{as}$] energy gap. This is known as an orbital counter-complementarity effect.[44, 49] This leads to a reduction of the J_{AFM} contribution, and in this instance, to the observation of ferromagnetic exchange. To confirm this, calculations were performed on complexes **1** and **4** where the carboxylate bridges were replaced with water ligands to give two compounds of formula $[Cr_2(Me\text{-}deaH)_2(H_2O)_2Cl_2]^{2+}$ (**1a**) and (**4a**) but with different structural parameters (Figure S28). These models yield *J* values of +3.2 cm^{-1} and -0.6 cm^{-1}, respectively. The removal of the carboxylate-bridge clearly enhances the J_{AFM} contribution. This is also reflected in the computed MO energies, where as we move from complex **1** (**4**) to **1a** (**4a**), the $[(d_{yz})_s\text{-}(d_{yz})_{as}]$ gap increases (*vide infra*; see Figures 5 and S29). This follows for all complexes **1**-**8** where there is a near linear relationship between the MO energies and the *J* values.

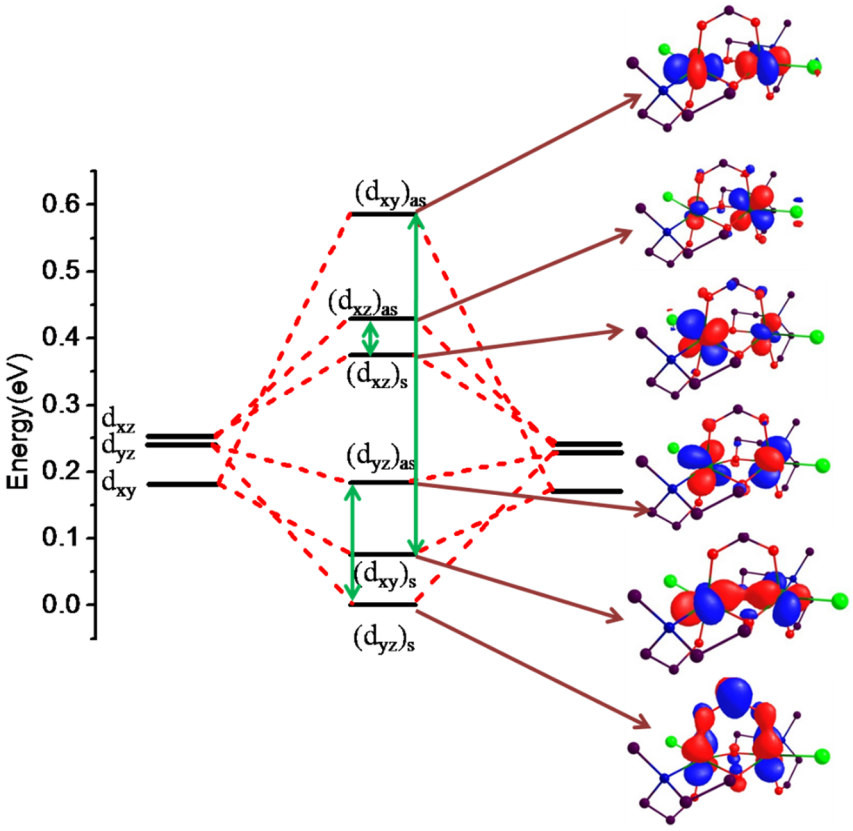

Figure 4. DFT derived qualitative MO diagram for **1**, with corresponding orbital diagrams. The green arrows highlight the difference between symmetric and anti-symmetric orbitals.

The magnitude of the computed *J* values for compounds **3** and **6** are found to be comparatively small. This is attributed to the larger energy difference between the symmetric and antisymmetric combinations caused by structural alteration; in particular the small θ values which increase the $[(d_{xy})_s\text{-}(d_{xy})_{as}]$ energy gap. For complex **9**, all three orbital energy gaps are relatively large, and the d_{xy} and d_{yz} orbitals are near degenerate due to the removal of the counter-complementarity effect.

We now turn to the analysis of the overlap between SOMOs employing Kahn's methodology. As the AFM part of the change is directly proportional to the overlap integral, this can provide a clue to the origin of the FM coupling observed. The computed overlap integrals for complexes **1**-**9** are given in Table S4. For complex **1** calculations reveal four dominant overlaps $d_{xy}|p_x|d_{xy}$, $d_{xy}|p_x|d_{yz}$, $d_{xy}|p_x|d_{xz}$ and $d_{yz}|p_y|d_{yz}$, with $d_{xy}|p_x|d_{xy}$ contributing to the AFM part of the exchange, J_{AFM}. Spin density plots reveal cubic spin density on the metal ions resulting from the t_{2g}^3 configuration of the Cr(III) centres (Figure 5), with intersection of the directional nodal planes of the three t_{2g} orbitals generating a hole in the face of the 'cube'. The spin density of the Cr(III) centres is greater than 3.0, implying a dominant spin polarisation mechanism is present. Spin densities on the nitrogen and chlorine atoms show only spin polarisation, with the oxygen atoms exhibiting a mixture of both spin polarisation and spin delocalisation. Strong π-donation of β-electrons from the Cl ions to the empty β-Cr(III) orbitals occurs, leading to residual positive spin densities on the Cl ions in all structures.

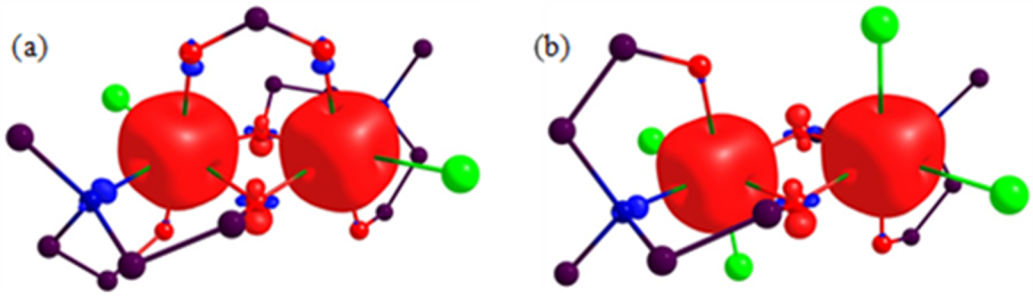

Figure 5. Spin density plots for complex **1** (a) and complex **9** (b).

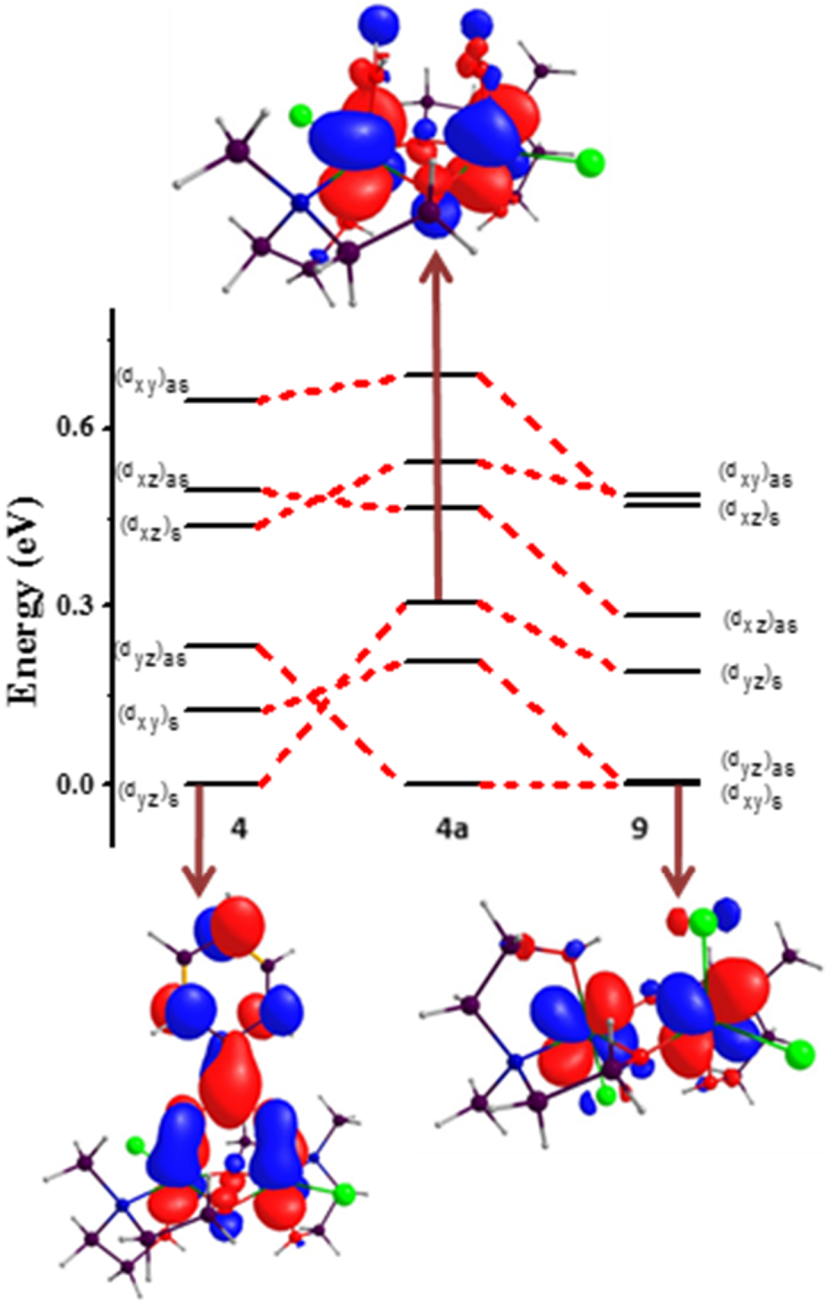

Figure 6. Qualitative MO diagram of **4**, **4a** and **9** with corresponding orbital diagrams. In **4a** the carboxylate-bridge has been replaced by water ligands.

One potentially pertinent structural difference between compounds **1**-**8** lies in the nature of the substituent present in the carboxylate group. We therefore investigated the effect of introducing halide atoms to the carboxylates in a model complex of formula $[Cr_2(Me\text{-}deaH)_2(O_2CX)Cl_2]Cl$ where X = F, Cl, Br and I (Figure S30). C-X bond distances were fixed based

on literature values. All four substitutions were found to yield *J* values in the range 6.2 - 6.4 cm^{-1}, revealing minimal variation in *J* upon changing the halide. The π^* orbital of the carboxylate, which is responsible for the counter-complementary effect, is unaltered by this substitution resulting in little change in orbital energies.

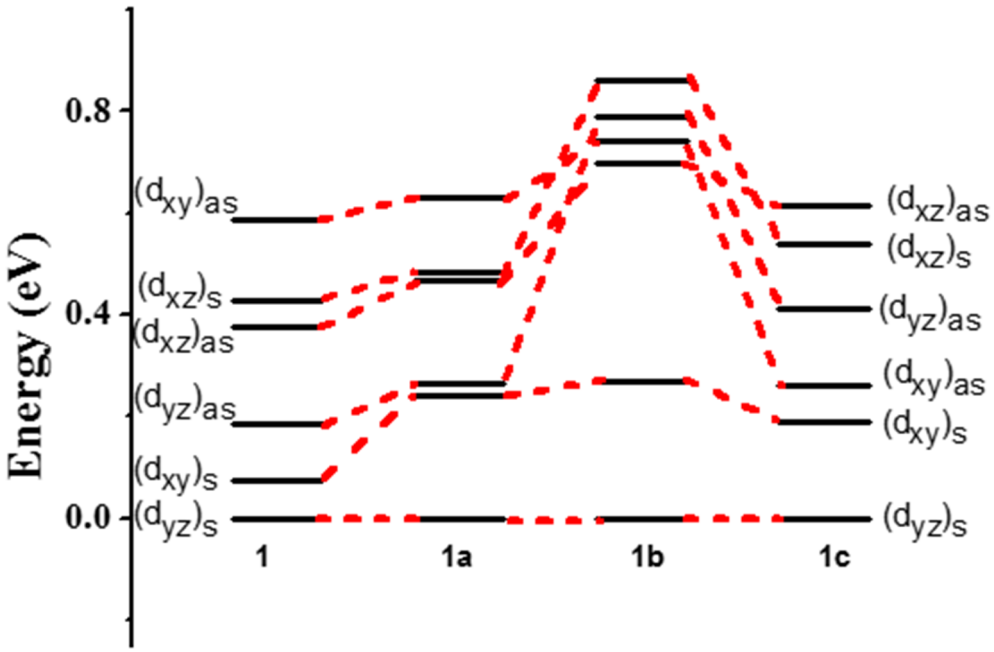

Figure 7. Evolution of d-orbital energies from complex **1** to model complexes **1a**-**c**. **1a** = carboxylate removed; **1b** = one bridging –OR group removed; **1c** = both bridging –OR groups removed.

To further probe the nature of the individual bridges on the magnitude and sign of *J*, detailed calculations on **1** were undertaken whereby each bridging ligand was removed individually (Figures 7 and S31). In model **1b** one of the bridging OR groups has been removed leading to super-exchange *via* the carboxylate and one OR group (Figure S31a). This was found to yield very strong antiferromagnetic exchange with *J* = -98.7 cm^{-1} due to the very large orbital energy gaps induced. In model **1c** both bridging OR groups were removed (Figure S31b); this results in a weaker antiferromagnetic exchange, *J* = -7.7 cm^{-1}. The magnitude of the computed *J* values correlate nicely to the symmetric and antisymmetric orbital energy gaps shown in Figure 7. A similar trend is also seen if we compare the orbital energies of complex **4**,

4a, and **9** (Figure 6). Removal of the carboxylate bridge in **4** leads to model **4a**, where the energy of the $(d_{yz})_{as}$ decreases dramatically, falling below $(d_{xy})_s$ and $(d_{yz})_s$, and becoming the lowest lying energy orbital. The orbital ordering computed for complex **9** is similar to **4a**, reiterating that the carboxylate plays a major role in switching the nature of magnetic coupling.

To fully comprehend the experimentally observed trend in the *J* values for this family, a magneto-structural correlation has been developed on a model complex of **1** (Figure S32) for four of the structural parameters described earlier: ϕ, ψ, θ and τ (there are no significant changes in r in **1**-**9**; Figure 8).

Cr-O-Cr bond angle (ϕ). The GHP model stipulates that a large Cr-O-Cr bond angle leads to ferromagnetic coupling.[1] Here, ϕ has been varied from 83 - 108° revealing an exponential decay, with small angles (83-98°) yielding strong AFM coupling and large angles (98-108°) yielding weak FM behaviour ($-149 < J < +0.59$ cm^{-1}; Figure 8a). As ϕ decreases, the number and strength of overlaps between the d_{xz} and d_{yz} orbitals increases, the $d_{yz}|p_z|d_{xz}$ overlap particularly so, leading to very strong antiferromagnetic coupling (Table S7). This is due to these orbitals lying along the Cr-O_{carb} bond direction. The d_{xy}-d_{xy} overlap was also found to increase with smaller angles as the Cr-Cr separation decreases. The MO energies of the symmetric and antisymmetric combinations are shown in Figure 9a for three representative points along the correlation. From this figure we see that: (i) the $[(d_{xy})_s$-$(d_{xy})_{as}]$ energy gap remains unaltered, suggesting that the d_{xy} orbitals are not involved significantly with respect to this parameter; (ii) the $[(d_{yz})_s$-$(d_{yz})_{as}]$ energy gap changes drastically with angle - with a very large gap at the lower angles, decreasing to near degenerate orbitals at 93° and increasing again at 108°; (iii) the $[(d_{xz})_s$-$(d_{xz})_{as}]$ gap is larger at lower angles and is the largest contributor to the net AFM exchange at an angle of 83°. This gap diminishes with increasing angle, suggesting smaller contribution to J_{AFM} at larger angles.

Cr-O-Cr-O dihedral angle (ψ). The dihedral angle was varied from 0 - 23°, resulting in a relatively small variation in *J* ($-6.5 < J < +7.0$ cm^{-1}; Figure 8b). As ψ decreases, the *J* value decreases in an exponential manner with smaller angles yielding weak AFM coupling, and larger angles yielding weak FM coupling. As the dihedral angle decreases, the d_{xz}-d_{yz}, d_{yz}-d_{xy}

and d_{xy}-d_{xz} overlaps are enhanced leading to AFM coupling in the more planar structure. From the MO energies in Figure 9b we see that: (i) as ψ decreases the $[(d_{xy})_s$-$(d_{xy})_{as}]$ energy gap increases substantially leading to a large J_{AFM} contribution when the $[Cr(OR)_2Cr]$ moiety is planar; (ii) both the $[(d_{yz})_s$-$(d_{yz})_{as}]$ and $[(d_{xz})_s$-$(d_{xz})_{as}]$ energy gaps decrease with increasing ψ, suggesting a smaller contribution to J_{AFM} at larger dihedral angles.

Out of plane displacement of alkyl groups (θ). θ was varied from 20 - 56°, affording a linear relationship whereby smaller angles yield weak FM coupling and large angles strong FM coupling ($+3.6 < J < +9.9$ cm^{-1}; Figure 8c). This agrees with the experimental results obtained for compounds **6** and **8**. As θ increases the overlap between the d_{xz} and d_{yz} orbitals decreases, enhancing the FM coupling. From the MO energies in Figure 9c it can be seen that as θ increases, the energy gap between $[(d_{xy})_s$-$(d_{xy})_{as}]$, $[(d_{yz})_s$-$(d_{yz})_{as}]$ and $[(d_{xy})_s$-$(d_{xy})_{as}]$ decreases, suggesting a smaller contribution to J_{AFM}, and as a consequence an increase in the observed *J* value.

Cr-O_{carb} distance (τ). As the carboxylate-bridge has been shown to be pivotal in determining the sign of *J*, an additional correlation has been developed for the Cr-O_{carb} distance, here being varied from 1.6 to 2. 2 Å. This correlation reveals that at very short Cr-O_{carb} distances the exchange is found to be AFM. As the distance increases the coupling becomes FM at 1.63 Å, before decreasing slowly in magnitude (Figure 8d). Overlap calculations (Figure 9d) reveal that at very short distances the overlap between d_{xy}-d_{xz}, d_{xz}-d_{xz} orbitals increases, leading to AFM exchange. More importantly, at very short Cr-O_{carb} distances, $(d_{yz})_s$ is strongly destabilised beyond the $(d_{yz})_{as}$ orbital, leading to a larger energy gap. As the distance decreases, this energy gap decreases leading to a reduction in the AFM coupling. The correlation shows an optimum Cr-O_{carb} distance of 1.8 Å, where $(d_{yz})_s$ and $(d_{yz})_{as}$ are degenerate leading to a maximum in the FM exchange. Further increasing the distance leads to $(d_{yz})_s$ becoming the ground state, enhancing the $[(d_{yz})_s$-$(d_{yz})_{as}]$ energy gap leading to a small decrease in the FM exchange.

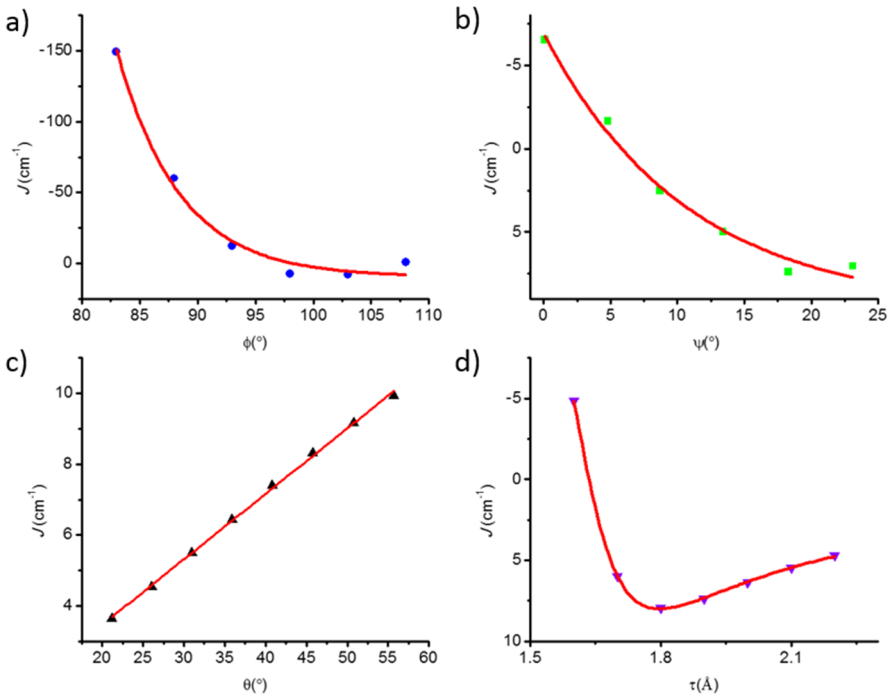

Figure 8. M-S correlations for the four parameters as computed by DFT. (a) Cr-O-Cr angle, ϕ (with fit giving J = 9.81 + 6.85 exp(-Φ/5.44) (R2 = 0.98341)). (b) Cr-O-Cr-O dihedral angle, ψ (with fit giving J = 9.65 - 16.56 exp(-Ψ/10.76) (R2 = 0.98771)). (c) Out of plane displacement of the alkyl group, θ (with fit giving J = -0.23 + 0.18θ (R2 = 0.99877)) (d) Cr-O_{carb} distance, τ.

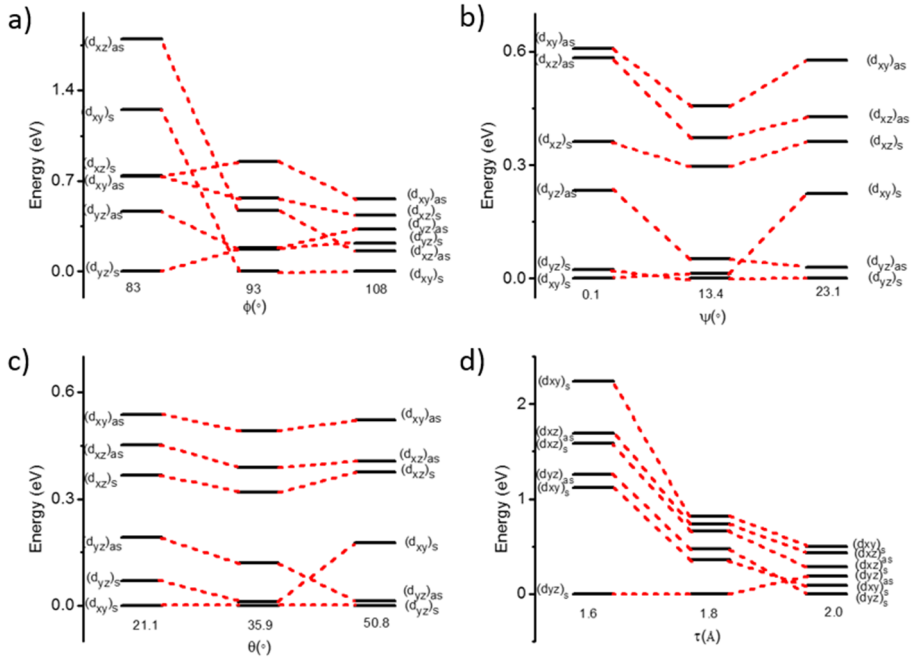

Figure 9. Illustration of the splitting of the MOs for the developed magneto-structural correlations for (a) Cr-O-Cr angle (ϕ), (b) Cr-O-Cr-O dihedral angle (ψ), (c) out of plane displacement of the alkyl group (θ), and (d) Cr-O_{carb} distance (τ).

3.4 Conclusions

A family of Cr(III) dimers of general formula $[Cr_2(R^1\text{-deaH})_2(O_2CR_2)Cl_2]Cl$ has been synthesised using a combination of carboxylate and diethanolamine ligands. The compound $[Cr_2(Me\text{-deaH})_2Cl_4]$ was synthesised in order to study the effect of removing/adding the carboxylate bridge. Direct current magnetic susceptibility and magnetisation measurements show ferromagnetic exchange interactions between the Cr(III) centres in the carboxylate bridged family, with coupling constants in the range $+0.37 < J < +8.02$ cm^{-1}. Removal of the carboxylate to produce the dialkoxide-bridged complex results in antiferromagnetic exchange between the Cr(III) ions. DFT calculations reveal the origin of the ferromagnetic exchange to be an orbital counter-complementarity effect. In particular, the addition of the bridging carboxylate results in the carboxylate MOs mixing with the Cr $(d_{yz})_s$ orbital leading to a decrease in the $[(d_{yz})_s\text{-}(d_{yz})_{as}]$ energy gap.

Complexes **1**-**8** represent only the fifth set of Cr(III) dimers to exhibit ferromagnetic exchange, and the first family of complexes containing multiple members to have a detailed magneto-structural correlation developed. They also provide a clear rationale for the ferromagnetic exchange seen in the polynuclear complexes $[Cr_4S(O_2CCH_3)_8(H_2O)_4](BF_4)_2$ and $[Cr_{10}(OR)_{20}(O_2CR')_{10}]$ which hitherto have had no explanation. It also suggests a simple blueprint for the construction of ferromagnetically coupled Cr(III) cages of any nuclearity – exploit the orbital counter-complementarity effect by combining heteroleptic ligand sets, here alkoxides and carboxylates. The $[M^{III}(OR)_2(OCO)]$ bridging unit employed here is an extremely common building block in Mn(III) and Fe(III) chemistry, and we therefore see no reason why similar cages of Cr(III) cannot be made, potentially opening the door to new families of complexes containing multiple Cr(III) ions with controllable exchange interactions.

3.5 Supplementary Information

Table S1. Crystallographic information for compounds **1**-**4**.

Compound	**1**	**2**	**3**	**4**
Formula	$C_{11}H_{25}Cl_3Cr_2N_2O_6$	$C_{12}H_{27}Cl_3Cr_2N_2O_6$	$C_{15}H_{33}Cl_3Cr_2N_2O_6$	$C_{17}H_{29}Cl_3Cr_2N_2O_6$
$D_{calc.}$/ g cm^{-3}	1.721	1.703	1.594	1.618
μ/mm^{-1}	1.596	1.538	1.335	1.311
FW/g mol^{-1}	491.68	505.70	547.78	567.77
Colour	dark green	dark green	pale green	dark purple
Shape	block	block	plate	block
Size/mm^3	0.41×0.14×0.07	0.39×0.33×0.25	0.53×0.37×0.03	0.47×0.28×0.19
T/K	120.0	120.0	120.0	120.0
Crystal System	monoclinic	monoclinic	orthorhombic	monoclinic
Flack/Hooft Parameters	-	0.005(10)/-0.003(9)	-	-
Space Group	$P2_1/c$	$P2_1$	Pbca	$P2_1/c$
a/Å	7.1130(3)	7.10996(16)	14.0747(4)	16.1908(3)
b/Å	10.2464(5)	10.2978(2)	10.3531(2)	10.41623(19)
c/Å	26.0466(13)	13.8317(3)	31.3324(10)	14.1087(3)
α/°	90	90	90	90
β/°	91.273(4)	103.201(2)	90	101.560(2)
γ/°	90	90	90	90
V/Å^3	1897.88(15)	985.95(4)	4565.6(2)	2331.11(8)
Z (Z')	4 (1)	2 (1)	8 (1)	4 (1)
Wavelength/Å	0.71073	0.71073	0.71073	0.71073
Radiation type	MoK_α	MoK_α	MoK_α	MoK_α
Θ_{min}/° - Θ_{max}/°	3.076 - 28.753	2.943 – 31.252	2.767 - 31.223	2.970 – 31.306
Measured Refl.	111506	31889	48743	48698
Independent Refl.	5954	5981	6888	7156
Reflections Used	5411	5674	5507	6488
R_{int}	0.0863	0.0503	0.0806	0.0417
Parameters	226	237	264	281
Restraints	2	1	2	0
Largest Peak	0.552	0.347	0.520	0.516
Deepest Hole	-0.587	-0.487	-0.559	-0.469
GooF	1.117	1.057	1.110	1.040
wR_2 (all data) (wR_2)	0.0984 (0.0970)	0.0582 (0.0564)	0.0990 (0.0915)	0.0696 (0.0671)
R_1 (all data) (R_1)	0.0483 (0.0419)	0.0302 (0.0274)	0.0720 (0.0506)	0.0334 (0.0286)
CCDC Number	1579642	1579643	1579644	1579645

Table S1 cont. Crystallographic information for compounds **5**-**8**.

Compound	**5**	**6**	**7**	**8**
Formula	$C_{17}H_{27}Cl_5Cr_2N_2O_6$	$C_{22}H_{39}Cl_3Cr_2N_2O_6$	$C_{13}H_{29}Cl_3Cr_2N_2O_6$	$C_{42}H_{76}Cl_6Cr_4N_4O_{13}$
$D_{calc.}$/ g cm^{-3}	1.660	1.494	1.646	1.525
μ/mm^{-1}	12.174	1.087	1.449	1.119
FW/g mol^{-1}	636.65	637.90	519.73	1265.76
Colour	dark purple	pale green	dark green	dark green
Shape	plate	plate	block	block
Size/mm^3	0.32×0.07×0.03	0.45×0.32×0.02	0.51×0.24×0.23	0.35×0.09×0.05
T/K	120.0	120.0	120.0	120.0
Crystal System	triclinic	orthorhombic	monoclinic	monoclinic
Space Group	P-1	Pbca	$P2_1/c$	$P2_1/c$
a/Å	10.2393(2)	14.0888(6)	11.5711(3)	7.1699(2)
b/Å	14.2193(3)	10.2661(4)	13.2720(3)	11.0066(3)
c/Å	18.1746(4)	39.2028(19)	13.6565(3)	34.9817(7)
α/°	76.834(2)	90	90	90
β/°	81.3824(19)	90	90.948(2)	93.103(2)
γ/°	89.2989(19)	90	90	90
V/Å^3	2546.84(10)	5670.2(4)	2096.96(9)	2756.58(12)
Z (Z')	4 (2)	8 (1)	4 (1)	2 (0.5)
Wavelength/Å	1.54184	0.71073	0.71073	0.71073
Radiation type	CuK_α	MoK_α	MoK_α	MoK_α
Θ_{min}/° - Θ_{max}/°	3.193 – 76.399	2.892 – 25.350	3.413 – 29.786	2.845 - 29.773
Measured Refl.	51940	41273	36587	48300
Independent Refl.	10528	5174	5540	7202
Reflections Used	9114	3810	4952	5556
R_{int}	0.0909	0.1282	0.0434	0.0586
Parameters	593	329	264	365
Restraints	4	2	43	9
Largest Peak	1.591	0.490	0.813	0.449
Deepest Hole	-1.041	-0.388	-0.495	-0.496
GooF	1.040	0.933	1.079	1.034
wR_2 (all data) (wR_2)	0.1546 (0.1471)	0.1536 (0.1334)	0.0955 (0.0924)	0.0860 (0.0813)
R_1 (all data) (R_1)	0.0632 (0.0560)	0.0823 (0.0522)	0.0475 (0.0415)	0.0629 (0.0407)
CCDC Number	1579647	1579648	1579649	1579650

Table S1 cont. Crystallographic information for compound **9**.

Compound	**9**
Formula	$C_{10}H_{24}Cl_4Cr_2N_2O_4$
$D_{calc.}$/ g cm^{-3}	1.813
μ/mm^{-1}	1.851
FW/g mol^{-1}	482.11
Colour	dark purple
Shape	block
Size/mm^3	0.34×0.12×0.07
T/K	120.0
Crystal System	monoclinic
Space Group	$P2_1/n$
a/Å	6.8880(2)
b/Å	9.9275(3)
c/Å	12.9510(3)
α/°	90
β/°	94.457(3)
γ/°	90
V/Å^3	882.91(4)
Z (Z')	2 (0.5)
Wavelength/Å	0.71073
Radiation type	MoK_α
Θ_{min}/° - Θ_{max}/°	3.155 – 29.807
Measured Refl.	15425
Independent Refl.	2315
Reflections Used	2149
R_{int}	0.0378
Parameters	148
Restraints	0
Largest Peak	0.378
Deepest Hole	-0.395
GooF	1.083
wR_2 (all data) (wR_2)	0.0576 (0.0560)
R_1 (all data) (R_1)	0.0284 (0.0250)
CCDC Number	1579651

For Figures S1-S33 and Tables S2-S7 please refer to the “Chapter 3 SI” file on the memory stick supplied with the thesis.

3.6 References

1. J. Glerup, D. J. Hodgson and E. Pedersen, *Acta Chem. Scand. A.*, 1983, **37**, 161-164.
2. T. F. Tekut, C. J. O'Connor and R. A. Holwerda, *Inorg. Chem.*, 1993, **32**, 324-328.
3. H. S. Cheng and L. S. Wang, *Phys. Rev. Lett.*, 1996, **77**, 51-54.
4. E. D. Estes, R. P. Scaringe, W. E. Hatfield and D. J. Hodgson, *Inorg. Chem.*, 1976, **15**, 1179-1182.
5. F. S. Delgado, J. Sanchiz, T. Lopez, F. Lloret, M. Julve and C. Ruiz-Perez, *Crystengcomm*, 2010, **12**, 2711-2721.
6. C. Reber, H. U. Güdel, L. Spiccia and W. Marty, *Inorg. Chem.*, 1987, **26**, 3186-3191.
7. R. Sanzenbacher, A. Bottcher, H. Elias, M. Huber, W. Haase, J. Glerup, T. B. Jensen, M. Neuburger, M. Zehnder, J. Springborg and C. E. Olsen, *Inorg. Chem.*, 1996, **35**, 7493-7499.
8. T. J. Morsing, H. Weihe and J. Bendix, *Eur. J. Inorg. Chem.*, 2014, **2014**, 5990-5996.
9. A. Bino, D. C. Johnston, D. P. Goshorn, T. R. Halbert and E. I. Stiefel, *Science*, 1988, **241**, 1479-1481.
10. E. J. L. McInnes, C. Anson, A. K. Powell, A. J. Thomson, S. Poussereau and R. Sessoli, *Chem. Commun.*, 2001, 89-90.
11. D. M. Low, G. Rajaraman, M. Helliwell, G. Timco, J. van Slageren, R. Sessoli, S. T. Ochsenbein, R. Bircher, C. Dobe, O. Waldmann, H. U. Güdel, M. A. Adams, E. Ruiz, S. Alvarez and E. J. L. McInnes, *Chem. Eur. J.*, 2006, **12**, 1385-1396.
12. Y. Nishida and S. Kida, *J. Chem. Soc., Dalton Trans.*, 1986, 2633-2640.
13. H. W. L. Fraser, G. S. Nichol, G. Velmurugan, G. Rajaraman and E. K. Brechin, *Dalton Trans.*, 2017, **46**, 7159-7168.
14. D. Foguet-Albiol, K. A. Abboud and G. Christou, *Chem. Commun.*, 2005, 4282-4284.
15. D. Foguet-Albiol, T. A. O'Brien, W. Wernsdorfer, B. Moulton, M. J. Zaworotko, K. A. Abboud and G. Christou, *Angew. Chem. Int. Ed.*, 2005, **44**, 897-901.
16. R. W. Saalfrank, R. Prakash, H. Maid, F. Hampel, F. W. Heinemann, A. X. Trautwein and L. H. Böttger, *Chem. Eur. J.*, 2006, **12**, 2428-2433.
17. G. Abbas, Y. H. Lan, G. E. Kostakis, W. Wernsdorfer, C. E. Anson and A. K. Powell, *Inorg. Chem.*, 2010, **49**, 8067-8072.
18. A. M. Ako, V. Mereacre, R. Clérac, I. J. Hewitt, Y. H. Lan, C. E. Anson and A. K. Powell, *Dalton Trans.*, 2007, 5245-5247.
19. O. V. Nesterova, M. V. Kirillova, M. da Silva, R. Boca and A. J. L. Pombeiro, *Crystengcomm*, 2014, **16**, 775-783.
20. J. W. Sharples and D. Collison, *Coord. Chem. Rev.*, 2014, **260**, 1-20.
21. A. J. Tasiopoulos and S. P. Perlepes, *Dalton Trans.*, 2008, 5537-5555.
22. V. V. Semenaka, O. V. Nesterova, V. N. Kokozay, R. I. Zybatyuk, O. V. Shishkin, R. Boca, C. J. Gomez-Garcia, J. M. Clemente-Juan and J. Jezierska, *Polyhedron*, 2010, **29**, 1326-1336.
23. S. K. Langley, D. P. Wielechowski, N. F. Chilton, B. Moubaraki and K. S. Murray, *Inorg. Chem.*, 2015, **54**, 10497-10503.
24. S. K. Langley, C. M. Forsyth, B. Moubaraki and K. S. Murray, *Dalton Trans.*, 2015, **44**, 912-915.
25. G. M. Sheldrick, *Acta Crystallogr. Sect. C: Cryst. Struct. Commun.*, 2015, **71**, 3-8.
26. O. V. Dolomanov, L. J. Bourhis, R. J. Gildea, J. A. K. Howard and H. Puschmann, *J. Appl. Crystallogr.*, 2009, **42**, 339-341.

27. G. A. Bain and J. F. Berry, *J. Chem. Educ.*, 2008, **85**, 532.
28. A. D. Becke, *J. Chem. Phys.*, 1993, **98**, 5648-5652.
29. A. Schafer, H. Horn and R. Ahlrichs, *J. Chem. Phys.*, 1992, **97**, 2571-2577.
30. A. Schafer, C. Huber and R. Ahlrichs, *J. Chem. Phys.*, 1994, **100**, 5829-5835.
31. Gaussian 09, Revision A.02, M. J. Frisch, G. W. Trucks, H. B. Schlegel, G. E. Scuseria, M. A. Robb, J. R. Cheeseman, G. Scalmani, V. Barone, G. A. Petersson, H. Nakatsuji, X. Li, M. Caricato, A. Marenich, J. Bloino, B. G. Janesko, R. Gomperts, B. Mennucci, H. P. Hratchian, J. V. Ortiz, A. F. Izmaylov, J. L. Sonnenberg, D. Williams-Young, F. Ding, F. Lipparini, F. Egidi, J. Goings, B. Peng, A. Petrone, T. Henderson, D. Ranasinghe, V. G. Zakrzewski, J. Gao, N. Rega, G. Zheng, W. Liang, M. Hada, M. Ehara, K. Toyota, R. Fukuda, J. Hasegawa, M. Ishida, T. Nakajima, Y. Honda, O. Kitao, H. Nakai, T. Vreven, K. Throssell, J. A. Montgomery, Jr., J. E. Peralta, F. Ogliaro, M. Bearpark, J. J. Heyd, E. Brothers, K. N. Kudin, V. N. Staroverov, T. Keith, R. Kobayashi, J. Normand, K. Raghavachari, A. Rendell, J. C. Burant, S. S. Iyengar, J. Tomasi, M. Cossi, J. M. Millam, M. Klene, C. Adamo, R. Cammi, J. W. Ochterski, R. L. Martin, K. Morokuma, O. Farkas, J. B. Foresman and D. J. Fox, Gaussian Inc., Wallingford CT, 2016.
32. F. K. Larsen, E. J. L. McInnes, H. El Mkami, J. Overgaard, S. Piligkos, G. Rajaraman, E. Rentschler, A. A. Smith, G. M. Smith, V. Boote, M. Jennings, G. A. Timco and R. E. P. Winpenny, *Angew. Chem. Int. Ed.*, 2003, **42**, 101-105.
33. K. S. Pedersen, G. Lorusso, J. J. Morales, T. Weyhermuller, S. Piligkos, S. K. Singh, D. Larsen, M. Schau-Magnussen, G. Rajaraman, M. Evangelisti and J. Bendix, *Angew. Chem. Int. Ed.*, 2014, **53**, 2394-2397.
34. M. Atanasov, C. Busche, P. Comba, F. El Hallak, B. Martin, G. Rajaraman, J. van Slageren and H. Wadepohl, *Inorg. Chem.*, 2008, **47**, 8112-8125.
35. C. E. Talbot-Eeckelaers, G. Rajaraman, J. Cano, G. Aromí, E. Ruiz and E. K. Brechin, *Eur. J. Inorg. Chem.*, 2006, 3382-3392.
36. S. Piligkos, H. Weihe, E. Bill, F. Neese, H. El Mkami, G. M. Smith, D. Collison, G. Rajaraman, G. A. Timco, R. E. P. Winpenny and E. J. L. McInnes, *Chem. Eur. J.*, 2009, **15**, 3152-3167.
37. P. Christian, G. Rajaraman, A. Harrison, J. J. W. McDouall, J. T. Raftery and R. E. P. Winpenny, *Dalton Trans.*, 2004, 1511-1512.
38. S. K. Singh, K. S. Pedersen, M. Sigrist, C. A. Thuesen, M. Schau-Magnussen, H. Mutka, S. Piligkos, H. Weihe, G. Rajaraman and J. Bendix, *Chem. Commun.*, 2013, **49**, 5583-5585.
39. T. Gupta and G. Rajaraman, *Chem. Commun.*, 2016, **52**, 8972-9008.
40. L. Noodleman, *J. Chem. Phys.*, 1981, **74**, 5737-5743.
41. P. J. Hay, J. C. Thibeault and R. Hoffmann, *J. Am. Chem. Soc.*, 1975, **97**, 4884-4899.
42. E. Ruiz, J. Cano, S. Alvarez and P. Alemany, *J. Comput. Chem.*, 1999, **20**, 1391-1400.
43. E. Ruiz, Alvarez, S. , Rodríguez-Fortea, A. , Alemany, P. , Pouillon, Y. and Massobrio, C, in *Magnetism: Molecules to Materials II*, eds. J. S. Miller and M. Drillon, Wiley-VCH, Weinheim, 2001, p. 227.
44. O. Kahn, *Molecular Magnetism*, Wiley, 1993.
45. C. A. Daul, I. Ciofini and A. Bencini, in *Reviews of Modern Quantum Chemistry*, World Scientific, 2002, vol. II, pp. 1247-1294.
46. D. Venegas-Yazigi, D. Aravena, E. Spodine, E. Ruiz and S. Alvarez, *Coord. Chem. Rev.*, 2010, **254**, 2086-2095.
47. O. Kahn and O. Guillou, *Research Frontiers in Magnetochemistry*, World Scientific, Singapore, 1993.
48. O. Kahn, *Angew. Chem.-Int. Edit. Engl.*, 1985, **24**, 834-850.

49. L. L. Wang, Y. M. Sun, Z. N. Qi and C. B. Liu, *J. Phys. Chem. A*, 2008, **112**, 8418-8422.

CHAPTER 4:

ORDER IN DISORDER: SOLUTION AND SOLID–STATE STUDIES OF $[M^{III}_2\ M^{II}_5]$ WHEELS (M^{III} = Cr, Al; M^{II} = Ni, Zn)

4.1 Introduction

Heterometallic complexes containing transition metal ions have long been investigated across a breadth of chemical disciplines ranging from the synthesis of model complexes representing the active sites of proteins,[1] molecular catalysts for water oxidation,[2] the construction of supramolecular cages, capsules[3] and porous materials,[4] and the elucidation of magneto-structural relationships in molecule-based magnets.[5] In the latter, heterometallic species have been employed to deliberately control exchange interactions in cyanide-bridged Prussian blue analogues,[6] obtain enhanced magnetocaloric effects in cryogenic coolers,[7] enforce spin frustration effects in high symmetry cages,[8] understand the origins of the slow relaxation dynamics in single-molecule magnets (SMMs)[9] and single-chain magnet (SCMs),[10] and for the development of molecules that may act as quantum bits (qubits).[11] A prominent, thoroughly investigated example of the latter is the large family of compounds based on [$Cr^{III}_7Ni^{II}$] rings.[12] With this in mind, noting that recent reports of heterometallic 3d-3d cages are scarce in comparison to the plethora of 3d-4f species,[13, 14] we have initiated a project to examine the synthesis, structures and magnetic properties of heterometallic, mixed-valent species, beginning with the solution- and solid-state characterisation of [$M^{III}_2M^{II}_5$] 'wheels' where M^{III} = Cr, Al and M^{II} = Ni, Zn.

A search of the Cambridge structural database (CSD) reveals that for polymetallic molecules containing both Cr^{III} and Ni^{II} ions with a nuclearity of four or more, there are only ten unique structure types, and all but three belong to the [$Cr^{III}_7Ni^{II}$] family.[15] Examples include [$Cr_{14}Ni_2$] and [$Cr_{28}Ni_4$] 'linked rings',[16] wheels of varying size and metal ratios, such as [Cr_9Ni], [Cr_8Ni_2], [Cr_8Ni], [Cr_7Ni_2] and [Cr_6Ni_2],[17, 18] an '*S*-shaped' [$Cr_{12}Ni_3$] chain,[19] an unusual linear [Cr_3Ni_2] complex,[20] and perhaps most pertinent to this work, a [$CrNi_7$] wheel where the central M^{III} ion is surrounded by a ring of M^{II} ions.[21]

The seven-membered centred wheel (or Anderson-type structure) is a well-known topology for homometallic 3d transition metal cluster compounds. These include numerous examples of Ni_7,[22] Co_7,[23] and mixed-valence Mn_7 and Fe_7 species,[24, 25] with Cu_7 and Zn_7 examples known, but less common.[26, 27] Heterometallic versions of the structure with 3d transition metal ions are much less common, the only examples being [Mn_3Cr_4],[28] [Fe_3Mn_4],[29] [V_6M^{II}] (where M^{II} = Mn, Fe, Co or Ni),[30, 31] the aforementioned [CrM^{II}_6] (where M^{II} = Ni or Co).[21] with one example combining 3d-4d metal ions, [Mo_6Cr].[32] Herein we present the synthesis and characterisation

of a novel family of heterometallic Anderson-type wheels of general formula $[M^{III}_2M^{II}_5(hmp)_{12}](ClO_4)_4$ where M^{III} = Cr or Al and M^{II} = Ni or Zn.

4.2 Experimental

Materials and physical measurements

All chemicals were procured from commercial suppliers and used as received (reagent grade). Elemental analyses for C, H, N and metal ions on all compounds were performed by Medac Ltd. **Caution:** Perchlorate salts of metal complexes with organic ligands are potentially explosive.

Synthesis of $[Cr_2Ni_5(hmp)_{12}](ClO_4)_4\cdot 7MeOH$ (1)

$Ni(ClO_4)_2\cdot 6H_2O$ (0.366 g, 1 mmol), $CrCl_3\cdot 6H_2O$ (0.133 g, 0.5 mmol) and NaOMe (0.162 g, 3 mmol) were dissolved in MeOH (24 mL) to give a cloudy blue solution. Upon full dissolution, hmpH (0.285 mL, 3 mmol) was added dropwise affording a dark blue solution. The reaction was left overnight with continuous stirring. 12 ml samples of the resulting solution were then heated in Teflon-lined autoclaves at 100°C for 12 hours. After slowly cooling to room temperature the reaction vessels were allowed to sit undisturbed for 24 hours, yielding blue, block-shaped crystals suitable for X-ray diffraction. Yield 0.020 g (4.4% by Ni weight). Anal. Calcd (%) for $C_{72}H_{72}Cl_4Cr_2N_{12}Ni_5O_{28}$: C 41.32, H 3.47, Cr 4.97, Ni 14.02, N 8.03; found: C 40.68, H 3.45, Cr 5.12, Ni 14.15, N 7.52.

Synthesis of $[Cr_2Zn_5(hmp)_{12}](ClO_4)_4\cdot 9MeOH$ (2)

$Zn(ClO_4)_2\cdot 6H_2O$ (0.372 g, 1 mmol), $Cr(NO_3)_3\cdot 9H_2O$ (0.200 g, 0.5 mmol) and NaOMe (0.162 g, 3 mmol) were dissolved in MeOH (24 mL) to give a cloudy pink solution. Upon full dissolution, hmpH (0.285 mL, 3 mmol) was added dropwise and the reaction was left overnight with continuous stirring. 12 ml samples of the resulting cloudy purple solution were heated in Teflon-lined autoclaves at 100°C for 12 hours. After slowly cooling to room temperature the reaction vessels were allowed to sit undisturbed for 24 hours yielding light purple, plate-shaped crystals suitable for X-ray diffraction. Yield 0.143 g (29.7% by Zn weight). Anal. Calcd (%) for $C_{72}H_{72}Cl_4Cr_2N_{12}Zn_5O_{28}$: C 40.67, H 3.41, Cr 4.89, Zn 15.38, N 7.90; found: C 40.96, H 3.30, Cr 5.01, Zn 15.03, N 7.96.

Synthesis of $[Al_2Ni_5(hmp)_{12}](ClO_4)_4 \cdot 9MeOH$ (3)

$Ni(ClO_4)_2 \cdot 6H_2O$ (0.366 g, 1 mmol), $Al(NO_3)_3 \cdot 9H_2O$ (0.188 g, 0.5 mmol) and NaOMe (0.162 g, 3 mmol) were dissolved in MeOH (24 mL) to give a light green solution. Upon full dissolution, hmpH (0.285 mL, 3 mmol) was added dropwise giving a colour change to blue. The reaction was left overnight with continuous stirring. 12 ml samples of the resulting blue solution were heated in Teflon-lined autoclaves at 100°C for 12 hours. After slowly cooling to room temperature the reaction vessels were allowed to sit undisturbed for 24 hours yielding turquoise, plate-shaped crystals suitable for X-ray diffraction. Yield 0.052 g (11.2% by Ni weight). Anal. Calcd (%) for $C_{72}H_{72}Cl_4Al_2N_{12}Ni_5O_{28}$: C 42.34, H 3.55, Al 2.64, Ni 14.37, N 8.23; found: C 41.93, H 3.41, Al 2.55, Ni 15.06, N 8.37.

Synthesis of $[Al_2Zn_5(hmp)_{12}](ClO_4)_4 \cdot 8MeOH$ (4)

$Zn(ClO_4)_2 \cdot 6H_2O$ (0.372 g, 1 mmol), $Al(NO_3)_3 \cdot 9H_2O$ (0.188 g, 0.5 mmol) and NaOMe (0.162 g, 3 mmol) were dissolved in MeOH (24 mL) to give a cloudy white solution. Upon full dissolution, hmpH (0.285 mL, 3 mmol) was added dropwise and the reaction was left overnight with continuous stirring. 12 ml samples of the resulting cloudy white solution were heated in Teflon-lined autoclaves at 100°C for 12 hours. After slowly cooling to room temperature the reaction vessels were allowed to sit undisturbed for 24 hours yielding colourless, plate-shaped crystals suitable for X-ray diffraction. Yield 0.075 g (16.1% by Zn weight). Anal. Calcd (%) for $C_{72}H_{72}Cl_4Al_2N_{12}Zn_5O_{28}$: C 41.65, H 3.50, Al 2.60, Zn 15.75, N 8.10; found: C 40.99, H 3.45, Al 2.58, Zn 15.60, N 8.22.

X-ray crystallography

Diffraction data for samples **1**-**4** were collected using Bruker SMART APEXII (**1**) or Rigaku Oxford Diffraction SuperNova (**2**-**4**) diffractometers with MoK_α (**1**, **2** & **4**) and CuK_α (**3**) radiation, and are given in Table 3 in the Supplementary Information. An Oxford Cryosystems Cryostream 700+ low temperature device was used to maintain a crystal temperature of 120.0 K for all experiments. The structures were solved using ShelXT and refined with version ShelXL interfaced through Olex2.[33, 34] All non-hydrogen atoms were refined using anisotropic displacement parameters. H atoms were placed in calculated positions geometrically and refined using the riding model. Unit cell parameters for **2** were also obtained at T = 3.4 K – see the SI for details. CCDC: 1819131-1819134.

Magnetic data

Dc susceptibility and magnetisation data were measured on powdered, polycrystalline samples of **1**-**3** in the T = 2-300 K and B = 0-7 T temperature and field ranges on a Quantum Design MPMS XL SQUID magnetometer equipped with a 7 T dc magnet. Diamagnetic corrections were applied to the data using Pascal's constants.[35]

Solution NMR spectroscopy

NMR spectra were recorded in DMSO-d6 solutions on an 800 MHz Bruker AVANCE III spectrometer equipped with a 5 mm triple-resonance TCI cryoprobe. The 300 K 2D ^{1}H, ^{13}C HSQC spectrum of **4** was acquired using Bruker pulse program hsqcedetgpsisp2.3 allowing multiplicity-editing. The following parameters were used: t_1 and t_2 acquisition times of 19.5 and 116 ms, spectral widths of 130 and 11 in F_1 and F_2 ppm, respectively, 50% non-uniform sampling and relaxation times of 2 s, yielding the overall acquisition of 1 hour and 15 min. The 2D DOSY spectrum of **4** was acquired using the Bruker pulse program ledbpgp2s. 32.[36] Linear incrementation of pulsed field gradients (PFGs) from 2 to 100% of the maximum strength (53 Gauss/cm) was used together with a diffusion time of 100 ms and eddy current recovery time of 5 ms. The length of the diffusion coding PFGs was 1.5 ms; all other gradients were 600 μs long. The PFGs were Chirp pulse shaped. The data were fitted using a single exponential function.

Solid-state NMR spectroscopy

Single pulse ^{27}Al MAS NMR spectra was recorded on an Agilent 600 MHz NMR spectrometer (14.1 T) using 1.6 mm (30-28 kHz spinning speed) and 3.2 mm (15 kHz spinning speed) MAS NMR probes for compounds **3** and **4** respectively. The spectra are referenced to a 1 M $AlCl_3$ aqueous solution and were analysed using the VnmrJ software.

Mass spectrometry

Mass spectrometry was performed on compound **4** on a Synapt G2 (Waters., Manchester, UK) mass spectrometer, using a direct infusion electrospray ionization source (ESI), controlled using Masslynx v4.1 software. Due to the relatively low solubility of **4**, it was dissolved in acetonitrile with 10 % DMF at 50 μM. Prior to analysis, instruments were calibrated using a solution of sodium iodide (2 mg/mL) in 50:50 water:isopropanol. Capillary voltages were adjusted between 1.5 and 2.5 kV to optimize spray quality, while the sampling

cone and the extraction cone voltage were minimised to reduce breakdown of the assemblies. Source temperature was set at 80 °C. The data was analysed using MassLynx v4.1 software.

4.3 Results and discussion

Structural description

All four compounds are isostructural, and so for the sake of brevity we provide a generic description. The molecular structure of the cation of **1** is shown in Figure 1, with pertinent structural data listed in Tables 1 and 2. All four compounds crystallise in the trigonal space group $R\bar{3}$, with just the central metal ion, one outer metal ion, two hmp^- ligands and two ClO_4^- anions in the asymmetric unit. This presents two distinct metal sites in the cationic cluster: the central metal is always an M^{II} ion (Ni (**1**, **3**) or Zn (**2**, **4**)) bridged to each outer metal ion *via* two μ_3-OR groups belonging to two hmp^- ligands. Symmetry expansion therefore reveals the central metal ion to have a $[M^{II}O_6]$ octahedral coordination sphere. The six outer metal ions in the wheel are crystallographically equivalent: disorder is manifested with the M^{III} ions being equally distributed around all ring positions such that each site has an occupancy of 1/3 M^{III} and 2/3 M^{II}, and an average charge of +2.33. This was modelled with a 5:2 substitutional disorder ratio of metal centres by splitting the unique site into two separate parts with identical, constrained co-ordinates and anisotropic displacement parameters – see CIF files for full details. Thus the metallic skeleton can be described as a centred $[M^{III}_2M^{II}_5]$ hexagon or wheel existing as three isomers whereby the two M^{III} sites are located at positions 1,2 1,3 or 1,4 (in a 2:2:1 ratio) around the ring (*vide infra*) (Figure 5).

The outer metal ions are bridged to each other by one μ-OR (hmp^-) group on the 'outside' of the wheel and one μ_3-OR (hmp^-) group on the 'inside' of the wheel, their octahedral coordination geometries completed by two terminally bonded N-atoms from the same ligands. In total there are twelve hmp^- ligands adorning the outside of the cage, six above and six below the plane of seven metal ions. Charge balance is maintained through the presence of four ClO_4^- anions, two of which sit directly above and below the plane of the metal ions, the three O-atoms closely associated with the three methylene groups of the hmp^- ligands (Cl-O···H(CH_2) ≈ 2.7 Å). In the extended structure, the wheels of compounds **1**-**4** are arranged in layers in the *ab* plane, the perchlorate anions sitting in between. This produces an

aesthetically pleasing hexagonal close packed array when viewed down the *c*-axis (Figure 2). There are numerous short inter-molecular contacts between the aromatic rings of the hmp^- ligands on neighbouring wheels, with the closest C-C distances being ~3.8 Å, and between the aromatic rings and ClO_4^- anions, with closest C-O distances of ~3 Å.

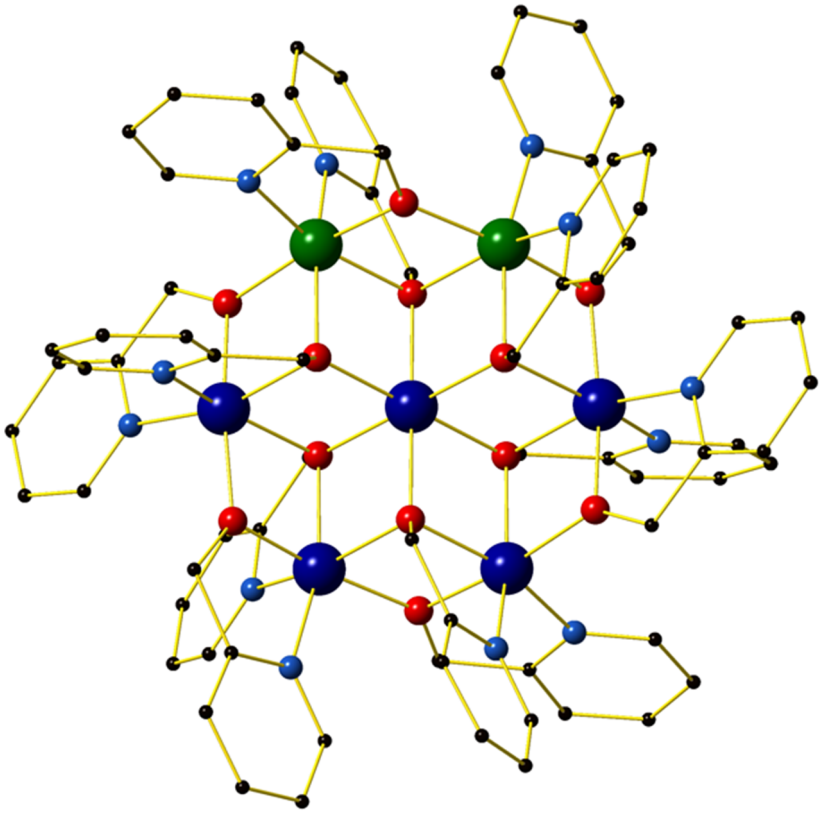

Figure 1. Molecular structure of the 1,2-isomer of the cation of compound **1**. Colour code: Cr = dark green, Ni = dark blue, O = red, N = light blue, C = black. H-atoms, perchlorate counter anions and solvent molecules of crystallisation are omitted for clarity.

Table 1. Pertinent structural parameters for the $M_{central}$-M_{outer} di-alkoxo bridge in **1**-**4**. r = M-O bond length, ϕ = M-O-M bridging angle.

Compound	M-M [Å]	r [Å]	ϕ [°]
1	3.120	2.040-2.111	96.41, 98.67
2	3.200	2.092-2.183	96.58, 99.41
3	3.091	2.013-2.094	96.23, 98.79
4	3.186	2.071-2.178	96.54, 99.95

Table 2. Pertinent structural parameters for the M_{outer}-M_{outer} di-alkoxo bridge in **1**-**4**. r = M-O bond length, ϕ = M-O-M bridging angle.

Compound	M-M [Å]	r [Å]	ϕ [°]
1	3.124	1.968-2.111	97.63, 103.92
2	3.210	1.963-2.183	97.32, 109.33
3	3.097	1.938-2.094	97.86, 105.70
4	3.197	1.944-2.178	97.57, 109.32

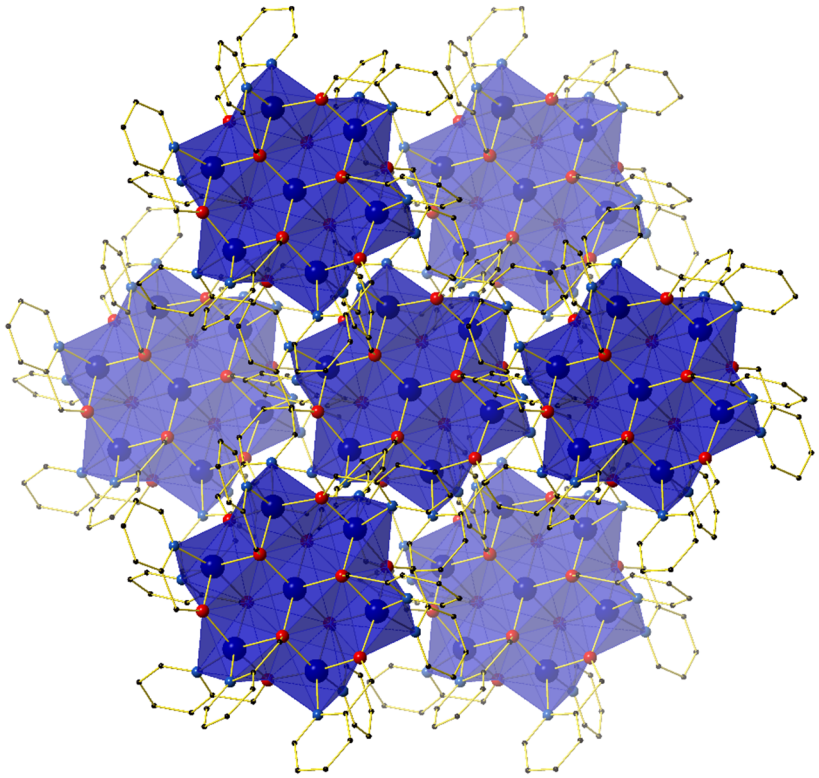

Figure 2. Crystal packing common to compounds **1**-**4** as viewed down the c-axis, highlighting the hexagonal close packed arrangement of layers of molecules. H atoms, solvent and anions omitted for clarity.

Solution NMR spectroscopy of 4

The 1D ^{1}H (Figure 3) and 2D ^{1}H, ^{13}C HSQC spectrum of **4** (Figure 4 and Supplementary Figure S1) show a large chemical shift dispersion of resonances corresponding to the individual signals of the hmp^{-} ligand. The 1D ^{1}H spectrum is dominated by a number of overlapping signals corresponding to different environments of H1' to H6 protons of hmp ligands

associated with different metal substitutions. This is due to a combination of unique through-bond and through-space effects in the individual complexes. In addition, the spectrum also contains signals of free hmpH originating from partially degraded **4** and some minor signals likely belonging to degradation products.

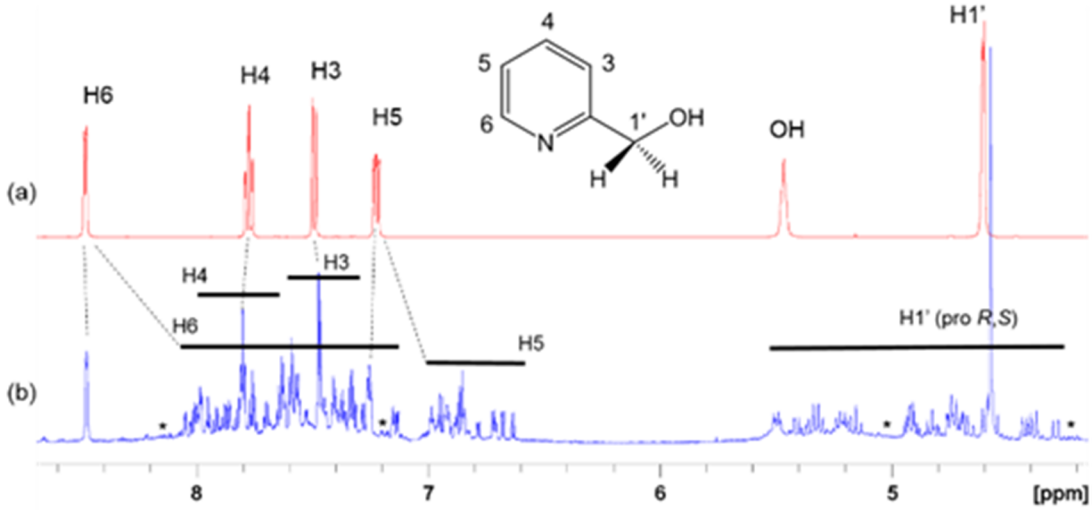

Figure 3. (a) ^{1}H NMR spectrum of 2-pyridinemethanol (hmpH) with assigned resonances. (b) ^{1}H NMR spectrum of **4**. The ranges of chemical shifts of different protons in **4**, as deduced by the analysis of 2D ^{1}H, ^{13}C HSQC spectrum, are indicated. Dashed lines point to the resonances of 2-pyridinemethanol on the sample of **4**.

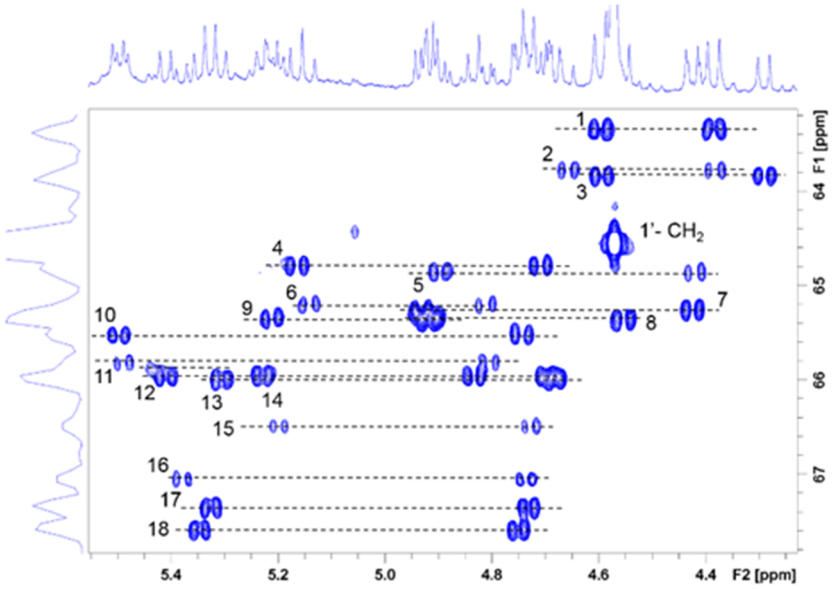

Figure 4. Partial 2D ^{1}H, ^{13}C HSQC spectrum of **4** showing the 1' CH_2 cross peaks. The corresponding *pro-S* and *pro-R* protons are connected by dashed lines and numbered from the low to high ^{13}C chemical shift.

The H6 and H5 ligand resonances are generally shielded, while the CH_2 protons are mostly deshielded relative to the corresponding protons of free hmp; the H3, H4 signals are less affected and protons of individual forms experience either shielding or deshielding. The largest spread of resonances is seen for diastereotopic H1' protons, followed by H6 protons, likely due to their closer proximity to the metal ions.

The CH_2 resonances, as seen in the 2D ^{1}H, ^{13}C HSQC spectrum (Figure 4), are particularly informative. The lack of rotation of this side chain causes the *pro-S* and *pro-R* protons to acquire a distinct chemical shift and a doublet character due to appearance of $^{2}J_{HH}$ couplings. Altogether 18 pairs of CH_2 resonances were identified, in perfect agreement with the model of the metal disorder (Figure 5). The intensity of these cross peaks is non-uniform, indicating that not all metal occupancies are equally probable.

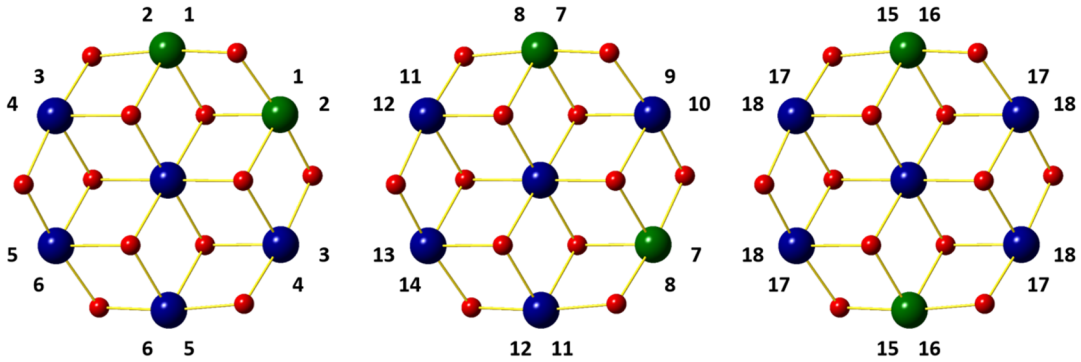

Figure 5. Schematic representation showing the 18 non-equivalent hmp^- ligand environments in compound **4**. Colour code as Figure 1.

The heterogeneity deduced from the inspection of the CH_2 resonances is also seen for C3/H3 to C6/H6 sites (Supplementary Figure S1). Here between 14 and 18 different correlations were identified for individual atom pairs. This reduction (maximum of 18) is caused by a degeneracy of chemical shifts in some structural isomers, resulting in signal overlap.

Complex **4** was further characterised by acquiring a diffusion ordered spectrum (DOSY) (Figure 6).[36] In this spectrum all ^{1}H resonance of **4** are placed on one line indicating identical diffusion properties, *i.e.* hydrodynamic radius of all complexes. The DOSY spectrum also contains signals of hmpH appearing, as expected, at much smaller diffusion coefficients. The variations in diffusion coefficient of hmpH observed for individual protons is caused by the varying degree of overlap with the signals of **4**, resulting in inaccurate positioning of its DOSY

signals in the spectrum. Minor signal intensities seen slightly above or below the line of the main resonances of **4** correspond to areas with a poor signal-to-noise ratio and cannot be reliably interpreted as larger or smaller molecules.

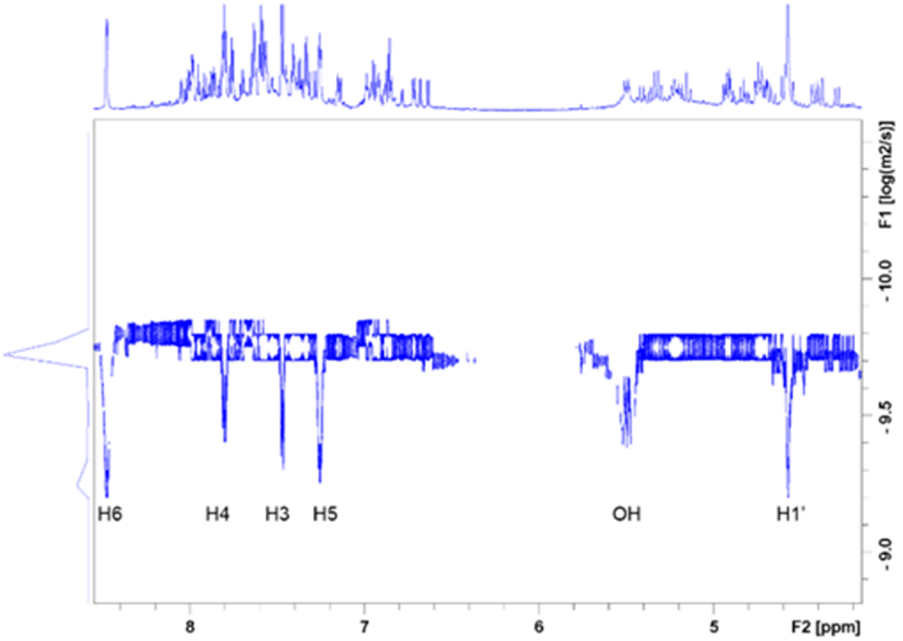

Figure 6. 2D DOSY spectrum of **4**. 'Free' uncoordinated hmpH forms in solution and the signals are labelled.

Summarising the information provided by the solution-state NMR: even though it was not possible to associate the individual cross peaks to specific isomers of **4**, the results shows that solution-state NMR spectroscopy of diamagnetic metal complexes can identify, and to some extent, qualify their structural heterogeneity, also providing information on their relative sizes. The solution-state NMR confirms the metal disorder observed in their solid-state structures.

Solid-state NMR spectroscopy

Solid state ^{27}Al MAS NMR was used to probe the local metal environments in **3** and **4**. The diamagnetic analogue **4** contains a single ^{27}Al resonance with second order quadrupole line-shape. The line-shape can be simulated by a single ^{27}Al NMR site with $\delta_{iso}(^{27}Al)$ = 18.9(10) ppm, C_Q = 5.25(5) MHz, and η = 0.87(5), as illustrated in Figure 7(a). The isotropic chemical

shift value is characteristic of octahedral Al and the fairly large quadrupole coupling constant, C_Q, implies a distorted bonding environment. The three possible combinations of the Al positions on the outer parts of the wheel (Figure 5) cannot be distinguished by solid state NMR, as the difference in isotropic shifts is negligible compared to the line-width, as also observed in ZnAl-layered double hydroxides,[37] which contain a similar structural building block.

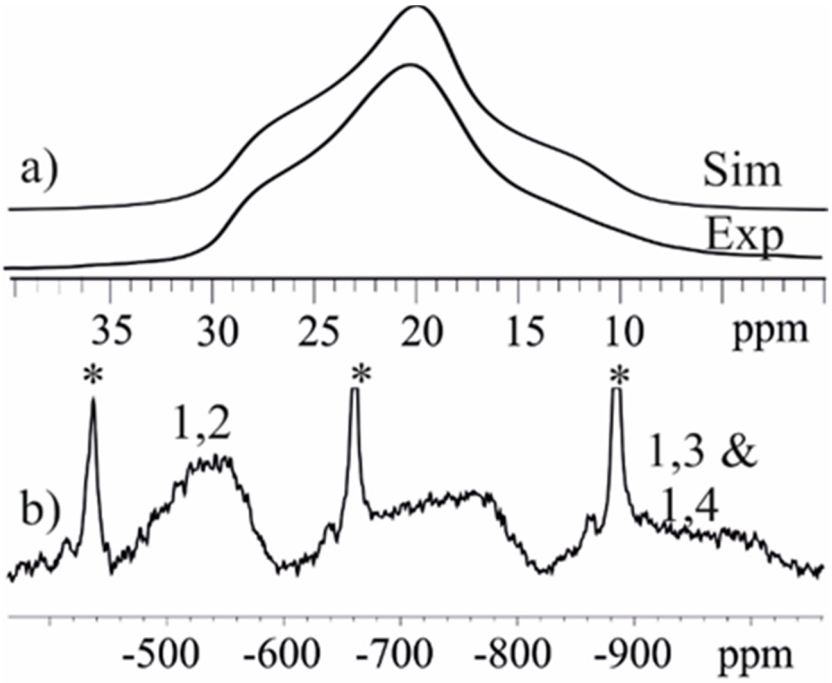

Figure 7 ^{27}Al MAS NMR spectra of a) diamagnetic **4** with simulation (Sim) using a single ^{27}Al site ($\delta_{iso}(^{27}Al)$ = 18.9ppm, C_Q = 5.25MHz, and η = 0.879), and b) paramagnetic **3** with two isotropic resonances from **3** as well as the spinning sidebands originating from the Al background in the NMR rotor marked *. The resonance at ~700-800 ppm is a spinning sideband from the two isotropic resonances (1,2 & 1,3 + 1,4). Notice that different axes are used in a) and b).

In contrast, the ^{27}Al MAS NMR spectrum of paramagnetic compound **3** shows the presence of two different ^{27}Al resonances with $\delta_{iso}(^{27}Al)$ = -550(40) ppm and -940(60) ppm (Figure 7(b)). The presence of paramagnetic Ni^{2+} results in a contact shift in addition to the diamagnetic isotropic shift,[38] which shift the resonances outside the conventional chemical shift range for diamagnetic materials. To a first approximation, the hyperfine shift in inorganic materials is proportional to the number of neighbouring Ni ions. Thus, the 1,2 confomer has two Ni ions, whereas both the 1,3 and 1,4 conformers have three Ni ions as neighbours. We therefore

assign the site at -560(40) ppm to the 1,2 conformer, whereas the other two coincide in the second resonance at -960(60) ppm. The resonances are very broad (20 kHz) due to fast relaxation caused by the paramagnetic Ni ions, and this does not allow us to resolve the 1,3 and 1,4 conformers.

Mass spectrometry

Electrospray ionisation mass spectrometry (ESI-MS) was carried out on a solution of **4** dissolved in acetonitrile and DMF, with the results showing that compound **4** is stable in solution as $[M+2H]^{2+}$ (Figure 8). The most intense peak in the spectrum corresponds to the ion $[M+2H]^{2+}$ where M = $[Al_2Zn_5(hmp)_{12}]$ $(ClO_4)_2$ and appears at *m/z* = 938. The unfragmented 4+ cationic part of the complex remains associated with two of the perchlorate counter ions. We speculate that these are most likely the two that sit above and below the wheel as these have closer contacts to the cationic cluster. No other peaks could be identified from the spectrum. The observed solution stability is in agreement with the findings from the solution-state NMR spectroscopy.

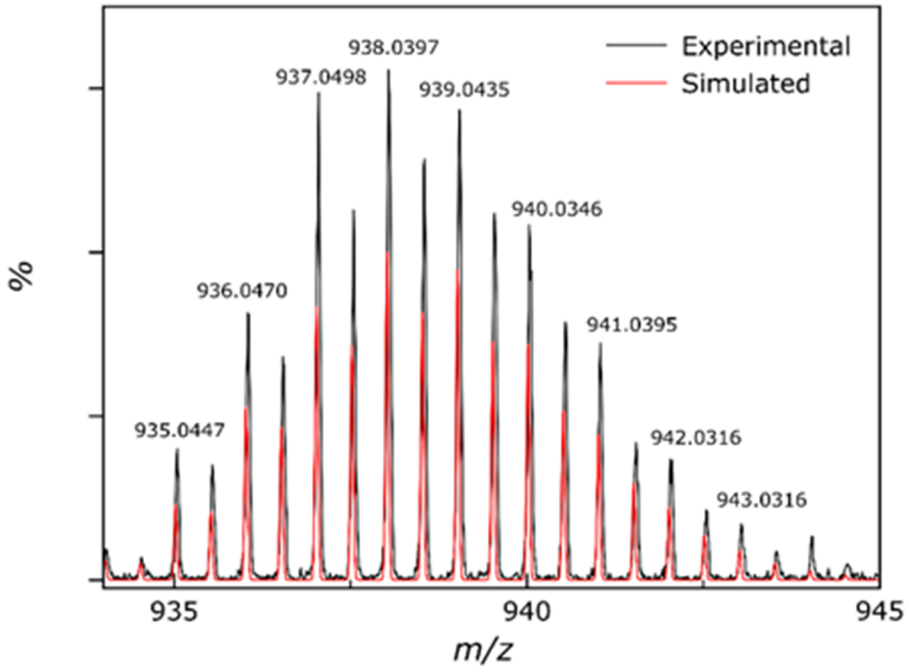

Figure 8 Experimental (black) and simulated (red) peaks for the partial mass spectrum of **4**, showing the $[M+2H]^{2+}$ ion. The % on y-axis represents relative intensity of peaks.

Magnetometry

The magnetic properties of $[Cr_2Ni_5]$ (**1**), $[Cr_2Zn_5]$ (**2**) and $[Al_2Ni_5]$ (**3**) were modelled using Heisenberg models for the various possible configurations (a), (b), and (c) displayed in Figure 9 and equivalently in Figure 5. Due to symmetry, configurations (a) and (b) contribute with a weight of 2/5 to the average magnetic observables, whereas (c) contributes 1/5.

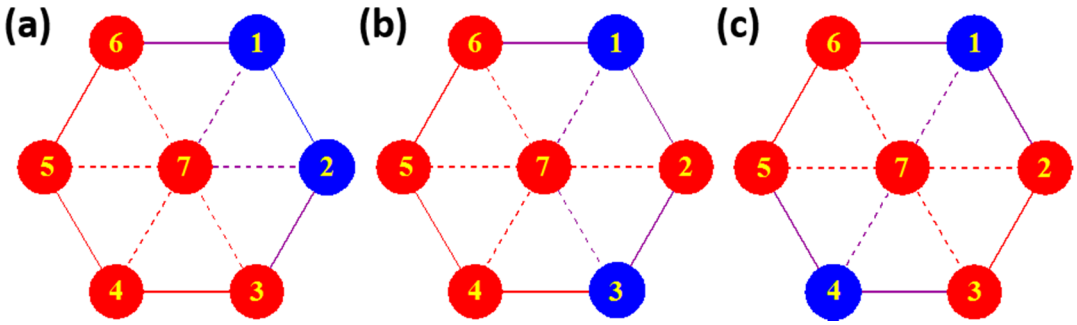

Figure 9. Arrangement of M^{III} (blue) and M^{II} (red) ions in the three realizations of the disordered compound $[M^{III}_2M^{II}_5]$. The solid and dashed lines denote the respective exchange interactions when applicable.

Our philosophy in attempting to fit the magnetic data for these rather complex and disordered molecules is to extract reasonably accurate values for the dominant exchange interactions using the simplest model possible, whilst avoiding 'over-analysis' and any exaggeration of the absolute precision of the parameters so-obtained. It is important to note that the employed model does not include additional (albeit small) contributions, such as anisotropies or next-nearest neighbour exchange interactions. Firstly, from compound **2** it was possible to fit $J_{Cr\text{-}Cr}$ as this exchange appears only in configuration (a). The respective Hamiltonian reads:

$$\hat{H} = -2\, J_{Cr-Cr}\, \hat{\vec{s}}_1 \cdot \hat{\vec{s}}_2$$

The measured data is consistent with $J_{Cr\text{-}Cr}$ = -1.0 cm^{-1} and g = 2.0 when fitted with this Hamiltonian (Figure 10).

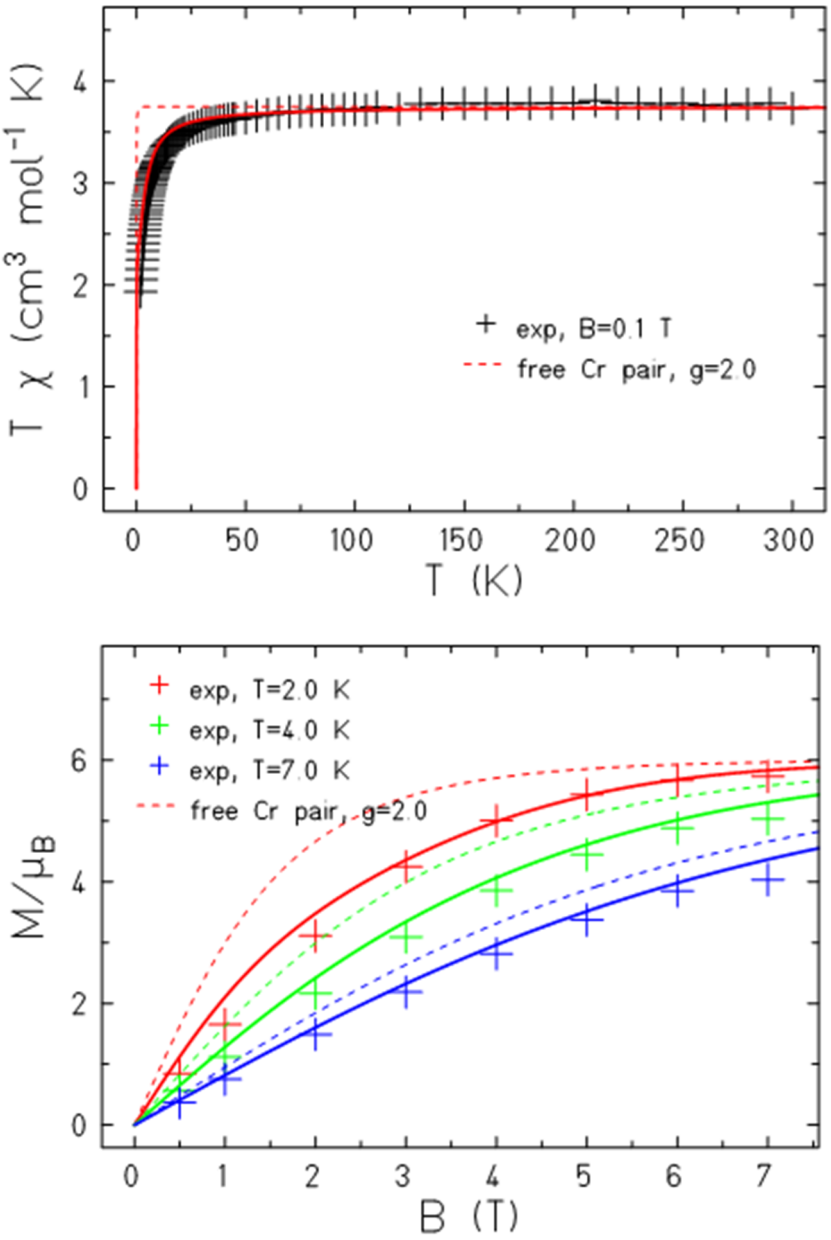

Figure 10. Experimental (+) and simulated (lines) magnetic susceptibility (top) and magnetisation (bottom) of **2**.

In order to model compound **3** two exchange interactions are necessary; $J_{Ni\text{-}Ni,r}$ for nearest neighbour exchange around the ring and $J_{Ni\text{-}Ni,c}$ for the exchange to the central Ni ion, fixing g_{Ni} = 2.15.

Good agreement with the experimental data, as observed in Figure 11, can be achieved upon modelling with an antiferromagnetic interaction between nearest neighbours on the ring, $J_{Ni\text{-}Ni,r}$ = -5.0 cm^{-1}, and a ferromagnetic interaction to the central Ni ion, $J_{Ni\text{-}Ni,c}$ = 10.0 cm^{-1}.

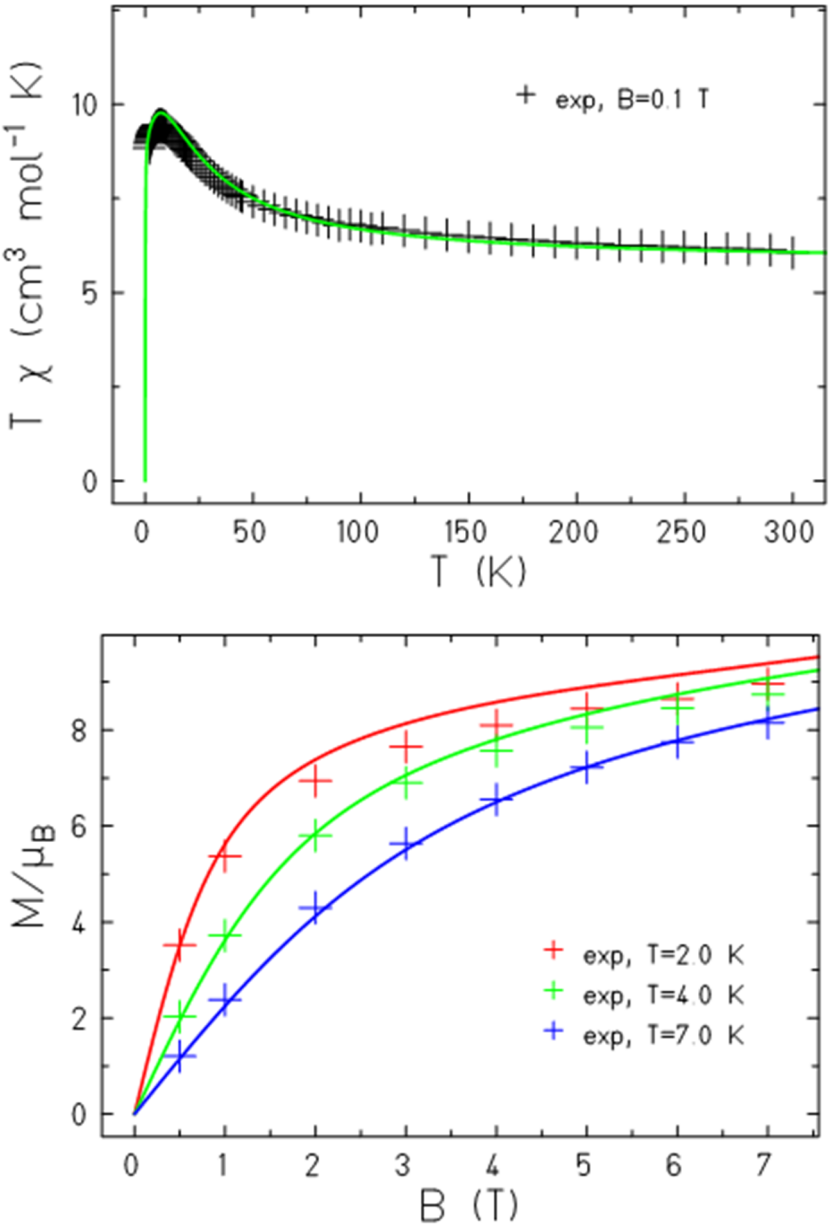

Figure 11. Experimental (+) and simulated (lines) magnetic susceptibility (a) and magnetisation (b) of **3**.

Assuming that the obtained exchange parameters $J_{Cr\text{-}Cr}$, $J_{Ni\text{-}Ni,r}$ and $J_{Ni\text{-}Ni,c}$ do not change their values in **1**, we can proceed to determine the remaining exchange parameters between Ni and Cr ions on the ring, $J_{Cr\text{-}Ni,r}$, as well as between a peripheral Cr ion and the central Ni ion, $J_{Cr\text{-}Ni,c}$. Looking at the magnetic susceptibility in Figure 12(a) one notices that the experimental data show a stronger polarization at small temperatures than expected from a simple combination of the data of **2** and **3**. Although one could speculate that such behaviour points at additional ferromagnetic interactions in **1**, the fitting appeared more complicated and not

fully conclusive. Indeed, we found two rather similar fits with opposite characteristics. In the first solution (solid coloured curves in Figure 12), $J_{Cr\text{-}Ni,r}$ = -1.2 cm^{-1}, $J_{Cr\text{-}Ni,c}$ = 2.6 cm^{-1}, the exchange between adjacent Ni and Cr ions on the ring is antiferromagnetic, with that between Cr ions on the ring and the central Ni ion, ferromagnetic. For the second solution (coloured curves in Figure 12), $J_{Cr\text{-}Ni,r}$ = 2.2 cm^{-1}, $J_{Cr\text{-}Ni,c}$ = -2.0 cm^{-1}; *i.e.* the inverse is true. For the spectroscopic splitting factors we assumed g_{Cr} = 2.0 and g_{Ni} = 2.15 as in **2** and **3**.

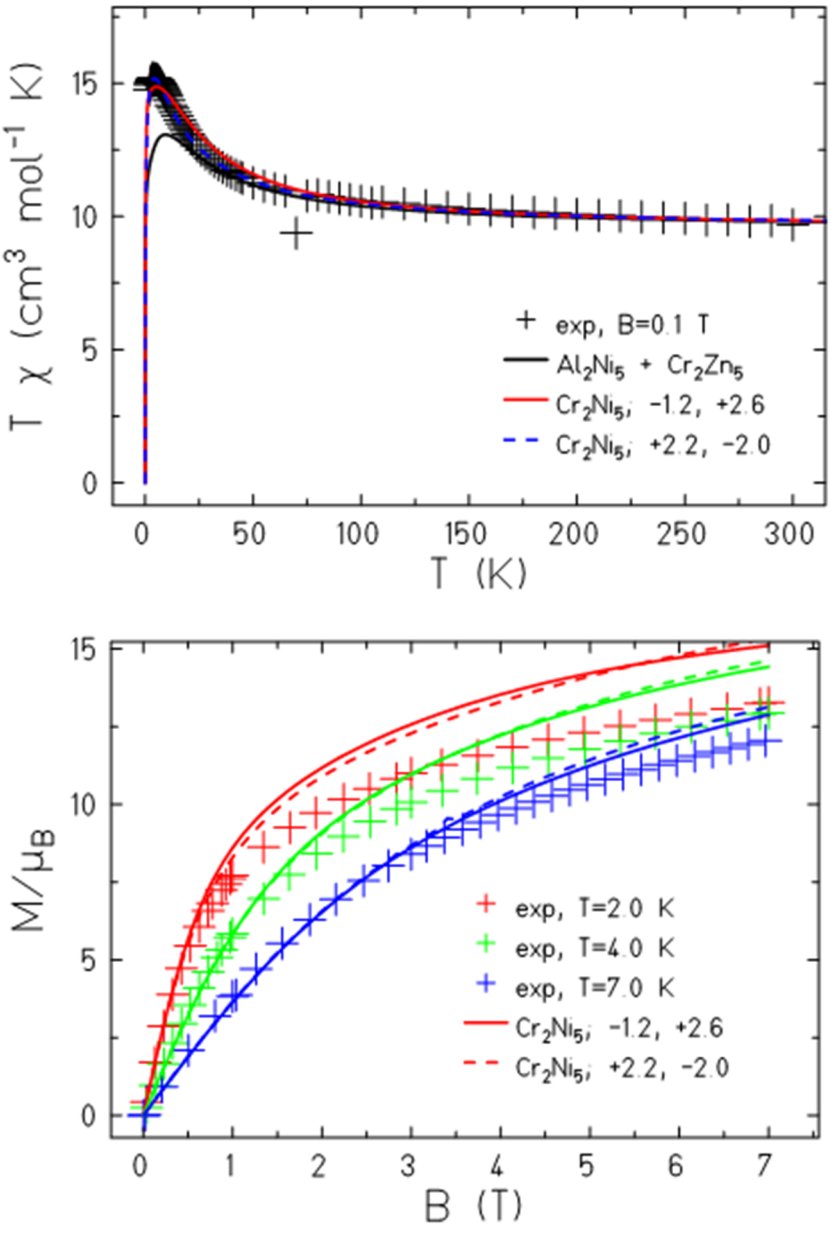

Figure 12. Experimental and simulated magnetic susceptibility (a) and magnetisation (b) of **1**. The solid coloured curves belong to the parameterization $J_{Cr\text{-}Ni,r}$ = -1.2 cm^{-1}, $J_{Cr\text{-}Ni,c}$ = 2.6 cm^{-1}; whereas the dashed ones belong to $J_{Cr\text{-}Ni,r}$ = 2.2 cm^{-1}, $J_{Cr\text{-}Ni,c}$ = -2.0 cm^{-1}.

Although the second data set appears to fit the susceptibility somewhat better, we believe that our measurements cannot discriminate between scenarios since the neglected single-ion anisotropy, especially of the Ni^{II} ions, may play a more prominent role in **1**. However, despite the limitations of the model and the simplistic methodology employed, agreement between experiment and simulation is remarkably good in all three cases, highlighting the advantage of being able to prepare and characterise all of the paramagnetic-diamagnetic 'building blocks' of the fully paramagnetic cage.

4.4 Conclusions

The solvothermal reaction between the perchlorate salt of M^{II} ions and either the chloride or nitrate salts of M^{III} ions in a basic solution of the hmpH ligand has yielded a new family of heterometallic Anderson-type wheels of general formula $[M^{III}_2M^{II}_5(hmp)_{12}](ClO_4)_4$. The wheels display substitutional disorder in the positions of the M^{III} and M^{II} ions around the outside ring, which has been quantified and characterised through the combination of single-crystal X-ray diffraction, and solution- and solid-state NMR spectroscopy. This reveals the presence of three isomers, with the Cr^{III} ions positioned at the 1,2 1,3 and 1,4 sites around the wheel. NMR and mass spectrometry data also confirm that the solid-state structure persists in solution. Magnetic susceptibility and magnetisation data for **1**-**3** was fitted in a sequential manner: the Cr-Cr exchange interaction was obtained from the data of complex **2**, and the Ni-Ni exchange interactions were obtained from the data of **3**. These values were then fixed, allowing the Cr-Ni interactions in **1** to be extracted. The combination of solution- and solid-state techniques has therefore proved invaluable in the quantitative understanding of the physical properties of a large, complex, and structurally disordered molecule.

4.5 Supplementary Information

Table S1. Crystallographic information for compounds **1**-**4**.

Compound	**1**	**2**	**3**	**4**
Formula	$C_{79}H_{100}Cl_4Cr_2N_{12}Ni_5O_{35}$	$C_{81}H_{108}Cl_4Cr_2N_{12}O_{37}Zn_5$	$C_{81}H_{108}Al_2Cl_4N_{12}Ni_5O_{37}$	$C_{80}H_{104}Al_2Cl_4N_{12}O_{36}Zn_5$
$D_{calc.}$/ g cm^{-3}	1.674	1.727	1.674	1.679
μ/mm^{-1}	1.439	1.706	3.195	1.511
FW/g mol^{-1}	2317.05	2414.44	2331.10	2332.36
Colour	blue	light purple	pale blue	colourless
Shape	block	plate	plate	plate
Size/mm^3	0.32×0.11×0.10	0.32×0.11×0.10	0.23×0.19×0.09	0.28×0.23×0.04
T/K	120.0	120.0	120.0	120.0
Crystal System	trigonal	trigonal	trigonal	trigonal
Space Group	R-3	R-3	R-3	R-3
a/Å	14.6131(3)	14.5920(3)	14.53160(10)	14.4962(5)
b/Å	14.6131(3)	14.5920(3)	14.53160(10)	14.4962(5)
c/Å	37.2857(9)	37.7623(14)	37.9260(9)	38.022(2)
α/°	90	90	90	90
β/°	90	90	90	90
γ/°	120	120	120	120
V/Å^3	6895.4(3)	6963.4(4)	6935.77(19)	6919.4(6)
Z (Z')	3 (0.16667)	3 (0.16667)	3 (0.16667)	3 (0.16667)
Wavelength/Å	0.71073	0.71073	1.54178	0.71073
Radiation type	MoK_α	MoK_α	CuK_α	MoK_α
Θ_{min}/° - Θ_{max}/°	1.638 – 25.339	2.792 – 25.350	3.700 – 76.591	2.810 – 26.372
Measured Refl.	26509	35087	32013	13554
Independent Refl.	2823	2846	3217	3142
Reflections Used	2044	2599	3044	2492
R_{int}	0.0491	0.0660	0.0502	0.0577
Parameters	186	202	186	187
Restraints	0	45	0	0
Largest Peak	0.976	1.903	0.878	1.427
Deepest Hole	-1.227	-0.593	-1.627	-0.919
GooF	1.086	1.150	1.134	1.092
wR_2 (all data) (wR_2)	0.1752 (0.1512)	0.1438 (0.1412)	0.2395 (0.2373)	0.1459 (0.1384)
R_1 (all data) (R_1)	0.0779 (0.0548)	0.0721 (0.0660)	0.0838 (0.0818)	0.0849 (0.0647)
CCDC Number	1819131	1819132	1819133	1819134

For Figure S1 please refer to the "Chapter 4 SI" file on the memory stick supplied with the thesis.

4.6 References

1. S. C. Lee and R. H. Holm, *Chem. Rev.*, 2004, **104**, 1135-1157.
2. J. D. Blakemore, R. H. Crabtree and G. W. Brudvig, *Chem. Rev.*, 2015, **115**, 12974-13005.
3. J. L. Atwood and J. M. Lehn, *Comprehensive Supramolecular Chemistry*, Pergamon, Oxford, 1996.
4. M. O'Keeffe and O. M. Yaghi, *Chem. Rev.*, 2012, **112**, 675-702.
5. R. D. Willett, D. Gatteschi and O. Kahn, *Magneto-Structural Correlations in Exchange Coupled Systems*, D. Reidel, Dordrecht, 1985.
6. J. N. Rebilly and T. Mallah, *Single-Molecule Magnets and Related Phenomena*, 2006, **122**, 103-131.
7. M. Evangelisti and E. K. Brechin, *Dalton Trans.*, 2010, **39**, 4672-4676.
8. J. Schnack, *Dalton Trans.*, 2010, **39**, 4677-4686.
9. C. J. Milios and R. E. P. Winpenny, *Molecular Nanomagnets and Related Phenomena*, 2015, **164**, 1-109.
10. C. Coulon, V. Pianet, M. Urdampilleta and R. Clérac, *Molecular Nanomagnets and Related Phenomena*, 2015, **164**, 143-184.
11. D. Aguilà, L. A. Barrios, V. Velasco, O. Roubeau, A. Repollés, P. J. Alonso, J. Sesé, S. J. Teat, F. Luis and G. Aromí, *J. Am. Chem. Soc.*, 2014, **136**, 14215-14222.
12. J. Ferrando-Soria, E. M. Pineda, A. Chiesa, A. Fernandez, S. A. Magee, S. Carretta, P. Santini, I. J. Vitorica-Yrezabal, F. Tuna, G. A. Timco, E. J. L. McInnes and R. E. P. Winpenny, *Nat. Commun.*, 2016, **7**.
13. L. R. Piquer and E. C. Sañudo, *Dalton Trans.*, 2015, **44**, 8771-8780.
14. R. E. P. Winpenny, *Chem. Soc. Rev.*, 1998, **27**, 447-452.
15. F. K. Larsen, E. J. L. McInnes, H. El Mkami, J. Overgaard, S. Piligkos, G. Rajaraman, E. Rentschler, A. A. Smith, G. M. Smith, V. Boote, M. Jennings, G. A. Timco and R. E. P. Winpenny, *Angew. Chem. Int. Ed.*, 2003, **42**, 101-105.
16. G. A. Timco, E. J. L. McInnes, R. G. Pritchard, F. Tuna and R. E. P. Winpenny, *Angew. Chem. Int. Ed.*, 2008, **47**, 9681-9684.
17. G. A. Timco, A. S. Batsanov, F. K. Larsen, C. A. Muryn, J. Overgaard, S. J. Teat and R. E. P. Winpenny, *Chem. Commun.*, 2005, 3649-3651.
18. E. J. L. McInnes, G. A. Timco, G. F. S. Whitehead and R. E. P. Winpenny, *Angew. Chem. Int. Ed.*, 2015, **54**, 14244-14269.
19. S. L. Heath, R. H. Laye, C. A. Muryn, N. Lima, R. Sessoli, R. Shaw, S. J. Teat, G. A. Timco and R. E. R. Winpenny, *Angew. Chem. Int. Ed.*, 2004, **43**, 6132-6135.
20. O. S. Manole, A. S. Batsanov, Y. T. Struchkov, G. A. Timko, L. D. Synzheryan and N. V. Gerbeleu, *Koord. Khim.*, 1994, **20**, 231-237.
21. F. E. Kakaroni, A. Collet, E. Sakellari, D. I. Tzimopoulos, M. Siczek, T. Lis, M. Murrie and C. J. Milios, *Dalton Trans.*, 2018, **47**, 58-61.
22. J. Zhang, P. Teo, R. Pattacini, A. Kermagoret, R. Welter, G. Rogez, T. S. Hor and P. Braunstein, *Angew. Chem. Int. Ed.*, 2010, **49**, 4443-4446.
23. R. Pattacini, P. Teo, J. Zhang, Y. H. Lan, A. K. Powell, J. Nehrkorn, O. Waldmann, T. S. A. Hor and P. Braunstein, *Dalton Trans.*, 2011, **40**, 10526-10534.
24. R. W. Saalfrank, T. Nakajima, N. Mooren, A. Scheurer, H. Maid, F. Hampel, C. Trieflinger and N. Daub, *Eur. J. Inorg. Chem.*, 2005, 1149-1153.
25. H. Oshio, N. Hoshino, T. Ito, M. Nakano, F. Renz and P. Gütlich, *Angew. Chem. Int. Ed.*, 2003, **42**, 223.
26. M. Tesmer, B. Müller and H. Vahrenkamp, *Chem. Commun.*, 1997, 721-722.

27. J. A. Przyojski, N. N. Myers, H. D. Arman, A. Prosvirin, K. R. Dunbar, M. Natarajan, M. Krishnan, S. Mohan and J. A. Walmsley, *J. Inorg. Biochem.*, 2013, **127**, 175-181.
28. V. V. Semenaka, O. V. Nesterova, V. N. Kokozay, R. I. Zybatyuk, O. V. Shishkin, R. Boca, D. V. Shevchenko, P. Huang and S. Styring, *Dalton Trans.*, 2010, **39**, 2344-2349.
29. R. W. Saalfrank, R. Prakash, H. Maid, F. Hampel, F. W. Heinemann, A. X. Trautwein and L. H. Böttger, *Chem. Eur. J.*, 2006, **12**, 2428-2433.
30. M. I. Khan, S. Tabussum and R. J. Doedens, *Chem. Commun.*, 2003, 532-533.
31. M. I. Khan, S. Tabussum, R. J. Doedens, V. O. Golub and C. J. O'Connor, *Inorg. Chem.*, 2004, **43**, 5850-5859.
32. S. Golhen, L. Ouahab, D. Grandjean and P. Molinie, *Inorg. Chem.*, 1998, **37**, 1499-1506.
33. G. M. Sheldrick, *Acta Crystallogr. Sect. C: Cryst. Struct. Commun.*, 2015, **71**, 3-8.
34. O. V. Dolomanov, L. J. Bourhis, R. J. Gildea, J. A. K. Howard and H. Puschmann, *J. Appl. Crystallogr.*, 2009, **42**, 339-341.
35. G. A. Bain and J. F. Berry, *J. Chem. Educ.*, 2008, **85**, 532.
36. D. H. Wu, A. D. Chen and C. S. Johnson, *J. Magn. Reson., Ser A*, 1995, **115**, 260-264.
37. S. S. C. Pushparaj, C. Forano, V. Prevot, A. S. Lipton, G. J. Rees, J. V. Hanna and U. G. Nielsen, *J. Phys. Chem. C*, 2015, **119**, 27695-27707.
38. S. A. Rouf, V. B. Jakobsen, J. Mares, N. D. Jensen, C. J. McKenzie, J. Vaara and U. G. Nielsen, *Solid State Nucl. Magn. Reson.*, 2017, **87**, 29-37.

CHAPTER 5:

CAGES ON A PLANE: A STRUCTURAL MATRIX FOR MOLECULAR 'SHEETS'

5.1 Introduction

Paramagnetic metal ions arranged in triangular topologies have long held academic interest in the field of molecule-based magnetism,[1] since they can lead to the observation of, for example, ferromagnetic exchange in partial cubanes,[2] tuneable exchange between metal ions separated by two atom bridges,[3] antisymmetric exchange effects in heterometallic 3d-4d complexes,[4] and geometric spin frustration in antiferromagnetically coupled cages[5] and 2-3D materials (*e.g.* the kagomé lattice) possessing high symmetry.[6]

In 3d transition metal chemistry the molecular triangle is most commonly found in one of two structure types: a) the oxo-centred planar triangle $[M_3O]^{n+}$, as personified by the basic metal carboxylates,[7] where all four atoms lie on (or nearly on) the same plane, or b) the $[M_3O_4]^{n+}$ partial cubane where the metal ions and O-atoms lie on different planes, *i.e.* a cube missing one metal vertex. The latter moiety also often acts as the building block for the creation of large and (occasionally) very large molecules whose structures conform to molecular 'sheets', *i.e.* the metallic skeleton of the complex grows in 2D. From a structural/synthetic perspective this is simple to understand as a series of O-bridged, edge- and vertex-sharing metal triangles (Figure 1). For example, two edge-sharing triangles form tetranuclear $[M_4O_2]^{n+}$ or $[M_4O_6]^{n+}$ butterflies or partial cubanes (Figure 1a-b), with detailed magneto-structural correlations developed for Fe[8] and Mn.[9] Such triangles and butterflies/partial cubanes are by far the most common building blocks seen in large cages containing multiple 3d $M_n^{II/III}$ ions ($n > 4$).

Continued edge-sharing growth in just one dimension/direction from triangle to butterfly/partial cubane to larger species results in the formation of molecular rods (Figure 1c), a pertinent example being the use of tripodal alcohol ligands to direct the formation of Mn_6, Mn_7, Mn_8, Mn_{12} complexes.[10] Growth in two dimensions/directions leads to planar disc-like complexes (Figures 1d-i), the most common of which is the Anderson-type wheel. This structure describes a centred hexagon, with homometallic,[11] heterometallic,[12] homovalent[13] and heterovalent[14] examples known. Larger complexes are somewhat unusual, but are all characterised by beautiful structural aesthetics, the presence of the Anderson moiety at the core of their metallic skeletons, and interesting physical properties. For example, $[Ni_{10}]$ (Figure 1e) is a rare example of a large nuclearity Ni single-molecule magnet (SMM),[15] mixed-valent $[Co_{13/14}]$ cages (Figures 1f-g) display ferromagnetic exchange interactions between the Co^{II} ions,[16] $[Fe_{17/19}]$ is an example of a trapped/molecular mineral phase with $S \geq 33/2$,[17] two

[Mn_{19}] cages possess a similar brucite-like core (Figure 1h), one displaying intramolecular ferrimagnetic exchange and long range magnetic order,[18a] and the other being a very rare example of a Mn-alkoxide, while [Co_{24}] was the first polynuclear Co^{II} species to exhibit slow relaxation of the magnetization (Figure 1i).[19] It is also interesting to note a common thread in the synthesis of each of these species: the use of alkoxide-based bridging ligands.

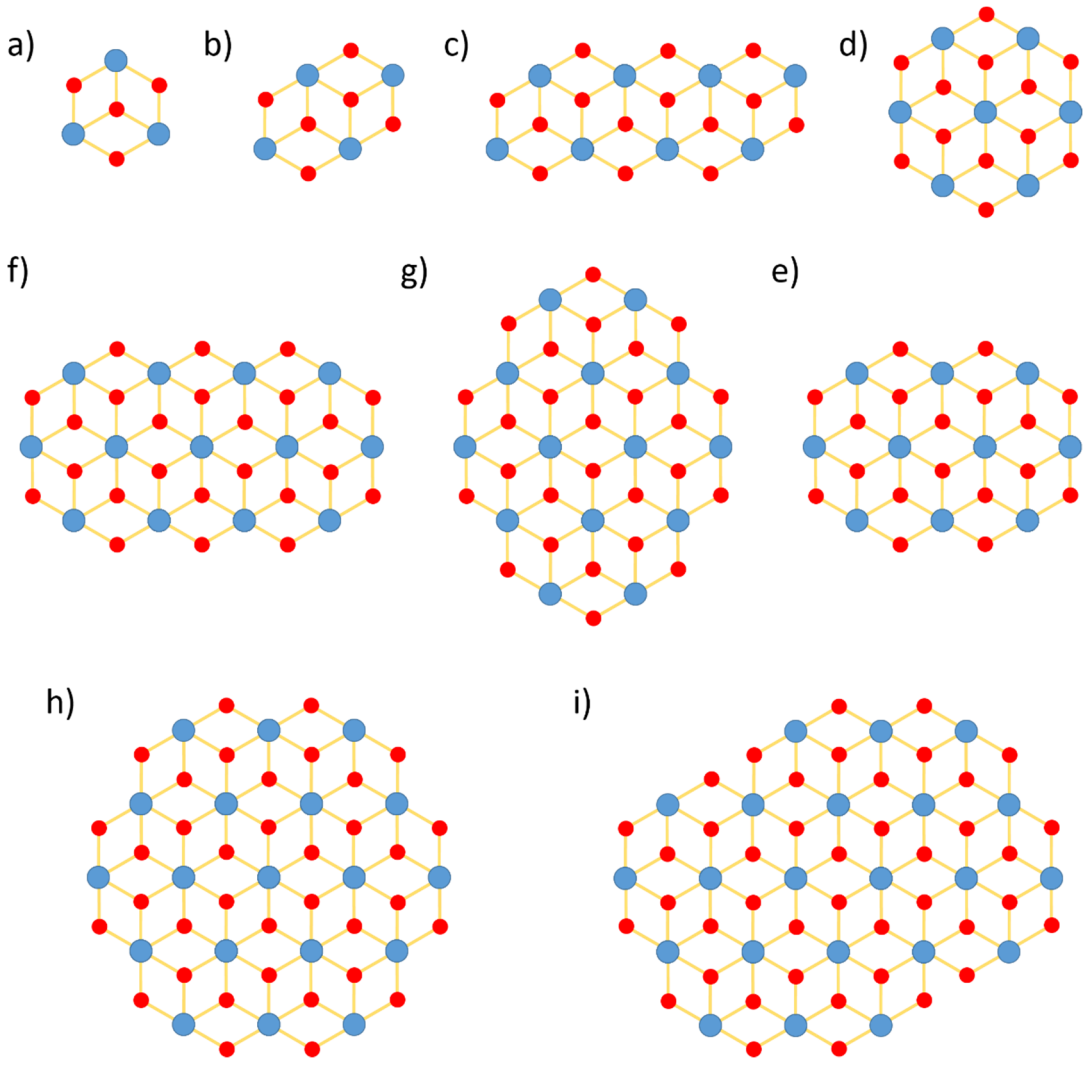

Figure 1. Schematic showing the metal oxygen cores of a variety of transition metal based cages based on triangular [M_3] building blocks; (a) $[M_3O_4]^{n+}$ partial cubane, (b) $[M_4O_6]^{n+}$ butterflies, (c) molecular rods, (d) Anderson-type wheels, (e) [Ni_{10}], (f) [Co_{13}], (g) [Co_{14}], (h) [Mn_{19}], (i) [Co_{24}] showing only the 22 metal sites sitting on the same plane.

We recently reported a small family of Anderson-type complexes of general formula $[M^{III}_2M^{II}_5(hmp)_{12}]^{4+}$ (M^{III} = Cr or Al and M^{II} = Ni or Zn, hmpH = 2-pyridinemethanol) in which

the two M^{III} sites were disordered around the outer wheel.[20] The relative ease of synthesis of these species and their stability in both the solid and solution state suggested that more family members could be made simply by changing the identity of both the M^{III} and M^{II} ions. This family is expanded to include M^{II} = Cu, Co, Mn and Fe, and M^{III} = Al and Cr, alongside the serendipitous self-assembly of the related, but larger complex $[Al^{III}_6Cu^{II}_7(OH)_{12}(hmp)_{12}](ClO_4)_6(NO_3)_2$.

5.2 Experimental

Materials and physical measurements

All chemicals were procured from commercial suppliers and used as received (reagent grade). Elemental analyses for C, H, N and metal ions were performed by Medac Ltd.

Synthesis of $[Cr_2Co_5(hmp)_{12}](ClO_4)_4 \cdot 9MeOH$ (1)

$Co(ClO_4)_2 \cdot 6H_2O$ (0.366 g, 1 mmol) and $CrCl_3 \cdot 6H_2O$ (0.133 g, 0.5 mmol) were dissolved with NaOMe (0.162 g, 3 mmol) in MeOH (24 ml) to give a clear brown solution. Upon full dissolution, hmpH (0.285 ml, 3 mmol) was added dropwise giving a colour change to red. The reaction was left overnight with continuous stirring. 12 ml samples of the resulting dark red solution were heated in Teflon-lined autoclaves at 100°C for 12 hours. After slowly cooling to room temperature the reaction vessels were allowed to sit undisturbed for 24 hours yielding dark pink, block-shaped crystals suitable for X-ray diffraction. Yield 0.139 g (26.6% by Co weight). Anal. Calcd (%) for $C_{79}H_{100}Cl_4Co_5Cr_2N_{12}O_{35}$: C 40.93, H 4.35, Cr 4.49, Co 12.71, N 7.25; found: C 40.21, H 4.36, Cr 4.88, Co 12.36, N 7.43.

Synthesis of $[Cr_2Fe_5(hmp)_{12}](ClO_4)_4 \cdot 9MeOH$ (2)

$Fe(ClO_4)_2 \cdot 6H_2O$ (0.363 g, 1 mmol) and $Cr(ClO_4)_3 \cdot 6H_2O$ (0.229 g, 0.5 mmol) were dissolved with NaOMe (0.162 g, 3 mmol) in MeOH (24 ml) to give a dark red solution. Upon full dissolution, hmpH (0.285 ml, 3 mmol) was added dropwise and the reaction left overnight with continuous stirring. 12 ml samples of the resulting dark brown solution were heated in Teflon-lined autoclaves at 100°C for 12 hours. After slowly cooling to room temperature the reaction vessels were allowed to sit undisturbed for 24 hours yielding dark brown, plate-shaped crystals suitable for X-ray diffraction. Yield 0.041 g (8.7% by Fe weight). Anal. Calcd

(%) for $C_{84}H_{80}Cl_4Cr_2Fe_5N_{12}O_{30}$: C 44.59, H 3.56, Cr 4.60, Fe 12.34, N 7.43; found: C 44.36, H 3.60, Cr 4.95, Fe 12.01, N 7.43.

Synthesis of $[Cr_2Mn_5(hmp)_{12}](ClO_4)_4 \cdot 10MeOH$ (3)

$Mn(ClO_4)_2 \cdot 6H_2O$ (0.365 g, 1 mmol) and $Cr(ClO_4)_3 \cdot 6H_2O$ (0.229 g, 0.5 mmol) were dissolved with NaOMe (0.162 g, 3 mmol) in MeOH (24 ml) to give a light pink cloudy solution. Upon full dissolution, hmpH (0.285 ml, 3 mmol) was added dropwise and the reaction was left overnight with continuous stirring. 12 ml samples of the resulting dark purple/red solution were heated in Teflon-lined autoclaves at 100°C for 12 hours. After slowly cooling to room temperature the reaction vessels were allowed to sit undisturbed for 24 hours yielding pale purple hexagonal crystals suitable for X-ray diffraction. Yield 0.021 g (4.4% by Mn weight). Anal. Calcd (%) for $C_{72}H_{72}Cl_4Cr_2Mn_5N_{12}O_{28}$: C 41.70, H 3.50, Cr 5.01, Mn 13.25, N 8.10; found: C 41.52, H 3.66, Cr 4.98, Mn 13.02, N 8.33.

Synthesis of $[Cr_2Cu_5(hmp)_{12}](ClO_4)_2(NO_3)_2 \cdot 16MeOH$ (4)

$Cu(ClO_4)_2 \cdot 6H_2O$ (0.371 g, 1 mmol) and $Cr(NO_3)_3 \cdot 9H_2O$ (0.200 g, 0.5 mmol) were dissolved with NaOMe (0.162 g, 3 mmol) in MeOH (24 ml) to give a pale green solution. Upon full dissolution, hmpH (0.285 ml, 3 mmol) was added dropwise giving a colour change to dark green/blue. The reaction was left overnight with continuous stirring. 12 ml samples of the resulting dark green solution were heated in Teflon-lined autoclaves at 100°C for 12 hours. After slowly cooling to room temperature the reaction vessels were allowed to sit undisturbed for 24 hours and the resulting solutions were left to slowly evaporate over 5 days, yielding light purple, plate-shaped crystals suitable for X-ray diffraction. Yield 0.104 g (20.4% by Cu weight). Anal. Calcd (%) for $C_{72}H_{72}Cl_2Cr_2Cu_5N_{14}O_{26}$: C 42.35, H 3.55, Cr 5.09, Cu 15.56, N 9.60; found: C 41.85, H 3.40, Cr 5.09, Cu 15.38, N 9.37.

Synthesis of $[Al_2Co_5(hmp)_{12}](ClO_4)_4 \cdot 9MeOH$ (5)

$Co(ClO_4)_2 \cdot 6H_2O$ (0.366 g, 1 mmol) and $Al(NO_3)_3 \cdot 9H_2O$ (0.188 g, 0.5 mmol) were dissolved with NaOMe (0.162 g, 3 mmol) in MeOH (24 ml) to give a pink solution. Upon full dissolution, hmpH (0.285 ml, 3 mmol) was added dropwise giving a colour change to red. The reaction was left overnight with continuous stirring. 12 ml samples of the resulting dark red solution were heated in Teflon-lined autoclaves at 100°C for 12 hours. After slowly cooling to room temperature the reaction vessels were allowed to sit undisturbed for 24 hours yielding pale brown, plate-shaped crystals suitable for X-ray diffraction. Yield 0.289 g (70.7% by Co weight).

Anal. Calcd (%) for $C_{72}H_{72}Al_2Cl_4Co_5N_{12}O_{28}$: C 42.31, H 3.55, Al 2.64, Co 14.42, N 8.22; found: C 41.81, H 3.38, Al 2.50, Co 14.34, N 7.99.

Synthesis of $[Cu_7Al_6(hmp)_{12}(OH)_{12}](ClO_4)_6(NO_3)_2 \cdot 21MeOH$ (6)

$Cu(ClO_4)_2 \cdot 6H_2O$ (0.371 g, 1 mmol) and $Al(NO_3)_3 \cdot 9H_2O$ (0.188 g, 0.5 mmol) were dissolved with NaOMe (0.162 g, 3 mmol) in MeOH (24 ml) to give a turquoise solution. Upon full dissolution, hmpH (0.285 ml, 3 mmol) was added dropwise giving a colour change to dark blue. The reaction was left overnight with continuous stirring. 12 ml samples of the resulting solution were heated in Teflon-lined autoclaves at 100°C for 12 hours. After slowly cooling to room temperature the dark blue solution was left to slowly evaporate yielding dark blue, block-shaped crystals suitable for X-ray diffraction. Yield 0.078 g (26.7% by Al weight). Anal. Calcd (%) for $C_{82}H_{124}Al_6Cl_6Cu_7N_{14}O_{64}$: C 31.27, H 3.97, Al 5.14, Cu 14.12, N 6.23; found: C 30.89, H 3.87, Al 5.11, Cu 14.30, N 6.20.

X-ray crystallography

Single crystal X-ray diffraction data for samples **1**-**6** were collected using a Rigaku Oxford Diffraction SuperNova diffractometer with MoK_α (**1** & **5**-**6**) or CuK_α (**2**-**4**) radiation. Experimental details are given in Tables S1 and S2 in the Supplementary Information. An Oxford Cryosystems Cryostream 700+ low temperature device was used to maintain a crystal temperature of 120.0 K for all experiments. The structures were solved using ShelXT and refined with version ShelXL interfaced through Olex2 (**1**-**2**, **4**-**6**), or Superflip and refined using ShelXL (**3**).[21-23] All non-hydrogen atoms were refined using anisotropic displacement parameters. H atoms were placed in calculated positions geometrically and refined using the riding model except for some in compound **6** which were refined freely. CCDC: 1855222-1855227.

Magnetic data

Magnetic susceptibility and magnetisation measurements were performed on powdered, polycrystalline samples of **1**-**6** in the T = 2-300 K and B = 0-7 T temperature and field ranges on a Quantum Design MPMS XL SQUID magnetometer equipped with a 7 T dc magnet. Hexadecane was employed to prevent potential torqueing of the crystallites. Diamagnetic corrections were applied to all data using Pascal's constants.[30]

4.3 Results and discussion

Structural description

There are two unique structure types present in **1**-**6**; compounds **1**-**5** possess the [M_7] Anderson-type structure, while **6** is an [M_{13}] cluster containing an Anderson core capped on each of its six edges by an additional metal ion. Crystallographic details for all complexes are given in Tables S1 and S2, with pertinent bond lengths and angles provided in Tables 1-3.

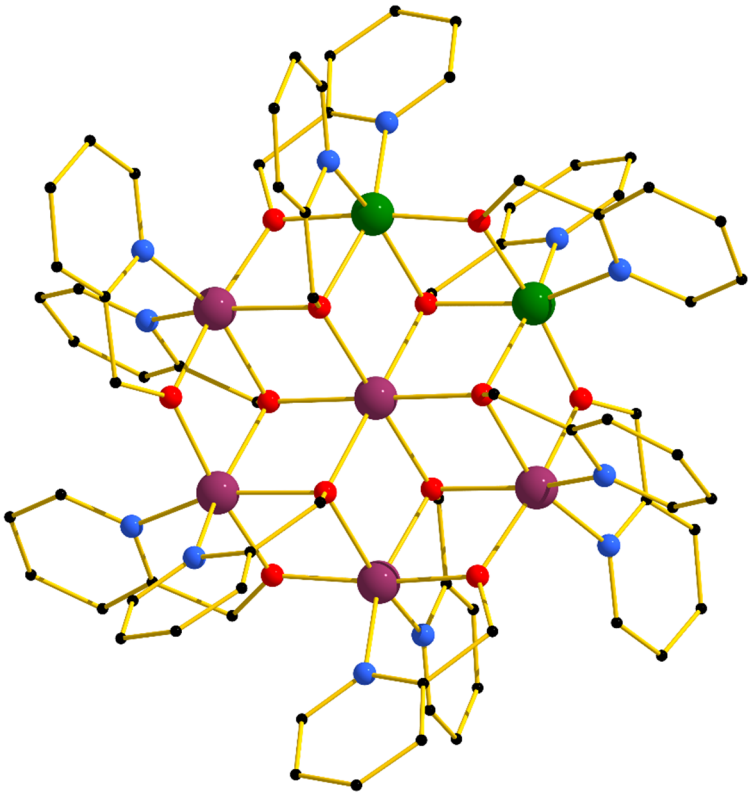

Figure 2. Molecular structure of the 1,2-isomer of the cation of compound **3**. Colour code: Cr = dark green, Mn = dark pink, O = red, N = light blue, C = black. H-atoms, perchlorate counter anions and solvent molecules of crystallisation are omitted for clarity.

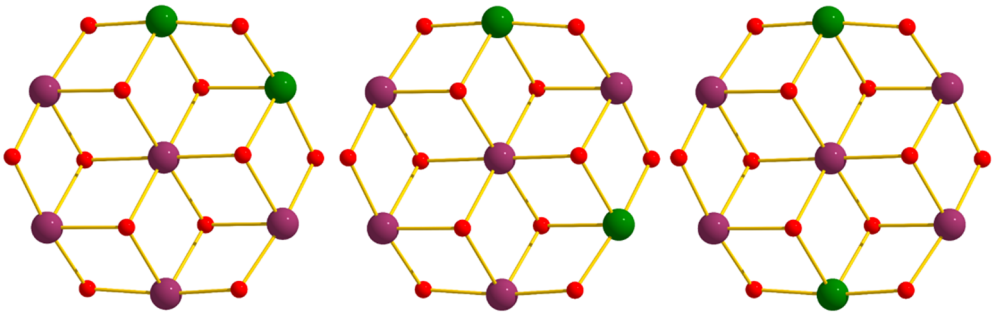

Figure 3. Schematic representation showing the three isomers for compound **3**: 1,2 (left), 1,3 (centre) and 1,4 (right).

We begin with a generic description of complexes **1**-**5**. Complexes **1**-**3** and **5** are isostructural, crystallising in the trigonal space group $R\bar{3}$ with the asymmetric unit (ASU) containing only the central metal ion, one outer metal ion, two hmp^- ligands and two ClO_4^- anions. The structure (Figures 2-3) is that of a centred metal hexagon in which the two M^{III} ions are disordered around the outer $[M_6]$ wheel. There are therefore two distinct metal sites in the $[M^{III}_2M^{II}_5]$ cluster, the central metal ion is always an M^{II} ion (Co (**1**, **5**), Fe (**2**), Mn (**3**)), which is bridged to the outer metal ions by six symmetry equivalent μ_3-OR groups from six hmp^- ligands. The central ion thus has a symmetry imposed, rigidly octahedral (O_h) $[M^{II}O_6]$ coordination sphere. The outer metal ions are all also symmetry equivalent, crystallographic disorder resulting in the M^{III} ions being equally distributed around all six positions, each with a 2/3 M^{II} - 1/3 M^{III} occupancy, with an average charge of +2.33. This was modelled as a 5:2 substitutional disorder ratio of metal centres by splitting the unique site into two separate parts with identical, constrained co-ordinates and anisotropic displacement parameters, and by fixing the occupancies such that they sum to give a 5:2 ratio of M^{II} to M^{III}. The disorder gives three distinct structural isomers with the M^{III} ions occupying outer ring positions 1,2 1,3 or 1,4 in a ratio of 2:2:1 (Figure 3).

Around the ring, the metal ions are connected by one μ-OR (hmp^-) group on the 'outside' of the wheel and one μ_3-OR (hmp^-) group on the 'inside' of the wheel. Two terminally bonded N-atoms from the hmp^- ligands complete the octahedral coordination spheres on each metal ion. A total of twelve hmp^- ligands therefore 'frame' the metal-oxygen core, six sitting above and six sitting below the metal ion plane. Charge balance is maintained through the presence of four ClO_4^- anions. Two sit one above / one below the plane of the metal core with their O-atoms closely associated to the three methylene groups of the hmp^- ligands, with Cl-O···H(CH_2) distances of approximately 2.6 Å. These interactions occur between cations lying above and below the ClO_4^- ion creating offset cation-anion columns down the *c*-axis of the unit cell. The remaining two ClO_4^- anions sit parallel to the plane of the cage, with analogous inter-molecular cation-anion interactions creating H-bonded sheets in the *ab* plane. The overall result is an aesthetically pleasing topology reminiscent of a hexagonal close packed (hcp) array of cages viewed down the *c*-axis (Figure S1).

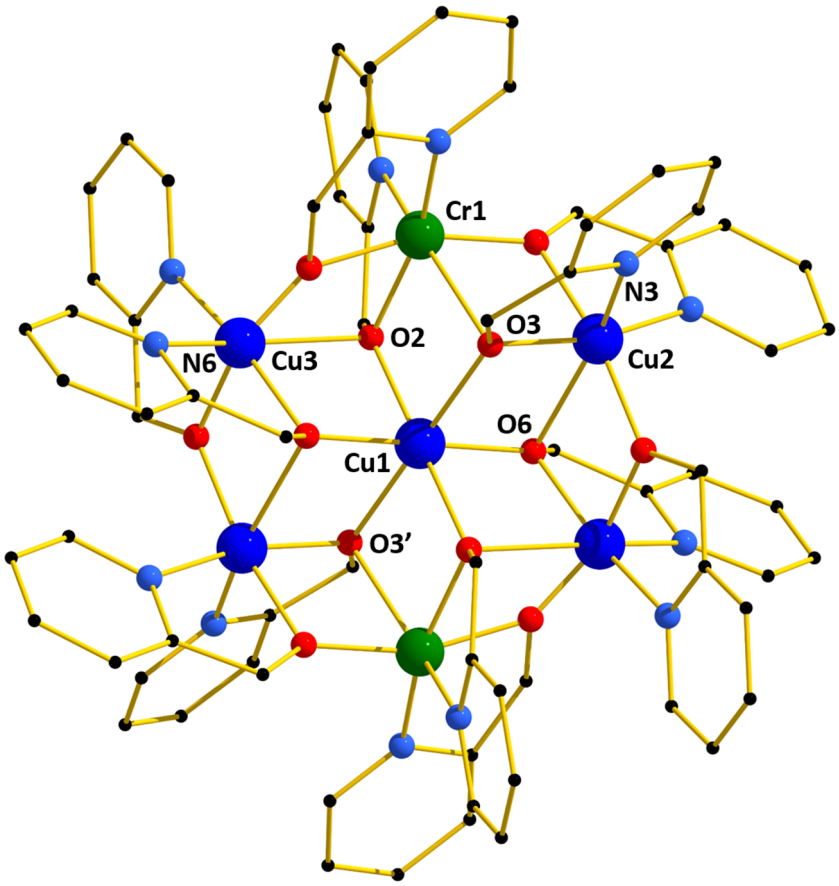

Figure 4. Molecular structure of the cation of compound **4**. Colour code: Cr = green, Cu = dark blue, O = red, N = light blue, C = black. H-atoms, counter anions and solvent molecules omitted for clarity.

Compound **4** (Figure 5) crystallises in the monoclinic space group *I*2/a, with half the molecular formula in the ASU. The structure is analogous to that seen for **1**-**3** and **5** but with the important exception that the two Cr^{III} sites in the outer wheel are now not disordered, instead being localised in the 1,4 positions, *i.e. trans* to each other. The reason for this, and the lowering of crystallographic symmetry, is not clear but may be associated with the presence of Jahn-Teller (JT) distortions at the four peripheral Cu^{II} sites (Cu2-N3 = 2.032 Å; Cu2-O6 = 2.402 Å; Cu3-N6 = 2.080 Å; Cu3-O2 = 2.345 Å), and at the central Cu^{II} site (Cu1-O3/O3' = 2.213 Å). Charge balance is maintained through the presence of two ClO_4^- and two NO_3^- anions. The cation-anion interactions are largely similar to that seen above, with the molecules forming layers in the *ab* plane, with the NO_3^- anions lying between the planes and the ClO_4^- anions lying within the planes. However in this case the cations are not off-set, instead they sit directly above/below nearest neighbours along the *c*-axis of the unit cell (Figure S2-S3).

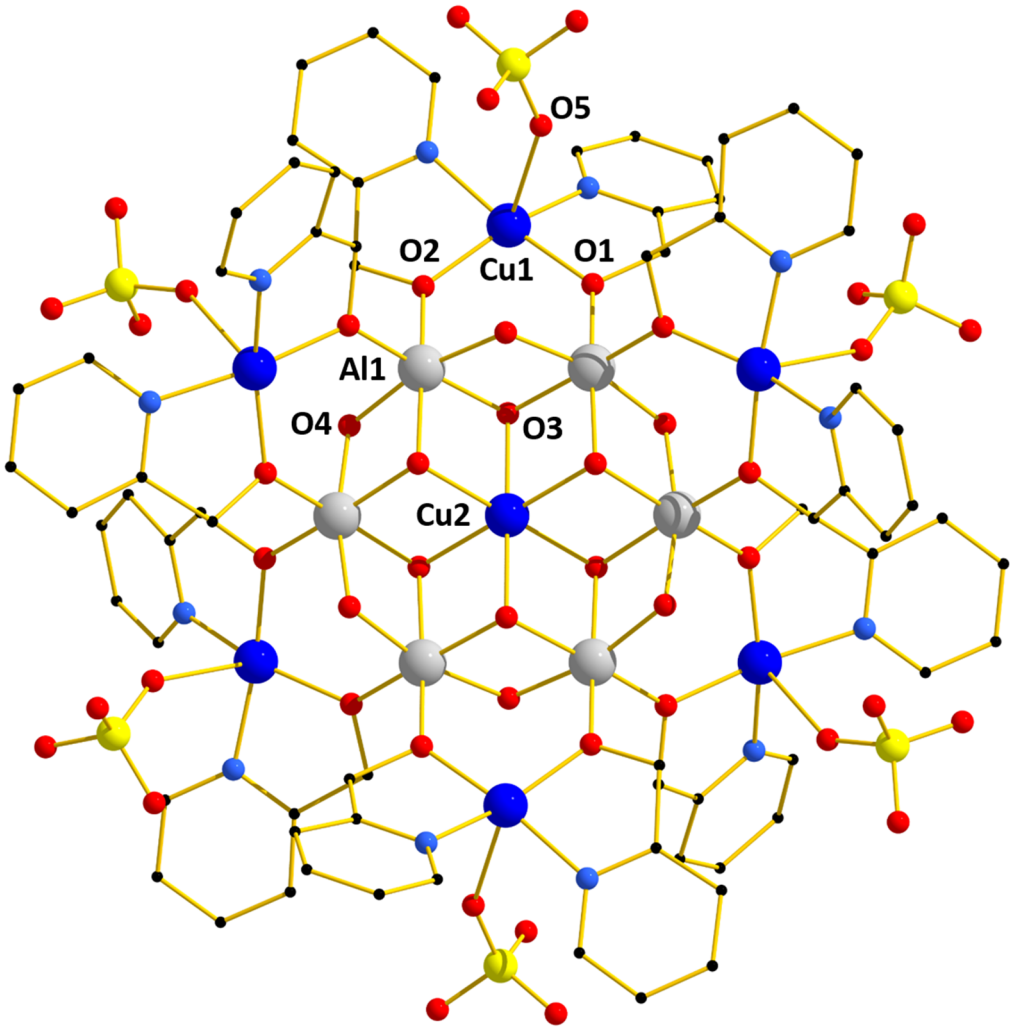

Figure 5. Molecular structure of the cation of complex **6**. Colour code: Al = silver, Cu = dark blue, O = red, N = light blue, C = black, Cl = yellow. H atoms and counter ions omitted for clarity.

Complex **6** crystallises in the trigonal space group $R\bar{3}$, with the ASU containing the central Cu^{II} ion (Cu2), one Al^{III} ion, one outer Cu^{II} ion (Cu1), two OH^- ions (O3, O4), two hmp^- ligands, one ClO_4^- anion and 1/3 of an NO_3^- anion (Figure 4b). The central core contains an Anderson-like $[Cu^{II}Al^{III}_6]$ wheel with an octahedral Cu^{II} ion (Cu2-O3 = 2.043Å) in the central position bridged to a ring of six Al^{III} ions through six μ_3-OH^- ions. O_h symmetry is imposed on Cu2 as it sits on a special position with a 3-fold axis and an inversion centre. The Al^{III} ions are further bridged to each other *via* six μ-OH^- ions (O4), and to edge-capping Cu^{II} ions (Cu1) through the μ-hmp^- ligands. The Al^{III} ions are thus in octahedral geometries with $[AlO_6]$ coordination spheres, while the peripheral Cu^{II} ions are square-based pyramidal with $[CuN_2O_3]$ coordination spheres, the fifth site being occupied by a ClO_4^- ion (Cu1-O5 = 2.637 Å). When

viewed parallel to the central Anderson motif, it is clear that the metallic skeleton is not fully planar, with the six peripheral Cu^{II} ions (Cu1) sitting alternately above and below the plane (Figure 6). As these are chelated by the hmp^- ligands the latter also sit (six) above and (six) below the [$CuAl_6$] moiety. The packing of the molecules of **6** in the crystal (Figures S4-S5) is akin to that seen for complexes **1**-**3** and **5**, with offset columns of cations along the *c*-axis, the charge balancing NO_3^- counter ions lying between the sheets of cations present in the *ab* plane. Nearest inter-cluster contacts exist between aromatic rings on neighbouring molecules with C(Ar)-C(Ar) separations of ~3.4 Å, C(Ar)-H(CAr) of ~2.8 Å and C(Ar)-O(ClO_4^-) of ~3 Å.

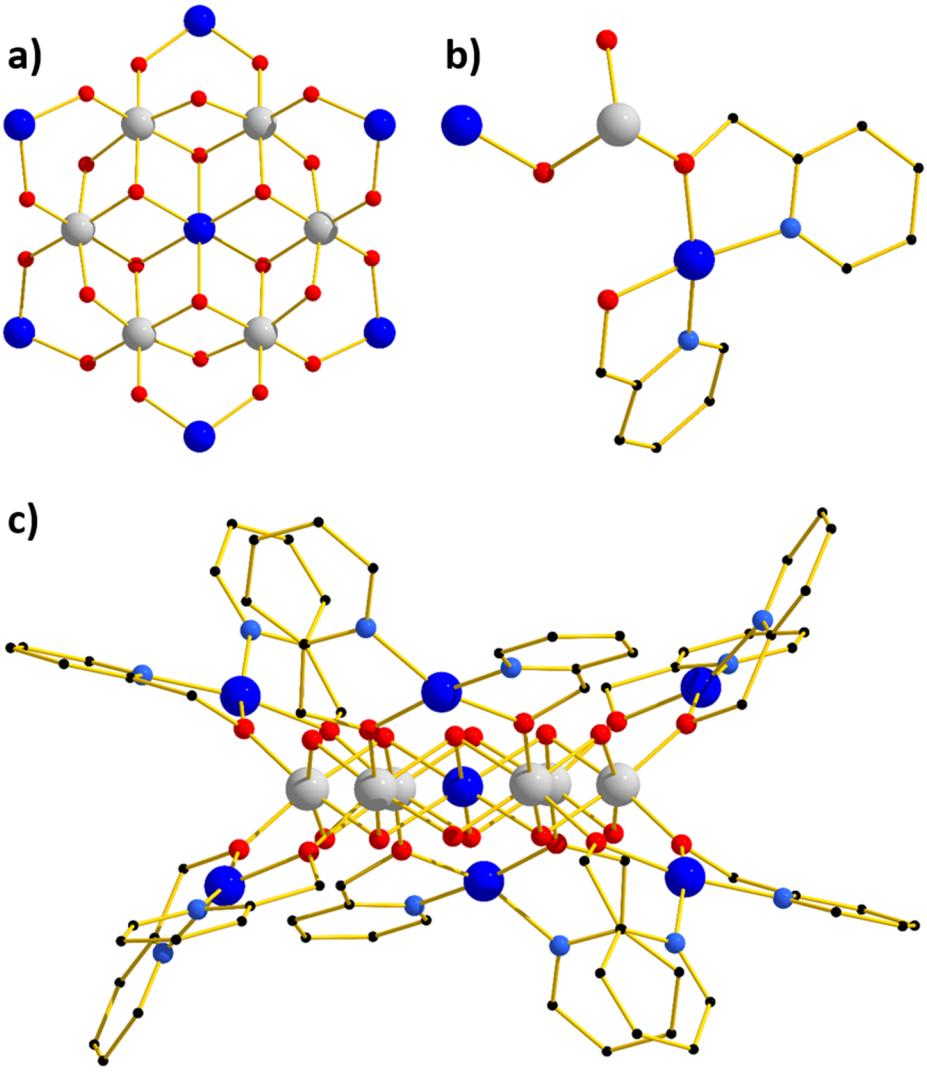

Figure 6. a) Metal-oxygen core of 6; b) ASU; c) side view highlighting the non-planarity of the outer Cu ions and associated chelating hmp- ligands. H-atoms, counter anions and solvent molecules of crystallisation omitted for clarity.

Table 1. Pertinent structural parameters for the $M_{central}$-M_{outer} di-alkoxo bridge in **1**-**5**. r = M-O bond length, ϕ = M-O-M bridging angle.

Compound	M-M [Å]	r [Å]	ϕ [°]
1	3.148	2.059-2.151	95.40-98.23
2	3.182	2.126-2.162	95.80-98.70
3	3.236	2.108-2.170	96.60-98.48
4	3.156-3.188	2.067-2.213	88.59-102.89
5	3.133	2.036-2.133	95.49-98.47

Table 2. Pertinent structural parameters for the M_{outer}-M_{outer} di-alkoxo bridge in **1**-**5**. r = M-O bond length, ϕ = M-O-M bridging angle.

Compound	M-M [Å]	r [Å]	ϕ [°]
1	3.156	1.987-2.151	97.09-104.73
2	3.191	1.981-2.162	97.92-107.47
3	3.245	1.974-2.177	98.67-102.73
4	3.163-3.216	1.571-2.402	91.70-144.85
5	3.141	1.956-2.133	97.77-105.81

Table 3. Pertinent structural parameters for the di-alkoxo bridges in compound **6**. r = M-O bond length, ϕ = M-O-M bridging angle.

Compound	M-M [Å]	r [Å]	ϕ [°]
$Cu_{central}$-Al_{ring}	2.984	1.943-2.043	96.76, 96.91
Al_{ring}-Al_{ring}	2.985	1.870-1.948	100.18, 105.73
Al_{ring}-Cu_{outer}	3.447, 3.451	1.866-1.945	129.77, 129.89

Magnetometry

Dc magnetic susceptibility (χ_M) measurements were carried out on powdered polycrystalline samples of compounds **1**-**6** in a B = 0.1 T applied magnetic field over the temperature range T = 2-300 K, and are plotted as the $\chi_M T$ product versus T in Figures 7 -8.

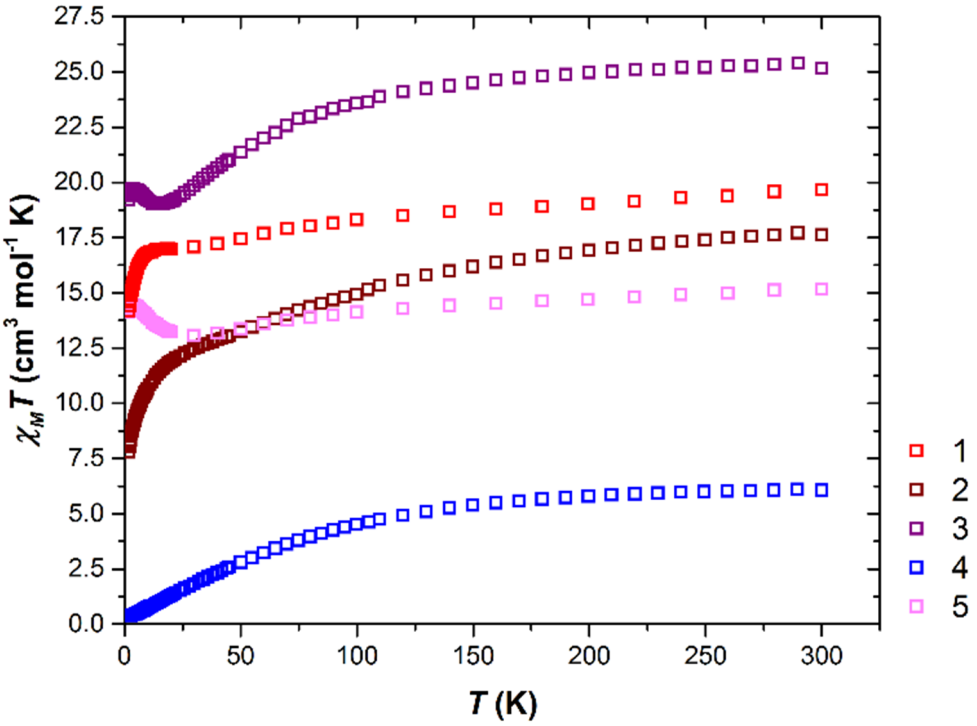

Figure 7. Plot of the $\chi_M T$ product versus T for complexes **1**-**5** in an applied field, B = 0.1 T.

For complexes **1**-**5** the experimental room temperature values of $\chi_M T$ are close to the Curie constants expected for five and two non-interacting M^{II} and M^{III} ions, respectively; **1**: 19.6 cm^3 K mol^{-1} (expected 16.2 cm^3 K mol^{-1}, g_{Cr} = 2.00, g_{Co} = 2.30); **2**: 17.7 cm^3 K mol^{-1} (expected 18.2 cm^3 K mol^{-1}, g_{Cr} =2.00, g_{Fe} = 2.20); **3**: 25.4 cm^3 K mol^{-1} (expected 25.6 cm^3 K mol^{-1}, g_{Cr} = g_{Mn} = 2.00); **4**: 6.1 cm^3 K mol^{-1} (expected 6.0 cm^3 K mol^{-1}, g_{Cr} = 2.00, g_{Cu} = 2.20); **5**: 13.7 (expected 12.4 cm^3 K mol^{-1}, g_{Cr} = 2.00, g_{Co} = 2.30). The temperature dependence of $\chi_M T$ for all five complexes down to approximately $T \approx 25$ K is rather similar, all decreasing slowly with decreasing temperature. For complex **1** the value of $\chi_M T$ then plateaus at a value of 17.0 cm^3 K mol^{-1}, before decreasing to a value of 14.2 cm^3 K mol^{-1} at 2 K. For complexes **3** and **5** the value of $\chi_M T$ increases to maximum values of 19.7 and 14.4 cm^3 k mol^{-1}, respectively. For complexes **2** and **4** the value of $\chi_M T$ continues to decrease, reaching T = 2 K values of 7.8 and 0.5 cm^3 K mol^{-1}, respectively. The behaviour in each case is therefore consistent with the presence of competing exchange interactions, as observed and quantified for the structurally analogous $[Cr_2Ni_5(hmp)_{12}]^{4+}$ family of complexes.[20] The positional disorder of the Cr^{III} ions and resulting different isomers, the large number of different exchange interactions and, in the case of complexes, **1**, **2**, **5**, the zero-field splitting effects of the M^{II} ions precludes any

detailed/quantitative analysis of the susceptibility data. Magnetisation (*M*) versus field data, collected for **1**-**5** in the *T* = 2-7 K and *B* = 0.5-7 T temperature and field ranges (Figures S6-S10) is consistent with this picture, in each case *M* rises rapidly with increasing *B* without reaching saturation.

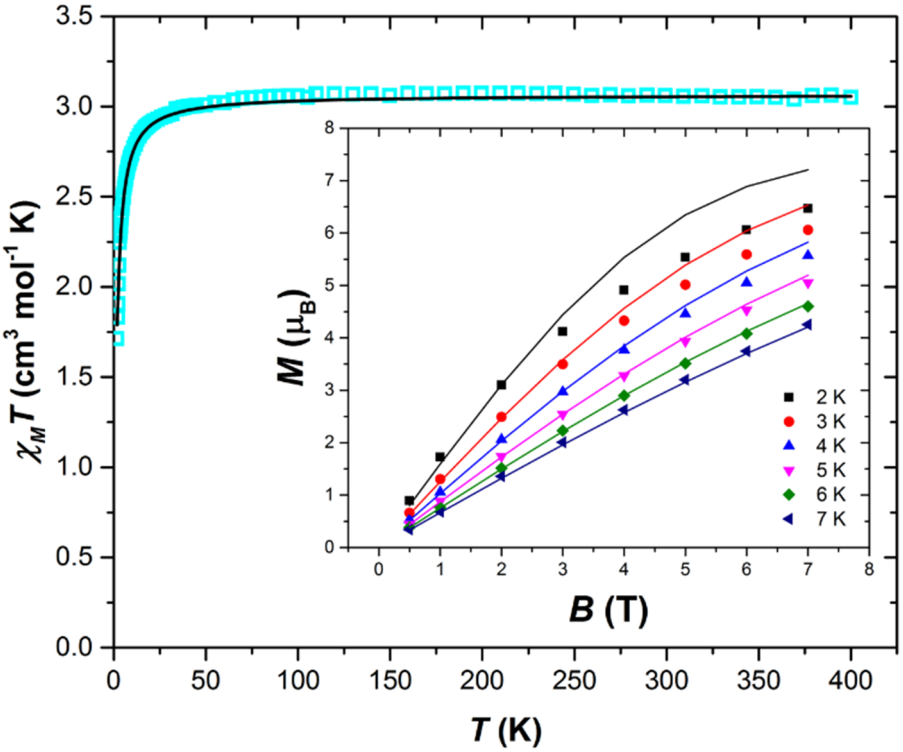

Figure 8. Plot of the $\chi_M T$ product versus *T* for complex **6** in an applied field, *B* = 0.1 T. The solid black line is a fit of the experimental data. Inset: Plot of the magnetisation (*M*) versus field (*B*) data for complex **6** in the indicated field and temperature ranges. The solid lines are fits of the experimental data.

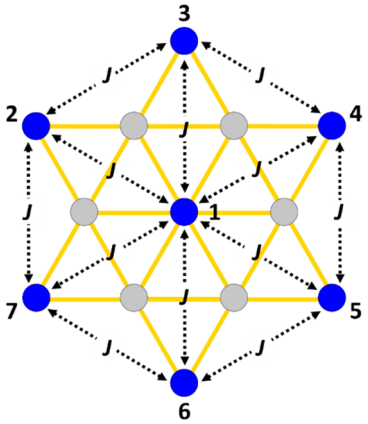

Figure 9. Coupling scheme for complex **6**, due to symmetry there are only two unique exchange pathways – $Cu_{central}$-Cu_{outer} and Cu_{outer}-Cu_{outer}, which are very similar and for the purpose of the fit we assume to be equal.

The dc susceptibility and magnetisation data for complex **6** is shown in Figure 8. The high temperature $\chi_M T$ value of 3.06 cm^3 K mol^{-1} is close to that expected for seven non-interacting (s = ½) Cu^{II} ions with g = 2.20 (3.2 cm^3 K mol^{-1}). This value remains constant in the T = 400 - 25 K temperature regime, before falling to a value of 1.7 cm^3 K mol^{-1} at T = 2 K. This is consistent with the presence of very weak antiferromagnetic exchange interactions between the Cu^{II} ions, as would be expected from the presence of a 3-atom (Cu-O-Al-O-Cu) bridge between neighbouring paramagnetic sites. Variable field susceptibility measurements confirmed the intramolecular nature of the exchange (Figure S11). The $\chi_M T$ and magnetisation data were fitted simultaneously using isotropic spin-Hamiltonian (1), where the indices i and j refer to two interacting Cu^{II} ions, μ_B is the Bohr magneton, B is the applied magnetic field, g is the g-factor of the Cu^{II} ions (fixed as axial g-values g = 2.21 (parallel), 2.06 (perpendicular)), $\hat{S}$ is a spin operator and J is the isotropic exchange interaction. Based on the coupling scheme in Figure 9 and assuming all interactions to be equivalent the second part of the Hamiltonian becomes $-2J(S_1S_2 + S_1S_3 + S_1S_4 + S_1S_5 + S_1S_6 + S_1S_7 + S_2S_3 + S_3S_4 + S_4S_5 + S_5S_6 + S_6S_7 + S_7S_2)$. Using this model, the best fit parameter was found to be J = -0.47 cm^{-1}.

$$\hat{H} = \mu_B B \sum_i g_i \hat{S}_i - 2J \sum_{ij} \hat{S}_i \hat{S}_j \qquad (1)$$

5.4 Conclusions

The use of 2-pyridinemethanol in heterometallic 3d cluster chemistry has led to the isolation of a large family of complexes of general formula $[M^{III}_2M^{II}_5(hmp)_{12}]^{4+}$ where M^{III} = Cr, Al and M^{II} = Mn, Fe, Co, Ni, Cu, Zn. These complexes all conform to the Anderson structure type describing a centred hexagon, in which the two M^{III} ions are disordered around the outer wheel. The only exceptions are observed for M^{III} = Cr and M^{II} = Cu where the same structure type forms but with the M^{III} localised in the 1,4-position, and for M^{III} = Al and M^{II} = Cu where a structurally related, but larger tridecanuclear $[M^{III}_6M^{II}_7(hmp)_{12}]^{20+}$ species is formed. The Anderson type structures all display competing magnetic exchange interactions as one might expect from planar complexes containing triangular building blocks, while the Cu^{II} ions $[M^{III}_6M^{II}_7(hmp)_{12}]^{20+}$ are weakly antiferromagnetic coupled through 3-atom Cu-O-Al-O-Cu moieties. The modular assembly of large heterometallic cages is extremely rare, interestingly

the only other example known is a family of Cr-based wheels which also show positional disorder at the metal sites.[24] Building larger molecular cages based on the Anderson core in '2D' such that they resemble larger and larger fragments of the kagomé lattice is of fundamental interest to chemists and physicists studying the unusual physical phenomena resulting from spin frustration.[25] The [M_{13}] structure type reported here is commonly observed in Al and Ga chemistry,[26-28] but previous examples in 3d chemistry are limited to just Ni and Co.[16,29]

5.5 Supplementary information

Table S1. Crystallographic information for compounds **1**-**4**.

Compound	**1**	**2**	**3**	**4**
Formula	$C_{81}H_{108}Cl_4Co_5Cr_2N_{12}O_{37}$	$C_{81}H_{108}Cl_4Cr_2Fe_5N_{12}O_{37}$	$C_{82}H_{112}Cl_4Cr_2Mn_5N_{12}O_{38}$	$C_{88}H_{136}Cl_2Cr_2Cu_5N_{14}O_{42}$
$D_{calc.}$/ g cm^{-3}	1.657	1.682	1.672	1.859
μ/mm^{-1}	1.272	9.765	8.898	4.629
FW/g mol^{-1}	2382.24	2366.84	2394.33	2554.70
Colour	dark pink	pale brown	pale purple	light purple
Shape	block	plate	plate	plate
Size/mm^3	0.32×0.11×0.10	0.14×0.10×0.03	0.20×0.16×0.02	0.22×0.16×0.03
T/K	120.0	120.0	120.0	120
Crystal System	trigonal	trigonal	trigonal	monoclinic
Space Group	R-3	R-3	R-3	*I*2/*a*
a/Å	14.7268(2)	14.6087(3)	14.7045(6)	14.5052(12)
b/Å	14.7268(2)	14.6087(3)	14.7045(6)	25.0735(19)
c/Å	38.1319(8)	37.9381(19)	38.106(5)	25.095(5)
α/°	90	90	90	90
β/°	90	90	90	90.268(13)
γ/°	120	120	120	90
V/Å^3	7162.0(2)	7011.8(5)	7135.4(11)	9127(2)
Z (*Z*')	3 (0.16667)	3 (0.16667)	3 (0.16667)	4 (0.5)
Wavelength/Å	0.71073	1.54184	1.54184	1.54184
Radiation type	MoK_α	CuK_α	CuK_α	CuK_α
Θ_{min}/° - Θ_{max}/°	3.112 – 29.648	3.495 – 76.728	3.479 – 50.499	3.520 – 50.436
Measured Refl.	43856	32839	17837	10864
Independent Refl.	4234	3272	1673	10864
Reflections Used	3674	2673	1482	5280
R_{int}	0.0503	0.0968	0.0736	.
Parameters	196	199	260	205
Restraints	18	37	137	28
Largest Peak	0.428	1.455	0.633	3.431
Deepest Hole	-0.733	-1.027	-0.432	-1.655
GooF	1.069	1.052	1.074	1.558
wR_2 (all data) (wR_2)	0.0914 (0.0883)	0.2197 (0.2052)	0.2110 (0.2045)	0.4931 (0.4601)
R_1 (all data) (R_1)	0.0521 (0.0425)	0.0822 (0.0712)	0.0797 (0.0737)	0.2423 (0.1868)
CCDC Number	1855223	1855227	1855222	1855225

Table S2. Crystallographic information for compounds **5** and **6**.

Compound	**5**	**6**
Formula	$C_{81}H_{108}Al_2Cl_4Co_5N_{12}O_{37}$	$C_{93}H_{168}Al_6Cl_6Cu_7N_{14}O_{75}$
$D_{calc.}$/ g cm^{-3}	1.637	1.468
μ/mm^{-1}	1.084	1.151
FW/g mol^{-1}	2332.20	3501.76
Colour	pale brown	dark blue
Shape	plate	block
Size/mm^3	0.27×0.07×0.03	0.32×0.24×0.17
T/K	120.0	120.01(10)
Crystal System	trigonal	trigonal
Space Group	R-3	*R*-3
a/Å	14.6812(5)	27.8468(6)
b/Å	14.6812(5)	27.8468(6)
c/Å	38.0235(14)	17.6945(7)
α/°	90	90
β/°	90	90
γ/°	120	120
V/Å^3	7097.5(5)	11882.8(7)
Z (*Z'*)	3 (0.16667)	3 (0.16667)
Wavelength/Å	0.71073	0.71073
Radiation type	MoK_α	MoK_α
Θ_{min}/° - Θ_{max}/°	3.121 – 25.340	2.856 – 25.345
Measured Refl.	38106	49850
Independent Refl.	2893	4843
Reflections Used	2560	4209
R_{int}	0.0900	0.0538
Parameters	196	274
Restraints	18	88
Largest Peak	0.728	1.219
Deepest Hole	-0.982	-0.604
GooF	1.136	1.055
wR_2 (all data) (wR_2)	0.1339 (0.1289)	0.1697 (0.1635)
R_1 (all data) (R_1)	0.0726 (0.0623)	0.0642 (0.0561)
CCDC Number	1855224	1855226

For Figures S1-S11 please refer to the "Chapter 5 SI" file on the memory stick supplied with the thesis.

5.6 References

1. O. Kahn, *Chem. Phys. Lett.*, 1997, **265**, 109-114.
2. B. Sarkar, M. S. Ray, Y.-Z. Li, Y. Song, A. Figuerola, E. Ruiz, J. Cirera, J. Cano and A. Ghosh, *Chem. Eur. J*., 2007, **13**, 9297-9309.
3. R. Inglis, S. M. Taylor, L. F. Jones, G. S. Papaefstathiou, S. P. Perlepes, S. Datta, S. Hill, W. Wernsdorfer and E. K. Brechin, *Dalton Trans.*, 2009, **0**, 9157-9168.
4. S. A. Magee, S. Sproules, A.-L. Barra, G. A. Timco, N. F. Chilton, D. Collison, R. E. P. Winpenny and E. J. L. McInnes, *Angew. Chem. Int. Ed*., 2014, **53**, 5310-5313.
5. V. O. Garlea, S. E. Nagler, J. L. Zarestky, C. Stassis, D. Vaknin, P. Kögerler, D. F. McMorrow, C. Niedermayer, D. A. Tennant, B. Lake, Y. Qiu, M. Exler, J. Schnack, and M. Luban, *Phys. Rev. B*, 2006, **73**, 024414.
6. J. Schnack, *Dalton Trans*., 2010, **39**, 4677-4686.
7. R. D. Cannon and R. P. White, *Prog. Inorg. Chem*., 2007, **36**, 195-298.
8. T. Cauchy, E. Ruiz and S. Alvarez, *J. Am. Chem. Soc.*, 2006, **128**, 15722-15727.
9. K. R. Vignesh, S. K. Langley, C. J. Gartshore, B. Moubaraki, K. S. Murray and G. Rajaraman, *Inorg. Chem.*, 2017, **56**, 1932-1949.
10. G. Rajaraman, M. Murugesu, E. C. Sañudo, M. Soler, W. Wernsdorfer, M. Helliwell, C. Muryn, J. Raftery, S. J. Teat, G. Christou and E. K. Brechin, *J. Am. Chem. Soc.*, 2004, **126**, 15445-15457.
11. J. J. Henkelis, L. F. Jones, M. P. de Miranda, C. A. Kilner and M. A. Halcrow, *Inorg. Chem*., 2010, **49**, 11127-11132.
12. R. W. Saalfrank, R. Prakash, H. Maid, F. Hampel, F. W. Heinemann, A. X. Trautwein and L. H. Böttger, *Chem. Eur. J.*, 2006, **12**, 2428-2433.
13. M. Tesmer, B. Müller and H. Vahrenkamp, *Chem. Commun.*, 1997, 721-722.
14. H. Oshio, N. Hoshino, T. Ito, M. Nakano, F. Renz and P. Gütlich, *Angew. Chem. Int. Ed.*, 2003, **42**, 223.
15. G. Aromí, S. Parsons, W. Wernsdorfer, E. K. Brechin and E. J. L. McInnes, *Chem. Commun.*, 2005, 5038-5040.
16. J.-D. Leng, S.-K. Xing, R. Herchel, J.-L. Liu and M.-L. Tong, *Inorg. Chem.*, 2014, **53**, 5458-5466; Y. Peng, C.-B. Tian, H.-B. Zhang, Z.-H. Li, P. Lin and S.-W. Du, *Dalton Trans.*, 2012, **41**, 4740-4743.
17. A. K. Powell, S. L. Heath, D. Gatteschi, L. Pardi, R. Sessoli, G. Spina, F. Delgiallo and F. Pieralli, *J. Am. Chem. Soc.*, 1995, **117**, 2491-2502.
18. Y.-K. Deng, H.-F. Su, J.-H. Xu, W.-G. Wang, M. Kurmoo, S.-C. Lin, Y.-Z. Tan, J. Jia, D. Sun and L.-S. Zheng, *J. Am. Chem. Soc*., 2016, **138**, 1328-1334; I. A. M. Pohl, L. G. Westin and M. Kritikos, 2001, **7**, 3438-3445.
19. E. K. Brechin, S. G. Harris, A. Harrison, S. Parsons, A. Gavin Whittaker and R. E. P. Winpenny, *Chem. Commun*., 1997, 653-654.
20. H. W. L. Fraser, G. S. Nichol, D. Uhrin, U. G. Nielsen, M. Evangelisti, J. Schnack and E. K. Brechin, *Dalton Trans.*, 2018, DOI: 10.1039/C8DT00685G.
21. G. M. Sheldrick, *Acta Crystallogr. Sect. C: Cryst. Struct. Commun*., 2015, **71**, 3-8.
22. O. V. Dolomanov, L. J. Bourhis, R. J. Gildea, J. A. K. Howard and H. Puschmann, *J. Appl. Crystallogr*., 2009, **42**, 339-341.
23. L. Palatinus and G. Chapuis, J. *Appl. Crystallogr*., 2007, **40**, 786-790.
24. E. J. McInnes, G. A. Timco, G. F. Whitehead and R. E. Winpenny, *Angew. Chem. Int. Ed.*, 2015, **54**, 14244-14269.
25. C. Schröder, H. Nojiri, J. Schnack, P. Hage, M. Luban and Paul Kögerler, *Phys. Rev. Lett*., 2005, **94**, 017205.

26. S. L. Heath, P. A. Jordan, I. D. Johnson, G. R. Moore, A. K. Powell and M. Helliwell, *J. Inorg. Biochem*., 1995, **59**, 785-794.
27. J. C. Goodwin, S. J. Teat and S. L. Heath, *Angew. Chem. Int. Ed*., 2004, **43**, 4037-4041.
28. M. K. Kamunde-Devonish, D. B. Fast, Z. L. Mensinger, J. T. Gatlin, L. N. Zakharov, M. R. Dolgos and D. W. Johnson, *Inorg. Chem*., 2015, 54, 3913-3920.
29. P. Yan, T. Chong-Bin, L. Yan-Hua, M. Nicola, L. Qi-Peng, Z. Hua-Bin, P. A. K. and D. Shao-Wu, *Eur. J. Inorg. Chem*., 2013, 5534-5540.
30. G. A. Bain and J. F. Berry, *J. Chem. Educ.*, 2008, **85**, 532.

CHAPTER 6:

VANADYL–BASED HETEROMETALLIC WHEELS

6.1 Introduction

Alongside its prominent role in polyoxometalate (POM) chemistry,[1] Vanadium has had significant impact in the field of molecule-based magnetism. For example, orthogonal magnetic orbitals were exploited to reveal ferromagnetic exchange in a [($V^{IV}O$)-Cu^{II}] dimer,[2] the Prussian blue $V[Cr(CN)_6]_{0.86}$ was one of the initial examples of a coordination compound exhibiting room temperature magnetic order,[3] Single-Molecule-Magnet (SMM) behaviour was observed in a [V^{III}_4] butterfly,[4] [V_{30}] and [V_{15}] POMs have been widely studied to examine the influence of geometrical spin-frustration and antisymmetric exchange,[5] and most recently monometallic V^{IV} compounds such as [$(Bu_4N)_2[V(C_8S_8)_3]$] and [VOPc] have been touted as excellent candidates for electron-spin based qubits.[6]

Heterometallic 3d cages containing vanadium are however rather rare, and indeed those containing nickel or cobalt are relatively scarce. A search of the CCDC database reveals only eight (Ni) and sixteen (Co) unique structure types with a nuclearity of four or more. When the nuclearity is increased to seven or more metal ions this number reduces to just four (Ni) and five (Co) examples.[7] There is just one example that possesses an Anderson-type structure, the complex $[MV^{IV}_6O_6\{(OCH_2CH_2)_2N(CH_2CH_2OH)\}_6]X$ where the six vanadyl moieties form a wheel that 'encapsulates' a variety of *s*- and 3*d* metal ions (M).[8] Herein, we report the syntheses, structures, magnetic and spectroscopic properties of two new members of this family, namely the complexes $[(V^{IV}O)_2M^{II}_5(hmp)_{10}Cl_2](ClO_4)_2 \cdot 2MeOH$ (where M^{II} = Ni (**1**) or Co (**2**)).

5.2 Experimental

Experimental procedures

All chemicals were procured from commercial suppliers and used as received (reagent grade). Elemental analyses for C, H, N, Ni, V and Co were performed by Medac Ltd.

Synthesis of $[(VO)_2Ni_5(hmp)_{10}Cl_2](ClO_4)_2 \cdot 2MeOH$ (1)

$Ni(ClO_4)_2 \cdot 6H_2O$ (0.366 g, 1 mmol) and VCl_3 (0.079 g, 0.5 mmol) were dissolved In MeOH (24 ml) with NaOMe (0.162 g, 3 mmol) to give a green solution. Upon full dissolution, hmpH (0.285 ml, 3 mmol) was added dropwise resulting in a darkening of the solution colour. The

reaction was left overnight with continuous stirring. 10 ml samples of the resulting dark green solution were heated in Teflon-lined autoclaves at 140°C for 24 hours. After slowly cooling to room temperature the reaction vessels were allowed to sit undisturbed for 24 hours yielding dark green, triangular prism-shaped crystals suitable for X-ray diffraction. Yield 0.126 g (34.2% by Ni weight). Anal. Calcd (%) for $C_{62}H_{68}Cl_4N_{10}Ni_5O_{22}V_2$: C 40.42, H 3.72, N 7.60, Ni 15.93, V 5.53; found: C 39.24, H 3.42, N 7.34, Ni 16.00, V 5.75.

Synthesis of $[(VO)_2Co_5(hmp)_{10}Cl_2](ClO_4)_2 \cdot 2MeOH$ (2)

$Co(ClO_4)_2 \cdot 6H_2O$ (0.366 g, 1 mmol) and VCl_3 (0.079 g, 0.5 mmol) were dissolved in MeOH (24 ml) with NaOMe (0.162 g, 3 mmol) to give a red/orange solution. Upon full dissolution, hmpH (0.285 ml, 3 mmol) was added dropwise resulting in a darkening of the solution colour. The reaction was left overnight with continuous stirring. 12 ml samples of the resulting solution were heated in Teflon-lined autoclaves at 100°C for 12 hours. After slowly cooling to room temperature the reaction vessels were allowed to sit undisturbed for 24 hours yielding red, plate-shaped single crystals suitable for X-ray diffraction. Yield 0.130 g (35.3% by Co weight). Anal. Calcd (%) for $C_{62}H_{68}Cl_4N_{10}Co_5O_{22}V_2$: C 40.39, H 3.72, N 7.58, Co 15.98, V 5.53; found: C 40.02, H 3.51, N 7.56, Co 16.11, V 5.76.

Crystallographic details

Diffraction data for samples **1**-**2** were collected using a Rigaku Oxford Diffraction SuperNova diffractometers with MoK_α radiation (details in Table S1). An Oxford Cryosystems Cryostream 700+ low temperature device was used to maintain a crystal temperature of 120.0 K for all experiments. The structures were solved using ShelXT and refined with version ShelXL interfaced through Olex2.[15, 16] All non-hydrogen atoms were refined using anisotropic displacement parameters. H atoms were placed in calculated positions geometrically and refined using the riding model. CCDC: 1847956-1847957.

Magnetic data collection

Magnetic susceptibility and magnetisation measurements in the temperature range T = 1.8-300 K were performed on a Quantum Design MPMS XL SQUID magnetometer equipped with

a 5 T dc magnet on finely ground samples of **1**-**2** in the field range, B = 0.1-5.0 T. The observed paramagnetic susceptibilities were corrected for diamagnetic contributions using Pascal's constants.[18]

4.3 Results and discussion

Structural description

The reaction of $M^{II}(ClO_4)_2 \cdot 6H_2O$ (M = Ni, Co) with VCl_3 and hmpH (2-(hydroxymethyl)pyridine) in a basic MeOH solution under solvothermal conditions produced dark green crystals of $[(VO)_2Ni_5(hmp)_{10}Cl_2](ClO_4)_4 \cdot 2MeOH$ (**1**) and red crystals of $[(VO)_2Co_5(hmp)_{10}Cl_2](ClO_4)_4 \cdot 2MeOH$ (**2**) in approximately 35% yield after 24 hours.‡ Both **1** and **2** crystallise in the monoclinic space group $P2_1/n$ (Table S1) with half the cationic cage, one perchlorate counter ion and one molecule of methanol in the asymmetric unit (ASU). The metallic skeleton describes a centred $[(V^{IV}O)_2M^{II}_5]$ wheel in which the vanadyl moieties (V1 and symmetry equivalent, s.e.) oppose each other on the outer $[V^{IV}_2M^{II}_4]$ rim, *i.e.* they occupy the 1,4-positions (Figure 1). The central M^{II} ion (M2) is bridged to each of the six outer ring metals by six μ_3-OR groups from six deprotonated hmp ligands. The four remaining hmp ligands each provide a μ-OR bridge on the exterior of the ring between one V^{IV} ion and one M^{II} ion. The two opposing Cl ions also μ-bridge in the external wheel, between M1 and M3 and s.e. All seven metal ions display distorted octahedral coordination geometries, with the vanadyl moiety showing a V=O bond length of 1.6096(12) and 1.621(4) Å for 1 and 2, respectively (Tables 1 and 2).

Table 1. Selected structural parameters for the bridging motifs between the metal ion pairs in compound **1**. These include: V-O bond length, M-O bond length, M-Cl bond length, M-O-M bond angle and M-Cl-M bond angle.

	V-O (Å)	M-O (Å)	M-Cl (Å)	M-O-M (°)	M-Cl-M (°)
V1/M1	1.969, 2.057	1.995, 2.094	-	95.93, 102.11	-
V1/M2	2.057, 2.177	2.094, 2.122	-	98.29, 101.24	-
V1/M3	2.014, 2.177	2.028, 2.090	-	96.81, 104.27	-
M1/M3	-	2.041, 2.081	2.405, 2.413	103.18	84.20
M1/M2	-	2.053-2.122	-	95.82, 98.33	-
M2/M3	-	2.041-2.094	-	97.40, 100.28	-

Table 2. Selected structural parameters for the bridging motifs between the metal ion pairs in compound **2**. These include: V-O bond length, M-O bond length, M-Cl bond length, M-O-M bond angle and M-Cl-M bond angle.

	V-O (Å)	M-O (Å)	M-Cl (Å)	M-O-M (°)	M-Cl-M (°)
V1/M1	1.969, 2.054	2.010, 2.133	-	96.05, 102.98	-
V1/M2	2.054, 2.180	2.115, 2.170	-	99.09, 101.33	-
V1/M3	2.013, 2.180	2.026, 2.126	-	96.68, 105.61	-
M1/M3	-	2.078, 2.108	2.422, 2.455	102.91	84.34
M1/M2	-	2.075-2.170	-	94.18, 97.78	-
M2/M3	-	2.075-2.126	-	97.17, 99.97	-

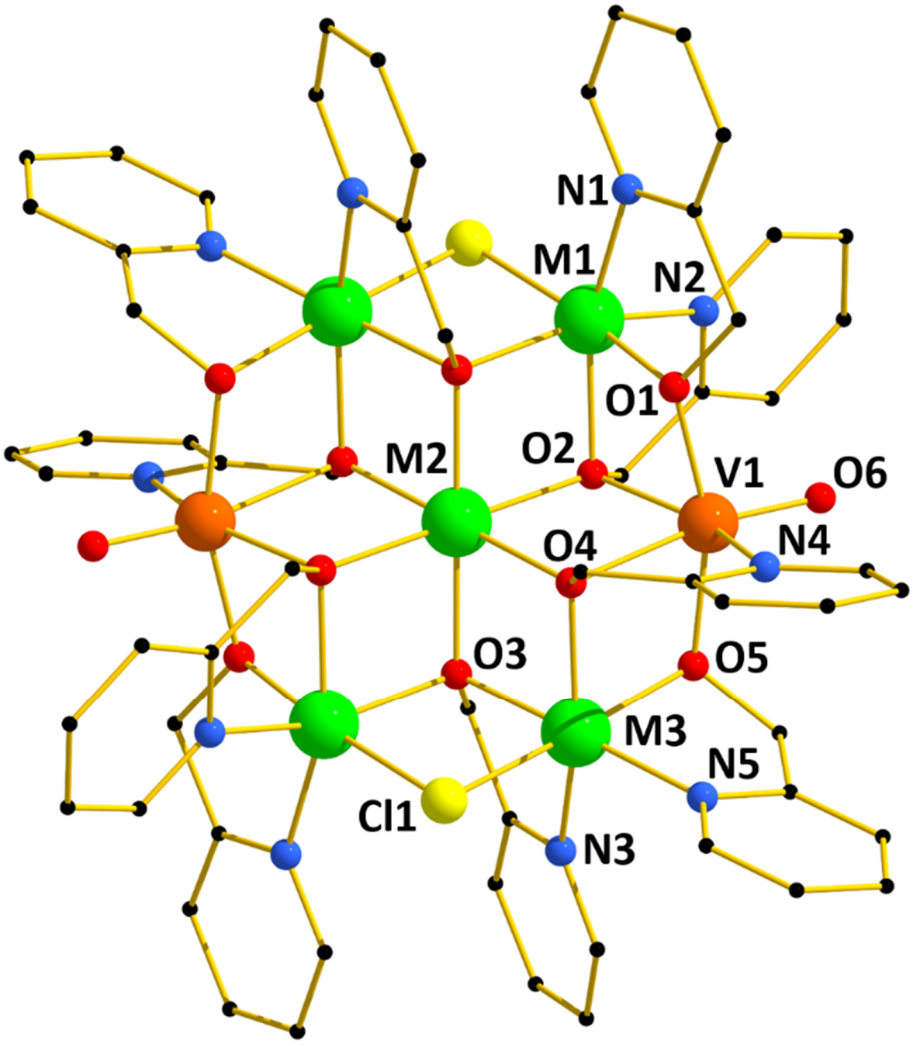

Figure 1. Molecular structure common to the cations in **1** and **2**. Colour code: V^{IV} = orange, M^{II} = green, Cl = yellow, O = red, N = light blue and C = black. H-atoms, perchlorate counter ions and solvent molecules of crystallisation are omitted for clarity.

The perchlorate anions and MeOH molecules of crystallisation H-bond to each other (O···O, ~2.8 Å), sitting in-between the planes of the cationic cages (Figure S1). The closest intermolecular contacts between cages exists between C(Ph) and H(C(Ph)) moieties with distances in the range ~2.3-2.8 Å, and between H(C(Ph)) and Cl units in the ring at ~2.9 Å. In the extended structure the molecules pack in columns down the *b* axis, with the columns arranged into rows with each neighbouring column composed of molecules which are eclipsed with respect to the adjacent column (Figure S2). Complexes **1** and **2** are structurally related to the $[M^{III}_2M^{II}_5(hmp)_{12}](ClO_4)_4$ (where M^{III} = Cr, Al; M^{II} = Ni, Zn) family of wheels we recently reported,[9] highlighting the apparent stability of the wheel structure and the modular nature of the system whereby different metals in different oxidation states can be combined with the same ligand set to afford analogous species. Note that in the latter family of compounds the M^{III} ion is positionally disordered around the external wheel while the V^{IV} is not.

Magnetometry

Dc molar magnetic susceptibility (χ_M) measurements were carried out on powdered polycrystalline samples of compounds **1** and **2** in an applied magnetic field, B = 0.1 T, over the temperature range T = 2-300 K, and are plotted as the $\chi_M T$ product versus T in Figures 2 and 4. The two compounds show very different behaviour. For compound **1** (Figure 2) the room temperature (290 K) value of 7.6 cm^3 K mol^{-1} is considerably higher than that expected for five non-interacting Ni^{II} ions (s = 1) and two non-interacting V^{IV} ions (s = 1/2) (6.8 cm^3 K mol^{-1}, with g_{Ni} = 2.20 and g_V = 2.00). As the temperature falls the susceptibility falls very slightly before rising sharply at low temperatures to a 2 K value of 13.6 cm^3 K mol^{-1}. This is consistent with the presence of competing antiferromagnetic and ferromagnetic interactions and suggests a greater prevalence of the latter. Magnetisation measurements showed a rise in magnetisation towards saturation at approximately 9 μ_B (Figure 2 inset), this could be tentatively aligned to a ground state of between S = 4 and S = 5.

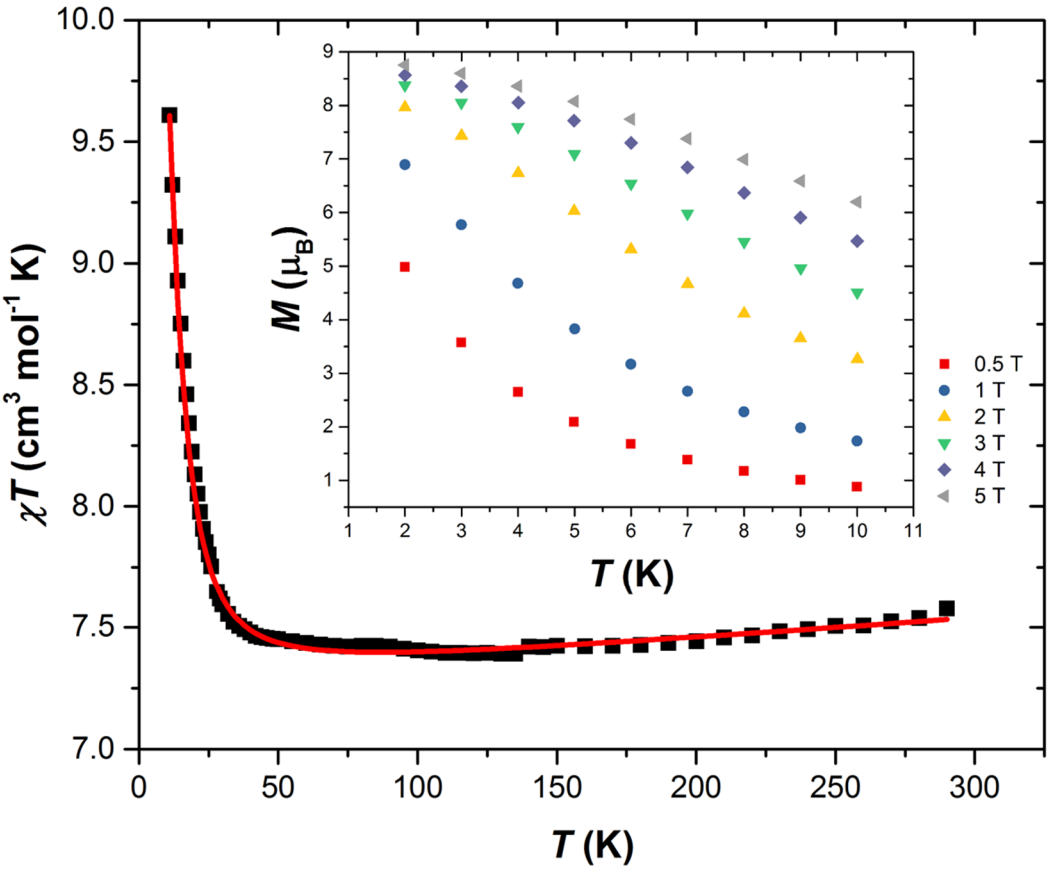

Figure 2. Plot of the $\chi_M T$ product versus T for compound **1** in an applied field, B = 0.1 T. The solid red line is a fit of the experimental data. Inset: Plot of the magnetisation (M) versus temperature (T) data for **1** in the indicated field and temperature ranges.

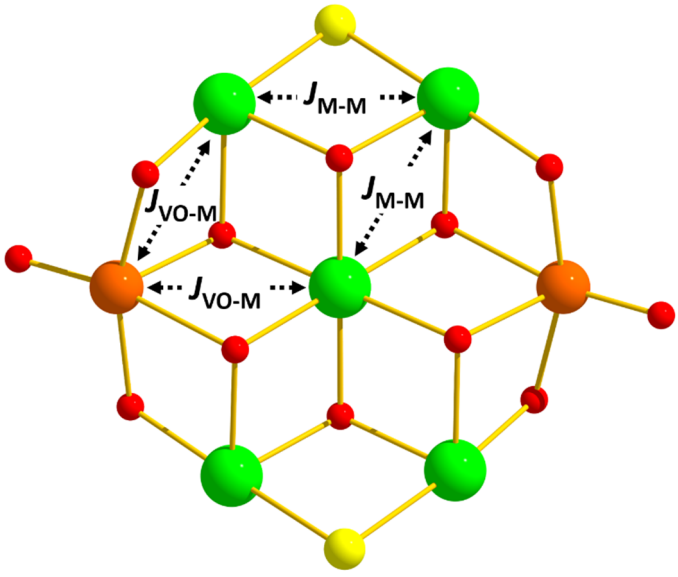

Figure 3. Structural representation of the coupling model for both compounds (green = M^{II} ions, orange = V^{IV} ions).

In the case of compound **2** (Figure 4), the room temperature (300 K) value of 8.7 cm^3 K mol^{-1} is much lower than that expected for five non-interacting Co^{II} ions (s = 3/2) and two non-interacting V^{IV} ions (s = 1/2) (13.1 cm^3 K mol^{-1}, with g_{Co} = 2.30 and g_V = 2.00). As the temperature falls the susceptibility slowly until 40 K when it shows a brief rise to a peak before falling again to a value of 6.3 cm^3 K mol^{-1} at 2 K. The initial decrease is consistent with the effect of the anisotropy of the Co^{II} ion and the peak suggests the presence of competing antiferromagnetic and ferromagnetic interactions and suggests a greater prevalence of the latter (similar to that seen in compound **1**) while the decrease at low temperature may be due to intermolecular interactions.

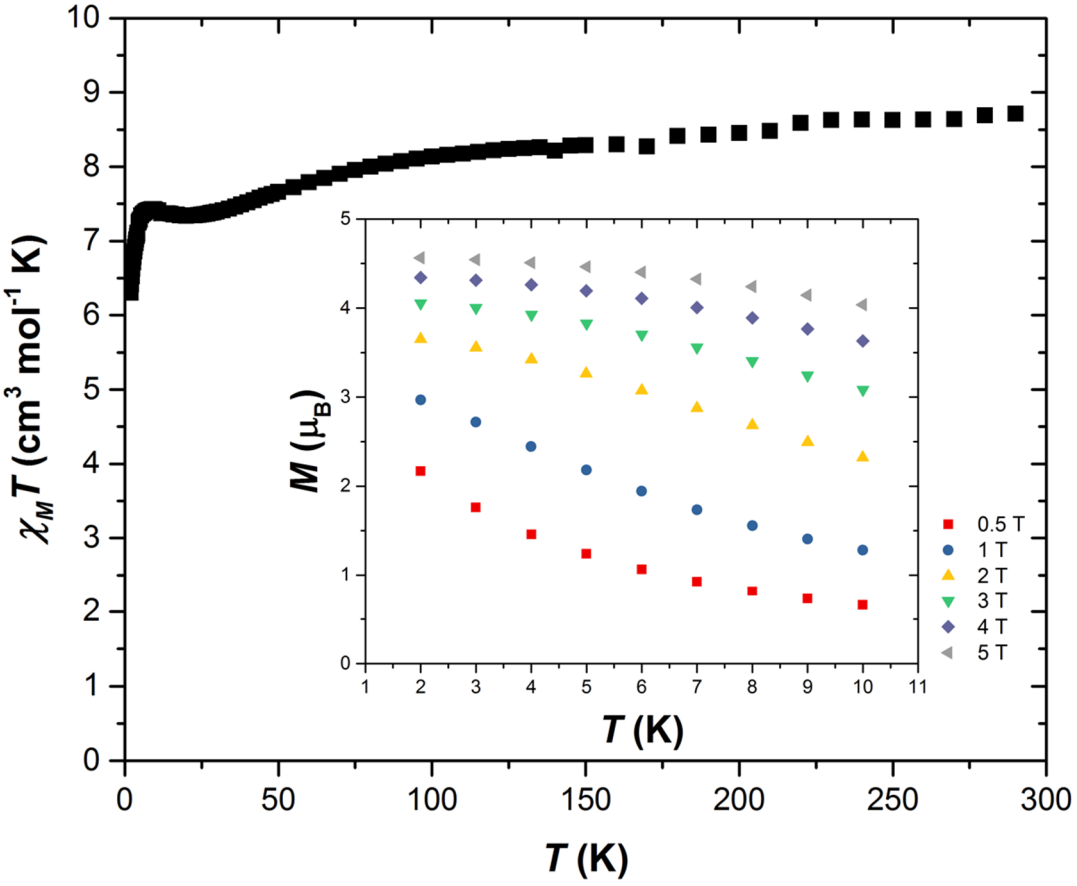

Figure 4. Plot of the $\chi_M T$ product versus T for compound **2** in an applied field, B = 0.1 T. The solid red line is a fit of the experimental data. Inset:

For interpretation of the magnetic exchange in these compounds we consider two unique exchange interactions (Figure 3), for simplification we consider M^{II}_{ring}-M^{II}_{ring} and M^{II}_{centre}-M^{II}_{ring}

to be the same, and we consider VO-M^{II}_{ring} and VO-M^{II}_{centre} to be equivalent. Based on this (admittedly greater simplified) model we used spin-Hamiltonian (1) where the indices *i* and *j* refer to the metal ions, μ_B is the Bohr magneton, *B* is the applied magnetic field, *g* is the *g*-factor of the metal ions (fixed as *g* = 2.00 for V^{IV} and *g* = 2.20 for Ni^{II}), $\hat{S}$ is a spin operator and *J* is the isotropic exchange interaction.

$$\hat{H} = \mu_B B \sum_i g_i \hat{S}_i - 2J \sum_{ij} \hat{S}_i \hat{S}_j \quad (1)$$

The experimental $\chi_M T$ product of each compound was numerically fitted to spin-Hamiltonian (1) by use of the simplex algorithm.[17] This resulted in the following best-fit parameters for **1**: $J_{Ni\text{-}Ni}$ = 1.66 cm^{-1} and $J_{Ni\text{-}VO}$ = -4.11 cm^{-1} (Figure 2). The ferromagnetic exchange for $J_{Ni\text{-}Ni}$ is consistent with previous examples seen in the literature for both dialkoxo bridged Ni_2 units with similar angles to those seen for Ni^{II}_{centre}-Ni^{II}_{ring}, and for alkoxo and chloro bridged Ni_2 units similar to those seen for Ni^{II}_{ring}-Ni^{II}_{ring}.[11] The nickel-vanadium interaction at first glance may be expected to be ferromagnetic due to the orthogonality of the magnetic orbitals of octahedral Ni^{II} ($d_{x^2-y^2}$ and d_{z^2}) and square-pyramidal $V^{IV}O$ (d_{xy}).[12] However it has been observed that when the dihedral angle between the basal planes of the two metal centres is sufficient, the orthogonality is broken resulting in antiferromagnetic exchange.[13] Thus the observation of AF exchange in the VO-Ni^{II}_{ring} and VO-Ni^{II}_{centre} interactions is feasible and consistent with the literature. For compound **2** the zero-field splitting of the Co^{II} ion precludes detailed extraction of magnetic exchange parameters for this compound.

5.4 Conclusions

A pair of structurally unique $[(V^{IV}O)_2M^{II}_5]$ (M = Ni, Co) Anderson-type wheels, with the V^{IV} ions opposing each other in the outer wheel, have been synthesised *via* solvothermal methods using the pro-ligand hmpH. Magnetic susceptibility and magnetization studies reveal competing exchange interactions between the metal centres.

The work expands upon previous studies of structurally analogous $[M^{III}_2M^{II}_5]$ wheels (M^{III} = Cr, Al; M^{II} = Ni, Zn) in which the M^{III} ions are positionally disordered around the outer wheel.

The observation of structurally related wheels containing metals in the II+, III+ and IV+ oxidation states points toward the stability of the structure, and suggests that an enormous number of complexes containing a combination of different metal ions and displaying different magnetic behaviours, may be isolable.[5,10]

5.5 Supplementary information

Table S1. Crystallographic information for compounds **1** and **2**.

Compound	**1**	**2**
Formula	$C_{62}H_{68}Cl_4N_{10}Ni_5O_{22}V_2$	$C_{62}H_{68}Cl_4Co_5N_{10}O_{22}V_2$
$D_{calc.}$/ g cm^{-3}	1.721	1.712
μ/mm^{-1}	1.779	1.613
FW/g mol^{-1}	1842.49	1843.59
Colour	dark green	pale brown
Shape	block	plate
Size/mm^3	0.52×0.29×0.16	0.50×0.14×0.06
T/K	120.0	120.0
Crystal System	monoclinic	monoclinic
Space Group	$P2_1/n$	$P2_1/n$
a/Å	15.7800(3)	15.7439(9)
b/Å	12.4392(2)	12.4867(5)
c/Å	19.0165(4)	18.9773(12)
α/°	90	90
β/°	107.745(2)	106.591(6)
γ/°	90	90
V/Å^3	3555.16(12)	3575.4(4)
Z (Z')	2 (0.5)	2 (0.5)
Wavelength/Å	0.71073	0.71073
Radiation type	MoK_α	MoK_α
Θ_{min}/° - Θ_{max}/°	3.072 – 32.985	3.079 – 28.897
Measured Refl.	90810	37370
Independent Refl.	12777	8344
Reflections Used	10678	5589
R_{int}	0.0447	0.0715
Parameters	516	479
Restraints	155	1
Largest Peak	0.678	1.013
Deepest Hole	-0.475	-0.678
GooF	1.042	1.041
wR_2 (all data) (wR_2)	0.0770 (0.0719)	0.1612 (0.1465)
R_1 (all data) (R_1)	0.0461 (0.0341)	0.1147 (0.0704)
CCDC Number	1847957	1847956

For Figures S1-S2 and Tables S2-S3 please refer to the “Chapter 6 SI” file on the memory stick supplied with the thesis.

5.6 References

1. M. T. Pope and A. Müller, *Angew. Chem., Int. Ed. Engl*. 1991, **30**, 34-48.
2. 0. Kahn, J. Galy, Y. Journaux, J. Jaud and I. Morgenstern Badarau, *J. Am. Chem. Soc*., 182, **104**, 2165-2176.
3. S. Ferlay, T. Mallah, R. Ouahès, P. Veillet and M. Verdaguer, *Nature*, 1995, **378**, 701−703.
4. S. L. Castro, Z. M. Sun, C. M. Grant, J. C. Bollinger, D. N. Hendrickson and G. Christou, *J. Am. Chem. Soc*., 1998, **120**, 2365-2375.
5. See, for example: a) J. Schnack, M. Luban and R. Modler, *Europhys. Lett*., 2001, **56**, 863–869. b) G. Chaboussant, S. T. Ochsenbein, A. Sieber, H.-U. Güdel, H. Mutka, A. Müller and B. Barbara, *Europhys. Lett*., 2004, **66**, 423-429. c) V. V. Maslyuk, I. Mertig, O. V. Farberovich, A. Tarantul and B. Tsukerblat, *Eur. J. Inorg. Chem*., 2013, 1897–1902. d) B. Botar, P. Kögerler and C. L. Hill, *Chem. Commun.*, 2005, 3138-3140.
6. a) J. M. Zadrozny, J. Niklas, O. G. Poluektov and D. E. Freedman, *J. Am. Chem. Soc*., 2014, **136**, 15841–15844. b) M. Atzori, L. Tesi, E. Morra, M. Chiesa, L. Sorace and R. Sessoli, *J. Am. Chem. Soc*., 2016, **138**, 2154–2157.
7. See, for example: R. H. Laye, F. K. Larsen, J. Overgaard, C. A. Muryn, E. J. L. McInnes, E. Rentschler, V. Sanchez, S. J. Teat, H. U. Güdel, O. Waldmann, G. A. Timco and R. E. P. Winpenny, *Chem. Commun.*, 2005, 1125-1127.
8. M. I. Khan, S. Tabussum, R. J. Doedens, V. O. Golub and C. J. O'Connor, *Inorg. Chem.*, 2004, **43**, 5850-5859.
9. H. W. L. Fraser, G. S. Nichol, D. Uhrín, U. G. Nielsen, M. Evangelisti, J. Schnack and E. K. Brechin, *Dalton Trans.*, 2018, **47**, 11834-11842.
10. O. Cador, D. Gatteschi, R. Sessoli, F. K. Larsen, J.Overgaard, A.-L. Barra, S. J. Teat, G. A. Timco and Richard E. P. Winpenny, *Angew. Chem. Int. Ed*., 2004, **43**, 5196–5200.
11. L. N. Zheng, S. Y. Zhang, K. Li, W. Q. Chen, Y. M. Chen, B. Xu, B. Hu, Y. H. Li and W. Li, *J. Mol. Struct.*, 2010, **984**, 153-156.
12. K. K. Nanda, S. Mohanta, S. Ghosh, M. Mukherjee, M. Helliwell and K. Nag, *Inorg. Chem.*, 1995, **34**, 2861-2869.
13. D. Mandal, P. B. Chatterjee, R. Ganguly, E. R. T. Tiekink, R. Clerac and M. Chaudhury, *Inorg. Chem.*, 2008, **47**, 584-591.
14. Y. Liang, Z. M. Zhang, Z. J. Liu, Y. Zhang, J. Zhang and E. B. Wang, *Crystengcomm*, 2014, **16**, 1187-1191.
15. G. M. Sheldrick, *Acta Crystallogr. Sect. C: Cryst. Struct. Commun.*, 2015, **71**, 3-8.
16. O. V. Dolomanov, L. J. Bourhis, R. J. Gildea, J. A. K. Howard and H. Puschmann, *J. Appl. Crystallogr.*, 2009, **42**, 339-341.
17. K. G. Murty, *Linear programming*, Wiley, 1983.
18. G. A. Bain and J. F. Berry, *J. Chem. Educ.*, 2008, **85**, 532.

CHAPTER 7: CONCLUSIONS AND FUTURE PERSPECTIVES

7.1 Conclusions

The aim of this project was to synthesise novel families of molecular magnets in which the structure could be extensively studied alongside the magnetic properties in order to better understand the relationship between these two aspects and thus develop 'magneto-structural correlations'.

Chapter 2 described the use of pyridine alcohol ligands with Cr(III) in the absence of additional co-ligands to form a family of di-alkoxo-bridged $[Cr_2(OR)_2]$ dimers. This family showed exclusively weak antiferromagnetic exchange interactions between the metal centres. DFT calculations reproduced the sign, magnitude and trend of the exchange coupling constants and were used to develop magneto-structural correlations. These revealed the importance of both the angle between the Cr_2O_2 plane and the O-R vector of the bridging group (θ) and the Cr-O-Cr-O dihedral angles (ψ) in modulating the sign and strength of *J*. This hinted at pathways to promote ferromagnetic interactions, in particular through distortion of the $[Cr_2(OR)_2]$ plane.

Chapter 3 built on the work from Chapter 2 with a view to deliberately synthesising ferromagnetically coupled chromium dimers. Our previous work along with hints from the small number of FM chromium compounds in the literature stimulated a move into heteroleptic systems. The synthesis and magnetic studies of a family of Cr(III) dimers of general formula $[Cr_2(R^1\text{-deaH})_2(O_2CR_2)Cl_2]Cl$ using a combination of carboxylate and diethanolamine ligands was described along with the compound $[Cr_2(Me\text{-deaH})_2Cl_4]$, which was synthesised to study the effect of removing/adding the carboxylate bridge. Magnetic studies revealed ferromagnetic exchange interactions between the Cr(III) centres in the carboxylate bridged family, and antiferromagnetic exchange between the Cr(III) ions when the carboxylate bridge was removed. Theoretical studies revealed the origin of the ferromagnetic exchange to be an orbital counter-complementarity effect. In particular, the addition of the bridging carboxylate results in the carboxylate MOs mixing with the Cr $(d_{yz})_s$ orbital leading to a decrease in the $[(d_{yz})_s\text{-}(d_{yz})_{as}]$ energy gap. Not only does this family represent a tripling of the known ferromagnetic Cr(III) dimers in the literature but also are the first to allow a detailed magneto-structural correlation to be developed and thus provide a clear rationale for the ferromagnetic exchange seen in the polynuclear complexes $[Cr_4S(O_2CCH_3)_8(H_2O)_4](BF_4)_2$ and $[Cr_{10}(OR)_{20}(O_2CR')_{10}]$ which hitherto had no explanation. Additionally this work suggested a simple blueprint for the construction of ferromagnetically

coupled Cr(III) cages of any nuclearity – exploit the orbital counter-complementarity effect by combining heteroleptic ligand sets, here alkoxides and carboxylates.

Chapter 4 moved on to the synthesis of heterometallic 3d-3d compounds containing Cr(III). The synthesis and structure of a new family of heterometallic Anderson-type wheels of general formula $[M^{III}_2M^{II}_5(hmp)_{12}](ClO_4)_4$ was described, where M^{III} = Cr, Al; M^{II} = Ni, Zn. This family of wheels display substitutional disorder in the positions of the M^{III} and M^{II} ions around the outside ring, which was quantified and characterised through the combination of single-crystal X-ray diffraction, and solution- and solid-state NMR spectroscopy revealing the presence of three isomers, with the Cr^{III} ions positioned at the 1,2, 1,3 and 1,4 sites around the wheel. The magnetic behaviour was examined in a sequential manner in order to extract all of the individual exchange interactions. The $[Cr^{III}_2Zn^{II}_5]$ analogue provided the Cr-Cr interaction, while the $[Al^{III}_2Ni^{II}_5]$ complex afforded the Ni-Ni interactions. Fixing these values then allowed extraction of the Cr-Ni interactions in $[Cr^{III}_2Ni^{II}_5]$. This worked remarkably well, and provided a beautifully simple example of how the analysis of the individual building blocks of a cluster can be combined to understand the large, complicated molecule.

Chapter 5 built on the work from chapter 4 and looked more widely at planar cages, expanding the family of heterometallic wheels ($[M^{III}_2M^{II}_5(hmp)_{12}]^{4+}$) to include M^{II} = Cu, Co, Mn and Fe, with M^{III} = Al or Cr. Magnetic studies for these compounds showed competing exchange interactions in all cases, largely due to the collection of triangular building blocks present in this structure type. In addition, it was shown that these structures can be enlarged to make bigger planar wheel structures with the synthesis of $[Al^{III}_6Cu^{II}_7(OH)_{12}(hmp)_{12}](ClO_4)_6(NO_3)_2$, this aesthetically pleasing compound showed weak antiferromagnetic exchange through the three atom O-Al-O bridge between copper centres.

Chapter 6 presented a final family of heterometallic wheels, a pair of structurally unique $[(V^{IV}O)_2M^{II}_5]$ (M = Ni, Co) Anderson-type wheels, with the V^{IV} ions opposing each other in the outer wheel. While being structurally related to those compounds discussed in chapters 4 and 5, the use of the V^{IV}=O unit acts to constrain the positional disorder. Magnetic studies showed competing interactions as expected for this system, however the magnetic data was fitted through simplification of the magnetic pathways. The observation of structurally related wheels containing metals in the II+, III+ and IV+ oxidation states (chapters 4-6) points toward the stability of the structure, and suggests that an enormous number of complexes

containing a combination of different metal ions and displaying different magnetic behaviours, may be isolable.

7.2 Applications and future perspectives

In order to put the field and the work within it into context it is prudent to look at the potential applications to which molecular magnets may appeal, as well as to look forward to where the field may progress in the future. Molecular magnets have been regularly discussed with regards to magnetic data storage, exploiting the molecular ability to act as a 1 or 0 (up or down) implies the potential for high-density (they represent the smallest possible unit) and high efficiency information storage.[1] If the field is going to make its mark in this area the operating temperatures at which retention of the magnetisation persists will need to reach at least liquid nitrogen levels (77 K), which is a considerable challenge. A major issue for any attempt at application in data storage (particularly in the case of 4f compounds where this phenomena is prolific) is the fast under barrier relaxation via quantum tunnelling, however this same property endears these compounds to quantum computing, due to entanglement of the spin states.[2]

Widespread speculation has been generated over the potential use of SMMs as quantum bits (qubits), in quantum computing. A quantum computer is a

device which utilises quantum phenomena (for instance the superposition of states and quantum entanglement) to perform complex operations much faster than classical computers.[3, 4] Qubits differ from classical bits in that not only can they have two isolated states (1 or 0) but they can have any quantum superposition of these states.[5] There are multiple approaches being researched as candidates for qubits, including photons, trapped ions, nuclear spins and superconducting circuits,[6, 7] but utilising electron spins in molecular magnets present a particularly appealing route. This is because of the huge advantages of the bottom up approach utilising chemical engineering to carefully control the quantum properties. In particular the ability to control the type of phase, the nature of the compound and its properties, and the method of addressing these properties (e.g. electrically, optically or magnetically). The idea is to assemble systems of well-defined molecular units weakly coupled to one another thus resulting in a superposition of states in which the spins of separate units are entangled.[8, 9] A system which has been particularly well studied involves

the $Cr^{III}_7Ni^{II}$ wheel of Winpenny et al, by treating this unit as a qubit and then linking two of these wheels together via a Ni^{II} complex, a pair of linked (encoded) qubits is created – by control of the excitation of the Ni^{II} ion (by a microwave pulse) a two-qubit gate is performed, making this system a switchable two-qubit register.[10] Further work to couple these units together via different linkers and demonstrate how these systems would function has been carried out displaying the process of quantum information processing, and showing the possibility for control both electrically and magnetically.[11] This area has become a hotbed of research within this field with a variety of other complex and interesting work emerging.[12-15]

The same properties that endear these systems to quantum computing also make them well suited for use in molecular spintronics, for instance as magnetic nano-switches.[1] Spintronic systems exploit the fact that spin-up and spin-down carriers are present in an electron current, these can carry information encoded in their spin-state and each type of carrier will interact in a different way with magnetic materials. This means that information encoded in the carriers (via their spins) is retained once the device is turned off and can be manipulated without using magnetic fields.[16] It is not only anisotropic systems which are of interest, high spin ground state isotropic systems also have significant potential for application in magnetic refrigeration (cryocooling or magnetic cooling).[17] This application utilises the magnetocaloric effect displayed by molecular magnets, whereby large changes in magnetisation with applied magnetic field and magnetic entropy decrease resulting in a cooling effect.[17] In these instances, an adiabatic demagnetisation process operates, which provokes a temperature drop and thus a magnetic field driven cooling process occurs.[18] Complexes of gadolinium and isotropic transition metal ions have been found to be particularly promising for magnetic cooling, especially in the ultralow temperature region, displaying this effect strongly.[19, 20] This technique is energy efficient and environmentally friendly, which would provide a good alternative to the expensive and rare helium-3 that is currently used for refrigeration at ultra-low temperatures.[17] One area where these could replace helium-3 is in medical imaging, specifically MRI, where supercooling of the magnets is needed. Molecular magnets can also be used in MRI as contrast and polarising agents, to dramatically improve the quality of the images produced for diagnosis as well as agents for magnetic hyperthermic treatment.[21, 22] Additional applications include molecular recognition, magnetic sensors, and magnetic separation media.[23]

For all of these applications not only the unusual phenomena but also the molecular nature of these materials that is important. Molecular materials hold key benefits in that they are monodisperse as well as being soluble in organic solvents, meaning they are solution-processable and therefore easier to use for applications. In addition, they can be highly tuneable through functionalisation or alteration of ligands and choice of metal centre. In the coming years one of the next steps forward will inevitably have to be incorporating molecular magnets into devices, turning the speculation into tangible utilisation.

This field has exploded over the last two decades and has taken large strides forward both in performance and understanding. This, coupled with increasing diversification of the plethora of research strands, entwining themselves with other fields to produce new areas of study, nurtures the belief that there are many more exciting twists and turns on the horizon.

7.3 References

1. M. Mannini, F. Pineider, P. Sainctavit, C. Danieli, E. Otero, C. Sciancalepore, A. M. Talarico, M.-A. Arrio, A. Cornia, D. Gatteschi and R. Sessoli, *Nat. Mater.*, 2009, **8**, 194-197.
2. G. Aromi, D. Aguila, P. Gamez, F. Luis and O. Roubeau, *Chem. Soc. Rev.*, 2012, **41**, 537-546.
3. M. N. Leuenberger and D. Loss, *Nature*, 2001, **410**, 789-793.
4. M. Ganzhorn, S. Klyatskaya, M. Ruben and W. Wernsdorfer, *Nature Nanotechnology*, 2013, **8**, 165-169.
5. S. Barnett, *Quantum Information*, Oxford University Press, Inc., 2009.
6. T. D. Ladd, F. Jelezko, R. Laflamme, Y. Nakamura, C. Monroe and J. L. O'Brien, *Nature*, 2010, **464**, 45-53.
7. Z. L. Xiang, S. Ashhab, J. Q. You and F. Nori, *Rev. Mod. Phys.*, 2013, **85**, 623-653.
8. S. Hill, R. S. Edwards, N. Aliaga-Alcalde and G. Christou, *Science*, 2003, **302**, 1015-1018.
9. A. Candini, G. Lorusso, F. Troiani, A. Ghirri, S. Carretta, P. Santini, G. Amoretti, C. Muryn, F. Tuna, G. Timco, E. J. L. McInnes, R. E. P. Winpenny, W. Wernsdorfer and M. Affronte, *Phys. Rev. Lett.*, 2010, **104**.
10. A. Chiesa, G. F. S. Whitehead, S. Carretta, L. Carthy, G. A. Timco, S. J. Teat, G. Amoretti, E. Pavarini, R. E. P. Winpenny and P. Santini, *Sci. Rep.*, 2014, **4**.
11. J. Ferrando-Soria, E. M. Pineda, A. Chiesa, A. Fernandez, S. A. Magee, S. Carretta, P. Santini, I. J. Vitorica-Yrezabal, F. Tuna, G. A. Timco, E. J. L. McInnes and R. E. P. Winpenny, *Nat. Commun.*, 2016, **7**.
12. A. Gaita-Arino, H. Prima-Garcia, S. Cardona-Serra, L. Escalera-Moreno, L. E. Rosaleny and J. J. Baldovi, *Inorg. Chem. Front.*, 2016, **3**, 568-577.
13. M. Shiddiq, D. Komijani, Y. Duan, A. Gaita-Arino, E. Coronado and S. Hill, *Nature*, 2016, **531**, 348-351.

14. C. Godfrin, A. Ferhat, R. Ballou, S. Klyatskaya, M. Ruben, W. Wernsdorfer and F. Balestro, *Phys. Rev. Lett.*, 2017, **119**, 187702.
15. S. G. McAdams, A. M. Ariciu, A. K. Kostopoulos, J. P. S. Walsh and F. Tuna, *Coord. Chem. Rev.*, 2017, **346**, 216-239.
16. L. Bogani and W. Wernsdorfer, *Nat. Mater.*, 2008, **7**, 179-186.
17. M. Evangelisti and E. K. Brechin, *Dalton Trans.*, 2010, **39**, 4672-4676.
18. V. Corradini, A. Ghirri, A. Candini, R. Biagi, U. del Pennino, V. De Renzi, G. Dotti, E. Otero, T. N. Hooper, R. Inglis, E. K. Brechin and M. Affronte, *Adv. Funct. Mater.*, 2014, **24**, 4782-4788.
19. T. N. Hooper, J. Schnack, S. Piligkos, M. Evangelisti and E. K. Brechin, *Angew. Chem. Int. Ed. Engl.*, 2012, **51**, 4633-4636.
20. J.-B. Peng, Q.-C. Zhang, X.-J. Kong, Y.-Z. Zheng, Y.-P. Ren, L.-S. Long, R.-B. Huang, L.-S. Zheng and Z. Zheng, *J. Am. Chem. Soc.*, 2012, **134**, 3314-3317.
21. A. Ito, M. Shinkai, H. Honda and T. Kobayashi, *J. Biosci. Bioeng.*, 2005, **100**, 1-11.
22. E. Duguet, S. Vasseur, S. Mornet and J.-M. Devoisselle, *Nanomedicine*, 2006, **1**, 157-168.
23. E. A. Vitol, V. Novosad and E. A. Rozhkova, *Nanomedicine*, 2012, **7**, 1611-1624.

Chapter 2: Magneto-structural correlations in a family of di-alkoxo bridged chromium dimers

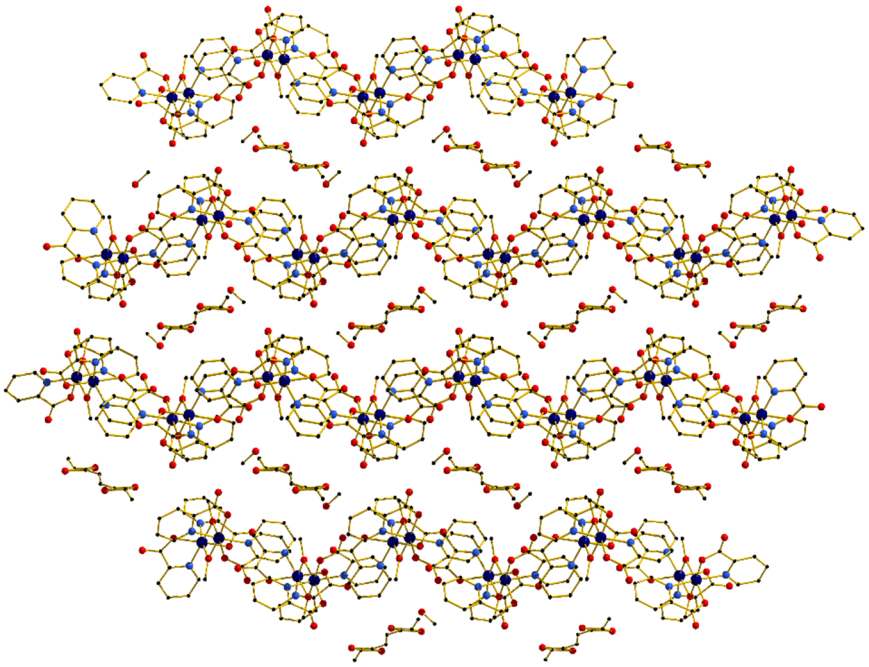

Figure S1. Packing diagram for compound **1** viewed along the *a*-axis.

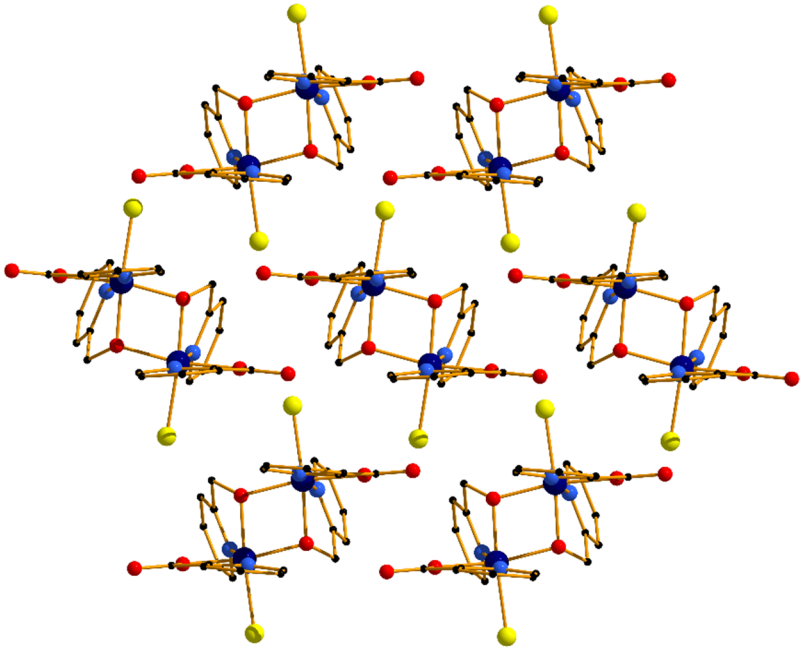

Figure S2. Packing diagram for compound **2** viewed along the *c*-axis. Compound **3** displays a similar extended structure.

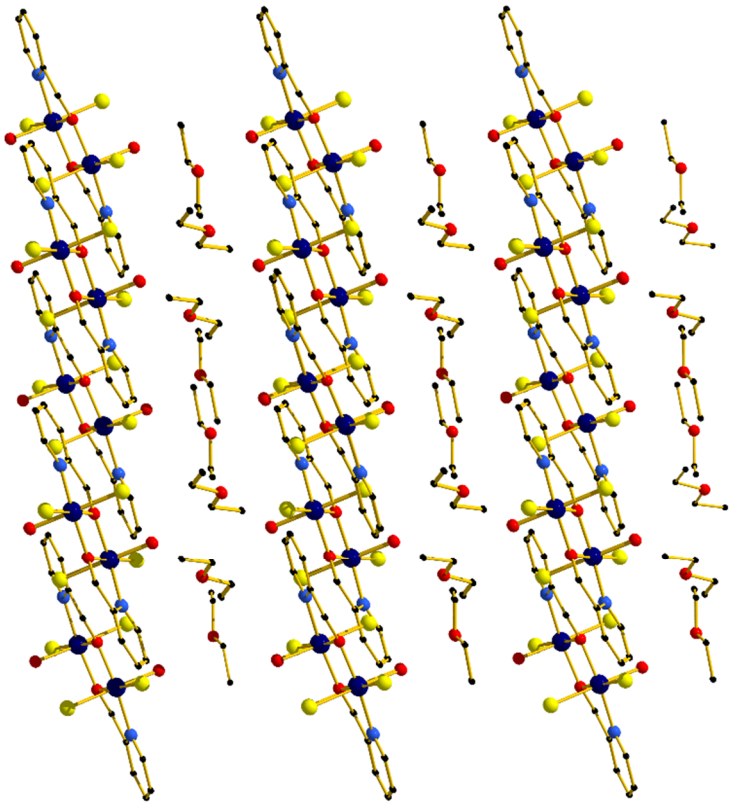

Figure S3. Packing diagram for compound **4** viewed along the *c*-axis.

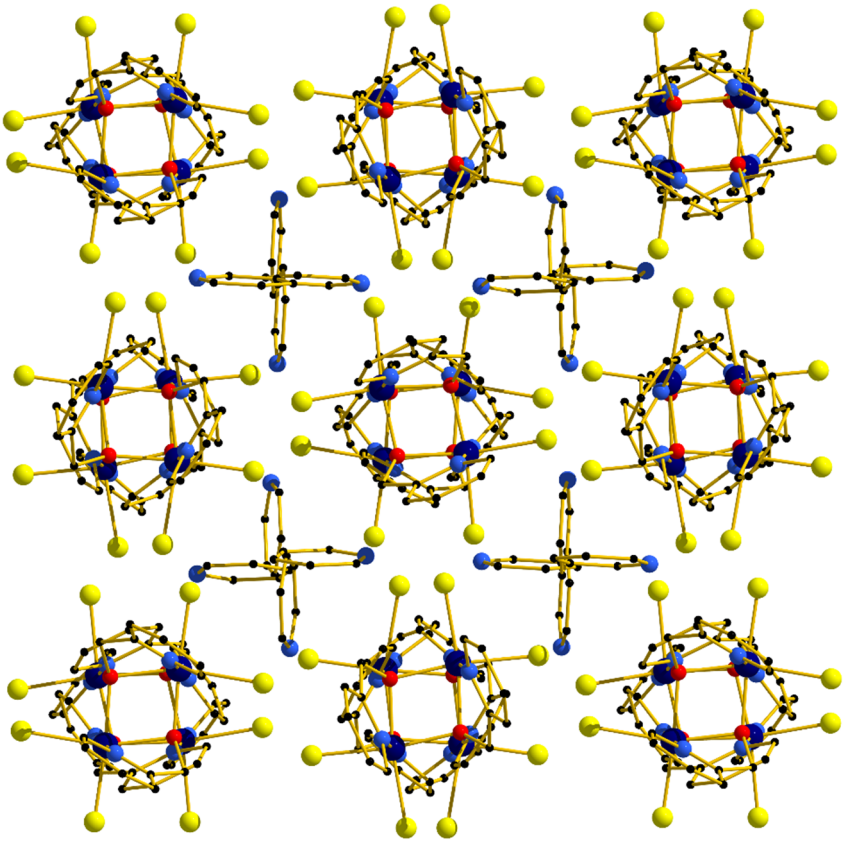

Figure S4. Packing diagram for compound **5** viewed along the c-axis.

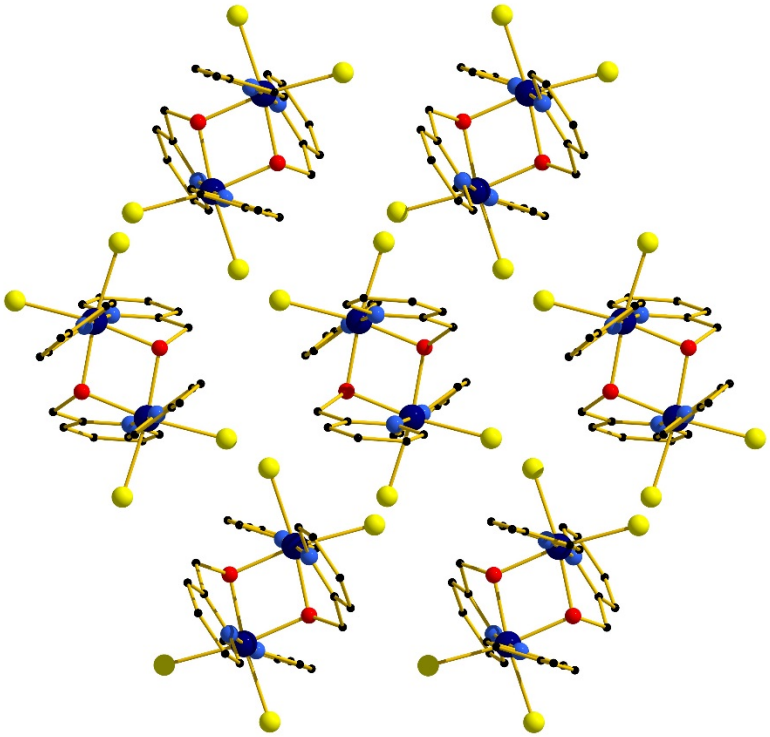

Figure S5. Packing diagram for compound **6** viewed along the b-axis.

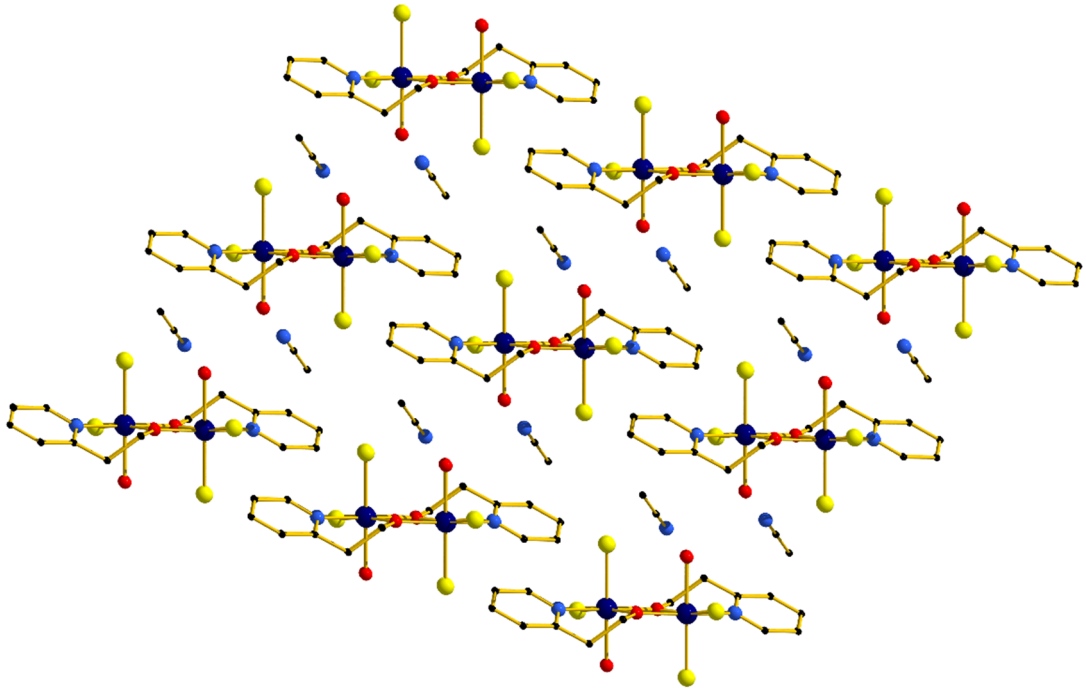

Figure S6. Packing diagram for compound **7** viewed along the *b*-axis.

Table S1. Crystallographic information for compounds **1**-**6**.

Compound	**1**	**2**	**3**	**4**	**5**	**6**
Formula	$C_{28.5}H_{29}Cr_2N_4O_{11}$	$C_{24}H_{20}Cl_2Cr_2N_4O_6$	$C_{24}H_{20}Br_2Cr_2N_4O_6$	$C_{20}H_{36}Cl_4Cr_2N_2O_6$	$C_{32}H_{32}Cl_4Cr_2N_6O_2$	$C_{24}H_{26}Cl_4Cr_2N_4O_2$
$D_{calc.}$/ g cm^{-3}	1.419	1.693	1.879	1.520	1.531	1.625
μ/mm^{-1}	0.717	1.136	4.019	1.183	8.539	10.720
Formula Weight	707.56	635.34	724.26	646.31	778.43	648.29
Colour	pink	brown	light purple	green	dark green	blue
Shape	block	block	prism	block	block	block
Size/mm^3	0.25x0.12x0.09	0.33x0.18x0.18	0.24x0.10x0.09	0.19x0.16x0.11	0.24x0.14x0.05	0.20×0.09×0.03
T/K	120.00	120.00	120.0	120.0	120.0	120.0
Crystal System	monoclinic	orthorhombic	orthorhombic	triclinic	tetragonal	monoclinic
Flack/Hooft Parameters	-	-0.003(5)/-0.018(4)	0.010(7)/0.028(7)	-	(n/a)/0.255(8)	-
Space Group	$P2_1/n$	$Pnn2$	$Pnn2$	P-1	$I4_1$	P2/c
a/Å	12.2931(8)	7.81306(10)	7.8068(2)	9.7732(4)	16.2418(2)	14.29325(19)
b/Å	21.3092(16)	12.17220(15)	12.2423(4)	10.4693(3)	16.2418(2)	14.06348(14)
c/Å	13.2192(8)	13.10384(16)	13.3916(4)	14.0067(7)	25.6069(6)	14.8511(2)
α/°	90	90	90	92.473(4)	90	90
β/°	106.939(7)	90	90	99.099(4)	90	117.3958(17)
γ/°	90	90	90	91.960(3)	90	90
V/Å^3	3312.6(4)	1246.20(3)	1279.88(7)	1412.58(10)	6755.0(2)	2650.46(7)
Z (Z')	4 (1)	2 (0.5)	2 (0.5)	2 (1)	8 (1)	4 (1)
Wavelength/Å	0.71073	0.71073	0.71073	0.71073	1.54178	1.54178
Radiation type	MoK_α	MoK_α	MoK_α	MoK_α	CuK_α	CuK_α
Θ_{min}/° - Θ_{max}/°	3.222 - 24.996	3.035 - 32.892	3.042 - 29.769	3.288 - 28.854	4.938 - 76.392	3.142 – 76.778
Measured Refl.	47599	45650	11349	22598	28737	43244
Independent Refl.	5824	4514	3209	6514	6396	5513
Reflections Used	4892	4406	3011	5624	5590	5054
R_{int}	0.0970	0.0356	0.0369	0.0452	0.0730	0.0554
Parameters	454	212	172	324	432	327
Restraints	31	1	1	6	247	0
Largest Peak	0.768	0.308	0.423	0.829	0.830	0.524
Deepest Hole	-0.585	-0.300	-0.500	-0.632	-0.608	-0.677
GooF	1.151	1.051	1.066	1.266	1.044	1.038
wR_2 (all data) (wR_2)	0.2129 (0.2054)	0.0528 (0.0522)	0.0570 (0.0549)	0.1652 (0.1608)	0.2107 (0.1952)	0.1227 (0.1198)
R_1 (all data) (R_1)	0.0979 (0.0830)	0.0225 (0.0215)	0.0344 (0.0304)	0.0862 (0.0728)	0.0858 (0.0739)	0.0455 (0.0428)

Table S2. Crystallographic information for compounds **7**-**8**.

Compound	**7**	**8**
Formula	$C_{18}H_{26}Cl_4Cr_2N_4O_4$	$C_{14}H_{16}Cl_2CrN_3O_2$
$D_{calc.}$/ g cm^{-3}	1.628	1.713
μ/mm^{-1}	11.459	1.145
Formula Weight	608.23	381.20
Colour	brown	green
Shape	block	block
Size/mm^3	0.09x0.06x0.04	0.22x0.05x0.04
T/K	120.0	120.0
Crystal System	triclinic	tetragonal
Flack/Hooft Parameters	-	-
Space Group	P-1	$P4_2/nbc$
a/Å	8.2906(3)	15.4761(3)
b/Å	8.5467(3)	15.4761(3)
c/Å	10.1679(4)	12.3453(3)
α/°	112.400(4)	90
β/°	101.243(3)	90
γ/°	102.099(3)	90
V/Å^3	620.49(4)	2956.82(13)
Z (Z')	1 (0.5)	8 (0.5)
Wavelength/Å	1.54178	0.71073
Radiation type	CuK$_\alpha$	MoK$_\alpha$
Θ_{min}/° - Θ_{max}/°	4.938 - 76.392	3.107 - 26.369
Measured Refl.	10079	134457
Independent Refl.	2577	1520
Reflections Used	2421	1516
R_{int}	0.0566	0.0725
Parameters	153	90
Restraints	3	3
Largest Peak	0.788	0.452
Deepest Hole	-0.520	-0.358
GooF	1.062	1.330
wR_2 (all data) (wR_2)	0.1287 (0.1262)	0.1087 (0.1086)
R_1 (all data) (R_1)	0.0488 (0.0466)	0.0491 (0.0489)

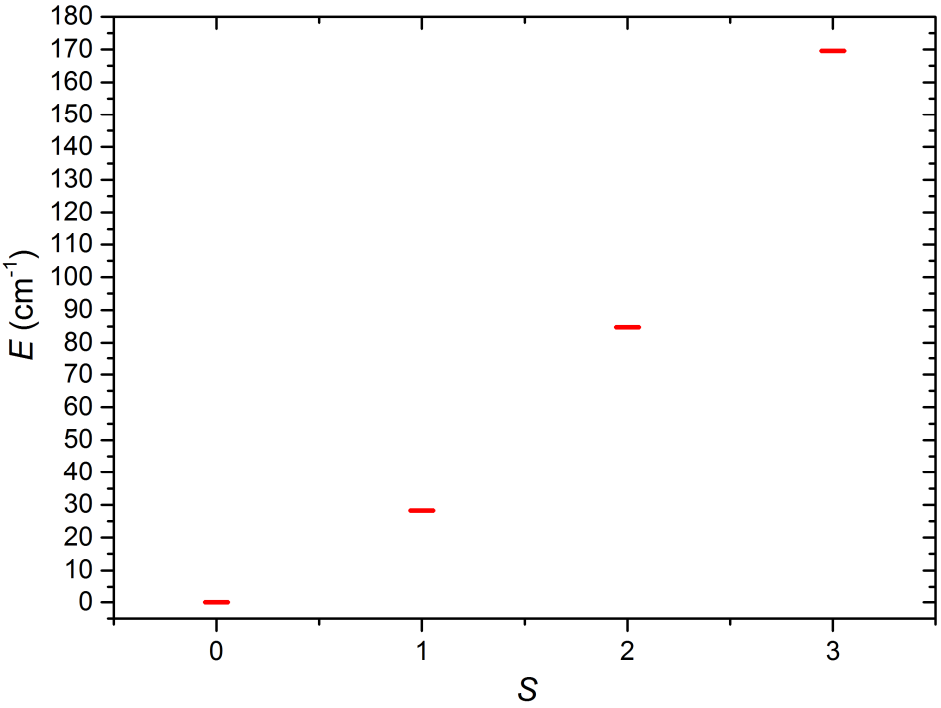

Figure S7. Energy levels of compound **1** at zero magnetic field for the isotropic spin-Hamiltonian (1) with best fit as detailed in the main text.

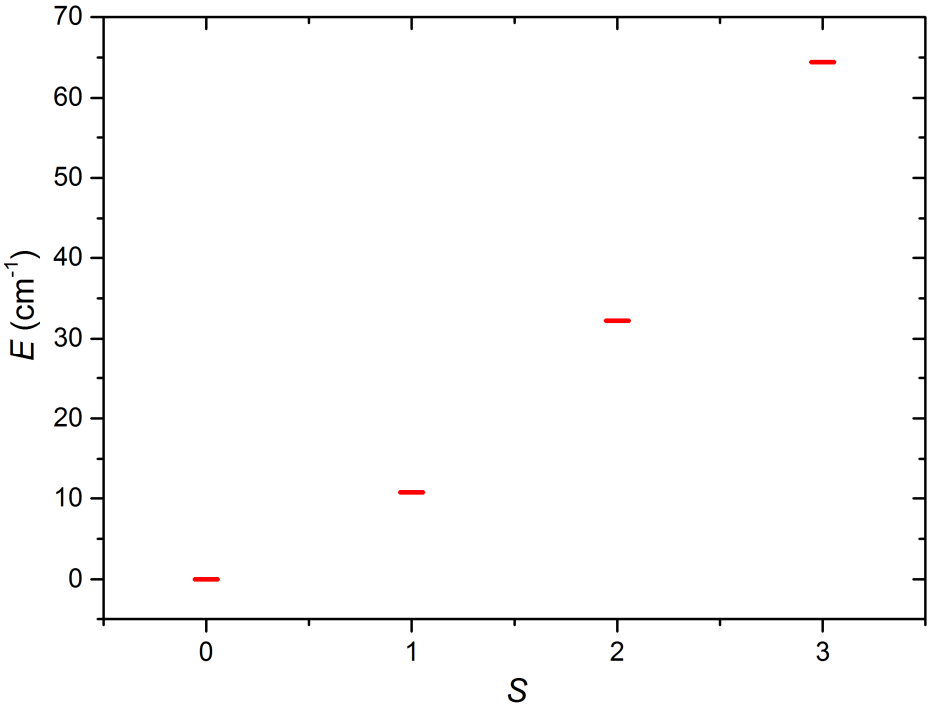

Figure S8. Energy levels of compound **2** at zero magnetic field for the isotropic spin-Hamiltonian (1) with best fit as detailed in the main text.

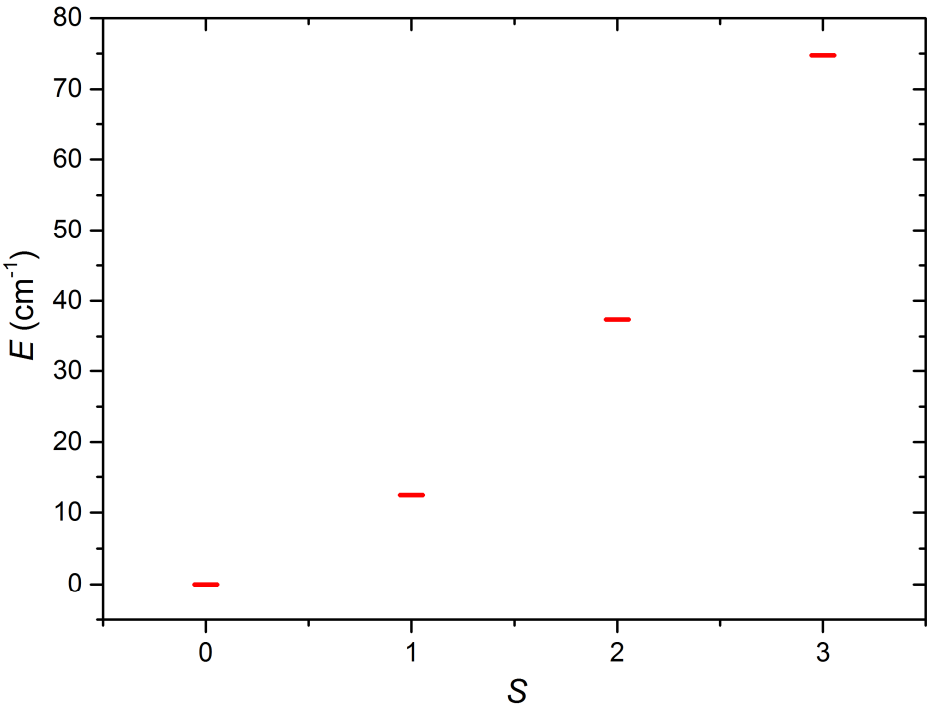

Figure S9. Energy levels of compound **3** at zero magnetic field for the isotropic spin-Hamiltonian (1) with best fit as detailed in the main text.

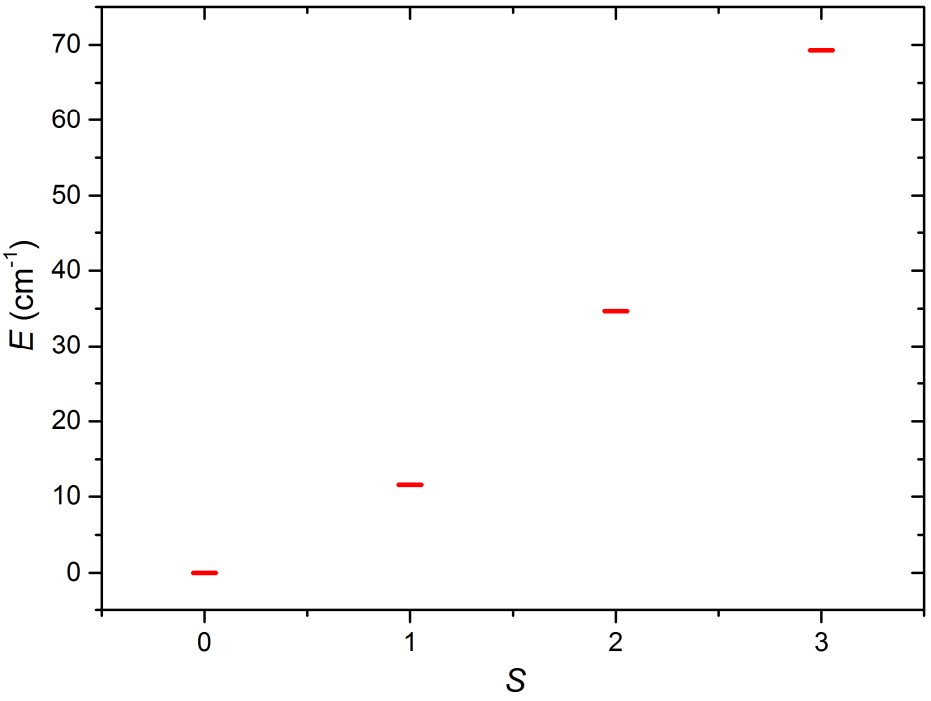

Figure S10. Energy levels of compound **4** at zero magnetic field for the isotropic spin-Hamiltonian (1) with best fit as detailed in the main text.

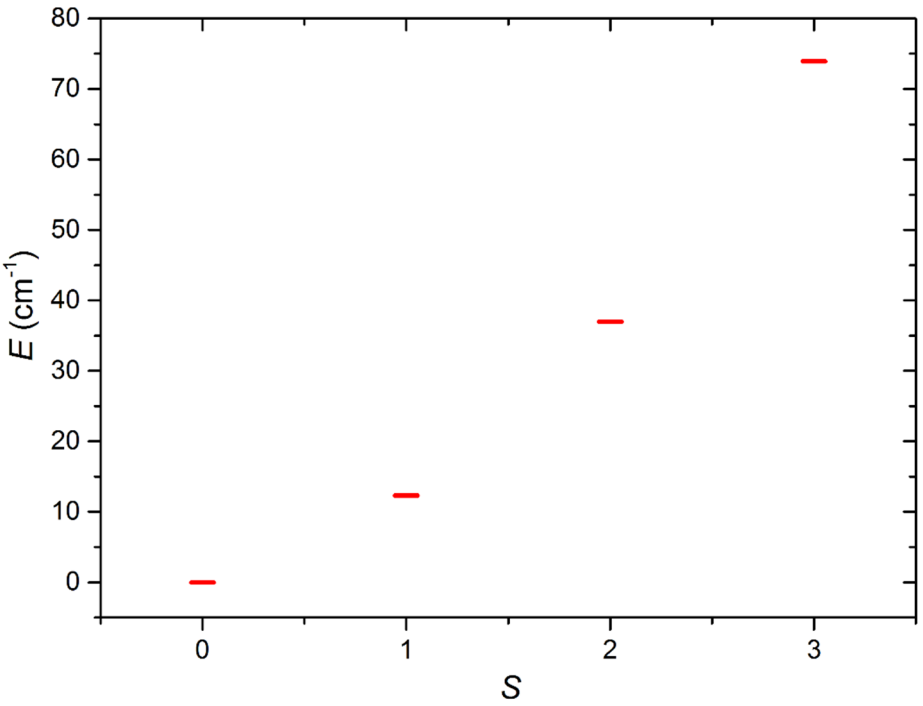

Figure S11. Energy levels of compound **5** at zero magnetic field for the isotropic spin-Hamiltonian (1) with best fit as detailed in the main text.

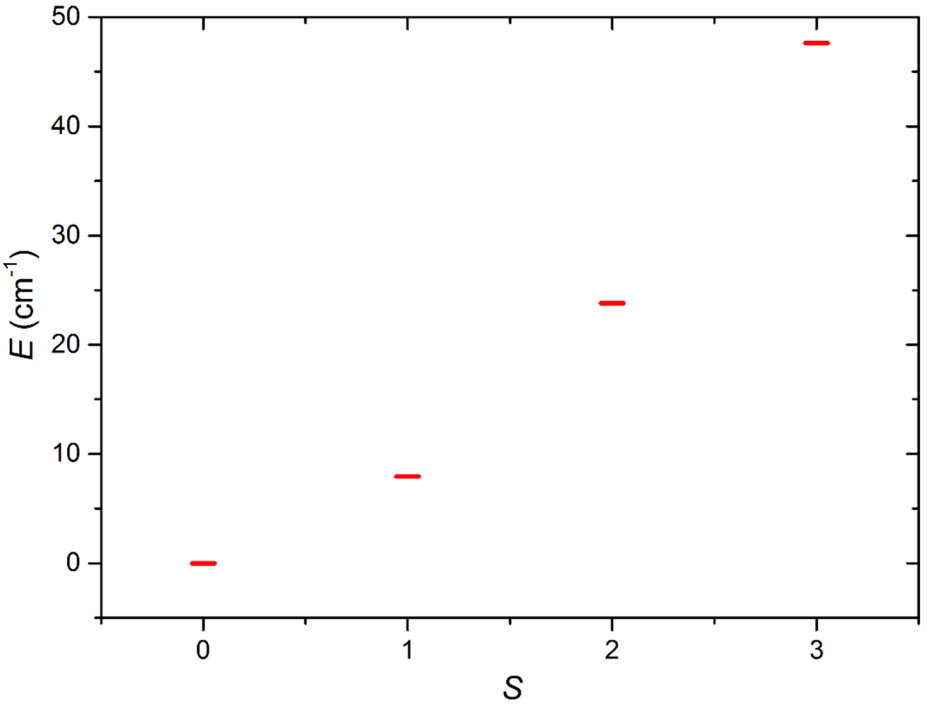

Figure S12. Energy levels of compound **6** at zero magnetic field for the isotropic spin-Hamiltonian (1) with best fit as detailed in the main text.

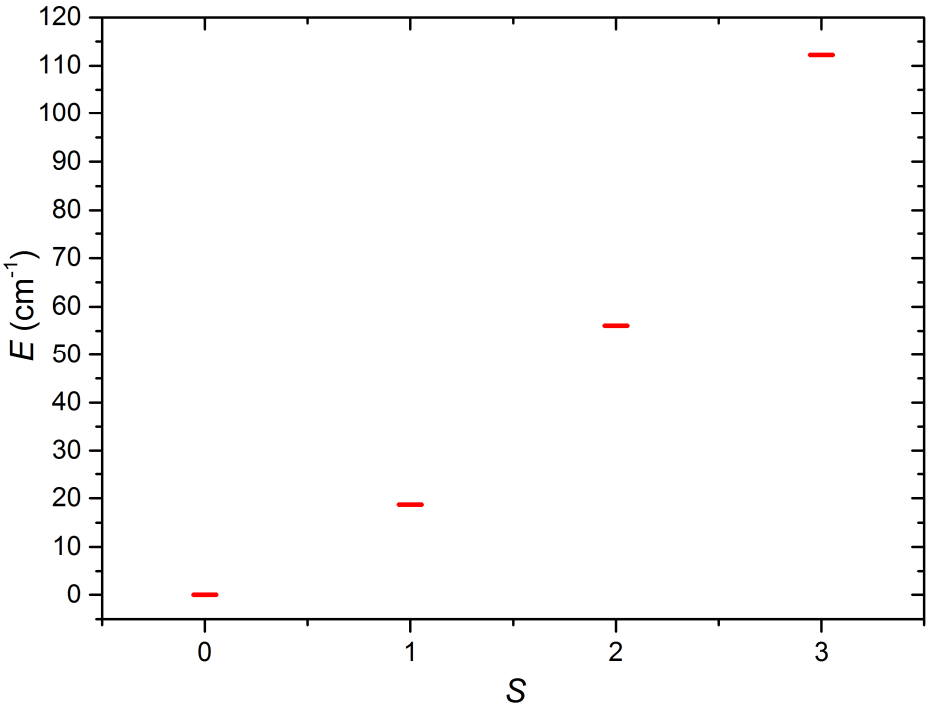

Figure S13. Energy levels of compound **7** at zero magnetic field for the isotropic spin-Hamiltonian (1) with best fit as detailed in the main text.

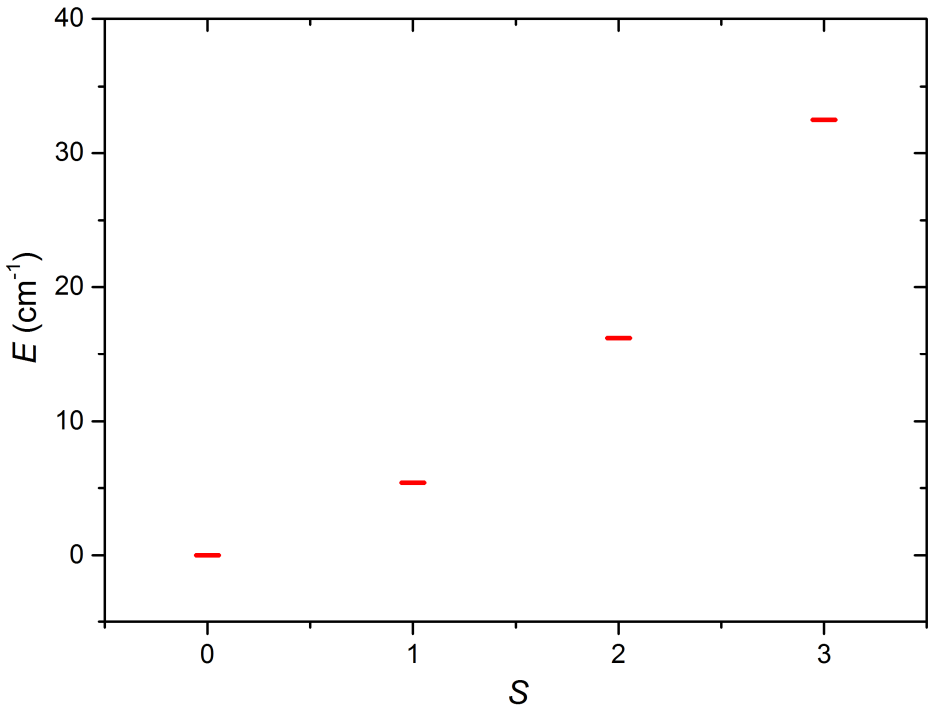

Figure S14. Energy levels of compound **8** at zero magnetic field for the isotropic spin-Hamiltonian (1) with best fit as detailed in the main text.

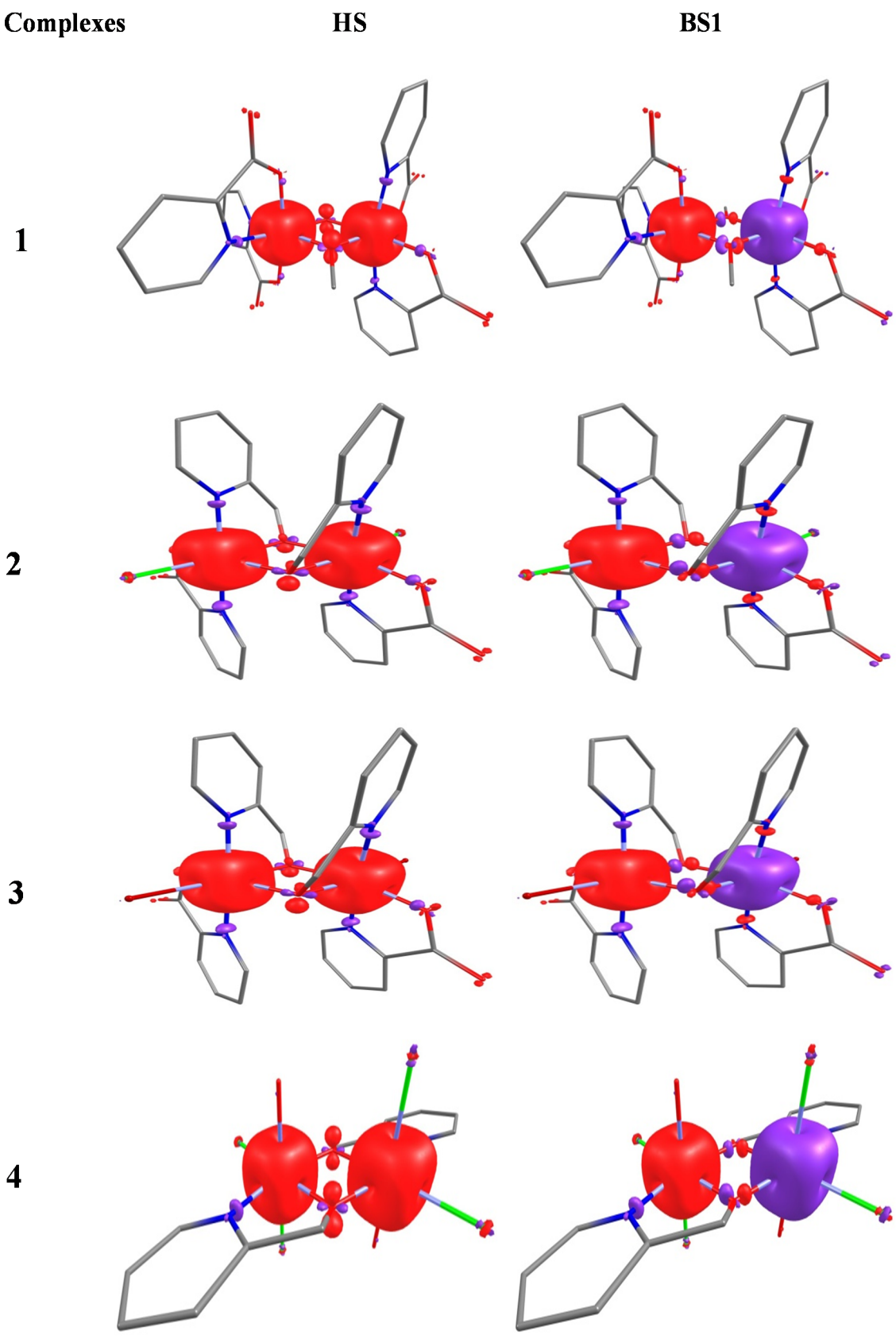

Figure S15. Spin density plots for complexes **1-4** at the UB3LYP/TZV level shown with isosurface values of 0.01 $Å^{-3}$.

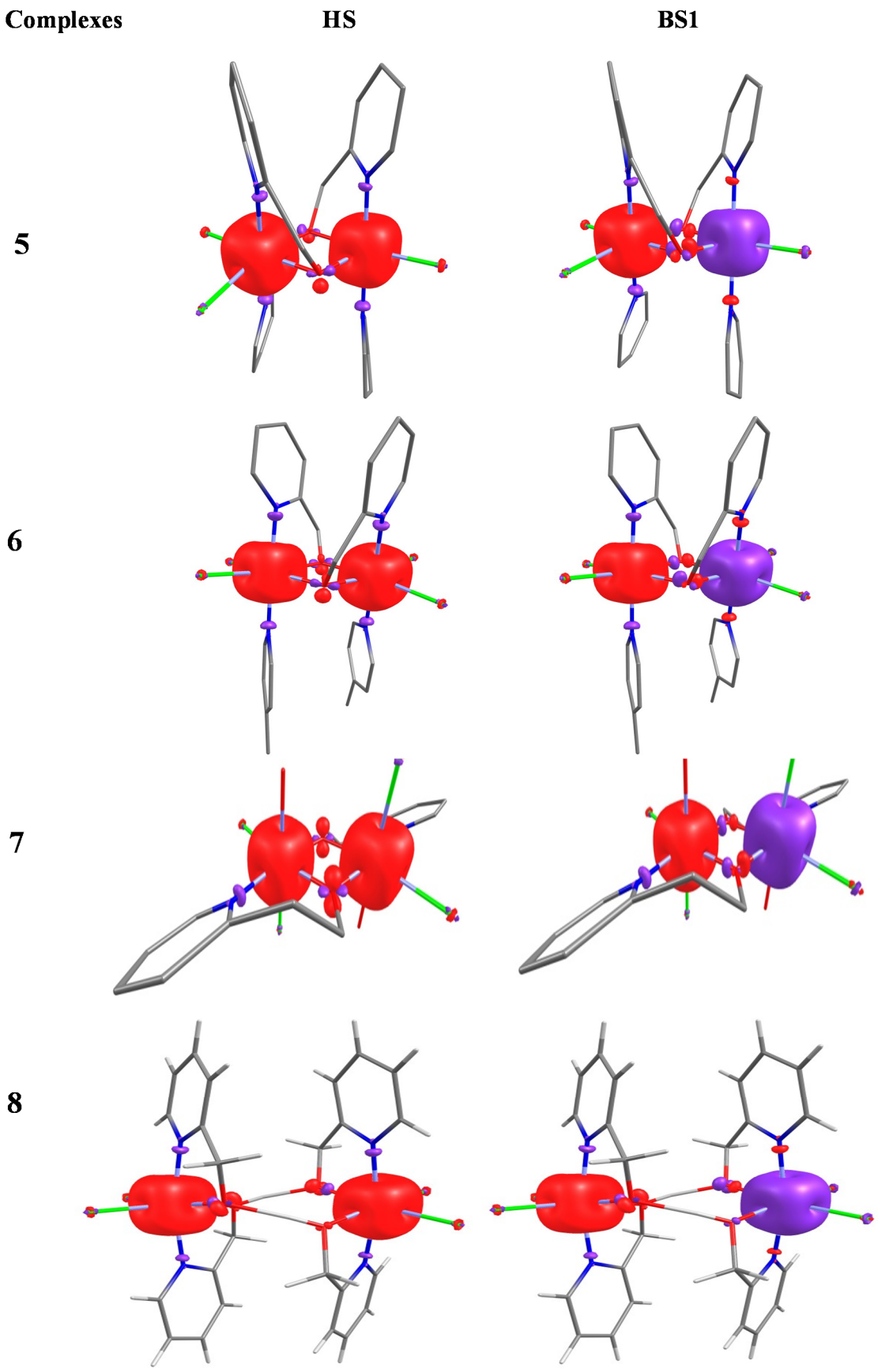

Figure S16. Spin density plots for complexes **4-8** at the UB3LYP/TZV level shown with isosurface values of 0.01 $Å^{-3}$.

Table S3. Calculated spin density values of complexes **1**-**8** at the UB3LYP/TZV level.

Complexes		Cr_1 Spin	Cr_2 Spin	O_1	O_2	Total Spin
1	HS	2.994	3.008	0.017	0.006	6
	BS1	2.986	-3.000	-0.009	-0.006	0
2	HS	3.024	3.024	-0.008	-0.008	6
	BS1	3.017	-3.020	0.003	-0.003	0
3	HS	3.040	3.040	-0.007	-0.007	6
	BS1	3.032	-3.030	0.004	-0.004	0
4a	HS	2.992	2.992	0.013	0.013	6
	BS1	2.988	-2.990	0.004	-0.004	0
4b	HS	2.997	2.997	0.012	0.012	6
	BS1	2.993	-2.990	0.008	-0.008	0
5a	HS	3.021	3.021	-0.017	-0.017	6
	BS1	3.014	-3.014	0.005	-0.005	0
5b	HS	2.994	2.994	-0.007	-0.007	6
	BS1	2.988	-2.988	0.011	-0.011	0
6a	HS	3.043	3.043	-0.006	-0.006	6
	BS1	3.037	-0.037	0.004	-0.004	0
6b	HS	3.043	3.043	-0.007	-0.007	6
	BS1	3.037	-3.037	-0.005	0.005	0
7	HS	3.022	3.022	0.012	0.012	6
	BS1	3.017	-3.020	0.013	-0.013	0
8	HS	3.008	3.008	0.013 0.002	0.023 0.013	6
	BS1	3.008	-3.010	0.012 -0.002	0.002 -0.012	0

Table S4. Calculated spin density values of complex **1** by varying θ.

Complex 1 (θ).		**Cr_1 Spin**	**Cr_2 Spin**	**O_1**	**O_2**	**Total Spin**
θ = 0°	HS	2.993	3.006	0.017	0.008	6
	BS1	2.985	-2.998	-0.008	-0.006	0
θ = 4°	HS	2.986	-3.000	0.017	0.006	0
	BS1	3.024	3.024	-0.009	-0.006	6
θ = 9°	HS	2.996	3.009	0.016	0.002	6
	BS1	2.987	-3.000	-0.009	-0.006	0
θ = 14°	HS	2.998	3.011	0.014	-0.002	6
	BS1	2.988	-3.002	-0.009	-0.005	0
θ = 19°	HS	3.000	3.014	0.011	-0.006	6
	BS1	2.990	-3.005	-0.009	-0.005	0
θ = 24°	HS	3.003	3.017	0.016	0.008	6
	BS1	2.993	-3.007	-0.009	-0.005	0
θ = 29°	HS	3.006	3.020	0.004	-0.014	6
	BS1	2.995	-3.011	-0.008	-0.004	0
θ = 34°	HS	3.009	3.024	0.000	-0.018	6
	BS1	2.998	-3.014	-0.008	-0.004	0
θ = 39°	HS	3.013	3.027	-0.004	-0.022	6
	BS1	3.001	-3.017	-0.008	-0.004	0
θ = 44°	HS	3.017	3.031	-0.007	-0.025	6
	BS1	3.004	-3.021	-0.008	-0.004	0

Table S5. Overlap integral values for complex **1**.

Beta → Alpha ↓	d_{yz}	d_{xz}	d_{xy}	d_{z^2}	$d_{x^2-y^2}$
d_{xy}	0.003	0.067	-0.032	-0.164	-0.021
d_{yz}	0.053	-0.071	0.034	-0.074	-0.036
d_{xz}	-0.319	-0.065	-0.156	0.062	0.012
d_{z^2}	0.050	-0.105	0.176	0.120	-0.003
$d_{x^2-y^2}$	0.027	0.035	0.017	0.069	-0.405

Table S6. Overlap integral values for complex **2**.

Beta → Alpha ↓	d_{yz}	d_{xz}	d_{xy}	d_{z^2}	$d_{x^2-y^2}$
d_{xy}	0.049	-0.060	-0.017	0.276	-0.155
d_{yz}	0.131	-0.138	0.049	0.007	-0.042
d_{xz}	-0.138	0.239	-0.060	0.088	-0.025
d_{z^2}	0.007	0.089	0.276	-0.106	-0.177
$d_{x^2-y^2}$	-0.042	0.025	-0.155	-0.177	-0.058

Table S7. Overlap integral values for complex **3**.

Beta → Alpha ↓	d_{yz}	d_{xz}	d_{xy}	d_{z^2}	$d_{x^2-y^2}$
d_{xy}	-0.205	0.132	-0.057	-0.031	-0.019
d_{yz}	0.305	-0.273	0.089	-0.118	0.082
d_{xz}	0.079	0.070	0.035	0.245	-0.126
d_{z^2}	-0.031	0.183	0.012	-0.076	-0.118
$d_{x^2-y^2}$	-0.019	-0.087	0.018	-0.118	-0.127

Table S8. Overlap integral values for complex **4a**.

Beta → Alpha ↓	d_{yz}	d_{xz}	d_{xy}	d_{z^2}	$d_{x^2-y^2}$
d_{xy}	-0.017	-0.064	-0.119	0.169	0.001
d_{yz}	0.085	-0.032	-0.017	-0.003	-0.016
d_{xz}	0.032	-0.050	0.064	0.044	-0.027
d_{z^2}	0.003	0.044	-0.169	0.111	-0.062
$d_{x^2-y^2}$	0.016	-0.028	-0.001	-0.062	-0.250

Table S9. Overlap integral values for complex **4b**.

Beta → Alpha ↓	d_{yz}	d_{xz}	d_{xy}	d_{z^2}	$d_{x^2-y^2}$
d_{xy}	0.024	-0.038	-0.015	-0.127	-0.058
d_{yz}	0.033	-0.175	-0.024	-0.036	-0.117
d_{xz}	-0.175	0.119	0.038	-0.049	0.045
d_{z^2}	0.036	0.049	-0.127	0.126	-0.022
$d_{x^2-y^2}$	0.117	-0.045	-0.058	-0.022	-0.229

Table S10. Overlap integral values for complex **7**.

Beta → Alpha ↓	d_{yz}	d_{xz}	d_{xy}	d_{z^2}	$d_{x^2-y^2}$
d_{xy}	0.244	0.129	-0.095	-0.073	0.034
d_{yz}	0.095	0.145	-0.248	-0.006	0.001
d_{xz}	0.145	-0.061	-0.124	0.098	-0.093
d_{z^2}	-0.006	0.098	0.073	0.198	-0.034
$d_{x^2-y^2}$	0.001	-0.093	-0.034	-0.034	-0.346

Table S11. Overlap integral values for complex **8**.

Beta → Alpha ↓	d_{yz}	d_{xz}	d_{xy}	d_{z^2}	$d_{x^2-y^2}$
d_{xy}	0.030	-0.020	-0.023	0.036	-0.012
d_{yz}	-0.001	0.052	0.030	0.062	0.022
d_{xz}	-0.052	0.003	0.020	0.022	-0.005
d_{z^2}	0.022	0.005	-0.012	0.097	-0.072
$d_{x^2-y^2}$	0.062	-0.022	0.036	-0.051	0.097

Table S12. Overlap integral values for complex **1** (θ = 24°).

Beta → Alpha ↓	d_{yz}	d_{xz}	d_{xy}	d_{z^2}	$d_{x^2-y^2}$
d_{xy}	0.095	0.106	0.111	-0.164	0.026
d_{yz}	0.005	0.131	-0.012	0.069	-0.048
d_{xz}	-0.115	-0.018	0.021	0.198	-0.017
d_{z^2}	-0.035	-0.083	0.196	0.094	0.040
$d_{x^2-y^2}$	-0.035	-0.032	-0.041	-0.070	-0.398

Table S13. Overlap integral values for complex **1** (θ = 44°).

Beta → Alpha ↓	d_{yz}	d_{xz}	d_{xy}	d_{z^2}	$d_{x^2-y^2}$
d_{xy}	-0.046	-0.107	-0.035	-0.263	-0.019
d_{yz}	-0.014	-0.086	-0.033	0.054	-0.035
d_{xz}	0.101	-0.026	-0.018	0.236	0.019
d_{z^2}	-0.063	-0.082	0.223	0.045	-0.097
$d_{x^2-y^2}$	-0.023	-0.006	-0.040	-0.046	-0.356

Table S14. Overlap integral values for complex **1** (ψ = 0.9°).

Beta → Alpha ↓	d_{yz}	d_{xz}	d_{xy}	d_{z^2}	$d_{x^2-y^2}$
d_{xy}	0.003	0.067	-0.032	-0.164	-0.021
d_{yz}	0.053	-0.071	0.034	-0.074	-0.036
d_{xz}	-0.319	-0.065	-0.156	0.062	0.012
d_{z^2}	0.027	0.035	0.017	0.069	-0.405
$d_{x^2-y^2}$	0.050	-0.105	0.176	0.120	-0.003

Table S15. Overlap integral values for complex **1** (ψ = 17.4°).

Beta → Alpha ↓	d_{yz}	d_{xz}	d_{xy}	d_{z^2}	$d_{x^2-y^2}$
d_{xy}	0.015	0.158	0.019	-0.139	-0.029
d_{yz}	0.049	-0.052	0.037	-0.048	-0.079
d_{xz}	0.187	-0.074	-0.046	0.114	-0.037
d_{z^2}	-0.112	-0.049	-0.123	0.033	-0.486
$d_{x^2-y^2}$	0.002	-0.066	0.108	0.070	0.007

Table S16. Overlap integral values for complex **1** (ψ = 27.6°).

Beta → Alpha ↓	d_{yz}	d_{xz}	d_{xy}	d_{z^2}	$d_{x^2-y^2}$
d_{xy}	0.089	-0.041	0.026	-0.125	0.055
d_{yz}	0.049	-0.094	0.045	-0.051	-0.065
d_{xz}	0.197	-0.110	-0.095	0.091	-0.065
d_{z^2}	-0.019	-0.113	-0.216	-0.008	-0.460
$d_{x^2-y^2}$	0.075	0.063	0.085	0.018	-0.117

Table S17. Pertinent structural parameters for the di-alkoxo bridged compounds **a**-**g** from the literature. r = Cr-O bond length, ϕ = Cr-O-Cr bridging angle, θ = dihedral angle between the bridging Cr_2O_2 plane and the OR vector of the bridging group, ψ = Cr-O-Cr-O dihedral angle, and J_{exp} is the experimentally determined exchange.

	Compound	**Cr-Cr [Å]**	**r [Å]**	**ϕ [°]**	**θ [°]**	**ψ [°]**	**J_{exp} [cm^{-1}]**
a	$[Cr(acac)_2(OMe)]_2$ [ref. 66]	3.028	1.950-1.973	101.0	29.81	1.37	-4.9
b	$[Cr(tmhd)_2(OMe)]_2$ [ref. 67] (tmhd = 2,2,6,6-tetramethyl-3,5-heptanedionato)	3.032	1.950-1.958	101.74	31.2	0.0	-4.45
c	$[Cr(3\text{-}Br\text{-}acac)_2(OEt)]_2$ [ref. 68]	3.027	1.949-1.953	101.8	18.3	0.0	-8.94
d	$[Cr(3\text{-}Br\text{-}acac)_2(OMe)]_2$ [ref. 68]	3.038	1.961-1.963	101.44	25.52	0.0	-5.04
e	$[Cr(3\text{-}Cl\text{-}acac)_2(OMe)]_2$ [ref. 69]	3.025	1.959	101.09	24.42	0.0	-5.04
f	$[Cr(L_1)(OMe)]_2$ [ref. 70] (L_1 = Tetrahydrosalen = N,N'-bis(2-hydroxybenzyl)-1,2-ethanediamine)	3.033	1.957-1.968	101.17	4.05	0.0	-10.8
g	$[Cr(HL)_2(OMe)]_2$ [ref. 71] (H_2L = 2-salicyloylhydrazono-1,3-dithiolane)	3.024	1.950-1.975	100.91	27.27	1.84	-10.75

Chapter 3: A simple methodology for constructing ferromagnetically coupled Cr(III) compounds

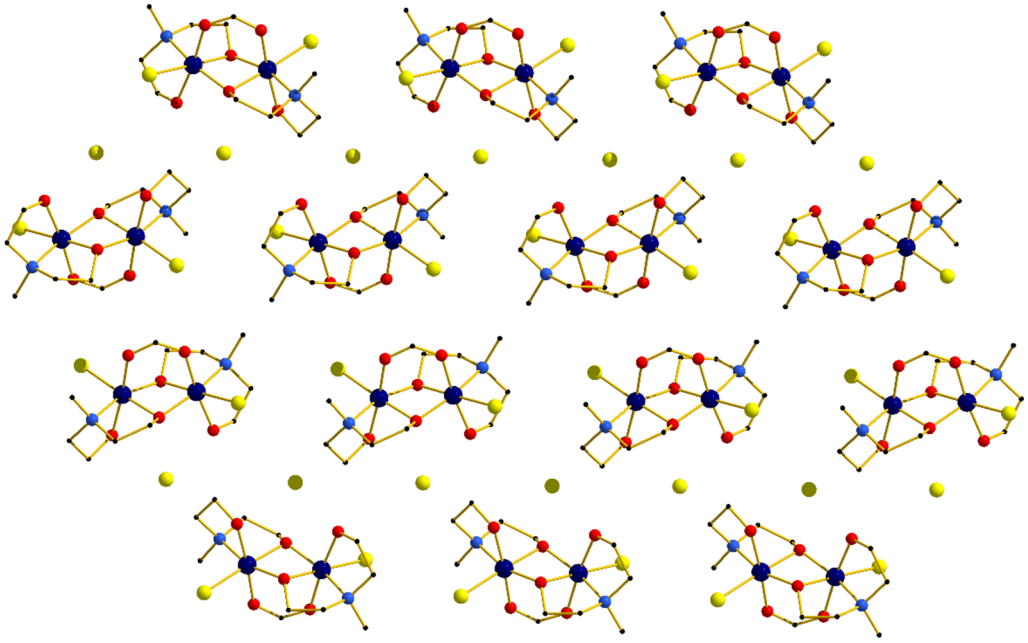

Figure S1. Packing diagram for compound **1** viewed along the *a*-axis.

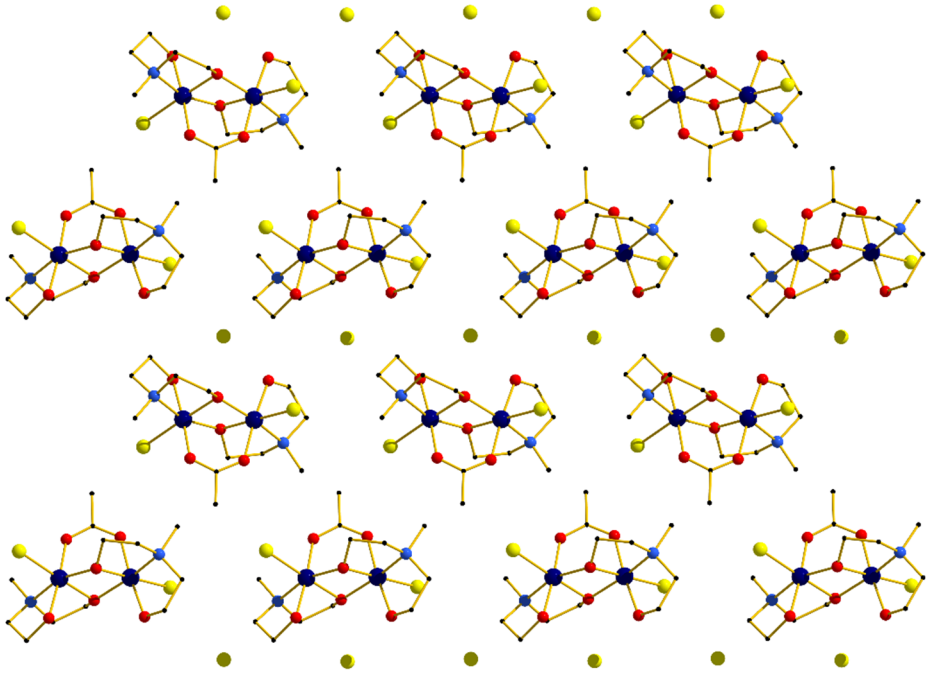

Figure S2. Packing diagram for compound **2** viewed along the *a*-axis.

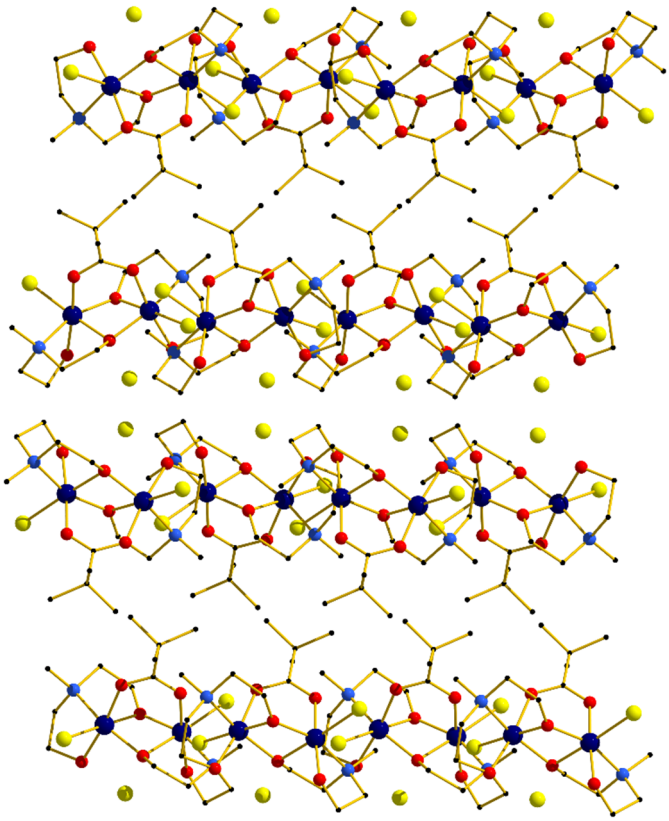

Figure S3. Packing diagram for compound **3** viewed along the *a*-axis.

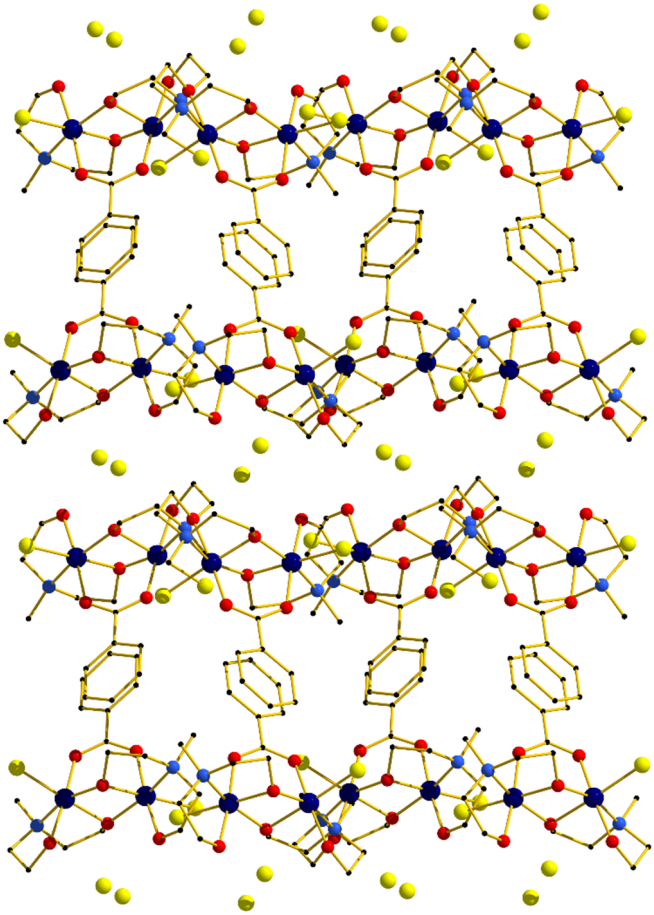

Figure S4. Packing diagram for compound **4** viewed along the *c*-axis.

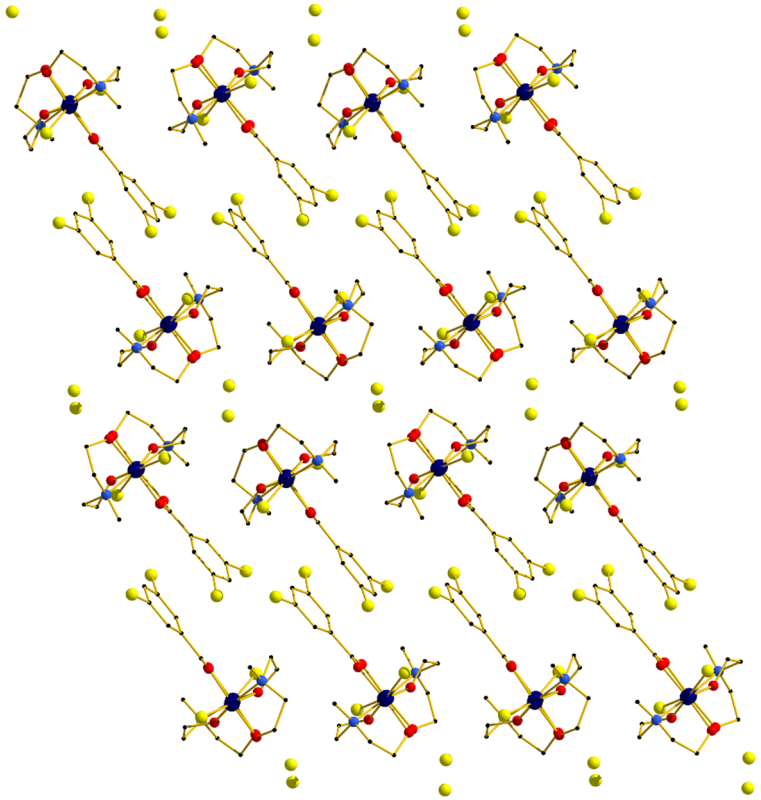

Figure S5. Packing diagram for compound **5** viewed along the *a*-axis.

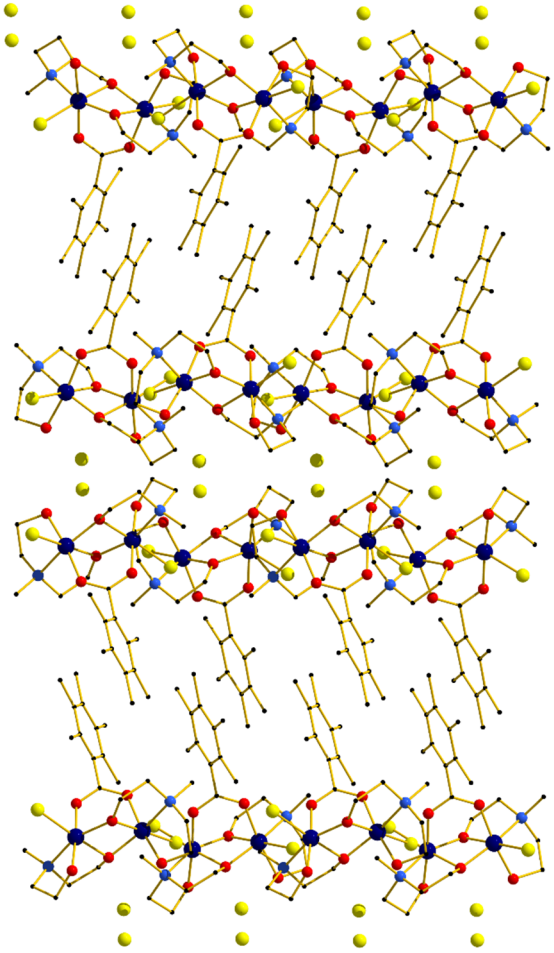

Figure S6. Packing diagram for compound **6** viewed along the *a*-axis.

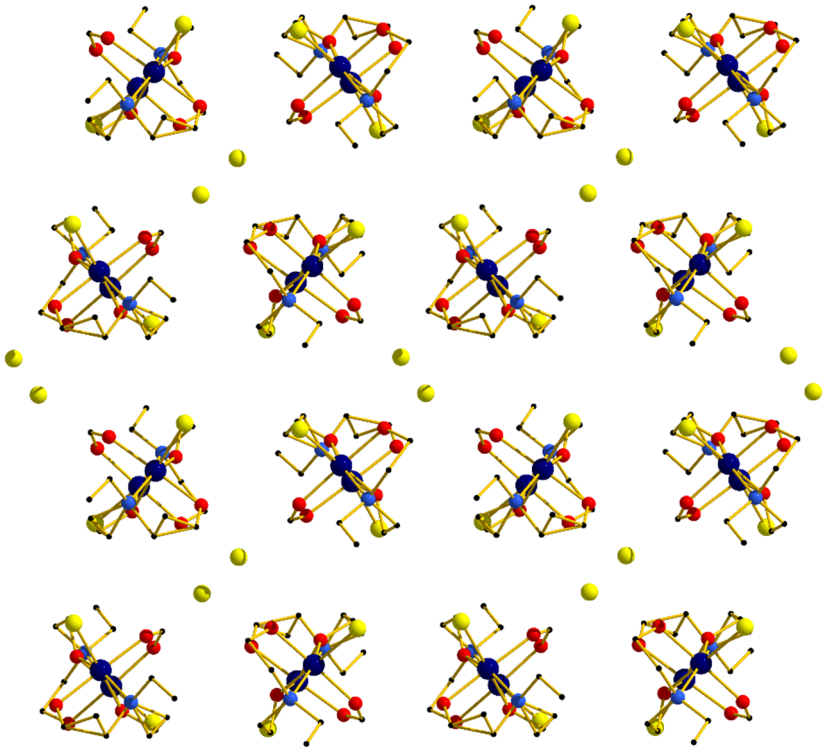

Figure S7. Packing diagram for compound **7** viewed along the *a*-axis.

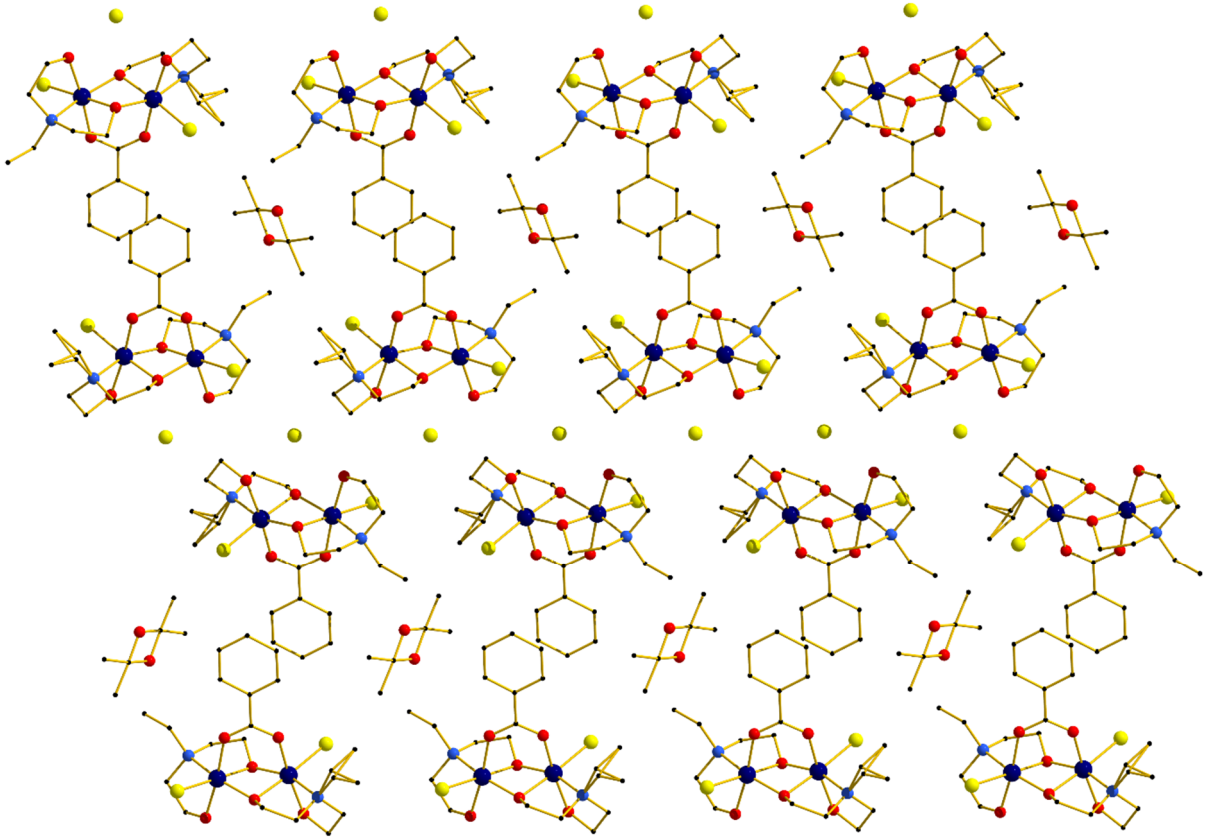

Figure S8. Packing diagram for compound **8** viewed along the *a*-axis.

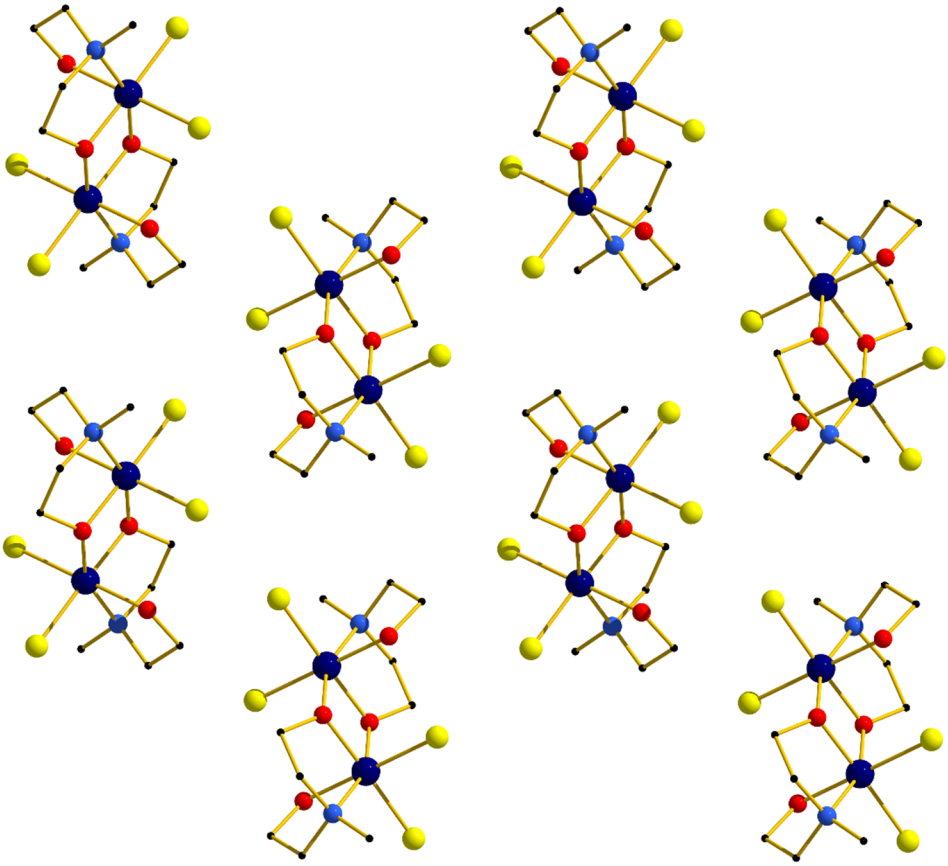

Figure S9. Packing diagram for compound **9** viewed along the *a*-axis.

Table S1. Crystallographic information for compounds **1**-**6**.

Compound	**1**	**2**	**3**	**4**	**5**	**6**
Formula	$C_{11}H_{25}Cl_3Cr_2N_2O_6$	$C_{12}H_{27}Cl_3Cr_2N_2O_6$	$C_{15}H_{33}Cl_3Cr_2N_2O_6$	$C_{17}H_{29}Cl_3Cr_2N_2O_6$	$C_{17}H_{27}Cl_5Cr_2N_2O_6$	$C_{22}H_{39}Cl_3Cr_2N_2O_6$
$D_{calc.}$/ g cm^{-3}	1.721	1.703	1.594	1.618	1.660	1.494
μ/mm^{-1}	1.596	1.538	1.335	1.311	12.174	1.087
Formula Weight	491.68	505.70	547.78	567.77	636.65	637.90
Colour	dark green	dark green	pale green	dark purple	dark purple	pale green
Shape	block	block	plate	block	plate	plate
Size/mm^3	0.41×0.14×0.07	0.39×0.33×0.25	0.53×0.37×0.03	0.47×0.28×0.19	0.32×0.07×0.03	0.45×0.32×0.02
T/K	120.0	120.0	120.0	120.0	120.0	120.0
Crystal System	monoclinic	monoclinic	orthorhombic	monoclinic	triclinic	orthorhombic
Flack/Hooft Parameters	-	0.005(10)/-0.003(9)	-	-	-	-
Space Group	$P2_1/c$	$P2_1$	Pbca	$P2_1/c$	P-1	Pbca
a/Å	7.1130(3)	7.10996(16)	14.0747(4)	16.1908(3)	10.2393(2)	14.0888(6)
b/Å	10.2464(5)	10.2978(2)	10.3531(2)	10.41623(19)	14.2193(3)	10.2661(4)
c/Å	26.0466(13)	13.8317(3)	31.3324(10)	14.1087(3)	18.1746(4)	39.2028(19)
α/°	90	90	90	90	76.834(2)	90
β/°	91.273(4)	103.201(2)	90	101.560(2)	81.3824(19)	90
γ/°	90	90	90	90	89.2989(19)	90
V/Å^3	1897.88(15)	985.95(4)	4565.6(2)	2331.11(8)	2546.84(10)	5670.2(4)
Z (Z')	4 (1)	2 (1)	8 (1)	4 (1)	4 (2)	8 (1)
Wavelength/Å	0.71073	0.71073	0.71073	0.71073	1.54184	0.71073
Radiation type	MoK_α	MoK_α	MoK_α	MoK_α	CuK_α	MoK_α
Θ_{min}/° - Θ_{max}/°	3.076 - 28.753	2.943 – 31.252	2.767 - 31.223	2.970 – 31.306	3.193 – 76.399	2.892 – 25.350
Measured Refl.	111506	31889	48743	48698	51940	41273
Independent Refl.	5954	5981	6888	7156	10528	5174
Reflections Used	5411	5674	5507	6488	9114	3810
R_{int}	0.0863	0.0503	0.0806	0.0417	0.0909	0.1282
Parameters	226	237	264	281	593	329
Restraints	2	1	2	0	4	2
Largest Peak	0.552	0.347	0.520	0.516	1.591	0.490
Deepest Hole	-0.587	-0.487	-0.559	-0.469	-1.041	-0.388
GooF	1.117	1.057	1.110	1.040	1.040	0.933
wR_2 (all data) (wR_2)	0.0984 (0.0970)	0.0582 (0.0564)	0.0990 (0.0915)	0.0696 (0.0671)	0.1546 (0.1471)	0.1536 (0.1334)
R_1 (all data) (R_1)	0.0483 (0.0419)	0.0302 (0.0274)	0.0720 (0.0506)	0.0334 (0.0286)	0.0632 (0.0560)	0.0823 (0.0522)

Table S2. Crystallographic information for compounds **7**-**9**.

Compound	**7**	**8**	**9**
Formula	$C_{13}H_{29}Cl_3Cr_2N_2O_6$	$C_{42}H_{76}Cl_6Cr_4N_4O_{13}$	$C_{10}H_{24}Cl_4Cr_2N_2O_4$
$D_{calc.}$/ g cm^{-3}	1.646	1.525	1.813
μ/mm^{-1}	1.449	1.119	1.851
Formula Weight	519.73	1265.76	482.11
Colour	dark green	dark green	dark purple
Shape	block	block	block
Size/mm^3	0.51×0.24×0.23	0.35×0.09×0.05	0.34×0.12×0.07
T/K	120.0	120.0	120.0
Crystal System	monoclinic	monoclinic	monoclinic
Flack/Hooft Parameters	-	-	-
Space Group	$P2_1/c$	$P2_1/c$	$P2_1/n$
a/Å	11.5711(3)	7.1699(2)	6.8880(2)
b/Å	13.2720(3)	11.0066(3)	9.9275(3)
c/Å	13.6565(3)	34.9817(7)	12.9510(3)
α/°	90	90	90
β/°	90.948(2)	93.103(2)	94.457(3)
γ/°	90	90	90
V/Å^3	2096.96(9)	2756.58(12)	882.91(4)
Z (Z')	4 (1)	2 (0.5)	2 (0.5)
Wavelength/Å	0.71073	0.71073	0.71073
Radiation type	MoK_α	MoK_α	MoK_α
Θ_{min}/° - Θ_{max}/°	3.413 – 29.786	2.845 - 29.773	3.155 – 29.807
Measured Refl.	36587	48300	15425
Independent Refl.	5540	7202	2315
Reflections Used	4952	5556	2149
R_{int}	0.0434	0.0586	0.0378
Parameters	264	365	148
Restraints	43	9	0
Largest Peak	0.813	0.449	0.378
Deepest Hole	-0.495	-0.496	-0.395
GooF	1.079	1.034	1.083
wR_2 (all data) (wR_2)	0.0955 (0.0924)	0.0860 (0.0813)	0.0576 (0.0560)
R_1 (all data) (R_1)	0.0475 (0.0415)	0.0629 (0.0407)	0.0284 (0.0250)

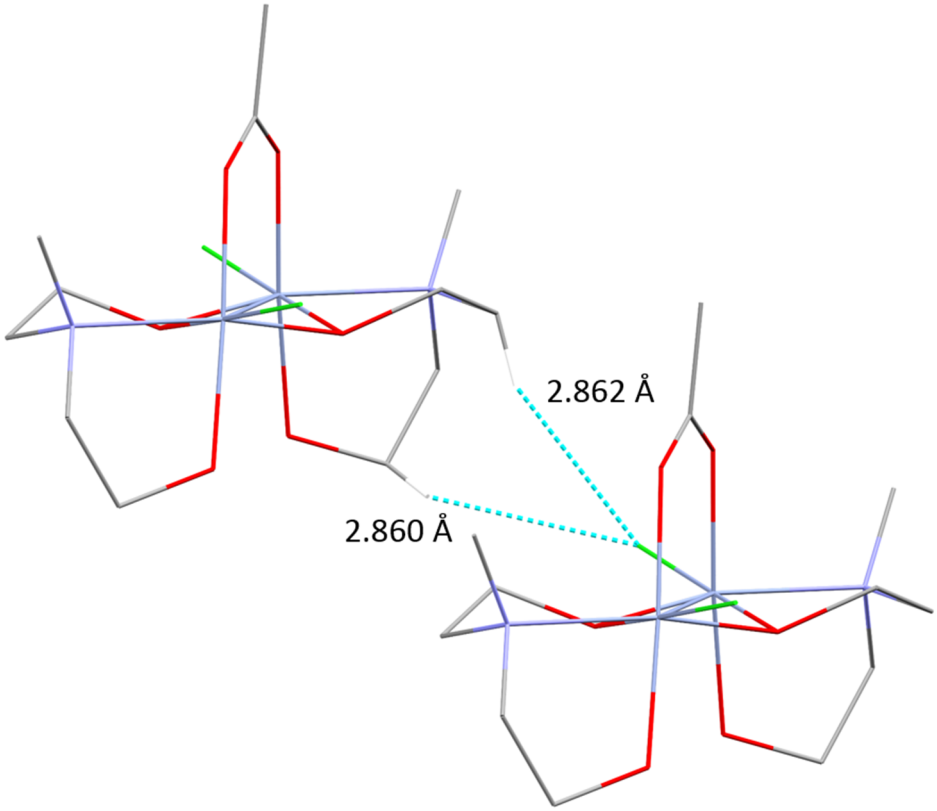

Figure S10. Representative diagrammatic example of $d_{H(Me)\text{-}Cl}$ closest interactions between two dimers in compound **2**. Non-relevant hydrogens and anions have been omitted for clarity.

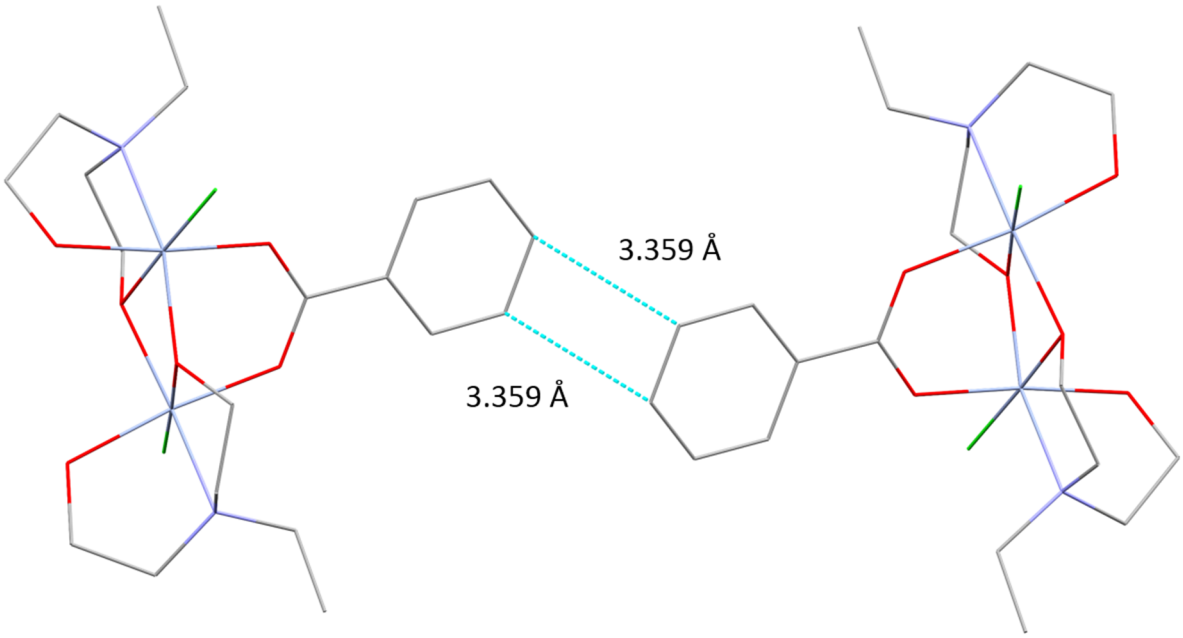

Figure S11. Representative diagrammatic example of $d_{\pi\text{-}\pi}$ closest interactions between two dimers in compound **8**. Hydrogens and anions have been omitted for clarity.

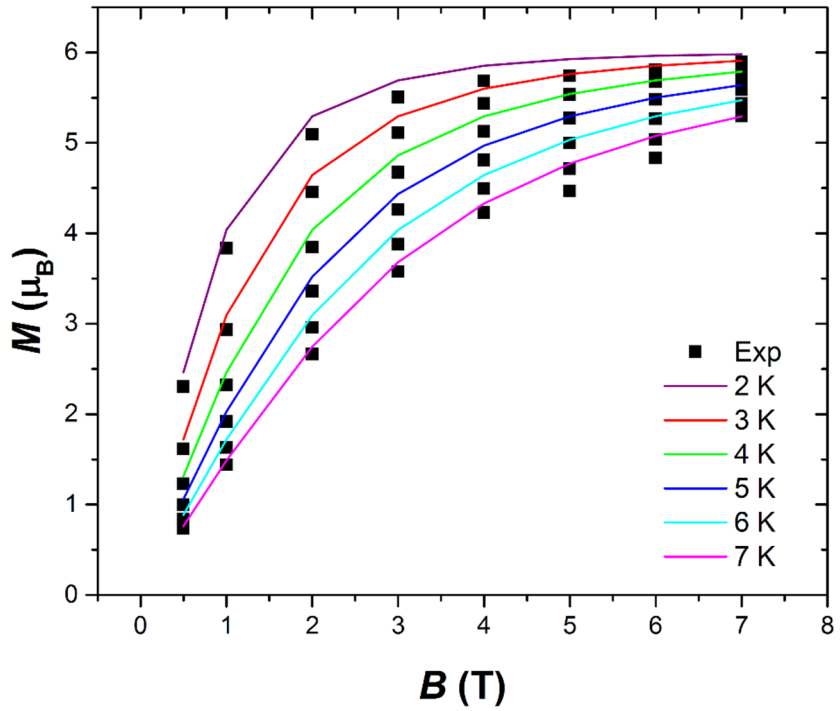

Figure S12. Plot of the magnetization (*M*) versus field (*B*) for compound **1** in the indicated field and temperature ranges. The solid black lines are a fit of the experimental data. See text for full details.

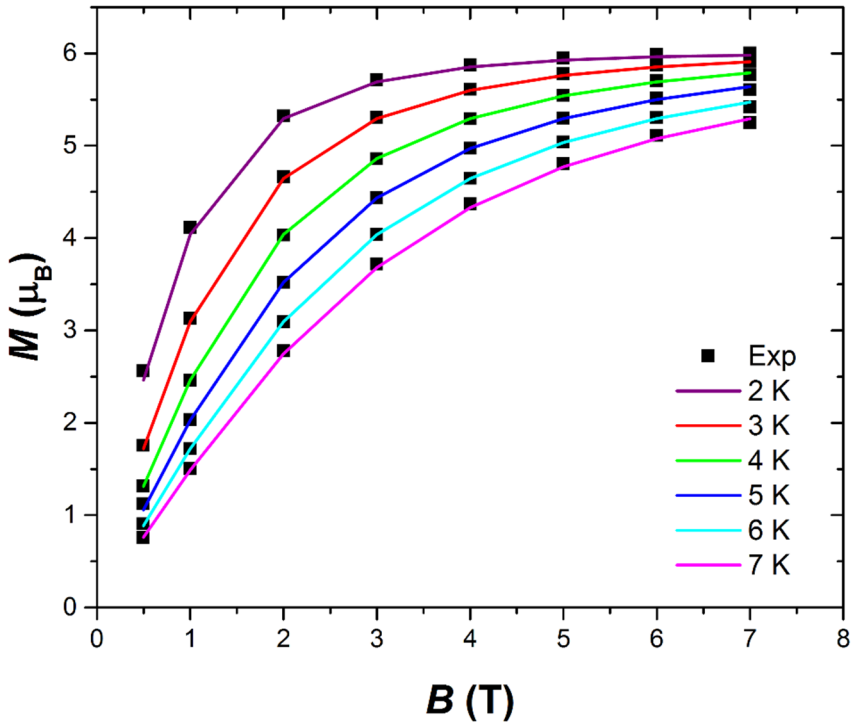

Figure S13. Plot of the magnetization (*M*) versus field (*B*) for compound **2** in the indicated field and temperature ranges. The solid black lines are a fit of the experimental data. See text for full details.

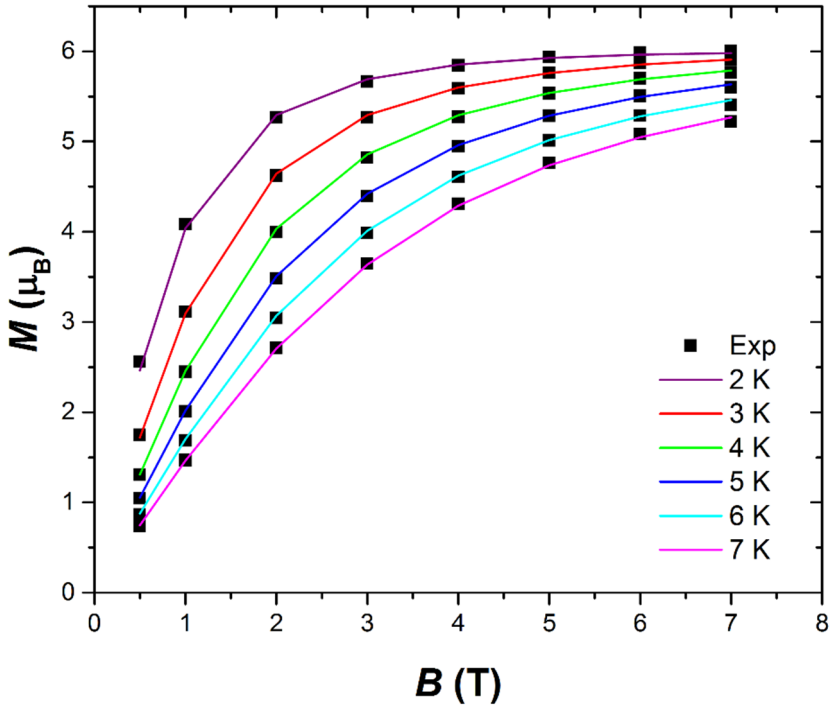

Figure S14. Plot of the magnetization (*M*) versus field (*B*) for compound **3** in the indicated field and temperature ranges. The solid black lines are a fit of the experimental data. See text for full details.

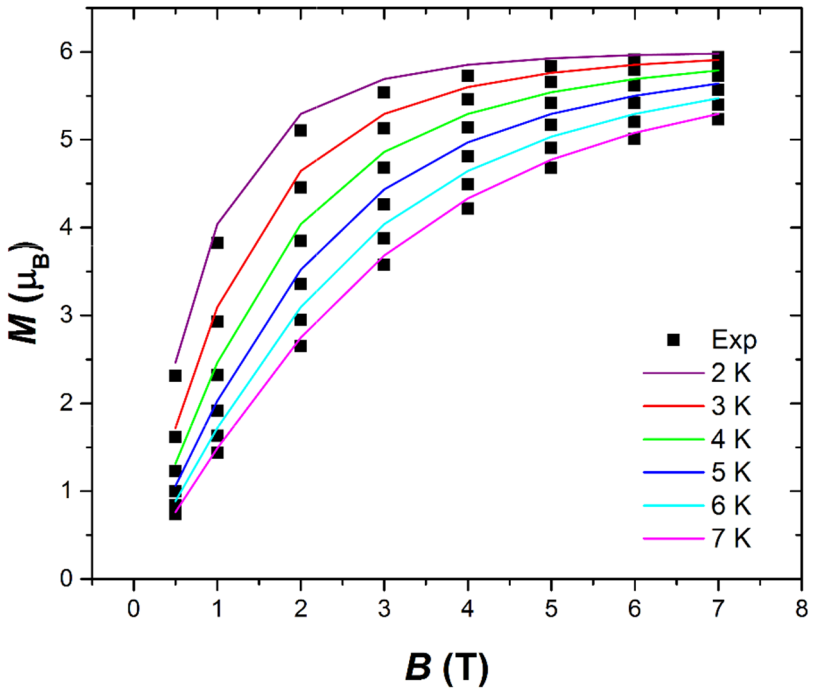

Figure S15. Plot of the magnetization (*M*) versus field (*B*) for compound **4** in the indicated field and temperature ranges. The solid black lines are a fit of the experimental data. See text for full details.

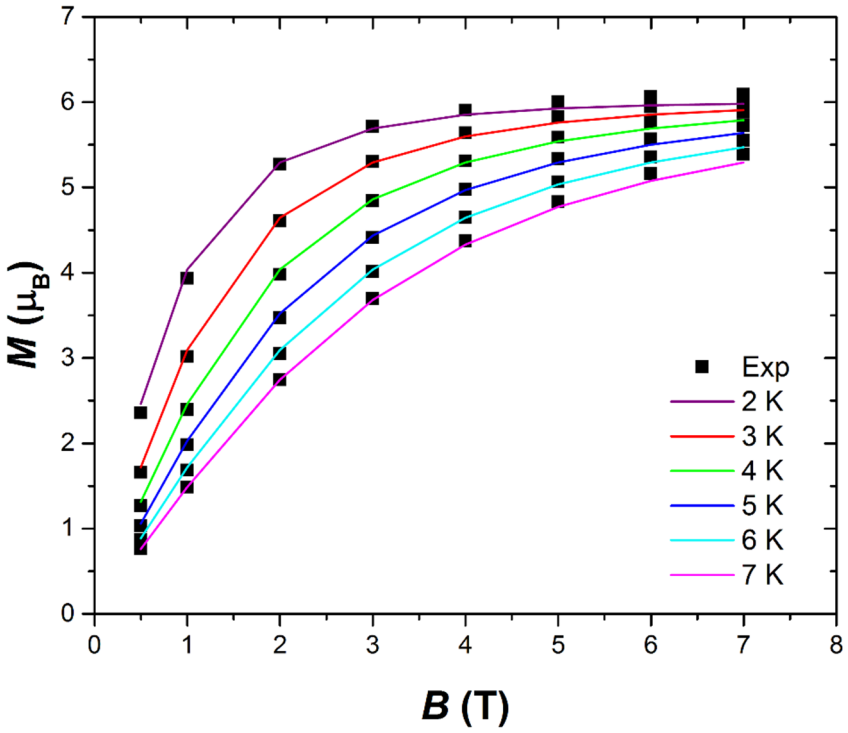

Figure S16. Plot of the magnetization (*M*) versus field (*B*) for compound **5** in the indicated field and temperature ranges. The solid black lines are a fit of the experimental data. See text for full details.

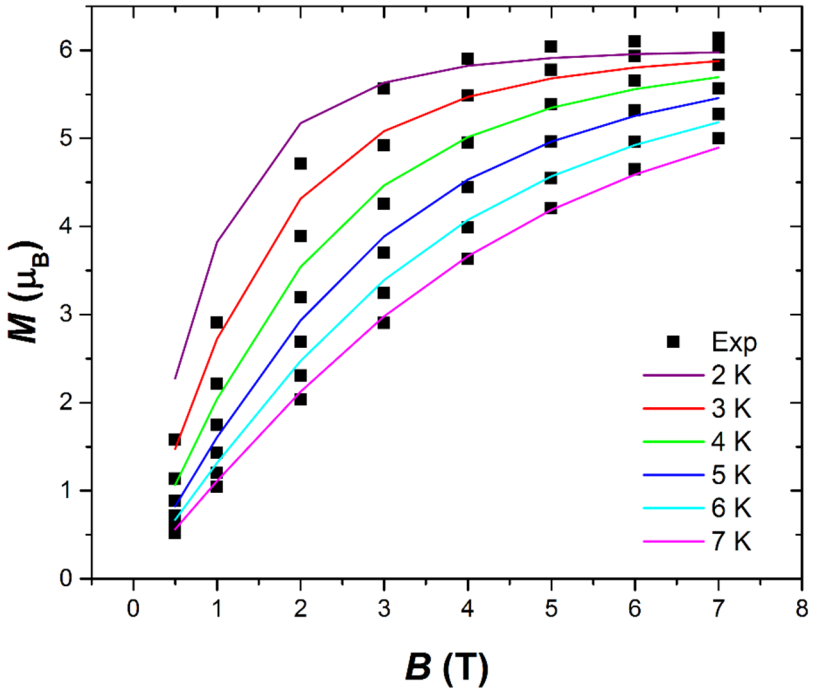

Figure S17. Plot of the magnetization (*M*) versus field (*B*) for compound **6** in the indicated field and temperature ranges. The solid black lines are a fit of the experimental data. See text for full details.

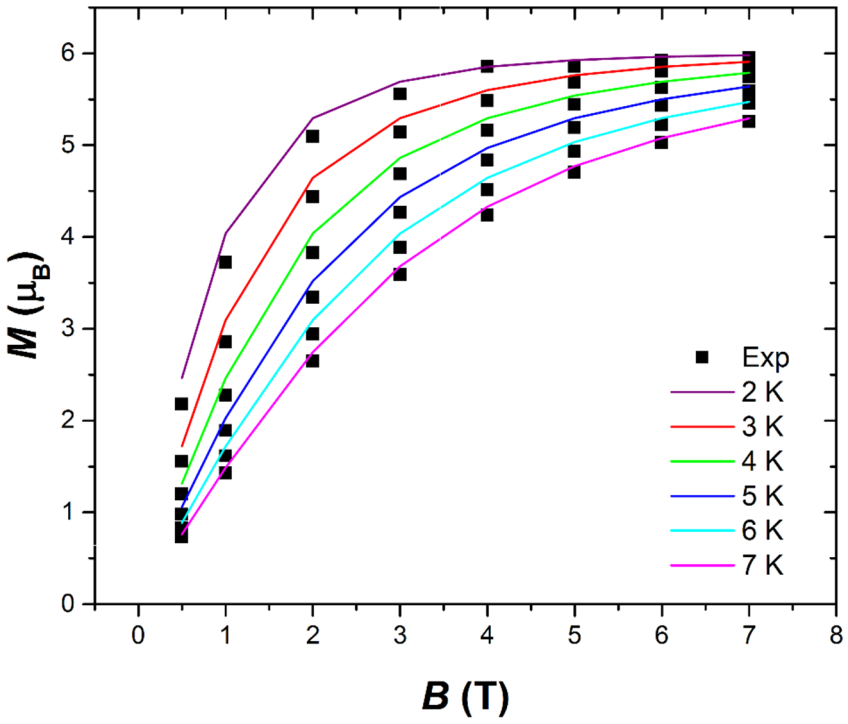

Figure S18. Plot of the magnetization (*M*) versus field (*B*) for compound **7** in the indicated field and temperature ranges. The solid black lines are a fit of the experimental data. See text for full details.

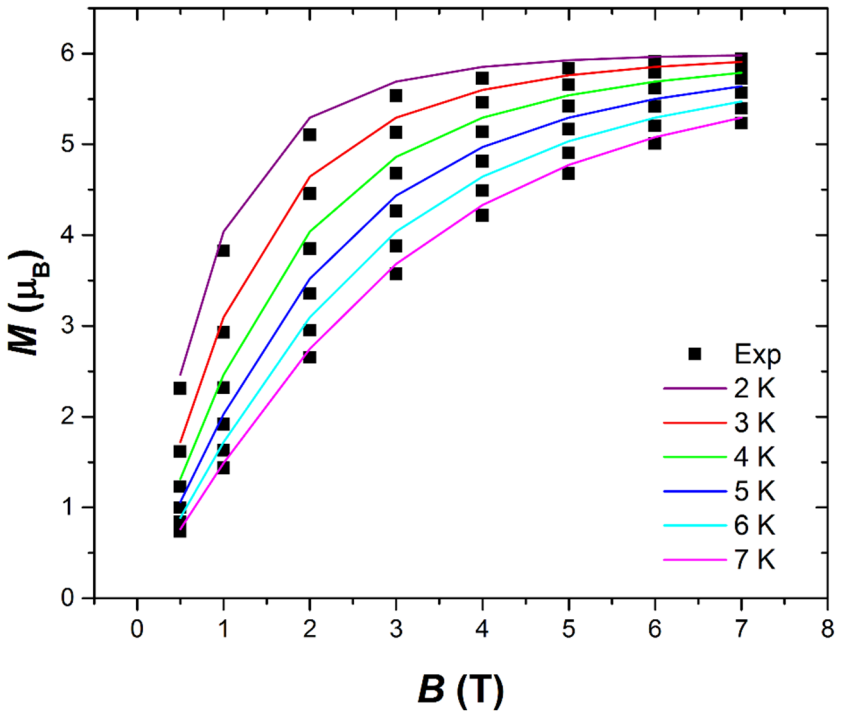

Figure S19. Plot of the magnetization (*M*) versus field (*B*) for compound **8** in the indicated field and temperature ranges. The solid black lines are a fit of the experimental data. See text for full details.

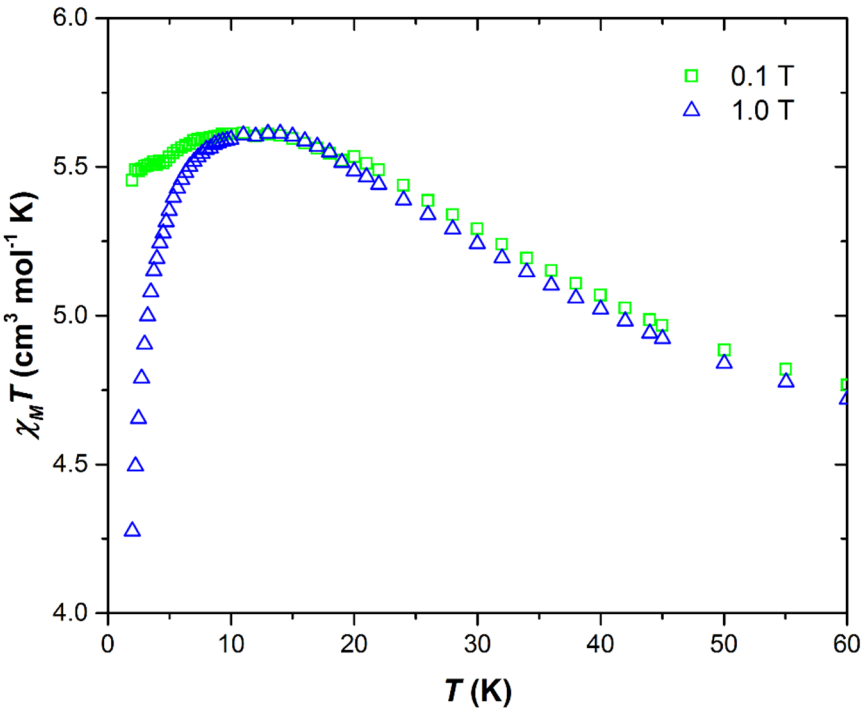

Figure S20. Plot of the $\chi_M T$ product versus T for complex **1** in applied fields of 0.1 T and 1.0 T as shown. The graph shows the field dependence of the intermolecular interactions. See main text for full details.

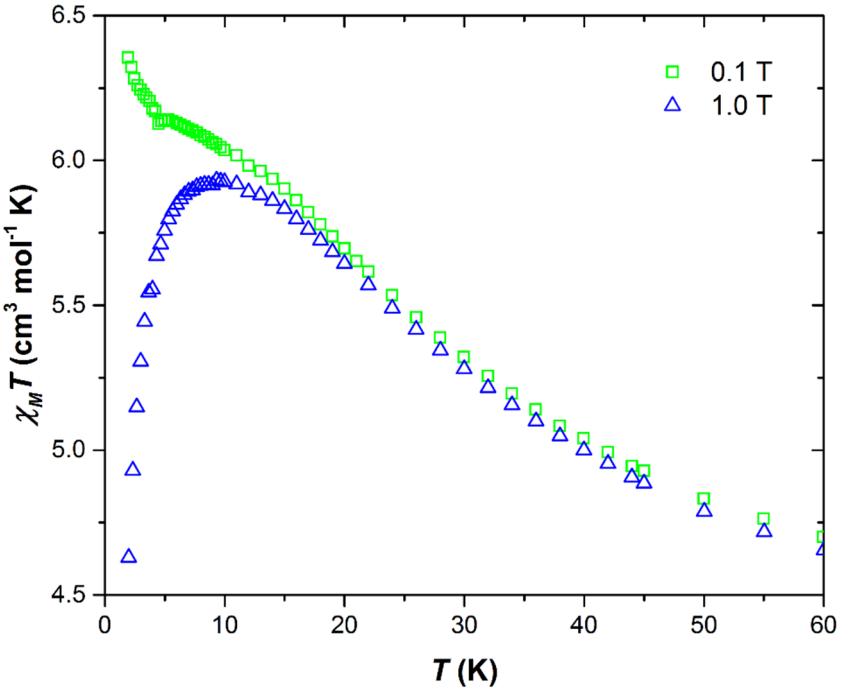

Figure S21. Plot of the $\chi_M T$ product versus T for complex **2** in applied fields of 0.1 T and 1.0 T as shown. The graph shows the field dependence of the intermolecular interactions. See main text for full details.

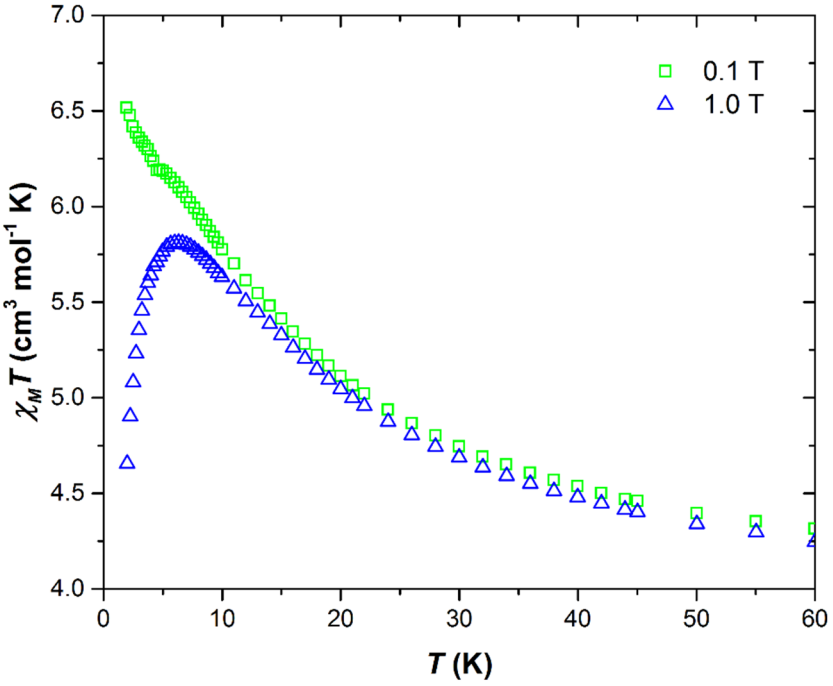

Figure S22. Plot of the $\chi_M T$ product versus T for complex **3** in applied fields of 0.1 T and 1.0 T as shown. The graph shows the field dependence of the intermolecular interactions. See main text for full details.

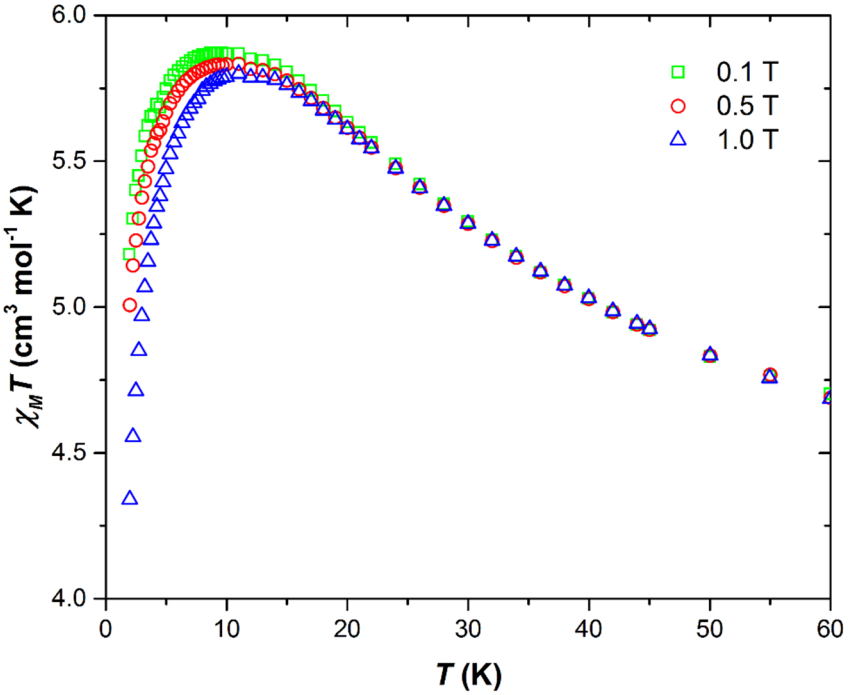

Figure S23. Plot of the $\chi_M T$ product versus T for complex **4** in applied fields of 0.1 T, 0.5 T and 1.0 T as shown. The graph shows the field dependence of the intermolecular interactions. See main text for full details.

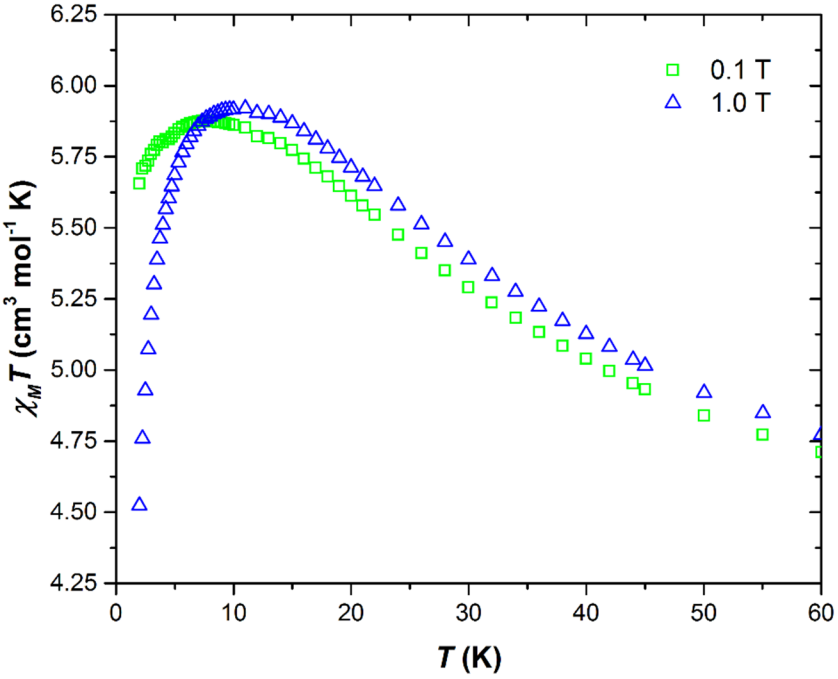

Figure S24. Plot of the $\chi_M T$ product versus T for complex **5** in applied fields of 0.1 T and 1.0 T as shown. The graph shows the field dependence of the intermolecular interactions. See main text for full details.

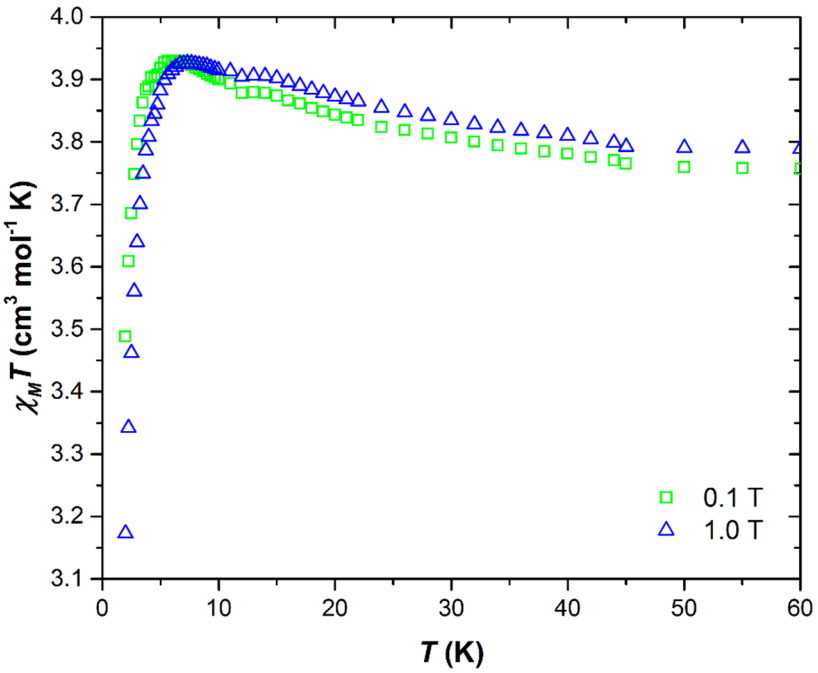

Figure S25. Plot of the $\chi_M T$ product versus T for complex **6** in applied fields of 0.1 T and 1.0 T as shown. The graph shows the field dependence of the intermolecular interactions. See main text for full details.

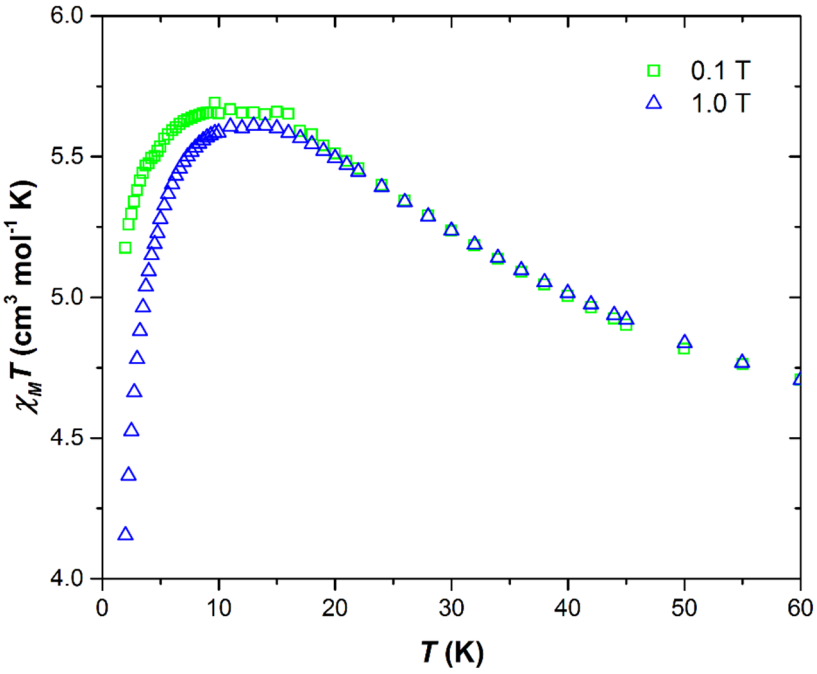

Figure S26. Plot of the $\chi_M T$ product versus T for complex **7** in applied fields of 0.1 T and 1.0 T as shown. The graph shows the field dependence of the intermolecular interactions. See main text for full details.

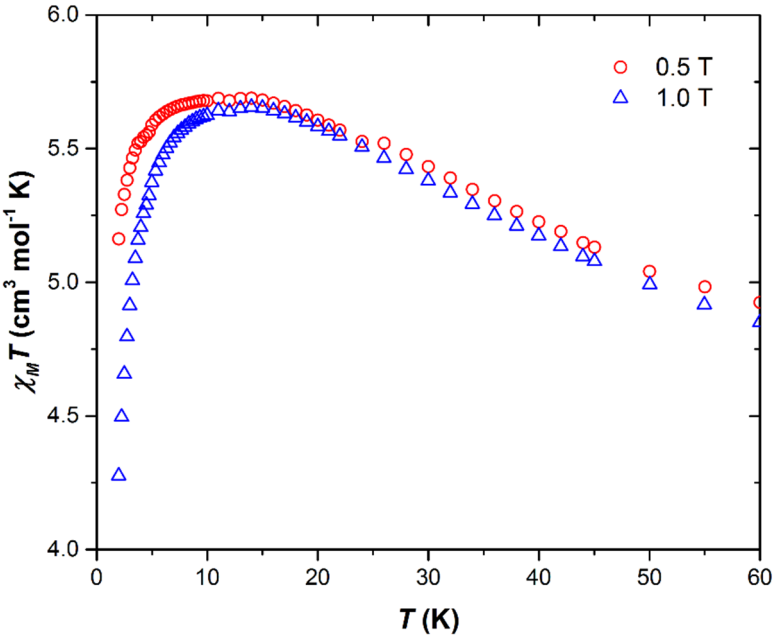

Figure S27. Plot of the $\chi_M T$ product versus T for complex **8** in applied fields of 0.5 T and 1.0 T as shown. The graph shows the field dependence of the intermolecular interactions. See main text for full details.

Table S3. *J* values using the GHP model.

Complex	*J* (cm^{-1})
1	0.65
2	-1.34
3	21.38
4	0.42
5	11.87
6	10.60
7	15.86
8	17.30
9	-682.46

Table S4. Overlap integrals for compounds **1**-**9**.

Overlap integral of complex **1**

Beta **Alpha**	$\mathbf{d_{xy}}$	$\mathbf{d_{yz}}$	$\mathbf{d_{xz}}$
$\mathbf{d_{xy}}$	0.137	-0.153	-0.217
$\mathbf{d_{yz}}$	-0.100	-0.21	-0.041
$\mathbf{d_{xz}}$	0.038	-0.006	-0.049

Overlap integral of complex **2**

Beta **Alpha**	$\mathbf{d_{xy}}$	$\mathbf{d_{yz}}$	$\mathbf{d_{xz}}$
$\mathbf{d_{xy}}$	-0.075	0.031	-0.034
$\mathbf{d_{yz}}$	0.024	-0.011	-0.003
$\mathbf{d_{xz}}$	0.097	-0.017	-0.157

Overlap integral of complex **3**

Beta **Alpha**	$\mathbf{d_{xy}}$	$\mathbf{d_{yz}}$	$\mathbf{d_{xz}}$
$\mathbf{d_{xy}}$	-0.080	-0.103	0.004
$\mathbf{d_{yz}}$	0.065	-0.006	0.083
$\mathbf{d_{xz}}$	-0.023	-0.003	0.303

Overlap integral of complex **4**

Beta **Alpha**	$\mathbf{d_{xy}}$	$\mathbf{d_{yz}}$	$\mathbf{d_{xz}}$
$\mathbf{d_{xy}}$	-0.079	0.095	-0.001
$\mathbf{d_{yz}}$	-0.079	-0.130	-0.049
$\mathbf{d_{xz}}$	0.006	-0.068	0.042

Overlap integral of complex **5**

Beta **Alpha**	$\mathbf{d_{xy}}$	$\mathbf{d_{yz}}$	$\mathbf{d_{xz}}$
$\mathbf{d_{xy}}$	0.078	0.162	0.087
$\mathbf{d_{yz}}$	-0.151	-0.246	-0.048
$\mathbf{d_{xz}}$	0.071	-0.063	0.037

Overlap integral of complex **6**

Beta **Alpha**	$\mathbf{d_{xy}}$	$\mathbf{d_{yz}}$	$\mathbf{d_{xz}}$
$\mathbf{d_{xy}}$	0.021	-0.074	0.008
$\mathbf{d_{yz}}$	0.111	0.043	-0.158
$\mathbf{d_{xz}}$	0.012	-0.084	0.064

Overlap integral of complex **7**

Beta **Alpha**	$\mathbf{d_{xy}}$	$\mathbf{d_{yz}}$	$\mathbf{d_{xz}}$
$\mathbf{d_{xy}}$	-0.069	-0.067	0.009
$\mathbf{d_{yz}}$	-0.181	0.016	-0.161
$\mathbf{d_{xz}}$	0.038	-0.068	0.038

Overlap integral of complex **8**

Beta Alpha	d_{xy}	d_{yz}	d_{xz}
d_{xy}	-0.069	-0.067	0.009
d_{yz}	-0.181	0.016	-0.161
d_{xz}	0.038	-0.069	0.038

Overlap integral of complex **9**

Beta Alpha	d_{xy}	d_{yz}	d_{xz}
d_{xy}	-0.115	0.036	-0.079
d_{yz}	0.036	0.047	-0.101
d_{xz}	0.079	0.101	0.150

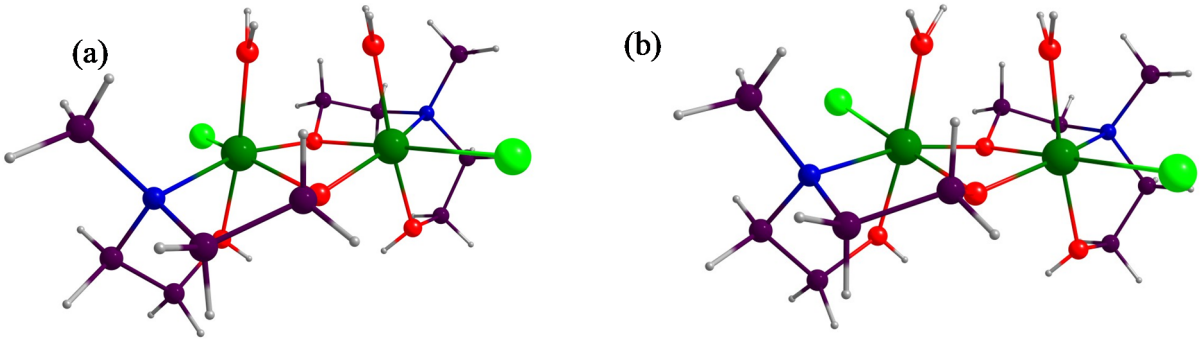

Figure S28. Structure of complexes (a) **1a** and (b) **4a**.

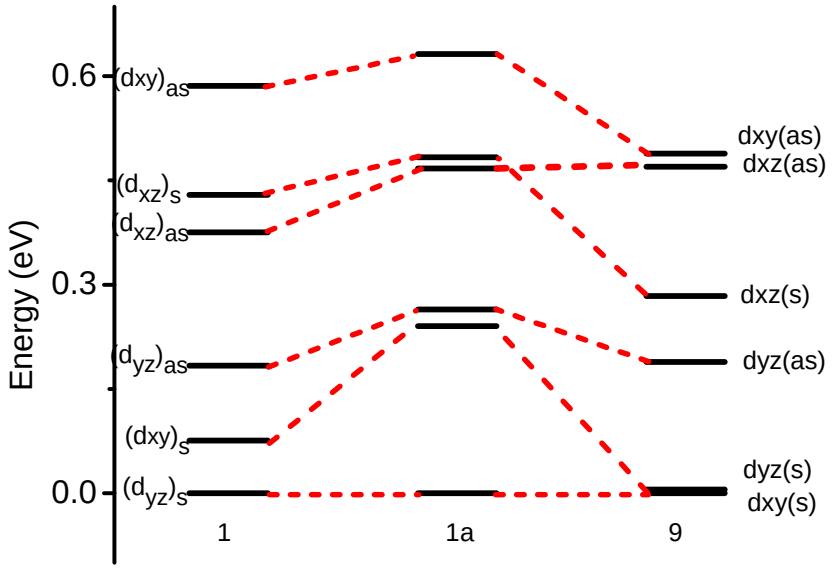

Figure S29. MO energy level splitting for **1**, **1a** and **9**.

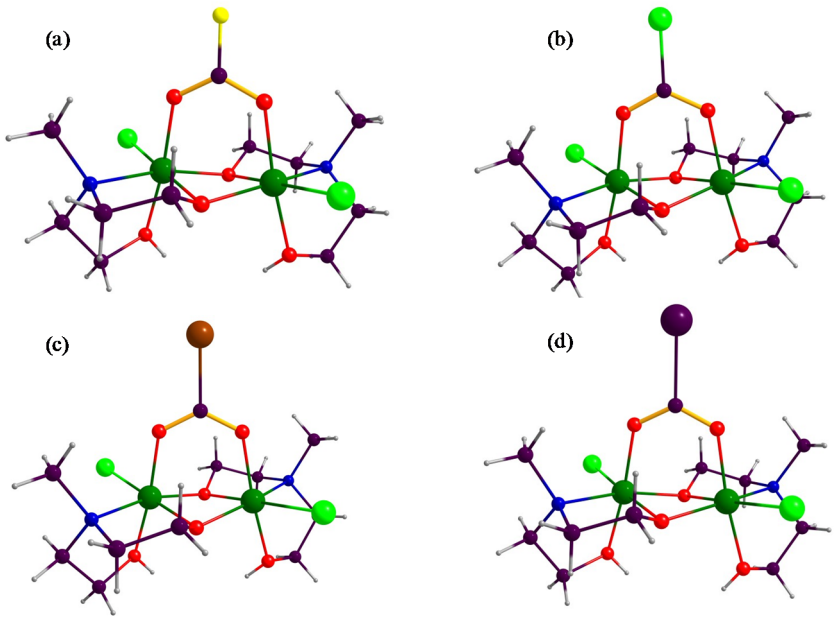

Figure S30. Halogen substitution in **1**. Substitution with fluorine (a), chlorine (b), bromine (c) and iodine (d).

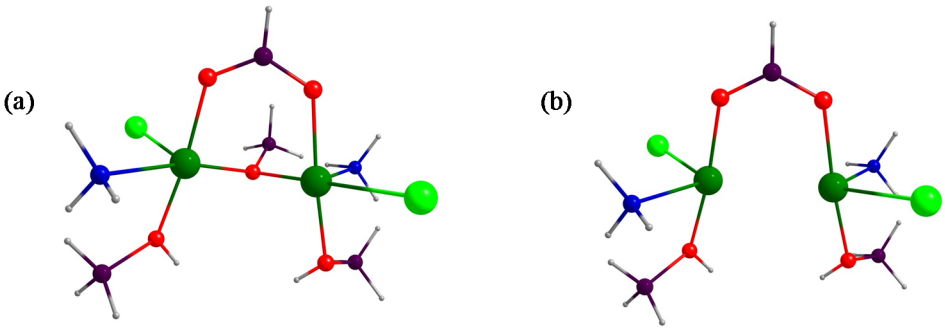

Figure S31. (a) Structure of complex **1b**. (b) Structure of complex **1c**.

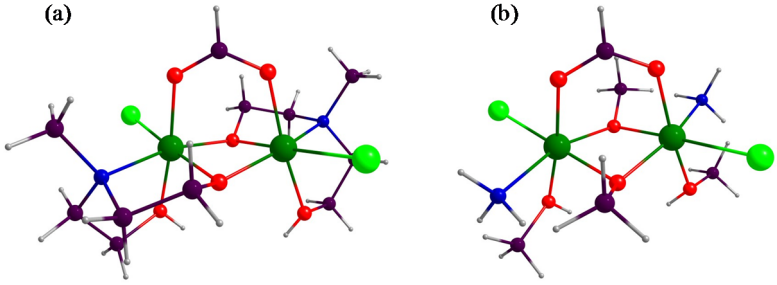

Figure S32. (a) Structure of complex **1** (J = 6.3 cm^{-1}). (b) Structure of the model complex derived from complex **1** (J = 7.4 cm^{-1}) for the magneto-structural correlation.

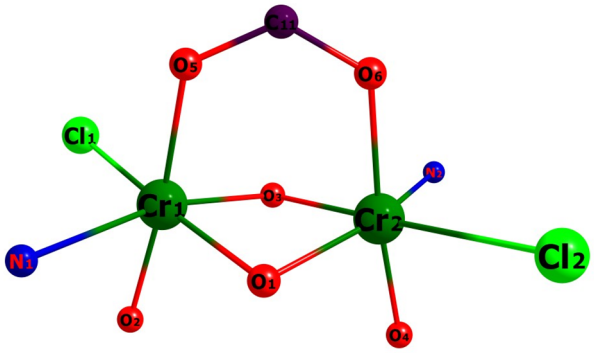

Figure S33. Model complex showing the atomic numbering scheme for spin density calculations.

Table S5. DFT computed spin densities of the chromium ions and atoms bonded to chromium ions for **1**-**9**.

	1		**2**		**3**		**4**		**5**	
	HS	**BS**	**HS**	**BS**	**HS**	**HS**	**HS**	**BS**	**HS**	**BS**
Cr1	3.015	3.012	3.014	3.010	3.006	3.006	3.009	3.004	3.009	3.005
Cr2	3.009	-3.006	3.011	-3.007	3.002	3.002	3.009	-3.004	3.012	-3.007
O1	0.008	-0.003	0.000	-0.000	-0.000	-0.000	-0.001	-0.001	-0.002	-0.000
O2	-0.012	-0.011	-0.012	-0.012	-0.013	-0.013	-0.012	-0.012	-0.013	-0.013
O3	-0.000	0.001	-0.002	0.002	0.010	0.010	0.000	0.002	-0.001	0.002
O4	-0.012	0.011	-0.013	-0.012	-0.014	-0.014	-0.012	0.011	-0.012	0.011
O5	-0.014	-0.037	-0.013	-0.033	-0.014	-0.014	-0.012	-0.029	-0.012	-0.030
O6	-0.014	0.036	-0.013	0.032	-0.013	-0.013	-0.014	0.030	-0.012	0.028
N1	-0.043	-0.045	-0.042	-0.043	-0.042	-0.042	-0.042	-0.043	-0.041	-0.041
N2	-0.043	0.045	-0.042	0.043	-0.043	-0.043	-0.042	0.043	-0.040	-0.040
Cl1	0.026	0.024	0.026	0.024	0.030	0.030	0.029	0.027	0.029	0.027
Cl2	0.029	-0.026	0.030	-0.028	0.032	0.032	0.032	-0.029	0.026	-0.024

	6		**7**		**8**		**9**	
	HS	**BS**	**HS**	**BS**	**HS**	**BS**	**HS**	**BS**
Cr1	3.014	3.011	3.009	3.005	3.006	3.004	3.015	3.010
Cr2	3.005	-2.998	3.012	-3.007	3.001	-2.997	3.015	-3.010
O1	-0.001	-0.001	-0.002	-0.000	-0.001	0.000	-0.000	0.001
O2	-0.012	-0.012	-0.013	-0.013	-0.011	-0.011	-0.010	-0.009
O3	0.014	0.003	-0.001	0.002	0.002	0.001	-0.000	-0.001
O4	-0.012	0.012	-0.012	0.011	-0.013	0.013	-0.010	0.009
O5	-0.013	-0.034	-0.012	-0.030	-0.014	-0.037	0.011(Cl3)	0.011(Cl3)
O6	-0.015	0.033	-0.012	0.028	-0.012	0.037	0.020(Cl4)	0.020(Cl4)
N1	-0.044	-0.045	-0.041	-0.041	-0.043	-0.045	-0.037	0.038
N2	-0.041	0.042	-0.040	-0.040	-0.038	0.038	-0.038	-0.038
Cl1	0.024	0.021	0.029	0.027	0.032	0.030	-0.011	0.011
Cl2	0.032	-0.032	0.026	-0.024	0.036	-0.034	0.020	-0.020

Table S6. Spin density for models **4a** and **4b**.

	4a		4b	
	HS	**BS**	**HS**	**BS**
Cr1	2.869	2.866	3.002	2.996
Cr2	2.862	-2.868	2.999	-2.993
O1	-0.010	-0.000	0.004	-0.001
O2	-0.011	-0.010	-0.015	-0.014
O3	-0.010	0.001	0.006	0.001
O4	-0.011	0.010	-0.014	0.014
O5	0.162	0.143	-0.008	-0.009
O6	0.158	-0.140	-0.007	0.008
N1	-0.032	-0.033	-0.048	-0.049
N2	-0.033	0.034	-0.049	0.050
Cl1	0.013	0.011	0.035	0.033
Cl2	0.015	-0.012	0.039	-0.037

	1-F		1-Cl		1-Br		1-I	
	HS	**BS**	**HS**	**BS**	**HS**	**BS**	**HS**	**BS**
Cr1	3.009	3.005	3.011	3.007	3.012	3.009	3.014	3.010
Cr2	3.004	-2.999	3.005	-3.002	3.006	-3.003	3.008	-3.004
O1	0.002	-0.003	0.002	-0.003	0.001	-0.002	0.001	-0.003
O2	-0.013	-0.012	-0.013	-0.012	-0.012	-0.012	-0.012	-0.012
O3	0.001	0.001	0.000	0.001	0.000	0.001	0.000	0.001
O4	-0.012	0.011	-0.012	0.011	-0.012	0.012	-0.012	0.011
O5	-0.009	-0.026	-0.009	-0.029	-0.010	-0.030	-0.011	-0.031
O6	-0.009	0.025	-0.010	0.028	-0.010	0.029	-0.011	0.030
N1	-0.044	-0.045	-0.044	-0.046	-0.044	-0.045	-0.044	-0.045
N2	-0.045	0.046	-0.044	0.046	-0.044	0.046	-0.044	0.046
Cl1	0.028	0.026	0.027	0.025	0.027	0.025	0.027	0.025
Cl2	0.030	-0.028	0.030	-0.028	0.030	-0.028	0.030	-0.027
F/Cl/Br/I	-0.001	0.000	-0.006	0.000	3.012	3.009	-0.010	0.000

Table S7. Overlap integral with magneto-structural correlations.

Cr-O-Cr angle:

Φ = 83°

Alpha Beta	**d_{xy}**	**d_{xz}**	**d_{yz}**
d_{xy}	-0.079	0.126	-0.084
d_{xz}	-0.150	-0.292	-0.309
d_{yz}	0.112	-0.426	-0.073

Φ = 88°

Alpha Beta	**d_{xy}**	**d_{xz}**	**d_{yz}**
d_{xy}	-0.092	0.044	-0.124

d_{xz}	-0.093	-0.342	-0.263
d_{yz}	0.167	-0.399	0.020

Φ = 93°

Alpha Beta	**d_{xy}**	**d_{xz}**	**d_{yz}**
d_{xy}	-0.069	-0.033	-0.131
d_{xz}	-0.036	-0.365	-0.197
d_{yz}	0.176	-0.329	0.056

Φ = 98°

Alpha Beta	**d_{xy}**	**d_{xz}**	**d_{yz}**
d_{xy}	-0.017	-0.093	-0.135
d_{xz}	0.011	-0.345	-0.136
d_{yz}	0.157	-0.215	0.052

Φ = 103°

Alpha Beta	**d_{xy}**	**d_{xz}**	**d_{yz}**
d_{xy}	0.038	0.125	-0.158
d_{xz}	-0.043	-0.255	-0.108
d_{yz}	0.155	-0.124	-0.041

Φ = 108°

Alpha Beta	**d_{xy}**	**d_{xz}**	**d_{yz}**
d_{xy}	0.051	-0.118	0.176
d_{xz}	0.047	-0.113	-0.114
d_{yz}	-0.175	0.087	0.041

Cr-O-Cr-O dihedral angle:

Ψ = 0.1°

Alpha Beta	**d_{xy}**	**d_{yz}**	**d_{xz}**
d_{xy}	0.197	0.183	0.285
d_{xz}	-0.104	0.737	-0.950
d_{yz}	-0.428	-0.082	-0.084

Ψ = 4.8°

Alpha Beta	**d_{xy}**	**d_{yz}**	**d_{xz}**
d_{xy}	-0.163	-0.102	0.234
d_{xz}	0.000	0.758	0.288
d_{yz}	-0.412	0.034	-0.059

Ψ = 8.7°

Alpha Beta	**d_{xy}**	**d_{yz}**	**d_{xz}**

d_{xy}	0.072	-0.139	0.159
d_{xz}	0.070	-0.777	-0.064
d_{yz}	-0.193	-0.123	-0.094

Ψ = 13.4°

Alpha Beta	d_{xy}	d_{yz}	d_{xz}
d_{xy}	0.005	-0.105	0.122
d_{xz}	0.024	-0.618	-0.006
d_{yz}	-0.153	0.006	-0.016

Ψ = 18.3°

Alpha Beta	d_{xy}	d_{yz}	d_{xz}
d_{xy}	-0.017	-0.093	-0.135
d_{xz}	0.011	-0.345	-0.136
d_{yz}	-0.157	-0.215	0.052

Ψ = 23.1°

Alpha Beta	d_{xy}	d_{yz}	d_{xz}
d_{xy}	-0.014	-0.472	-0.161
d_{xz}	0.140	-0.737	-0.236
d_{yz}	-0.249	-0.164	0.007

Cr-O_{carb} distance:

τ = 1.6 Å

Alpha Beta	d_{xy}	d_{yz}	d_{xz}
d_{xy}	-0.039	-0552	-0.105
d_{xz}	0.157	0.735	0.050
d_{yz}	0.230	0.145	-0.066

τ = 1.7 Å

Alpha Beta	d_{xy}	d_{yz}	d_{xz}
d_{xy}	-0.013	-0.363	-0.102
d_{xz}	0.127	0.772	0.056
d_{yz}	0.206	0.036	0.034

τ = 1.8 Å

Alpha Beta	d_{xy}	d_{yz}	d_{xz}
d_{xy}	-0.003	-0.147	-0.108
d_{xz}	0.073	0.487	0.082
d_{yz}	0.177	-0.248	0.068

τ = 1.9 Å

Alpha Beta	d_{xy}	d_{yz}	d_{xz}

d_{xy}	-0.017	-0.093	-0.135
d_{xz}	0.011	-0.345	-0.136
d_{yz}	-0.157	-0.215	0.052

τ = 2.0 Å

Alpha Beta	**d_{xy}**	**d_{yz}**	**d_{xz}**
d_{xy}	-0.138	0.148	-0.244
d_{xz}	0.175	0.202	-0.199
d_{yz}	0.214	-0.052	0.007

τ = 2.1 Å

Alpha Beta	**d_{xy}**	**d_{yz}**	**d_{xz}**
d_{xy}	-0.054	-0.311	0.452
d_{xz}	0.413	0.054	0.137
d_{yz}	0.411	0.389	-0.022

τ = 2.2 Å

Alpha Beta	**d_{xy}**	**d_{yz}**	**d_{xz}**
d_{xy}	-0.445	0.168	0.180
d_{xz}	-0.369	-0.511	0.032
d_{yz}	0.093	0.205	-0.445

<u>Out of plane shift:</u>

θ = 55.70°

Alpha Beta	**d_{xy}**	**d_{yz}**	**d_{xz}**
d_{xy}	-0.056	-0.035	-0.178
d_{xz}	0.028	-0.131	-0.222
d_{yz}	0.087	-0.194	0.020

θ = 50.74°

Alpha Beta	**d_{xy}**	**d_{yz}**	**d_{xz}**
d_{xy}	-0.042	-0.062	-0.154
d_{xz}	0.019	-0.194	-0.186
d_{yz}	0.108	-0.213	0.033

θ = 45.76°

Alpha Beta	**d_{xy}**	**d_{yz}**	**d_{xz}**
d_{xy}	-0.030	-0.080	-0.141
d_{xz}	0.013	-0.261	-0.159
d_{yz}	0.132	-0.217	0.044

θ = 40.79°

Alpha	**d_{xy}**	**d_{yz}**	**d_{xz}**

Beta			
d_{xy}	-0.017	-0.093	-0.135
d_{xz}	0.011	-0.345	-0.136
d_{yz}	-0.157	-0.215	0.052

θ = 35.89°

Alpha **Beta**	**d_{xy}**	**d_{yz}**	**d_{xz}**
d_{xy}	-0.047	0.103	-0.135
d_{xz}	0.011	-0.452	-0.110
d_{yz}	-0.185	-0.214	0.060

θ = 30.96°

Alpha **Beta**	**d_{xy}**	**d_{yz}**	**d_{xz}**
d_{xy}	0.062	0.113	-0.138
d_{xz}	-0.010	-0.553	0.083
d_{yz}	0.212	-0.212	0.069

θ = 26.03°

Alpha **Beta**	**d_{xy}**	**d_{yz}**	**d_{xz}**
d_{xy}	0.015	0.123	-0.142
d_{xz}	-0.021	-0.624	0.063
d_{yz}	0.236	0.208	0.077

θ = 21.20°

Alpha **Beta**	**d_{xy}**	**d_{yz}**	**d_{xz}**
d_{xy}	0.021	0.131	-0.144
d_{xz}	0.016	-0.662	0.053
d_{yz}	0.258	-0.202	-0.081

Chapter 4: Order in disorder: solution and solid-state studies of $[M^{III}_2M^{II}_5]$ wheels (M^{III} = Cr, Al; M^{II} = Ni, Zn)

Low temperature single-crystal X-ray crystallography

Low temperature single-crystal data of compound **2** were collected on XIPHOS I, a four-circle Huber goniometer equipped with an APEXII detector and rotating anode MoK_α radiation (λ = 0.71073 Å) focused using Helios optics.[1] The sample was mounted to a modified APD 202E Displex cryogenic refrigerator and cooled a rate of 1 K/minuet to a base temperature of 3.4 K. Cell indexing was carried out using the Bruker APEX III software. The low temperature sample environment allowed only unit cell parameters to be extracted at 3.4 K. On cooling the sample remains in the rhombohedral crystal system with unit cell parameters showing the expected thermal contraction from those determined at 120 K. This suggests that no large structural rearrangement occurs upon cooling. a,b = 14.522(0.001) Å, c = 36.2145(0.0029) Å, $\alpha = \beta = 90^o$, $\gamma = 120^o$, V = 6614.007(1.308) $Å^3$.

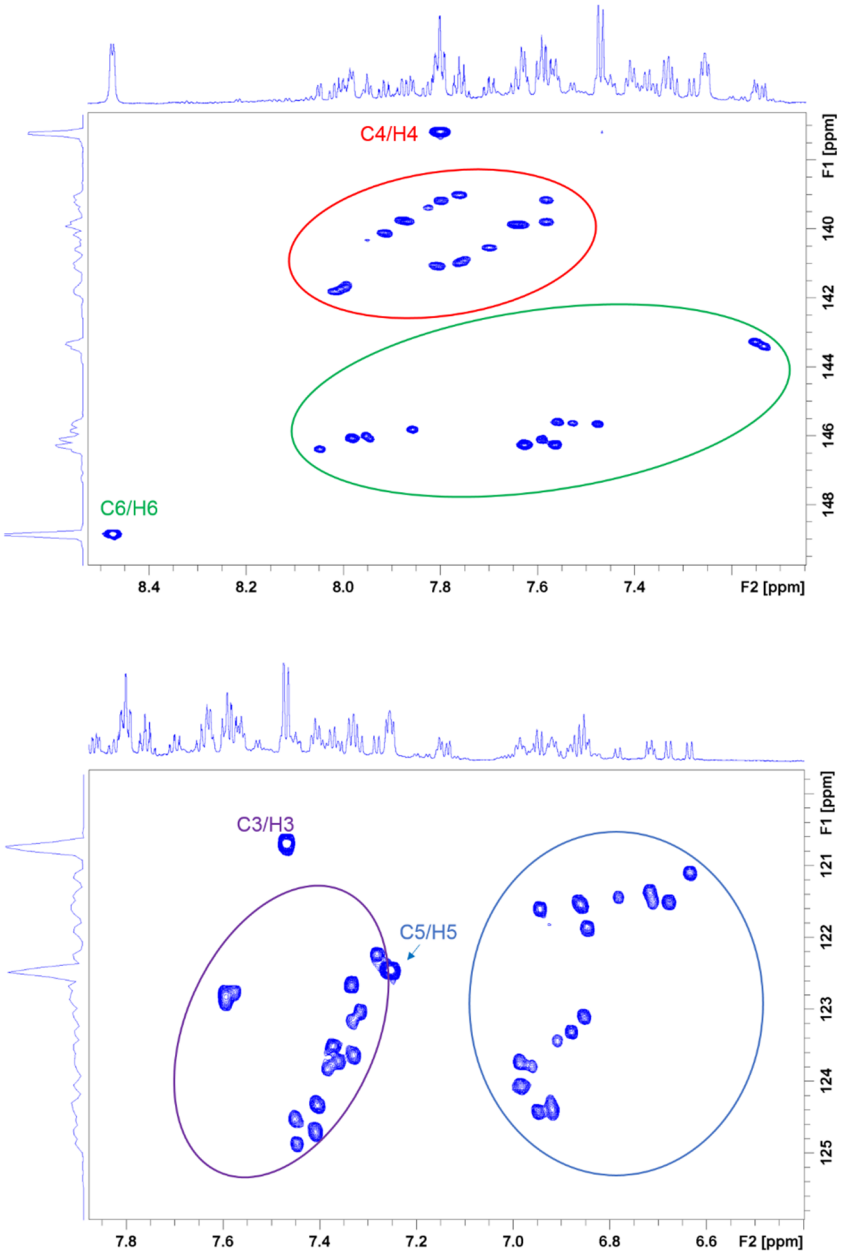

Figure S1. Partial 2D ^{1}H, ^{13}C HSQC spectrum of **4** showing (top) the C4/H4 and C6/H6 and (bottom) C3/H3 and C5/H5 cross peaks.

Table S1. Crystallographic information for compounds **1**-**4**.

Compound	**1**	**2**	**3**	**4**
Formula	$C_{79}H_{100}Cl_4Cr_2N_{12}Ni_5O_{35}$	$C_{81}H_{108}Cl_4Cr_2N_{12}O_{37}Zn_5$	$C_{81}H_{108}Al_2Cl_4N_{12}Ni_5O_{37}$	$C_{80}H_{104}Al_2Cl_4N_{12}O_{36}Zn_5$
$D_{calc.}$/ g cm^{-3}	1.674	1.727	1.674	1.679
μ/mm^{-1}	1.439	1.706	3.195	1.511
Formula Weight	2317.05	2414.44	2331.10	2332.36
Colour	blue	light purple	pale blue	colourless
Shape	block	plate	plate	plate
Size/mm^3	0.32×0.11×0.10	0.32×0.11×0.10	0.23×0.19×0.09	0.28×0.23×0.04
T/K	120.0	120.0	120.0	120.0
Crystal System	trigonal	trigonal	trigonal	trigonal
Space Group	R-3	R-3	R-3	R-3
a/Å	14.6131(3)	14.5920(3)	14.53160(10)	14.4962(5)
b/Å	14.6131(3)	14.5920(3)	14.53160(10)	14.4962(5)
c/Å	37.2857(9)	37.7623(14)	37.9260(9)	38.022(2)
α/°	90	90	90	90
β/°	90	90	90	90
γ/°	120	120	120	120
V/Å^3	6895.4(3)	6963.4(4)	6935.77(19)	6919.4(6)
Z (Z')	3 (0.16667)	3 (0.16667)	3 (0.16667)	3 (0.16667)
Wavelength/Å	0.71073	0.71073	1.54178	0.71073
Radiation type	MoK_α	MoK_α	CuK_α	MoK_α
Θ_{min}/° - Θ_{max}/°	1.638 – 25.339	2.792 – 25.350	3.700 – 76.591	2.810 – 26.372
Measured Refl.	26509	35087	32013	13554
Independent Refl.	2823	2846	3217	3142
Reflections Used	2044	2599	3044	2492
R_{int}	0.0491	0.0660	0.0502	0.0577
Parameters	186	202	186	187
Restraints	0	45	0	0
Largest Peak	0.976	1.903	0.878	1.427
Deepest Hole	-1.227	-0.593	-1.627	-0.919
GooF	1.086	1.150	1.134	1.092
wR_2 (all data) (wR_2)	0.1752 (0.1512)	0.1438 (0.1412)	0.2395 (0.2373)	0.1459 (0.1384)
R_1 (all data) (R_1)	0.0779 (0.0548)	0.0721 (0.0660)	0.0838 (0.0818)	0.0849 (0.0647)

References

1. M. R. Probert, C. M. Robertson, J. A. Coome, J. A. K. Howard, B. C. Michell and A. E. Goeta. *J. Appl. Crystallogr*., 2010, **43**, 1415-1418.

Chapter 5: Cages on a plane: a structural matrix for molecular 'sheets'

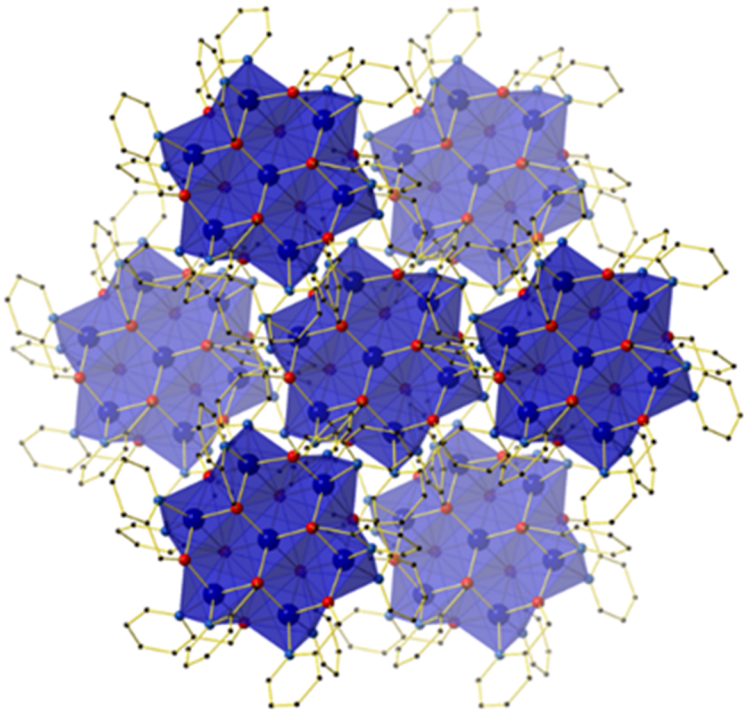

Figure S1. Crystal packing common to compounds **1**-**3** & **5** as viewed down the *c*-axis, highlighting the hexagonal packing arrangement formed by layers of molecules. H atoms, solvent molecules and counter anions omitted for clarity.

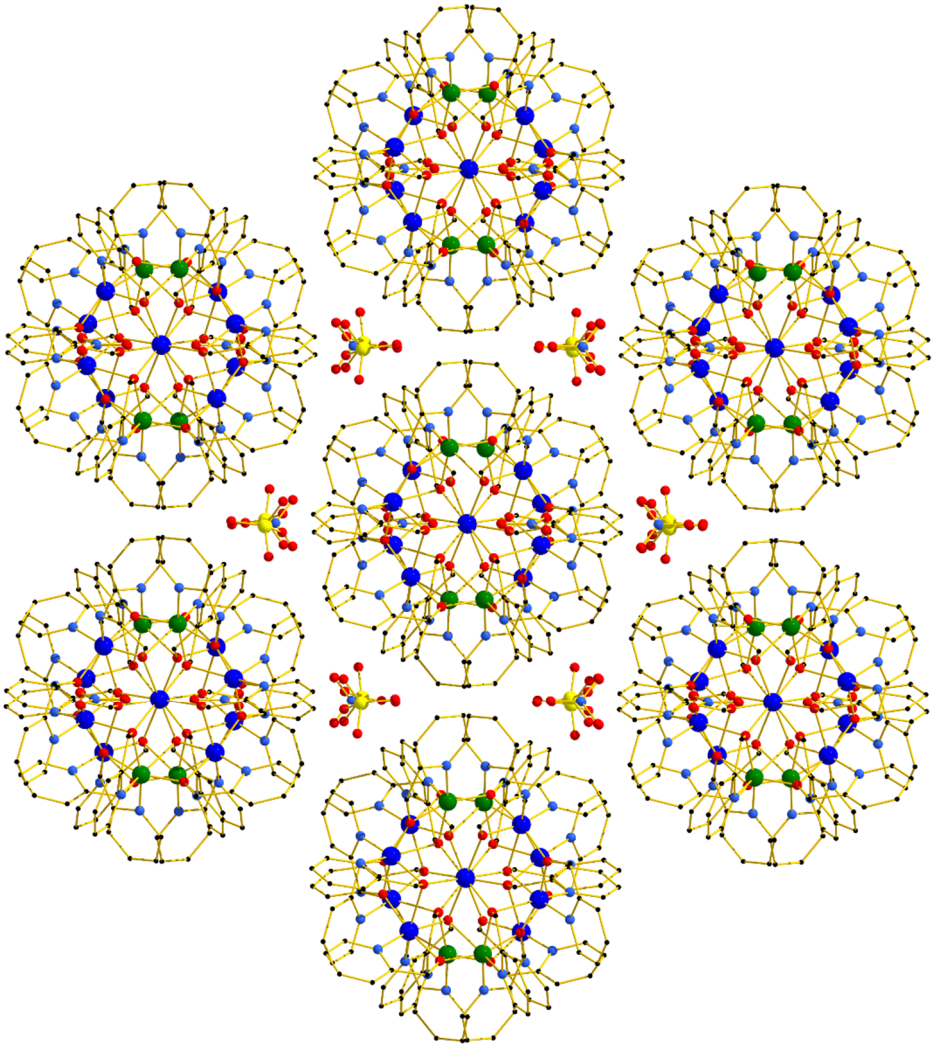

Figure S2. Packing diagram for compound **4** viewed down the *c*-axis. Colour code as Figure 4, Cl = yellow.

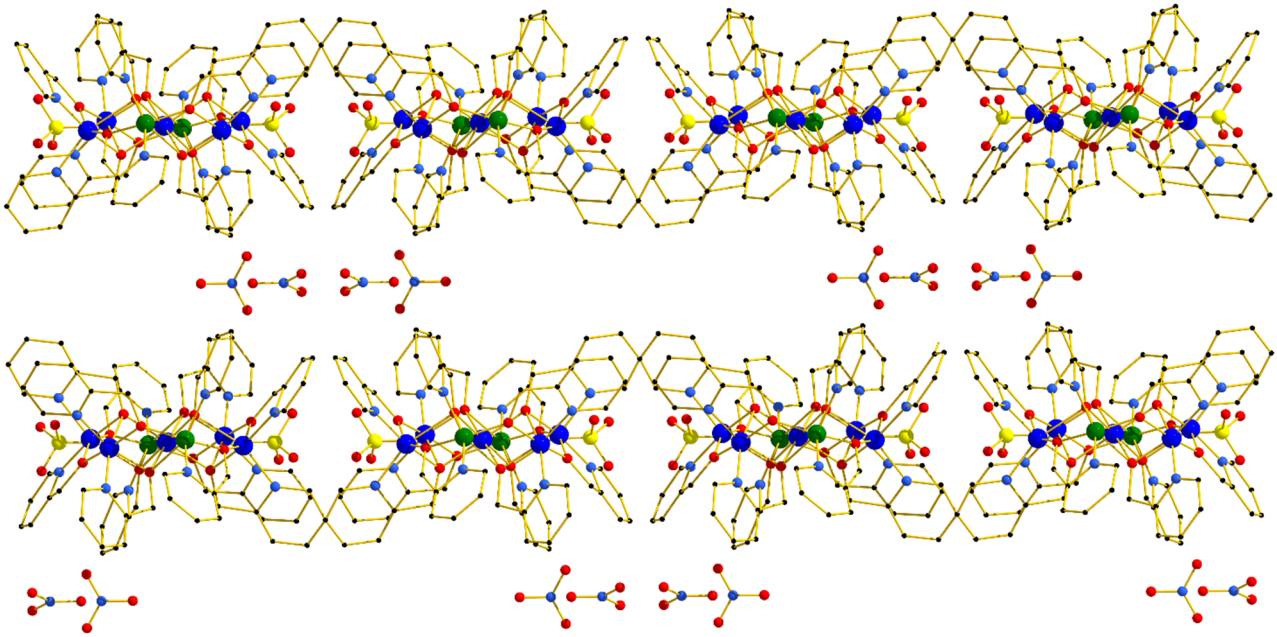

Figure S3. Packing diagram for compound **4** viewed down the *a*-axis. Colour code as Figure S2.

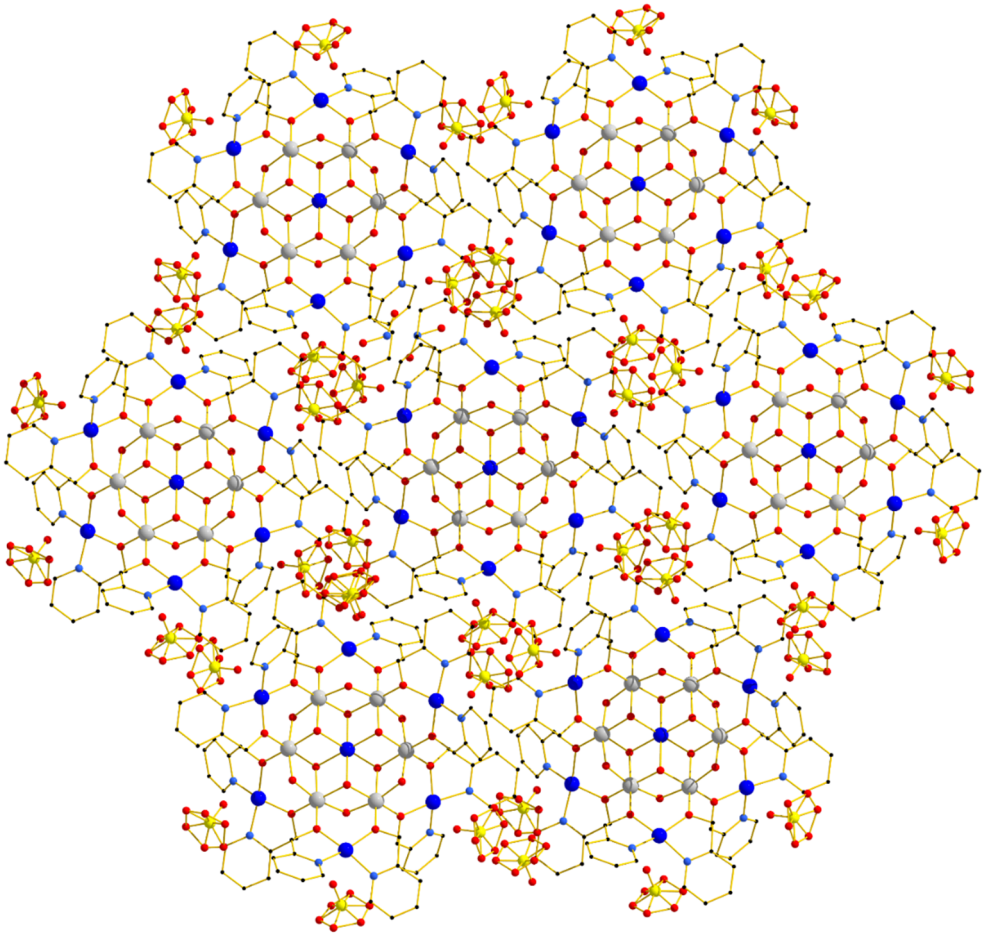

Figure S4. Packing diagram for compound **6** viewed down the *c*-axis. Colour code as Figure S3, Al = grey.

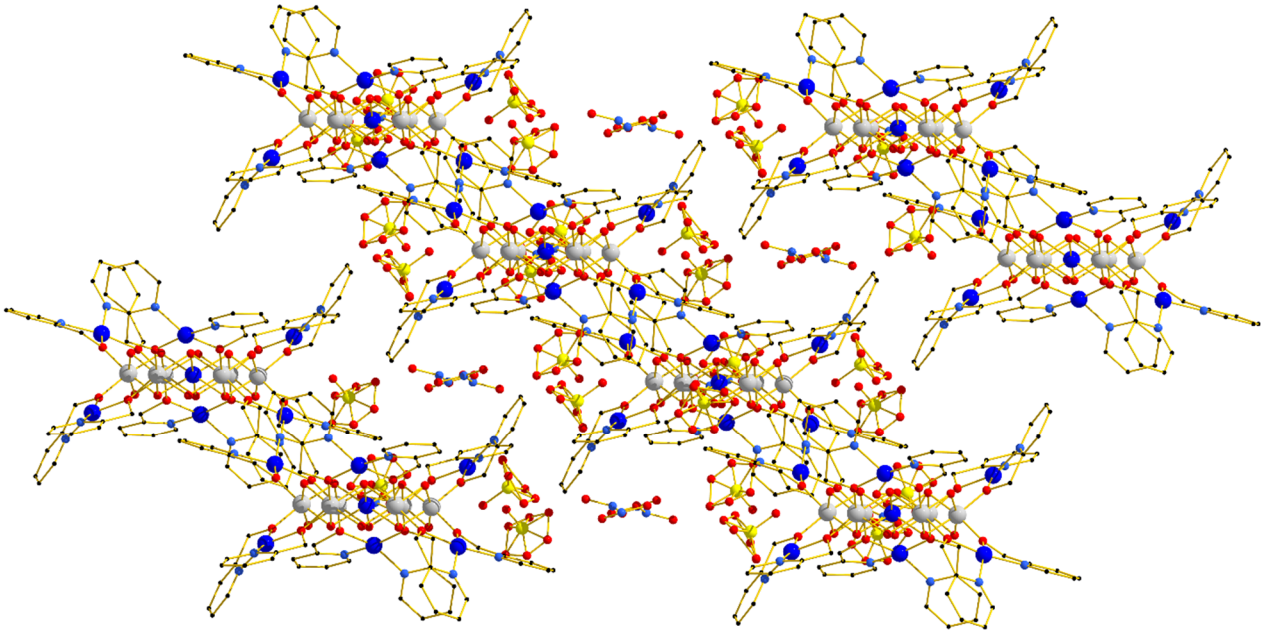

Figure S5. Packing diagram for compound **6** viewed down the *b*-axis. Colour code as Figure S3.

Table S1. Crystallographic information for compounds **1**-**6**.

Compound	**1**	**2**	**3**	**4**	**5**	**6**
Formula	$C_{81}H_{108}Cl_4Co_5Cr_2N_{12}O_{37}$	$C_{81}H_{108}Cl_4Cr_2Fe_5N_{12}O_{37}$	$C_{82}H_{112}Cl_4Cr_2Mn_5N_{12}O_{38}$	$C_{88}H_{136}Cl_2Cr_2Cu_5N_{14}O_{42}$	$C_{81}H_{108}Al_2Cl_4Co_5N_{12}O_{37}$	$C_{93}H_{168}Al_6Cl_6Cu_7N_{14}O_{75}$
$D_{calc.}$/ g cm^{-3}	1.657	1.682	1.672	1.859	1.637	1.468
μ/mm^{-1}	1.272	9.765	8.898	4.629	1.084	1.151
Formula Weight	2382.24	2366.84	2394.33	2554.70	2332.20	3501.76
Colour	dark pink	pale brown	pale purple	light purple	pale brown	dark blue
Shape	block	plate	plate	plate	plate	block
Size/mm^3	0.32×0.11×0.10	0.14×0.10×0.03	0.20×0.16×0.02	0.22×0.16×0.03	0.27×0.07×0.03	0.32×0.24×0.17
T/K	120.0	120.0	120.0	120	120.0	120.01(10)
Crystal System	trigonal	trigonal	trigonal	monoclinic	trigonal	trigonal
Space Group	R-3	R-3	R-3	*I*2/*a*	R-3	*R*-3
a/Å	14.7268(2)	14.6087(3)	14.7045(6)	14.5052(12)	14.6812(5)	27.8468(6)
b/Å	14.7268(2)	14.6087(3)	14.7045(6)	25.0735(19)	14.6812(5)	27.8468(6)
c/Å	38.1319(8)	37.9381(19)	38.106(5)	25.095(5)	38.0235(14)	17.6945(7)
α/°	90	90	90	90	90	90
β/°	90	90	90	90.268(13)	90	90
γ/°	120	120	120	90	120	120
V/Å^3	7162.0(2)	7011.8(5)	7135.4(11)	9127(2)	7097.5(5)	11882.8(7)
Z (Z')	3 (0.16667)	3 (0.16667)	3 (0.16667)	4 (0.5)	3 (0.16667)	3 (0.16667)
Wavelength/Å	0.71073	1.54184	1.54184	1.54184	0.71073	0.71073
Radiation type	MoK_α	Cu K_α	Cu K_α	Cu K_α	MoK_α	MoK_α
Θ_{min}/° - Θ_{max}/°	3.112 – 29.648	3.495 – 76.728	3.479 – 50.499	3.520 – 50.436	3.121 – 25.340	2.856 – 25.345
Measured Refl.	43856	32839	17837	10864	38106	49850
Independent Refl.	4234	3272	1673	10864	2893	4843
Reflections with I > 2(I)	3674	2673	1482	5280	2560	4209
R_{int}	0.0503	0.0968	0.0736	.	0.0900	0.0538
Parameters	196	199	260	205	196	274
Restraints	18	37	137	28	18	88
Largest Peak	0.428	1.455	0.633	3.431	0.728	1.219
Deepest Hole	-0.733	-1.027	-0.432	-1.655	-0.982	-0.604
GooF	1.069	1.052	1.074	1.558	1.136	1.055
wR_2 (all data) (wR_2)	0.0914 (0.0883)	0.2197 (0.2052)	0.2110 (0.2045)	0.4931 (0.4601)	0.1339 (0.1289)	0.1697 (0.1635)
R_1 (all data) (R_1)	0.0521 (0.0425)	0.0822 (0.0712)	0.0797 (0.0737)	0.2423 (0.1868)	0.0726 (0.0623)	0.0642 (0.0561)

Supplementary discussion: compound 4

This compound crystallized as apparently well-formed hexagonal plate-shaped crystals. Despite the optically attractive crystals the quality of the diffraction pattern was somewhat sub-par: weak (a 1 Å cut-off was applied during refinement) with some broad and diffuse streaking mixed with Bragg reflections. Plate stacking faults were assumed.

The original unit cell parameter determination suggested that the unit cell was hexagonal with $a = b = 28.97$ Å and $c = 25.10$ Å. With these unit cell parameters the structure solves to give two crystallographically inequivalent "wheels" and a model which refines to give classical R1 = 44.23%.

Further investigation of the diffraction pattern showed that a I-centred monoclinic cell (with parameters $a = 14.51$ Å, $b = 25.07$ Å, $c = 25.10$ Å, $\beta = 90.268°$) could be indexed. By iterative searching of the diffraction pattern two further orientations were found, each related by approximately 120°. The diffraction pattern was thus indexed and integrated as a three-component twin with each component rotated by approximately 120°, mimicking a hexagonal unit cell as shown in Figure S6.

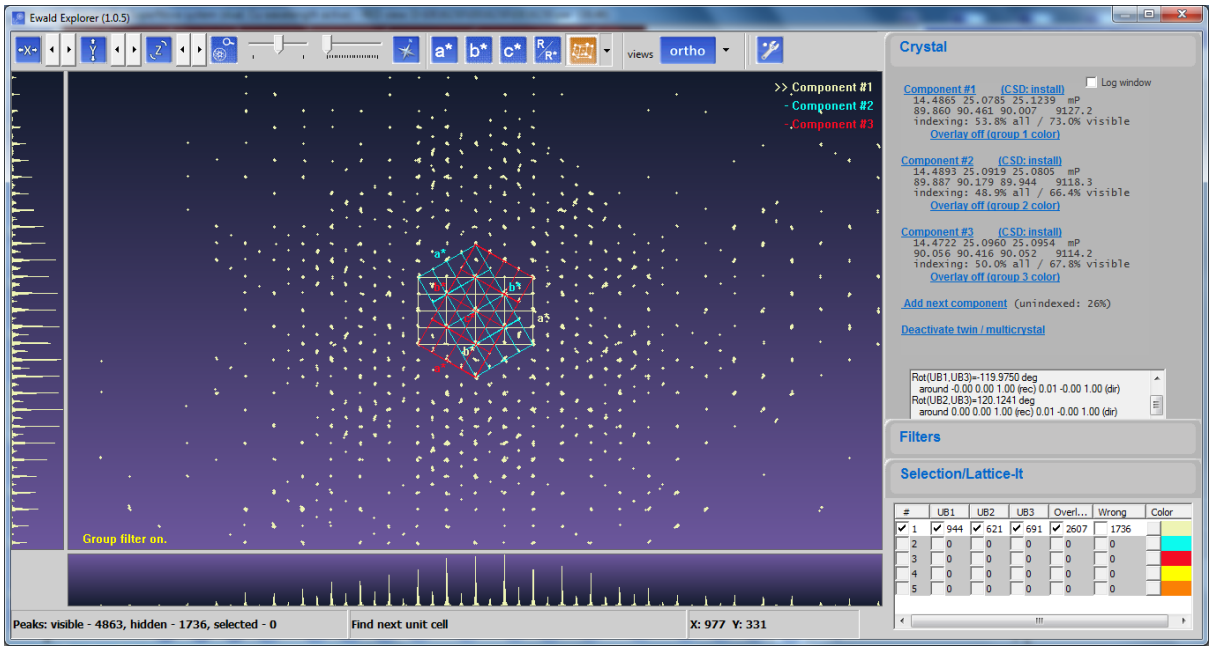

Figure S6. Reciprocal lattice plot (Ewald Explorer in CrysAlisPro) of the diffraction pattern of compound **4**. The three monoclinic unit cell orientations are indicated in the centre of the plot.

The structural model is not without problems. The metal centres were found easily by SHELXT and all non-H atoms of the wheel could be identified in a difference map without difficulty. The occupancies of the metals were allowed to refine and the location of the chromium centre was quite clear. Similarly, the atoms of the perchlorate counter ion were all easily identified. The nitrate anions were more

difficult to locate and were identified by looking for the shape of the species, over symmetry elements or not.

Refinement of the model proved more troublesome. All 6-membered rings have been fixed in place using the SHELXL AFIX 66 idealized hexagonal constraint. Similarly, the geometry in the Ph-C(H2)-O 'arm' was restrained using average bond distances determined by a search of the Cambridge Structural Database. The perchlorate anion was restrained using 1,2- and 1,3- distance restraints on all bonds and angles The nitrate anions were also restrained using 1,2- and 1,3- distance restraints. All of the metal sites, the chlorine, some oxygen and some nitrogen sites were refined using an isotropic model. All other sites were refined using an isotropic model for reasons of stability in the model. Some of the atoms were modelled with U(iso) allowed to refine, initially, and then fixed. This includes some atoms of the 6-membered rings.

No attempt to identify any solvent molecules was made. The SQUEEZE routine of PLATON, when fed a LIST 8-style structure factor file, was able to account for 524 electrons per unit cell. This approximates to 8 methanol per asymmetric unit or 16 per complete wheel. This missing additional solvent was included in the total chemical formula and derived values, triggering checkCIF alerts which should be ignored.

The model is presented refined as far as practical given the quality of the data and the twinning. The refinement restraints and constraints were needed to keep the model into the shape of something which was chemically reasonable. The structure is presented as part of a family of similar compounds, all with similar charge balance and other similar properties.

Twinning information (deconvoluted with CrysAlisPro):

Component 2 rotated by 120.0851° around [-0.00 0.00 1.00] (reciprocal) or [0.00 0.00 1.00] (direct).

Component 3 rotated by -119.9041° around [-0.00 0.00 1.00] (reciprocal) or [0.01 -0.00 1.00] (direct).

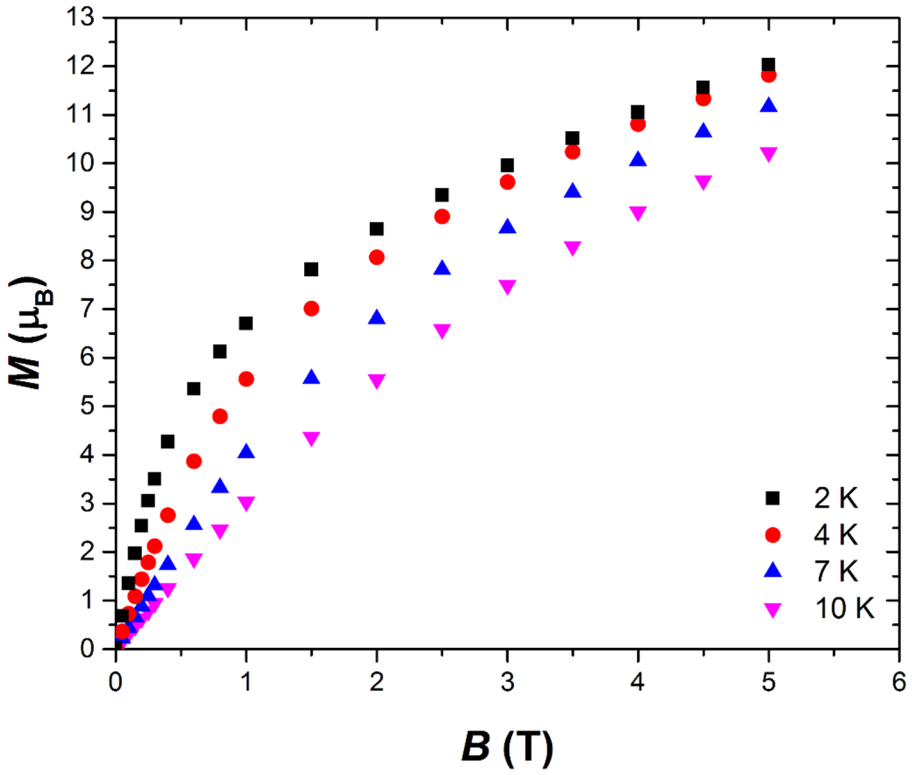

Figure S6. Plot of magnetisation (***M***) versus field (***B***) for compound **1** in the indicated field and temperature ranges.

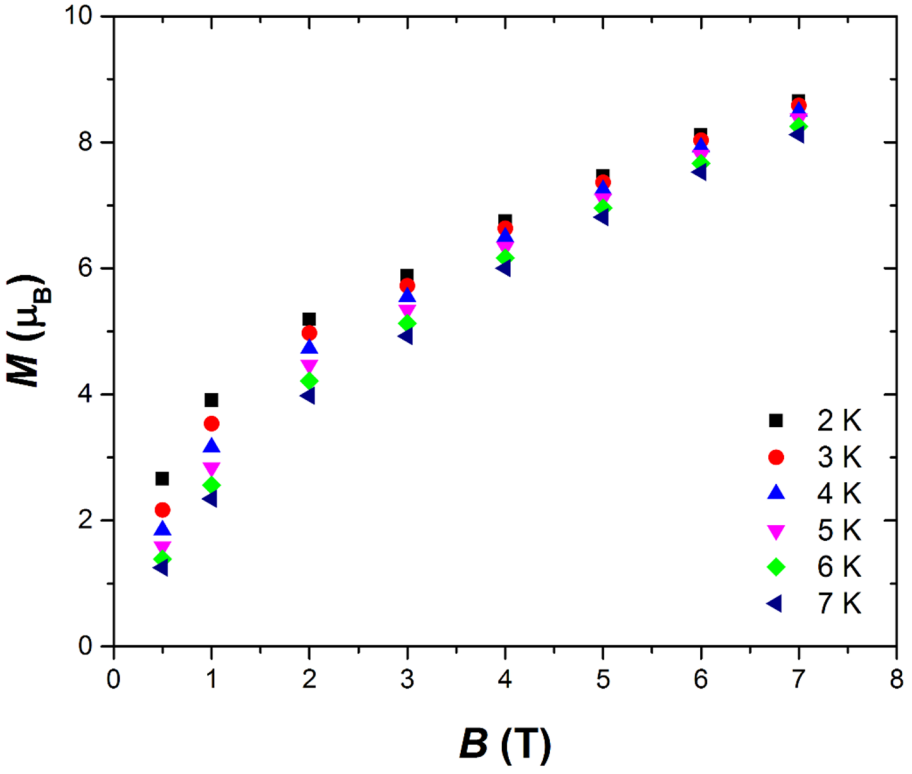

Figure S7. Plot of magnetisation (***M***) versus field (***B***) for compound **2** in the indicated field and temperature ranges.

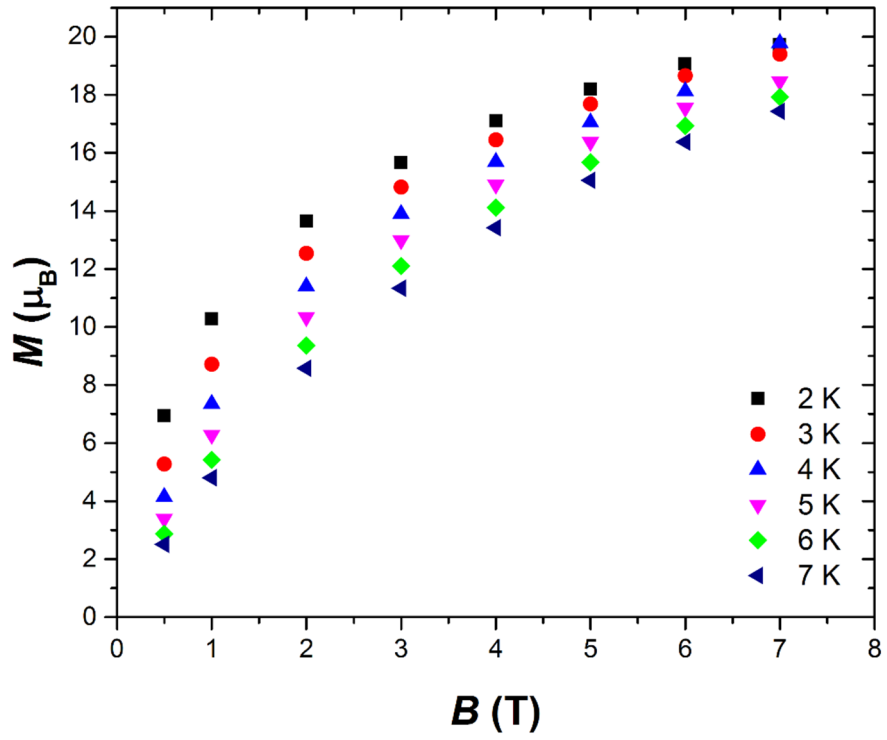

Figure S8. Plot of magnetization (***M***) versus field (***B***) for compound **3** in the indicated field and temperature ranges.

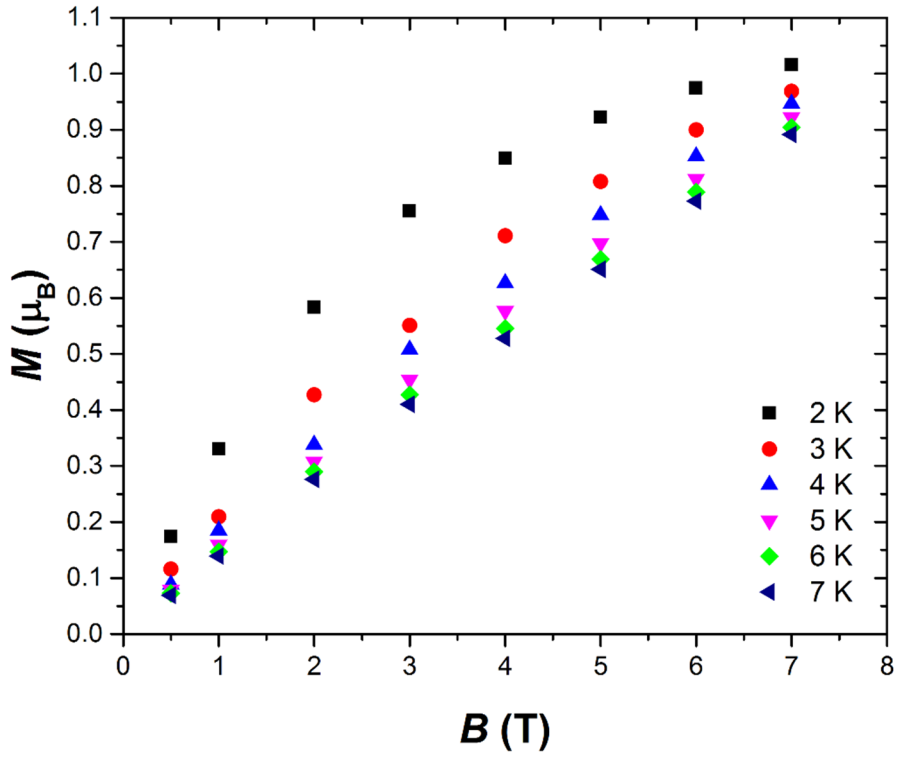

Figure S9. Plot of magnetisation (***M***) versus field (***B***) for compound **4** in the indicated field and temperature ranges.

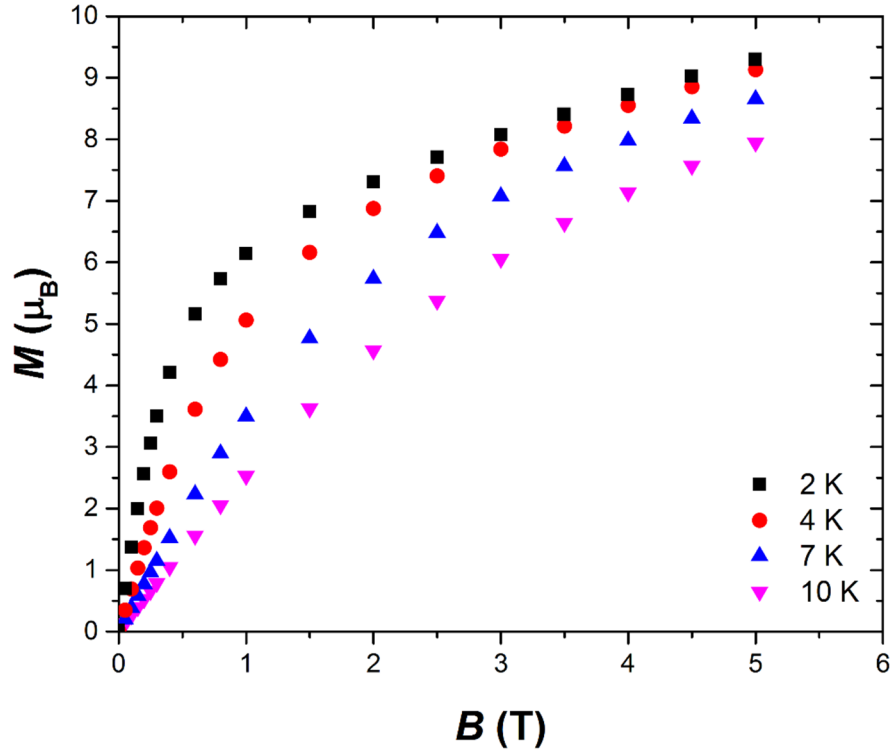

Figure S10. Plot of magnetization (***M***) versus field (***B***) for compound **5** in the indicated field and temperature ranges.

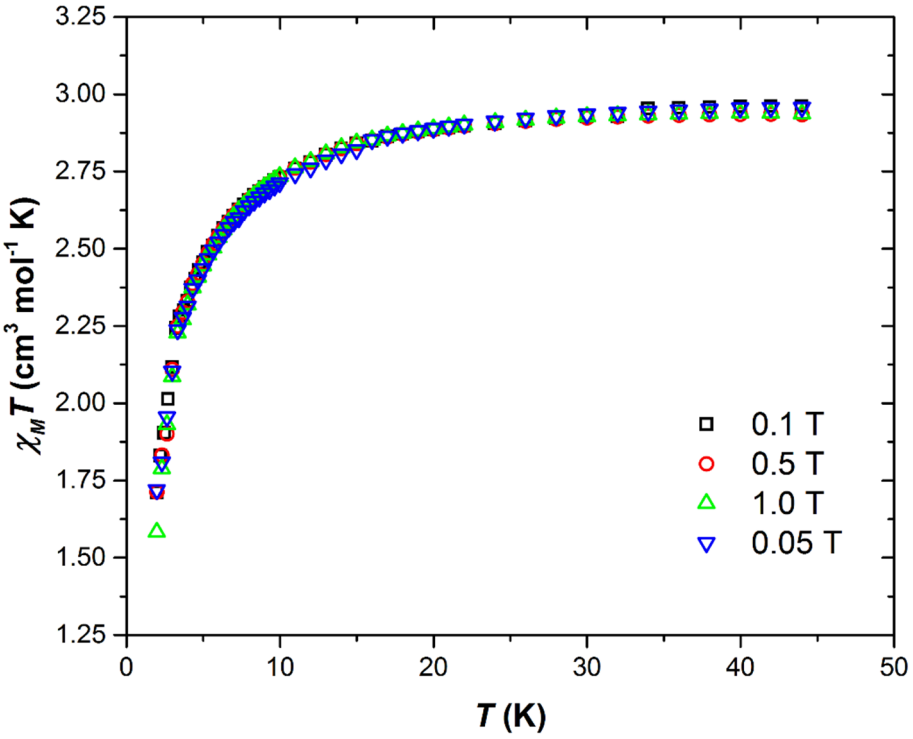

Figure S11. Plot of the $\chi_M T$ product versus *T* for complex **6** from 44-2 K under fields of 0.05, 0.1, 0.5 and 1.0 T. See text for details.

Chapter 6: Vanadyl-based hetereometallic wheels

Table S1. Crystallographic information for compounds **1**-**2**.

Compound	**1**	**2**
Formula	$C_{62}H_{68}Cl_4N_{10}Ni_5O_{22}V_2$	$C_{62}H_{68}Cl_4Co_5N_{10}O_{22}V_2$
$D_{calc.}$/ g cm^{-3}	1.721	1.712
μ/mm^{-1}	1.779	1.613
Formula Weight	1842.49	1843.59
Colour	dark green	pale brown
Shape	block	plate
Size/mm^3	0.52×0.29×0.16	0.50×0.14×0.06
T/K	120.0	120.0
Crystal System	monoclinic	monoclinic
Space Group	$P2_1/n$	$P2_1/n$
a/Å	15.7800(3)	15.7439(9)
b/Å	12.4392(2)	12.4867(5)
c/Å	19.0165(4)	18.9773(12)
α/°	90	90
β/°	107.745(2)	106.591(6)
γ/°	90	90
V/Å^3	3555.16(12)	3575.4(4)
Z (Z')	2 (0.5)	2 (0.5)
Wavelength/Å	0.71073	0.71073
Radiation type	MoK$_\alpha$	MoK$_\alpha$
Θ_{min}/° - Θ_{max}/°	3.072 – 32.985	3.079 – 28.897
Measured Refl.	90810	37370
Independent Refl.	12777	8344
Reflections Used	10678	5589
R_{int}	0.0447	0.0715
Parameters	516	479
Restraints	155	1
Largest Peak	0.678	1.013
Deepest Hole	-0.475	-0.678
GooF	1.042	1.041
wR_2 (all data) (wR_2)	0.0770 (0.0719)	0.1612 (0.1465)
R_1 (all data) (R_1)	0.0461 (0.0341)	0.1147 (0.0704)

Table S2. Selected structural parameters for the bridging motifs between the metal ion pairs in compound **1**. These include: V-O bond length, M-O bond length, M-Cl bond length, M-O-M bond angle and M-Cl-M bond angle.

	V-O (Å)	**M-O (Å)**	**M-Cl (Å)**	**M-O-M (°)**	**M-Cl-M (°)**
V1/M1	1.969, 2.057	1.995, 2.094	-	95.93, 102.11	-
V1/M2	2.057, 2.177	2.094, 2.122	-	98.29, 101.24	-
V1/M3	2.014, 2.177	2.028, 2.090	-	96.81, 104.27	-
M1/M3	-	2.041, 2.081	2.405, 2.413	103.18	84.20
M1/M2	-	2.053-2.122	-	95.82, 98.33	-
M2/M3	-	2.041-2.094	-	97.40, 100.28	-

Table S3. Selected structural parameters for the bridging motifs between the metal ion pairs in compound **2**. These include: V-O bond length, M-O bond length, M-Cl bond length, M-O-M bond angle and M-Cl-M bond angle.

	V-O (Å)	**M-O (Å)**	**M-Cl (Å)**	**M-O-M (°)**	**M-Cl-M (°)**
V1/M1	1.969, 2.054	2.010, 2.133	-	96.05, 102.98	-
V1/M2	2.054, 2.180	2.115, 2.170	-	99.09, 101.33	-
V1/M3	2.013, 2.180	2.026, 2.126	-	96.68, 105.61	-
M1/M3	-	2.078, 2.108	2.422, 2.455	102.91	84.34
M1/M2	-	2.075-2.170	-	94.18, 97.78	-
M2/M3	-	2.075-2.126	-	97.17, 99.97	-

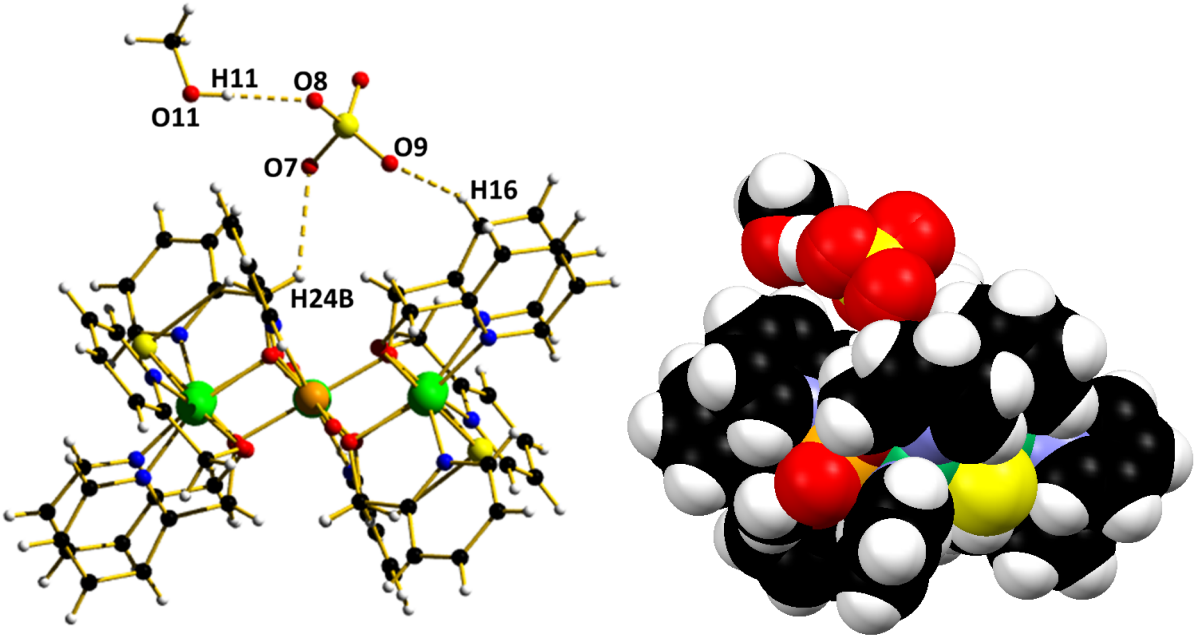

Figure S1. Illustration of the interaction between the MeOH molecules of crystallisation the ClO4- anions and the cations in **1** and **2**. Colour code as Figure 1. O8···H11 = 2.208 Å, O7···H24B = 2.595 Å, O9···H16 = 2.595 Å. The image on the right is the space-fill representation.

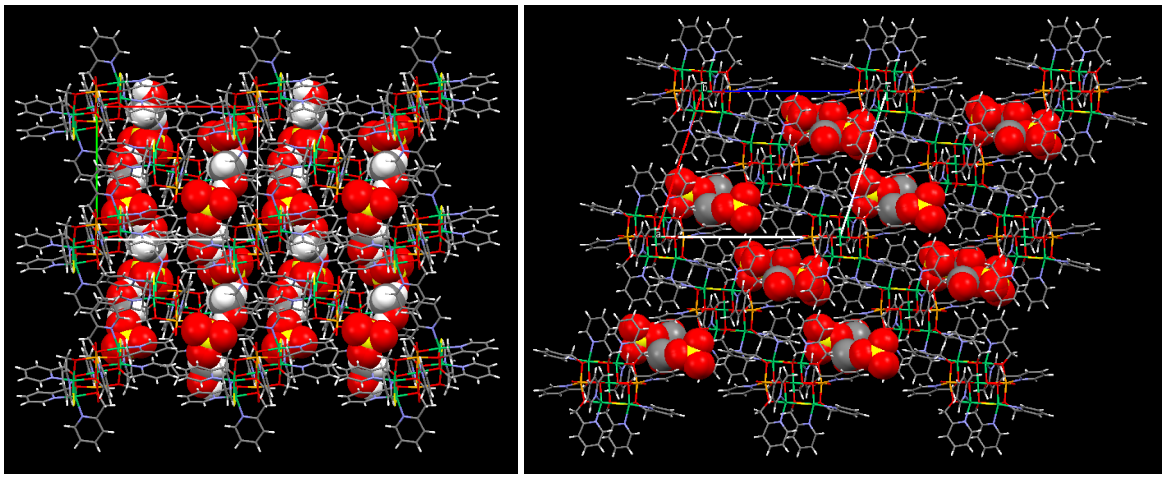

Figure S2. View of the extended structure in complex **1** down the *c* (left) and *b* (right) axes of the unit cell. The anions and solvent of crystallisation are depicted in space-fill and the cluster cations as capped sticks. Colour code as Figure 1.